NASA-CR-196749

MCAT Institute
Annual Report
94-01

Development of an Upwind, Finite-Volume Code with Finite-Rate Chemistry

Gregory A. Molvik

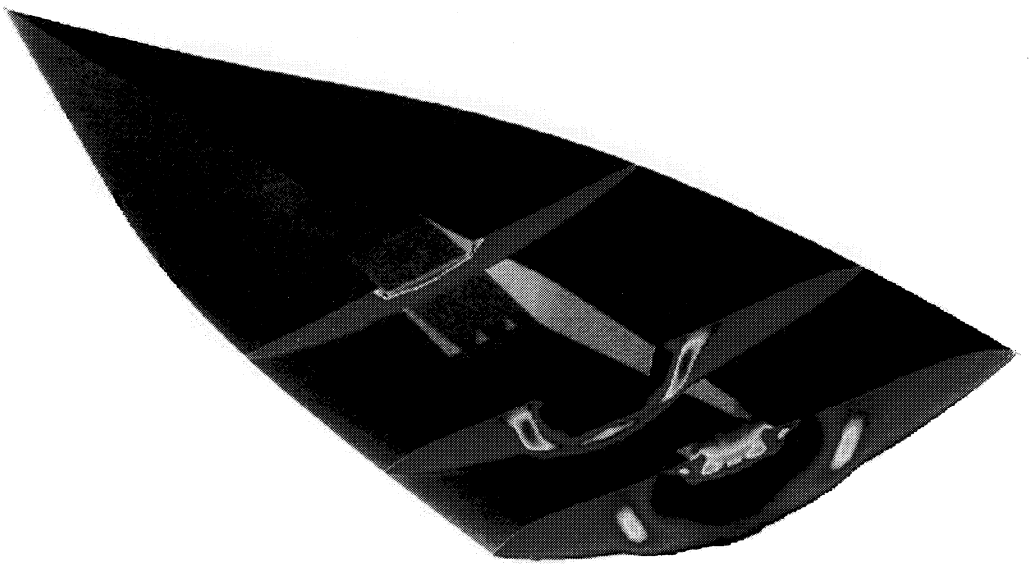

July 1994

NCC2-498

MCAT Institute
3933 Blue Gum Drive
San Jose, CA 95127

MCAT Institute

Development of an Upwind, Finite-Volume Code with Finite-Rate Chemistry

NCC2-498

Annual Report
July 31, 1994

Submitted to: NASA-Ames Research Center
Moffett Field, CA 94035
Dr. Terry L. Holst, Branch Chief
Dr. Scott L. Lawrence, Technical Monitor

Prepared by: MCAT Institute
3933 Blue Bum Drive
San Jose, CA 95127
Phone: (415)988-6514
Dr. Bala Balakrishnan, President
Dr. Gregory A. Molvik, Principal Investigator

ABSTRACT

Under this grant, two numerical algorithms were developed to predict the flow of viscous, hypersonic, chemically reacting gases over three-dimensional bodies. Both algorithms take advantage of the benefits of upwind differencing, total variation diminishing techniques and of a finite-volume framework, but obtain their solution in two separate manners. The first algorithm is a zonal, time-marching scheme, and is generally used to obtain solutions in the subsonic portions of the flow field. The second algorithm is a much less expensive, space-marching scheme and can be used for the computation of the larger, supersonic portion of the flow field. Both codes compute their interface fluxes with a temporal Riemann solver and the resulting schemes are made fully implicit including the chemical source terms and boundary conditions. Strong coupling is used between the fluid dynamic, chemical and turbulence equations. These codes have been validated on numerous hypersonic test cases and have provided excellent comparison with existing data.

INTRODUCTION

The design of recently proposed space transportation systems will, for the most part, be based on numerical simulations. This is because existing ground-based test facilities such as wind tunnels and arc jet heaters are expensive to operate and cannot duplicate the exact flight conditions of such vehicles. It is therefore the objective of this research to develop a computational tool capable of accurately predicting the flow of hypersonic, viscous, chemically-reacting flow about three-dimensional vehicles. It is the goal of this research to account for all relevant phenomenon in a numerical simulation. The chemical influence on a hypersonic flow field is apparent in the reduced heating rates to the Space Shuttle during reentry caused by chemical dissociation that takes place in the shock layer and by the non-catalytic behavior of the insulation tiles. Turbulence also plays an important role in performance of hypersonic vehicles and has a particularly strong impact on engine performance. Any proposed space transportation systems will also encounter these effects and hence should be included in the numerical simulation of such flow fields.

Numerical solutions to steady, hypersonic flow problems can be obtained with both time-marching and space-marching schemes. The large amounts of computer time required by time-marching algorithms can prohibit the computation of hypersonic flow fields about realistic geometries with a reasonable resolution. Space-marching schemes, on the other hand, can provide this resolution with relatively little computer time. However, each class of space-marching techniques has limitations on the type of flow field it is capable of computing. Parabolized Navier-Stokes (PNS) algorithms are limited to entirely supersonic flow fields with the exception of the subsonic viscous layer, and Viscous Shock Layer(VSL) techniques fail in the presence of both axial and crossflow separation. It is therefore advantageous to employ a space-marching scheme in the computation of the majority of the hypersonic flow field, and to use a time-marching scheme only in the flow field areas where the space-marching scheme fails. This combination of time- and space-marching techniques provides the required resolution about a hypersonic configuration in a reasonable amount of computer time.

Upwind numerical schemes have received wide recognition for their unsurpassed ability to capture flow field discontinuities without any user-specified smoothing terms. This property is very desirable for hypersonic computations in which numerous complex waves structures exist. And since these waves are typically very strong in such a flow field, the accurate prediction of their location and strength is required since small errors in these quantities can significantly affect the predicted dynamic loading and heat transfer on a vehicle.

Thermodynamic properties can be modeled several ways in a numerical simulation. The perfect gas model is the most simple however is not usually

valid for hypersonic computations. The assumption of chemical equilibrium can be employed in a hypersonic calculation and entails coupling a thermodynamic routine to the fluid dynamic equations. This can be done by either minimizing Gibbs Free Energy at each grid point in the computation or by utilizing a database of thermodynamic properties. The second approach can require much less computer time than the first with very little loss in accuracy. Chemical nonequilibrium effects are accounted for by solving additional conservation equations for each additional species. This can be done in either a strongly coupled or a loosely coupled manner. In a strongly coupled approach, the additional species equations are solved along with the fluid dynamic equations allowing information to readily flow between the two sets of governing equations. The weakly coupled approach allows the two equation sets to be solved separately which can reduce the required computer time per iteration. However since this second approach inhibits the flow of information between the two equation sets larger total computer times could become necessary to obtain a converged result. Finally, a thermo-chemical nonequilibrium computation is the most complete of the gas models by accounting for a nonuniform distribution of energy among the different modes. This is done by solving additional energy equations for each additional energy mode.

The primary task of this grant was the development and validation of an accurate numerical scheme for the computation of viscous, hypersonic, chemically-reacting flow fields. Two codes were created for this purpose. The first is a zonal, time-marching scheme. It is generally used to obtain the solution in the subsonic or separated regions of the hypersonic flow field. Extensive amounts of required computer time can prohibit the computation of an entire hypersonic flow field with a time-marching scheme of this nature. Hence, the second numerical scheme was developed. It is a Parabolized Navier-Stokes(PNS) space-marching scheme that obtains a solution in relatively little computer time and can be used to compute the larger supersonic portion of the flow field. The time-marching code has been given the name TUFF and the space-marching algorithm is referred to as STUFF. TUFF stands for "A Three-Dimensional, Upwind-Differenced, Finite-Volume Flow Solver with Fully Coupled Chemistry". The additional character in the space-marching code's name, STUFF, stands for Space-Marching.

NUMERICAL SCHEMES

The numerical schemes in both TUFF and STUFF are very similar and in fact, employ a lot of similar coding. This similarity is beneficial when using both codes on a single problem since compatibility of the two solutions is assured. It is also useful when making code changes since a change in one code can be directly implemented into the other code thereby making these codes ideal for research. Both codes employ a finite-volume philosophy to ensure that the schemes are fully conservative. Further, they obtain their upwind inviscid fluxes by employing a temporal Riemann solver that fully accounts for the gas model. A Total Variation Diminishing (TVD) technique allows extension of the schemes to higher orders of accuracy without introducing spurious oscillations. The schemes employ a strong coupling between the equation sets (including the

fluid-dynamic, species and turbulence equations) and are made fully implicit to eliminate the step-size restriction of explicit schemes. This is necessary since step-sizes in a viscous, chemically reacting calculation can be excessively small for an explicit scheme, and the resulting computer times prohibitively large. The schemes are made implicit by fully linearizing all of the fluxes and source terms and by employing a modified Newton iteration to eliminate any numerical errors that might occur. The viscous sublayer approximation is used in the space-marching algorithm to allow stable marching in the presence of a subsonic boundary layer. Lastly, a force and moment calculation are performed by integrating the inviscid as well as viscous forces over all viscous boundaries.

Both of the codes employ a versatile input routine that allows a wide range of problems to be solved. By changing a single parameter in the input deck, a one-, two- or three-dimensional analysis is possible. Further, the source terms for one-dimensional and two-dimensional, axi-symmetric problems are also options within the codes. A choice of integration options allows either an Approximate Factorization(AF) or an Lower-Upper(LU) factorization of the Left-Hand-Side to be performed. The LU scheme has the benefit of an unlimited time-step size and the AF scheme contains a superior implicit boundary condition treatment making the choice of integration option problem-dependent. The codes are capable of including thin-layer viscous terms in any of the non-space-marching directions. An option also exists in the time-marching code to use a constant time-step or a constant CFL number. Finally, all grid generation is external to the codes allowing the user to employ state-or-the-art interactive grid generation procedures.

A generalized, zonal capability was incorporated in the TUFF code to allow a greater flexibility of grid generation and to eliminate the memory limitations of large problems. It uses a patched grid technique that maintains conservation and allows a wide variety of grid topologies. This is done by defining the interface boundary as the union of all the face mesh points of the adjoining zones and triangulating them in a manner that maintains the original grid lines. Any gaps that are generated by this process are added/subtracted to/from the original cells in order to guarantee conservation. All of the zonal patching and metric computations are performed by the Conservative Interface Algorithm (CIA) code and are then supplied to the TUFF code for computation of the flow field. The CIA code serves as a preprocessor to TUFF and can also be used with other finite-volume codes to extend their capabilities. It has been successfully ported to the Compressible Navier-Stokes(CNS) code by Dr. Goetz Klopfer of MCAT Institute. The CIA code also has a generalized input allowing any boundary of any grid with any orientation to be zonal and further allows for curved zonal boundaries. The TUFF code uses the metrics computed by the CIA code to compute the inviscid and viscous interface fluxes.

Both the TUFF and STUFF codes have generalized boundary conditions that allow any boundary condition to be implemented on any boundary. Boundary conditions must be specified for the inviscid as well as the viscous fluxes. The boundary conditions on the inviscid flux are listed below:

- Zonal
- Reflective (solid wall)
- Non reflective (extrapolation)
- Fixed (free stream)
- Blunt Body Singularity
- Continuation (no change)
- Subsonic Inflow
- Subsonic Outflow
- Incompressible Inflow
- Incompressible Outflow
- Supersonic Blowing

Viscous boundary conditions must be specified on velocity, temperature, and species gradients. These boundary condition options are listed blow:

Velocity	• Viscous Zone • Inviscid • No Slip • Slip (for high altitude flows) • Viscous Inflow (Ablation or Blowing) • Viscous Outflow (Bleed)
Temperature	• Adiabatic • Specified Temperature • Radiative Equilibrium • Time of Flight
Catalycity	• Noncatalytic • Fully Recombined

For the approximate factorization option of the LHS, all of these boundary conditions are made fully implicit by linearizing them. The LU factorization option in the TUFF code only requires an explicit boundary condition.

The codes contain several gas models including non-equilibrium, equilibrium and perfect gas options. An incompressible option is also included in the TUFF code to fill out the range of models. The choice of model is made in the input deck by changing a single parameter. The equilibrium option currently uses Tannehill's curve its for air but may be changed by modifying a subroutine for the thermodynamics and another for the transport properties. The nonequilibrium option is also easily changed. Current nonequilibrium options exist for air, hydro-carbon/air, hydrogen/air and the Martian atmosphere. A choice of backward rate computations includes specific rates or a gibbs free-energy minimization computation for the backward rates. Recently, a two-temperature model was added to a version of the TUFF code however, at the close of this grant period was not in working condition. Further research is required to debug and validate this option.

Turbulence models that were implemented in the TUFF and STUFF codes include: the Baldwin-Lomax algebraic model and the Jones-Launder two-equation model. The Chien two-equation model was an option in early versions of these codes but because of problems around sharp convex corners, it was eliminated from the set or options. Transition is accounted for by either specifying the transition point or allowing the code to predict it based on Re_Θ/M. For the Baldwin Lomax model, the eddy viscosity is ramped up through the transition region, but this is not recommended for the two-equation option. The Zeeman compressibility correction is an option for the two-equation model and improves the computation of shear layers.

RESULTS

Numerous validation cases were performed with the TUFF and STUFF codes throughout the performance of this grant. A complete list of validation cases is included in Appendix A. Not included in this list are any problems that were absent of validation data including a NASP Diverter Door study, Transonic Sphere study and various other studies that were of interest to NASA and the Principal Investigator of this grant. Several cases are highlighted below.

Cone Test Case

The test case that was used throughout this grant to test all of the gas models and other enhancements to the TUFF and STUFF codes is that of a viscous, hypersonic, 5-degree cone. This test case proved to be very useful since it can be used as a test case for both codes and since extensive data exists for validation. The figure below shows the results of the STUFF code with the chemical non-equilibrium option.

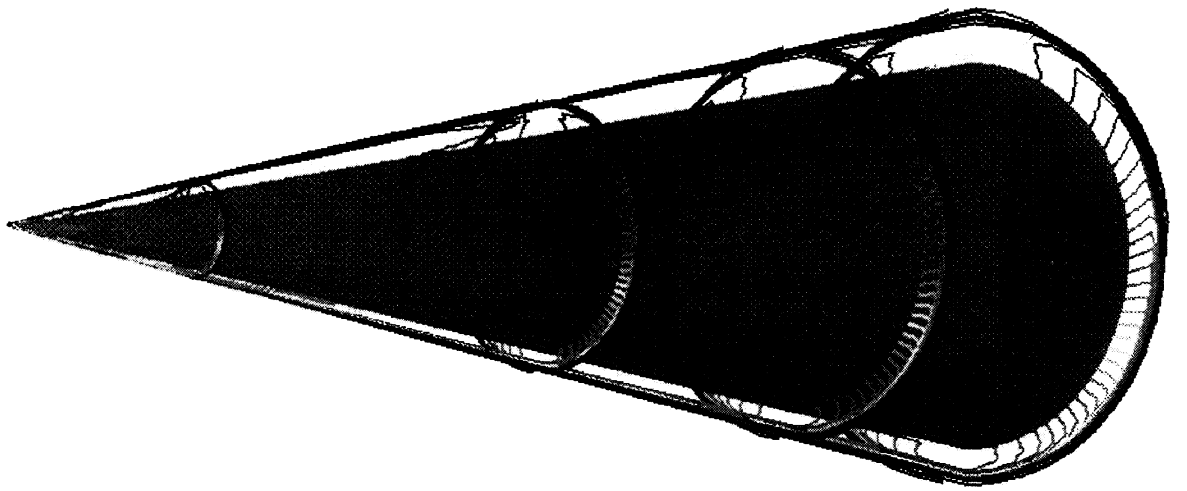

Figure 1. Pressure contours on a hypersonic 5 degree cone at an angle of attack.

Ribbed Blunt Cone Test Case

An experiment was conducted at the Ames Ballistic Range that provided ideal data for hypersonic code validation. In this experiment, blunt 5-degree cones were fired in air down the range. Two small shock generators (or ribs) were included to show the real-gas effects on the shape of the internal shock structure. Computations were performed with a combination of the TUFF and STUFF codes for validation purposes. The TUFF code was used to obtain the solution in the nose region and the STUFF code was used on the cone portion. The computed aerodynamic performance was compared with that of the experiment. Comparisons were also possible with the experimental shadowgraphs. The results of the experiment agreed quite well with those of the computations.

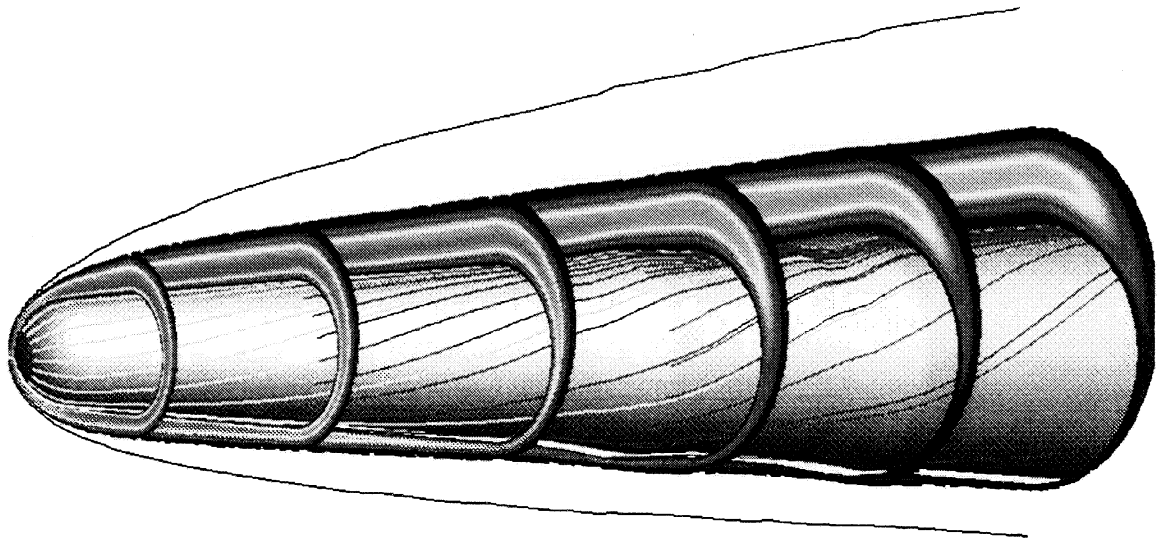

Figure 2. Atomic oxygen contours, surface stream lines and resulting shock on the ribbed blunt cone geometry at M=15, α=5°.

McDonnell Douglas Generic Option Test Case

A hypersonic test case was performed with the McDonnell Douglas Generic Option geometry. Since the experimental data on this geometry was not available, comparison is limited to that with different CFD codes. Several operating conditions were computed and compared including turbulent cases. Below is a figure showing the resulting atomic oxygen contours of the full scale geometry at a Mach number of 25.3 and Reynolds number of 3,300/m. This figure further shows an accumulation of hot, low-speed gas on the compression surface that would result in a degraded performance of a scramjet engine. The results of this test case along with other cases at other cruise conditions were in good agreement with other numerical data.

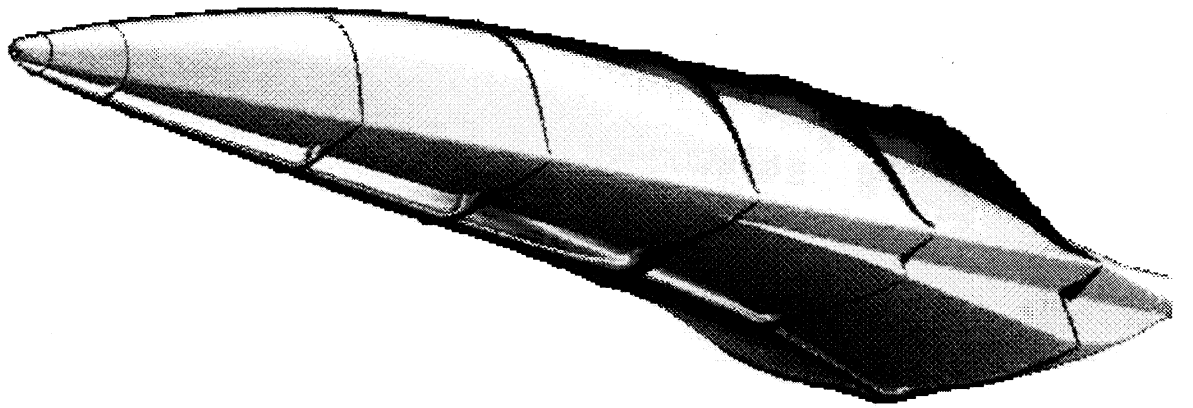

Figure 3. Atomic oxygen contours on the McDonnell Douglas Generic Option vehicle.

Hypersonic Diverter Door Demonstration Case

Of particular concern to designers of single-stage-to-orbit vehicles are the high aerodynamic and thermal loads on the vehicle in both the assent and reentry phases. A method to reduce these loads on the engine during reentry was conceived that included a door for the purpose of diverting the high speed flow around the engine. A numerical study was needed to determine the feasibility of this design.

The TUFF code was used to address the feasibility of this design. Because of the complexity of the design, a five-zone computation was necessary. The computations were performed at reentry conditions (M = 15, Re = 30,000/m) with fully turbulent flow. The figure below shows the temperature contours of the TUFF results. The solution indicated that the flow was unsteady and had periods of high energy flow entering the cavity. These results further indicated that improvements were needed to continue with this design.

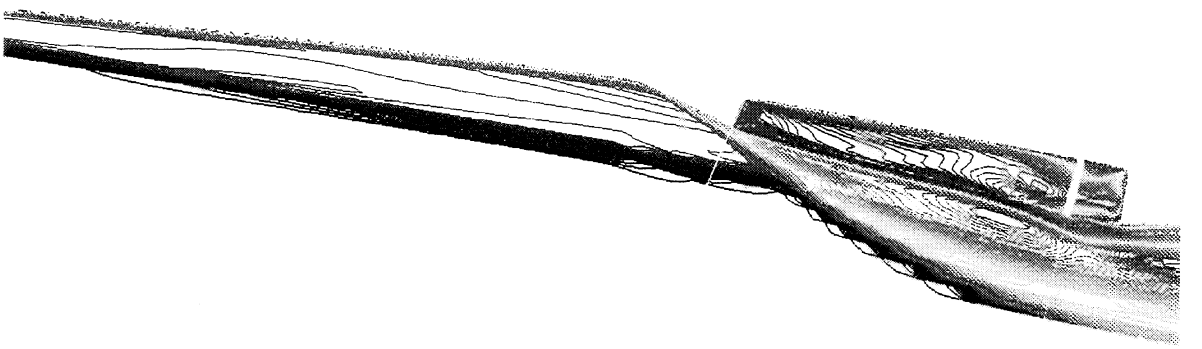

Figure 4. Temperature contours on the diverter door geometry showing the presence of very hot gasses within the cavity.

Hypersonic Research Vehicle Test Case

In support of the Hypersonic Research Program, the TUFF and STUFF codes were utilized in the conceptual design process of a hypersonic research vehicle (HRV). Engineering methods are traditionally used in the conceptual design process but can produce erroneous results in regions where simplifying assumptions break down. Further, these simplified methods lack the capability to predict any unforeseen physics associated with a particular design. CFD, on the other hand, can significantly improve the accuracy and detail of the results, but not without a penalty. Significant computer resources can be required for a complete CFD analysis of a hypersonic research vehicle with an integrated propulsion system.

The Ames HRV design (Mach No. = 8.0) is comprised of a waverider forebody with an integrated hydrocarbon scramjet engine. Waverider configurations have received a high degree of interest for their potentially high lift-to-drag ratios and their flow quality at the inlet plane. These characteristics are desirable for HRV missions, however the performance of the propulsion-integrated configuration may be much lower than that of the pure waverider shape. The propulsion system for the HRV is a hydrocarbon scramjet with augmented preburning. Hydrocarbon fuels offer sufficient specific impulse performance, heat sink capability and offer the potential of reduced vehicle size compared with hydrogen-powered designs. In addition, the handling and infrastructure requirements for the hydrocarbon fuels have a distinct advantage compared to cryogenic hydrogen. Because of the slow reaction rates of a hydrocarbon/air mixture in a supersonic stream, a mechanism is required to provide sufficient fuel/air temperatures for burning within the combustor. The concept developed for this purpose is an augmented preburner into which a small amount of fuel is burned with on-board liquid oxygen and injected into the airflow, upstream of the main fuel injector locations, thus ensuring that main fuel combustion is present and uninterrupted.

A nose-to-tail CFD analysis was conducted on the present design to determine the aerodynamic performance of the integrated waverider design and to access the feasibility of the current engine concept. Figure 5 shows the current HRV design along with CFD predicted pressure contours on several cross-flow planes. The bow shock remains attached to the waverider leading edge for the entire length of the vehicle. This feature is desirable since any spillage of the high pressure gasses onto the upper surface would reduce vehicle performance. The influence of the propulsion system on the pure waverider flow field is also shown in this figure by numerous pressure waves. These CFD results also show that the flow field quality at the inlet face is very good since the flow is uniform and little spillage is observed.

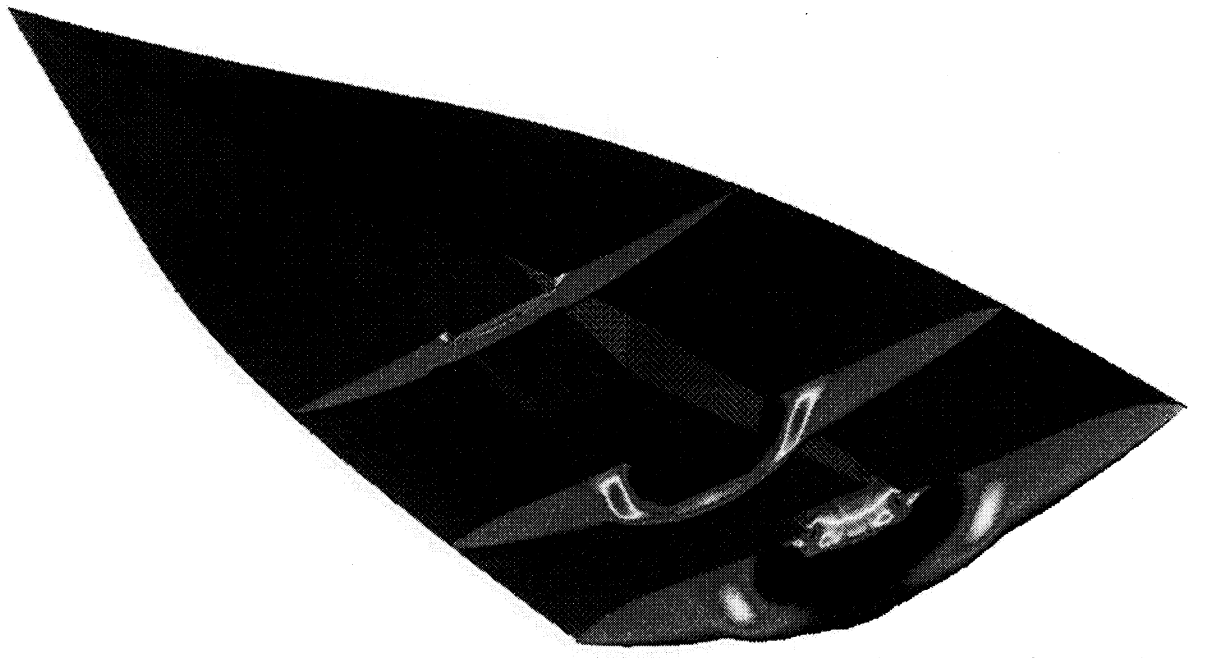

Figure 5. Pressure contours about the Ames Hydrocarbon fueled waverider HRV.

The current scramjet engine design is shown in the Figure 6 along with water contours at seven axial locations. This figure clearly shows the mechanism that is employed in the current design. The hot preburner gasses emerge from the preburner injector ports and mix with the oncoming air stream but still contain a very hot core just before main fuel injection station. This hot core, falling just above the main fuel injection, serves as a "pilot light" for main fuel injectors causing combustion of the main fuel to instantaneously occur. The main fuel injectors produce a significant amount of penetration without traversing the entire height of the scramjet. This figure indicates that the concept of preburning does indeed accomplish the task of maintaining combustion at the main fuel injection station and that an injector can be designed to provide significant flow path penetration without unstarting the engine.

The use of CFD in the conceptual design process proved to be invaluable. It answered critical questions concerning the basic concepts involved in the design of a HRV. The nose-to-tail analysis of the waverider HRV has clearly shown the benefits of the current design and has revealed areas for improvement. The analysis of the liquid oxygen-augmented preburning hydrocarbon scramjet indicates that the concept is viable and does indeed produce uninterrupted combustion of the main fuel within the scramjet engine.

Onera M6 Wing Test Case

The final test case included in this report is the Onera M6 Wing test case. This test case demonstrated the ability of the TUFF code to accurately predict the subsonic flow about a three-dimensional geometry. Comparison was made with experiment and with other numerical results and the TUFF results were in better agreement with experiment than most of the other codes. Results were obtained with the TUFF code with the LU option in roughly 4 hours on the Cray C90. The Figure below shows the surface pressure along with pressure comparisons with experiment.

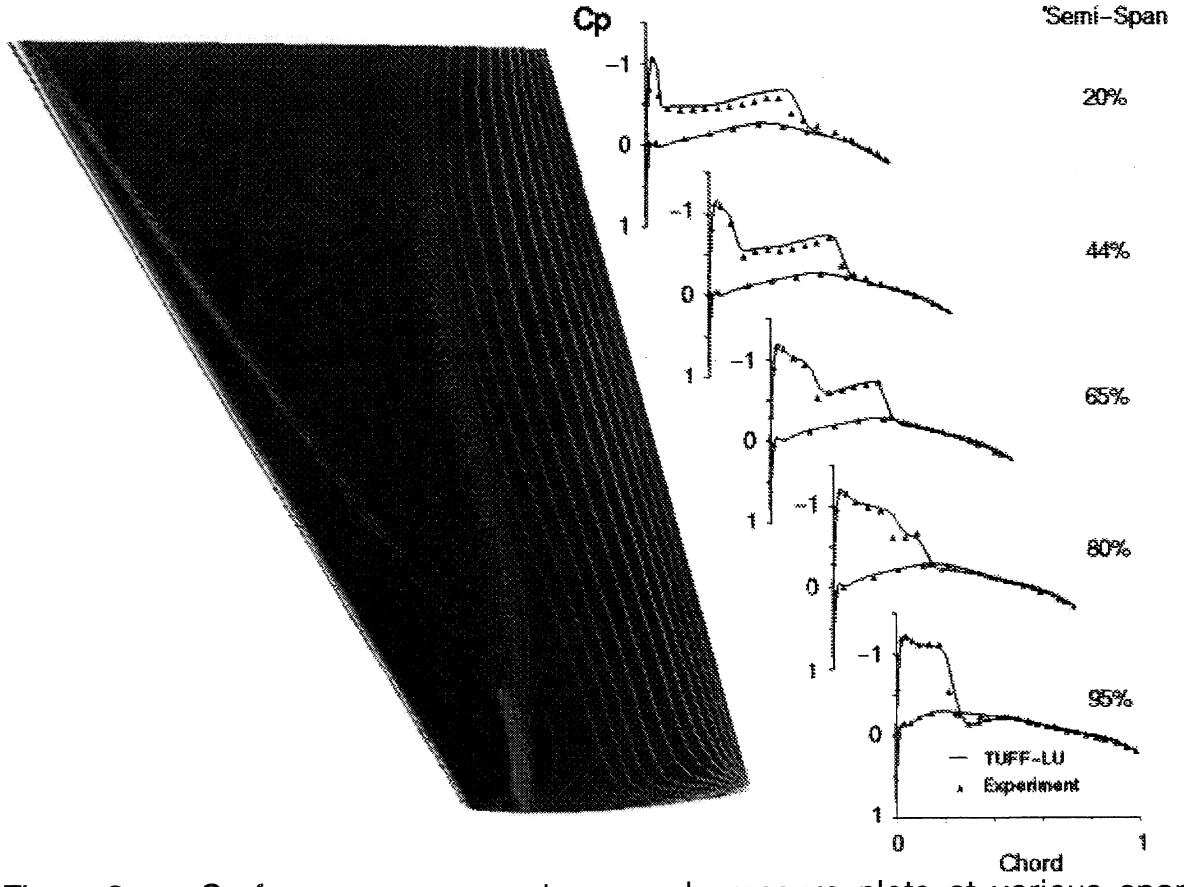

Figure 8. Surface pressure contours and pressure plots at various span locations.

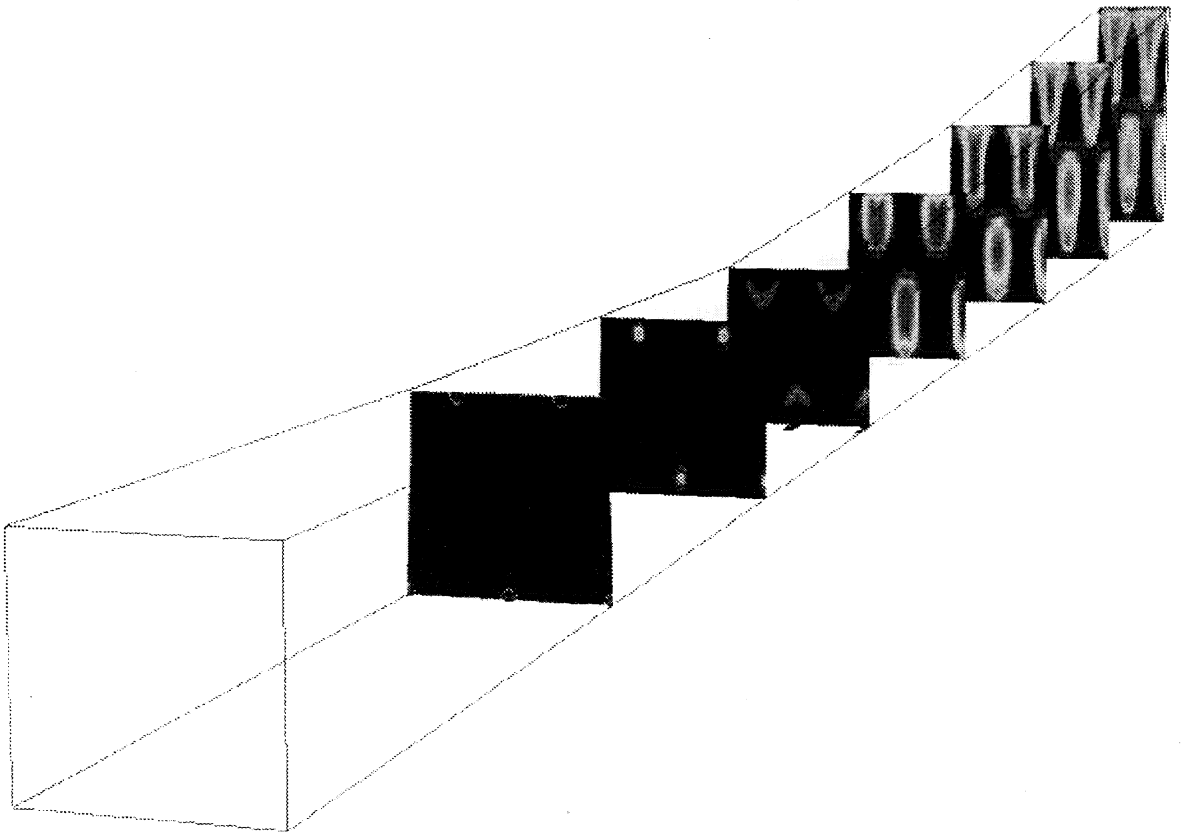

Figure 6. Water contours of the current hydrocarbon scramjet engine concept

PUBLICATIONS

1) Narayan, J. R., Molvik, G. A. and Wadawadigi, G., "Computation of High Speed Turbulent Reacting Flows Relevant to Scramjet Combustors," AIAA Paper No 94-2313, June 1994.

2) Molvik, G. A., Bowles, J. V and Huynh, L.C., "A Hypersonic Research Vehicle with Hydrocarbon Scramjet Propulsion: Design and Analysis," AIAA Paper No. 93-5097, November 1993.

3) Molvik, G. A., Bowles, J. V and Huynh, L.C., "Analysis of a Hypersonic Research Vehicle with a Hydrocarbon Scramjet Engine," AIAA Paper No. 93-0509, January 1993.

4) Molvik, G. A., Bowles, J. V and Huynh, L.C., "Analysis of a Hydrocarbon Scramjet with Augmented Preburning," AIAA Paper 92-3425, July 1992

5) Nichols, R. H., Mauss, J. R. and Molvik, G. A., "Calculation of High Speed Base Flows," AIAA Paper 92-2679, June 1992

6) Klopfer, G. H. and Molvik, G. A., "Conservative Multizonal Interface Algorithm for the 3-D Navier Stokes Equations," AIAA Paper 91- 1601, June 1991.

7) Molvik, G. A., "A Computational Model for the Prediction of Hypersonic, Reacting Flows", Ph.D. Thesis, Pennsylvania State University, 1989.

8) Strawa A. W., Molvik, G. A., Yates L. A., and Cornelison C., `` Experimental and Computational Results for 5 Degree Blunt Cones with Shock Generators at High Velocities", AIAA Paper 89-3377, August 1989.

9) Molvik, G. A. and Merkle, C. L., "A Set of Strongly Coupled, Upwind Algorithms for Computing Flows in Chemical Nonequilibrium", AIAA Paper 89-0199, January 1989.

APPENDIX A

TUFF/STUFF VALIDATION CASES

CASE	VALIDATED AGAINST EXP	COMP	ANALY
1) Inviscid Sphere			X
2) Inviscid Ramp			X
3) Viscous Flat Plate		X	X
4) Viscous Ramp		X	
5) Ram IIc	X	X	
6) Inviscid Cone		X	
7) Viscous Cone		X	
8) Sphere-Cylinder	X	X	
9) Blunt Cone with Shock Generators	X		
10) Transitional Flat Plate	X		
11) Transitional Cone	X	X	
12) McDonnell Douglas Generic Option II	X	X	
13) Zonal Inviscid Sphere			X
14) Zonal Flat Plate		X	
15) Zonal Viscous Sphere		X	
16) Transonic Nozzle			X

TUFF/STUFF VALIDATION CASES(Cont.)

CASE	VALIDATED AGAINST EXP	COMP	ANALY
17) Lewis Mach 5 Inlet	X	X	
18) Arc-Jet Test Case	X		
19) Zonal, Incompressible Cylinder			X
20) Laminar, Ethelene Flame	X	X	
21) OSU Waverider Forebody	X		X
22) Blunt Waverider	X	X	
23) Mixing/Shear Layer	X	X	
24) Ames Waverider Forebody			X
25) Ames Hydrocarbon Scramjet			X
26) Ames Hypersonic Research Vehicle			X
27) Turbulent Reacting Mixing Layer		X	
28) Turbulent Boundary Layer		X	
29) Burrows-Kurkov Test Case	X	X	
30) Onera M6 Wing Test Case	X	X	
31) Ogive Cylinder Test Case		X	
32) 3D Inviscid Ramp Case		X	

ATTACHMENTS

Copies of Papers

AIAA '89

AIAA-89-0199

A SET OF STRONGLY COUPLED, UPWIND ALGORITHMS FOR COMPUTING FLOWS IN CHEMICAL NONEQUILIBRIUM

G. A. Molvik, MCAT Institute, Moffett Field, CA and C. L. Merkle, Pennsylvania State University, University Park, PA

27th Aerospace Sciences Meeting
January 9–12, 1989/Reno, Nevada

A SET OF STRONGLY COUPLED, UPWIND ALGORITHMS FOR COMPUTING FLOWS IN CHEMICAL NONEQUILIBRIUM

Gregory A. Molvik†
MCAT Institute
NASA-Ames Research Center
Moffett Field, CA 94035

Charles L. Merkle‡
Department of Mechanical Engineering
Pennsylvania State University
University Park, PA 16802

ABSTRACT

Two new algorithms have been developed to predict the flow of viscous, hypersonic, chemically reacting gases over three-dimensional bodies. Both take advantage of the benefits of upwind differencing, Total Variation Diminishing (TVD) techniques and of a finite-volume framework, but obtain their solution in two separate manners. The first algorithm is a time-marching scheme, and is generally used to obtain solutions in the subsonic portions of the flow field. The second algorithm is a much less expensive, space-marching scheme and can be used for the computation of the larger, supersonic portion of the flow field. Both codes compute their interface fluxes with a new temporal Riemann solver and the resulting schemes are made fully implicit including the chemical source terms. Strong coupling is used between the fluid dynamic and chemical equations. These codes have been used to compute the hypersonic laminar flow of reacting air over a sphere-cylinder and over a cone at various angles of attack. Comparison of the results with existing data shows good agreement.

1. INTRODUCTION

The design of recently proposed space transportation systems such as the National Aerospace Plane[1] and the Aeroassisted Orbital Transfer Vehicle[2] will, for the most part, be based on numerical simulations. This is because existing ground-based test facilities such as wind tunnels and arc jet heaters cannot duplicate the exact flight conditions of such vehicles. It is therefore necessary to model all relevant phenomenon in an accurate numerical simulation. The presence of nonequilibrium effects in a hypersonic flow field is apparent in the reduced heating rates to the Space Shuttle during reentry caused by chemical dissociation that takes place in the shock layer and by the non-catalytic behavior of the insulation tiles.[3] The proposed space transportation systems will also encounter similar nonequilibrium effects and hence these effects should be included in the numerical simulation of such flow fields.

Many efforts in the past have included various degrees of nonequilibrium effects in numerical simulations. Chemical nonequilibrium have been included[3-13] by solving additional species conservation equations in either a strongly coupled or a weakly coupled manner. In a strongly coupled approach, the additional species equations are solved along with the fluid dynamic equations allowing information to readily flow between the two sets of governing equations. The weakly coupled approach allows the two equation sets to be solved separately which can reduce the required computer time per iteration. However since this second approach inhibits the flow of information between the two equation sets larger total computer times could become necessary to obtain a converged result. In addition to chemical nonequilibrium effects, thermal nonequilibrium effects can also be present in a hypersonic flow field. Pioneering research efforts [14-16] have been performed to include the effects thermal nonequilibrium in a numerical simulation. And even more recently, the effect of electro-magnetic radiation emanating from a nonequilibrium shock-layer on heat transfer has been addressed.[17]

Numerical solutions to steady, hypersonic flow problems have been obtained in the past using both time-marching[4-9] and space-marching[3,10-13] schemes. The large amounts of computer time required by time-marching algorithms can prohibit the computation of hypersonic flow fields about realistic geometries with any reasonable resolution. Space-marching schemes, on the other hand, can provide this resolution with relatively little computer time. However, each class of space-marching techniques has limitations on the type of flow field it is capable of computing. Parabolized Navier-Stokes (PNS) algorithms[10-12] are limited to entirely supersonic flow fields with the exception of the subsonic viscous layer, and Viscous Shock Layer(VSL) techniques[3,13] fail in the presence of both axial and cross-flow separation. It is therefore advantageous to employ a space-marching scheme in the computation of the majority of the hypersonic flow field, and to use a time-marching scheme only in the flow field areas where the space-marching scheme fails. This combination of a time-marching and a space-marching technique could provide the required resolution about a hypersonic configuration in a reasonable amount of computer time.

† Research Scientist, Member AIAA
‡ Professor, Member AIAA

Upwind numerical schemes have recently received wide recognition[18-25] for their unsurpassed ability to capture flow field discontinuities without any user-specified smoothing terms. This property is very desirable when computing hypersonic flow fields where numerous complex waves structures can exist. And since these waves are typically very strong in such a flow field, the accurate prediction of their location and strength is required since errors in these quantities can drastically alter the predicted dynamic loading and heat transfer on a vehicle.

In this paper, two numerical schemes are presented that incorporate several desirable features for the computation of viscous, hypersonic, chemically-reacting flow fields. The first is a time-marching scheme. It is generally used to obtain the solution in the subsonic or separated regions of the hypersonic flow field. Extensive amounts of required computer time can prohibit the computation of an entire hypersonic flow field with a time-marching scheme of this nature. Hence, the second numerical scheme was developed. It is a PNS space-marching scheme that obtains a solution in relatively little computer time and can be used to compute the larger supersonic portion of the flow field. Both codes employ a finite-volume philosophy to ensure that the schemes are fully conservative. Further, they obtain their upwind inviscid fluxes by employing a new temporal Riemann solver that accounts for the presence of a multicomponent mixture of gases. A Total Variation Diminishing (TVD) technique of the type outlined by Chakravarthy[24] allows extension of the schemes to higher orders of accuracy without introducing spurious oscillations. The schemes employ a strong coupling between the fluid dynamic and species conservation equations and are made fully implicit to eliminate the step-size restriction of explicit schemes. This is necessary since step-sizes in a viscous, chemically reacting calculation can be excessively small for an explicit scheme, and the resulting computer times prohibitively large. The schemes are made implicit by fully linearizing all of the fluxes and source terms and by employing a modified Newton iteration of the type described by Rai[25] to eliminate any linearization and approximate factorization error that might occur. Approximate factorization is employed to avoid solving many enormous banded matrices. Finally, the Vigneron approximation[26] is used in the space-marching algorithm to allow stable marching in the presence of a subsonic viscous layer.

2. GOVERNING EQUATIONS

2.1 Thin-Layer Navier-Stokes Equations

The equations governing the flow of viscous, chemically reacting gases can be written in integral form as:

$$\frac{d}{dt}\int_{\mathcal{V}} Q d\mathcal{V} + \int_{S} \mathrm{n}\cdot\mathrm{F} dS = \int_{\mathcal{V}} D d\mathcal{V} \qquad (1)$$

where $\mathcal{V}$ is a cell volume, $\mathrm{n}dS$ is a vector element of surface area with outward normal n, Q is the conserved variable per unit volume, F represents both the viscous and inviscid flux of Q through the cell faces and D consists the chemical source terms. In this equation, Q and D are algebraic vectors whose components are scalars and F is also an algebraic vector whose components are physical vectors.

The thin-layer approximation is made by neglecting all viscous transport terms except those normal to a viscous boundary. This is justified for flow fields with the moderate to high Reynolds numbers. The thin-layer Navier-Stokes equations can now be written for the generalized, six-sided cell volume shown in Fig. 1 by replacing the single surface integral in Eq. 1 with an integral over each cell face.

$$\frac{d}{dt}\int_{\mathcal{V}} Q d\mathcal{V} + \int\int (E_{i+\frac{1}{2}} - E_{i-\frac{1}{2}}) d\eta d\zeta$$

$$+ \int\int (F_{j+\frac{1}{2}} - F_{j-\frac{1}{2}}) d\xi d\zeta + \int\int (G_{k+\frac{1}{2}} - G_{k-\frac{1}{2}}) d\xi d\eta =$$

$$\frac{1}{Re}\int (S_{j+\frac{1}{2}} - S_{j-\frac{1}{2}}) d\xi d\zeta + \int_{\mathcal{V}} D d\mathcal{V} \qquad (2)$$

Here, ξ is the generalized streamwise coordinate, η is the body normal coordinate, and ζ represents the meridional coordinate. The indicies i, j and k represent the cell location in the ξ, η and ζ coordinate directions of the computational mesh respectively. A non-whole index, for instance $i+\frac{1}{2}$, corresponds to a cell interface.

By writing Eq. 1 for a generalized six-sided cell, three new family of fluxes are defined. The vectors E, F and G represent the inviscid flux through the cell interfaces with normals in the positive ξ-, η- and ζ-directions respectively. The dependent variables and these fluxes are presented below.

$$Q = \begin{pmatrix} \rho \\ \rho u \\ \rho v \\ \rho w \\ e \\ \rho_1 \\ \rho_2 \\ \vdots \\ \rho_{n-1} \end{pmatrix}, \quad E = \begin{pmatrix} \rho U \\ \rho U u + l_x p \\ \rho U v + l_y p \\ \rho U w + l_z p \\ (e+p)U \\ \rho_1 U \\ \rho_2 U \\ \vdots \\ \rho_{n-1} U \end{pmatrix},$$

$$F = \begin{pmatrix} \rho V \\ \rho V u + m_x p \\ \rho V v + m_y p \\ \rho V w + m_z p \\ (e+p)V \\ \rho_1 V \\ \rho_2 V \\ \vdots \\ \rho_{n-1} V \end{pmatrix}, \quad G = \begin{pmatrix} \rho W \\ \rho W u + n_x p \\ \rho W v + n_y p \\ \rho W w + n_z p \\ (e+p)W \\ \rho_1 W \\ \rho_2 W \\ \vdots \\ \rho_{n-1} W \end{pmatrix}$$

The metric quantities, l_x, l_y, and l_z are components of the cell face normal, l, pointing in the positive ξ-direction with length equal to the cell face area. Similarly, the other metric quantities are the components of the vectors m and n, which are the normal vectors of the other family of cell faces, and have length equal to their area. The volume

fluxes through each family of cell interfaces can now be defined:

$$U = l_x u + l_y v + l_z w \tag{3}$$
$$V = m_x u + m_y v + m_z w \tag{4}$$
$$W = n_x u + n_y v + n_z w \tag{5}$$

The only viscous flux remaining in the governing equations after the thin-layer approximation has been made is written as:

$$S = \frac{1}{\mathcal{V}} \begin{pmatrix} 0 \\ \ell_1 u_\eta + \ell_4 v_\eta + \ell_5 w_\eta \\ \ell_4 u_\eta + \ell_2 v_\eta + \ell_6 w_\eta \\ \ell_5 u_\eta + \ell_6 v_\eta + \ell_3 w_\eta \\ \frac{1}{2}\left(\ell_1 (u^2)_\eta + \ell_2 (v^2)_\eta + \ell_3 (w^2)_\eta\right) + \ell_7 T_\eta + \\ \ell_4 (uv)_\eta + \ell_5 (uw)_\eta + \ell_6 (vw)_\eta + \\ \ell_9 (c_1)_\eta + \ell_{10} (c_2)_\eta + \ldots + \ell_{n+7} (c_{n-1})_\eta \\ \ell_8 (c_1)_\eta \\ \ell_8 (c_2)_\eta \\ \vdots \\ \ell_8 (c_{n-1})_\eta \end{pmatrix}$$

The coefficients $\ell_1, \ell_2, \ldots, \ell_{n+7}$ have been defined as

$$\ell_1 = \mu \left[\frac{4}{3} m_x^2 + m_y^2 + m_z^2\right]$$
$$\ell_2 = \mu \left[m_x^2 + \frac{4}{3} m_y^2 + m_z^2\right]$$
$$\ell_3 = \mu \left[m_x^2 + m_y^2 + \frac{4}{3} m_z^2\right]$$
$$\ell_4 = \frac{\mu}{3} \left[m_x m_y\right]$$
$$\ell_5 = \frac{\mu}{3} \left[m_x m_z\right]$$
$$\ell_6 = \frac{\mu}{3} \left[m_y m_z\right]$$
$$\ell_7 = \beta_2 \kappa \left[m_x^2 + m_y^2 + m_z^2\right]$$
$$\ell_8 = \beta_3 \rho \mathcal{D} \left[m_x^2 + m_y^2 + m_z^2\right]$$
$$\ell_{s+8} = \ell_8 (h_s - h_n) \qquad s = 1, 2, \ldots, n-1$$

The chemical source term, D, has non-zero components corresponding to the species conservation equations. It is written as:

$$D = (0, 0, 0, 0, 0, \dot{w}_1, \dot{w}_2, \ldots, \dot{w}_{n-1})^T$$

where $\dot{w}_s$ is the mass production rate of species s due to any number of chemical reactions involving that species. This production rate is dependent up on the mixture temperature and on the species molar concentrations. The expressions for these production rates are given in Appendix A.

The density of the n^{th} species is determined by the following mass balance:

$$\rho_n = \rho - \sum_{s=1}^{n-1} \rho_s \tag{6}$$

Simply stated this expression says that the sum of the individual species densities must equal the total density. The equation of state for the mixture follows Dalton's law of partial pressures and is written as,

$$p = \frac{\beta_1 \rho T}{\mathcal{M}} \tag{7}$$

where the mixture molecular weight is determined by:

$$\mathcal{M} = \left(\sum_{s=1}^{n} \frac{c_s}{\mathcal{M}_s}\right)^{-1} \tag{8}$$

Here, c_s is the species mass fraction and is defined as ρ_s / ρ. The expression for total enthalpy is:

$$H = h + \frac{1}{2}(u^2 + v^2 + w^2) = \frac{e + p}{\rho} \tag{9}$$

This expression also provides the definition of total energy, e. The enthalpy of the mixture is determined by summing the individual contributions of each species.

$$h = \sum_{s=1}^{n} c_s h_s \tag{10}$$

The dimensional enthalpies and specific heats of each species are determined using the tables of Reference 27. Cubic spline interpolation is used to extract specific values from these tables. These tables use the following relationships (tildes denote dimensional quantities).

$$\tilde{h}_s = \tilde{T} \tilde{C}_{1,s}(\tilde{T}) + \tilde{h}_s^0 \tag{11}$$
$$\tilde{C}_{p,s} \equiv \frac{d\tilde{h}_s}{d\tilde{T}} = \tilde{C}_{2,s} \tag{12}$$

where, $\tilde{C}_{1,s}$ and $\tilde{C}_{2,s}$ are the values that are tabulated as functions of temperature, $\tilde{T}$. The frozen specific heat of the mixture is given by the following expression

$$\tilde{C}_{pf} \equiv \left.\frac{\partial \tilde{h}}{\partial \tilde{T}}\right|_{c_1, c_2, \ldots, c_n} = \sum_{s=1}^{n} c_s \tilde{C}_{p,s} \tag{13}$$

2.2 Transport Properties

All transport properties are those presented in Reference 27. The viscosity of a species, s, is calculated using the following curve fit.

$$\tilde{\mu}_s = 0.1 \exp\left[(A_s \log_e \tilde{T} + B_s) \log_e \tilde{T} + C_s\right] \tag{14}$$

where A_s, B_s and C_s are constants for each species. Eucken's formula is used to compute thermal conductivity

$$\tilde{\kappa}_s = \frac{\tilde{\mu}_s \tilde{\mathcal{R}}}{\tilde{\mathcal{M}}} \left(\frac{\tilde{C}_{p,s} \tilde{\mathcal{M}}_s}{\tilde{\mathcal{R}}} + \frac{5}{4}\right) \tag{15}$$

Wilke's mixing rule[28] is used to compute the mixture viscosity and thermal conductivity from those of the individual species. This is considered to be adequate for weakly ionizing gases.

$$\tilde{\mu} = \sum_{s=1}^{n} \frac{X_s \tilde{\mu}_s}{\phi_s}, \qquad \tilde{\kappa} = \sum_{s=1}^{n} \frac{X_s \tilde{\kappa}_s}{\phi_s} \tag{16}$$

where,

$$X_s = \frac{c_s \tilde{\mathcal{M}}}{\tilde{\mathcal{M}}_s} \tag{17}$$

$$\phi_s = \sum_{r=1}^{n} X_r \left[1 + \sqrt{\frac{\tilde{\mu}_s}{\tilde{\mu}_r}} \left(\frac{\tilde{\mathcal{M}}_r}{\tilde{\mathcal{M}}_s}\right)^{1/4}\right]^2 \left[\sqrt{8}\sqrt{1 + \frac{\tilde{\mathcal{M}}_s}{\tilde{\mathcal{M}}_r}}\right]^{-1} \tag{18}$$

If the binary Lewis numbers for all of the species are assumed to be the same, then a simple expression for the mixture's diffusion coefficient $\tilde{\mathcal{D}}$ results.

$$\tilde{\mathcal{D}} = \frac{\tilde{\kappa} \mathcal{L}e}{\tilde{\rho} \tilde{C}_{p,f}} \tag{19}$$

Currently, the effects of multicomponent diffusion are neglected. This assumption is adequate since the molecular weights of the species considered are not widely different.

2.3 Nondimensionalization

The nondimensionalization of all the quantities proceeds as follows (dimensional quantities are denoted by a tilde):

$$x, y, z = \frac{\tilde{x}, \tilde{y}, \tilde{z}}{\tilde{L}} \qquad p = \frac{\tilde{p}}{\tilde{\rho} \tilde{Q}_\infty^2} \qquad \dot{w}_s = \frac{\dot{\tilde{w}}_s \tilde{L}}{\tilde{\rho}_\infty \tilde{Q}_\infty}$$

$$u, v, w = \frac{\tilde{u}, \tilde{v}, \tilde{w}}{\tilde{Q}_\infty} \qquad h = \frac{\tilde{h}}{\tilde{Q}_\infty^2} \qquad \mu = \frac{\tilde{\mu}}{\tilde{\mu}_\infty}$$

$$\rho = \frac{\tilde{\rho}}{\tilde{\rho}_\infty} \qquad \mathcal{M} = \frac{\tilde{\mathcal{M}}}{\tilde{\mathcal{M}}_\infty} \qquad \kappa = \frac{\tilde{\kappa}}{\tilde{\kappa}_\infty}$$

$$T = \frac{\tilde{T}}{\tilde{T}_\infty} \qquad C_{p,f} = \frac{\tilde{C}_{p,f} \tilde{T}_\infty}{\tilde{Q}_\infty^2} \qquad \mathcal{D} = \frac{\tilde{\mathcal{D}}}{\tilde{\mathcal{D}}_\infty}$$

where $\tilde{Q}_\infty$ is the freestream velocity and $\tilde{L}$ is the geometric length scale which is typically set to unity. Using the notation of Reference 11, other nondimensional quantities appearing in the above equations are,

$$Re = \frac{\tilde{\rho}_\infty \tilde{Q}_\infty \tilde{L}}{\tilde{\mu}_\infty} \qquad \beta_2 = \frac{\tilde{\kappa}_\infty \tilde{T}_\infty}{\tilde{\mu}_\infty \tilde{Q}_\infty^2}$$

$$\beta_1 = \frac{\tilde{\mathcal{R}} \tilde{T}_\infty}{\tilde{\mathcal{M}} \tilde{Q}_\infty^2} \qquad \beta_3 = \frac{\tilde{\rho}_\infty \tilde{\mathcal{D}}_\infty}{\tilde{\mu}_\infty}$$

2.4 Chemistry Model

The chemistry model used in the present computations is air consisting of six species (plus electrons) undergoing seven reactions. The species considered are oxygen (O_2), atomic oxygen (O), atomic nitrogen (N), nitric oxide (NO), nitric oxide ion ($NO+$), nitrogen (N_2), and electrons (e^-). An assumption employed in this model is that the gas possesses a zero net local charge. This allows the conservation of electron mass equation to be eliminated from the set of governing equations. The reactions that are considered are:

$$\begin{array}{lllll}
(1)\ O_2 + M_1 & \rightleftharpoons 2O + M_1 & \\
(2)\ N_2 + M_2 & \rightleftharpoons 2N + M_2 & \\
(3)\ N_2 + N & \rightleftharpoons 2N + N & \\
(4)\ NO + M_3 & \rightleftharpoons N + O & +M_3 \\
(5)\ NO + O & \rightleftharpoons O_2 + N & \\
(6)\ N_2 + O & \rightleftharpoons NO + N & \\
(7)\ N + O & \rightleftharpoons NO^+ + e^- &
\end{array}$$

where M_1, M_2, and M_3 are catalytic third bodies. For the notation in Appendix C, this model has six species, ($n = 6$), seven reactions ($m = 7$) and ten reactants ($n_t = 10$). All of the needed reaction rates were obtained from Reference 27.

3. NUMERICAL FLUX

In this section the inviscid and viscous numerical fluxes are presented. First, the concept of an average flux on a cell interface must be addressed. This average flux(denoted with a $^-$), whether it be viscous or inviscid is written as:

$$\bar{F} = \frac{1}{\Delta\xi \Delta\zeta} \int_{\Delta\xi} \int_{\Delta\zeta} F d\zeta d\xi \tag{20}$$

The numerical flux, $\hat{F}$ is presented in this section and is an approximation of the cell face average flux, $\bar{F}$. The other inviscid numerical fluxes, $\hat{E}$ and $\hat{G}$ and the viscous numerical flux $\hat{S}$ are represented in a similar manner. The average dependent variables, $\bar{Q}$, are defined for each cell volume as,

$$\bar{Q} = \frac{1}{\Delta\xi \Delta\eta \Delta\zeta} \int_{\Delta\xi} \int_{\Delta\eta} \int_{\Delta\zeta} Q d\zeta d\eta d\xi \tag{21}$$

The grid size parameters $\Delta\xi$, $\Delta\eta$ and $\Delta\zeta$ are generally taken to be unity.

3.1 First Order Inviscid Flux

The numerical inviscid flux for a first-order accurate upwind algorithm is determined at a cell interface with the help of the Riemann problem. Figure 2 shows a Riemann problem set up at a cell interface. In general, the states to the left and right of the interface are known a priori and the solution to the Riemann problem consists of the strength, direction and velocity of any waves that emanate from the interface. With this information, one can determine the invariable state remaining at the cell interface for the time associated with the Riemann problem. And further, one can determine the flux of the dependent variables through the cell interface . One method of obtaining an approximate solution to this Riemann problem is the method outlined

by Roe.[21] It is this method that is currently used and is presented below.

In this approach, the flux at a cell interface is evaluated by first determining the flux change across each wave. The flux changes associated with waves traveling in the positive η-direction are given the symbol ΔF^+ and those in the negative direction are represented by ΔF^-. An eigenvalue analysis of the matrix $\frac{\partial \bar{F}}{\partial \bar{Q}}$, commonly referred to as B, reveals the speed and direction of each wave. Let the matrix $\mathbf{\Lambda}$ be a diagonal matrix consisting of these wave speeds. Details of this matrix are presented in Appendix A. The flux remaining at the interface for all time associated with this Riemann problem can then be represented by the following equations:

$$\hat{F}_{j+\frac{1}{2}} = \frac{1}{2}(F_j + F_{j+1} + \Delta F^-_{j+\frac{1}{2}} - \Delta F^+_{j+\frac{1}{2}}) \qquad (22)$$

Let $\mathbf{R}$ and $\mathbf{L}$ denote the matrix of right and left eigenvectors of the matrix $\mathbf{B}$ respectively, evaluated at the cell interface. The flux difference across the positive and negative velocity waves can be computed as follows,

$$\begin{aligned}\Delta F^+_{j+\frac{1}{2}} &= \frac{1}{2}\left(\mathbf{R}_{j+\frac{1}{2}}(\mathbf{\Lambda} + |\mathbf{\Lambda}|)_{j+\frac{1}{2}}\mathbf{L}_{j+\frac{1}{2}}\right)(\bar{Q}_{j+1} - \bar{Q}_j) \\ &= \mathbf{B}^+(\bar{Q}_{j+1} - \bar{Q}_j) \qquad (23)\\ \Delta F^-_{j+\frac{1}{2}} &= \frac{1}{2}\left(\mathbf{R}_{j+\frac{1}{2}}(\mathbf{\Lambda} - |\mathbf{\Lambda}|)_{j+\frac{1}{2}}\mathbf{L}_{j+\frac{1}{2}}\right)(\bar{Q}_{j+1} - \bar{Q}_j) \\ &= \mathbf{B}^-(\bar{Q}_{j+1} - \bar{Q}_j) \qquad (24)\end{aligned}$$

An entropy fix is used in the definition of the upwind flux to avoid expansion shocks and stream line separation problems. For further details of this entropy fix, the reader is referred to Reference 23.

The matrices $\mathbf{R}$, $\mathbf{L}$, and $\mathbf{\Lambda}$ are known functions of the dependent variables(see Appendix B). However, the dependent variables are not defined at the cell interfaces where these matrices must be evaluated. Roe[21] has developed a special averaging procedure to calculate the dependent variables on the cell interface for a perfect gas and satisfy the following criteria,

$$F_{j+1} - F_j = (\mathbf{B}^+ + \mathbf{B}^-)^{Roe}_{j+\frac{1}{2}}(\bar{Q}_{j+1} - \bar{Q}_j) \qquad (25)$$

The superscript ^{Roe} denotes a "Roe-averaged" quantity. Liu and Vinokur[29] have extended this analysis to include considerations for the presence of a multicomponent gas. By satisfying the relation above, the shock capturing capabilities of the algorithm are retained and correct wave speeds are assured. The Roe-averaging of the dependent variables described by Reference 29 proceeds as follows:

$$u_{j+\frac{1}{2}} = \frac{u_j\sqrt{\rho_j} + u_{j+1}\sqrt{\rho_{j+1}}}{\sqrt{\rho_j} + \sqrt{\rho_{j+1}}} \qquad (26)$$

$$v_{j+\frac{1}{2}} = \frac{v_j\sqrt{\rho_j} + v_{j+1}\sqrt{\rho_{j+1}}}{\sqrt{\rho_j} + \sqrt{\rho_{j+1}}} \qquad (27)$$

$$w_{j+\frac{1}{2}} = \frac{w_j\sqrt{\rho_j} + w_{j+1}\sqrt{\rho_{j+1}}}{\sqrt{\rho_j} + \sqrt{\rho_{j+1}}} \qquad (28)$$

$$H_{j+\frac{1}{2}} = \frac{H_j\sqrt{\rho_j} + H_{j+1}\sqrt{\rho_{j+1}}}{\sqrt{\rho_j} + \sqrt{\rho_{j+1}}} \qquad (29)$$

$$c_{s\,j+\frac{1}{2}} = \frac{c_{sj}\sqrt{\rho_j} + c_{sj+1}\sqrt{\rho_{j+1}}}{\sqrt{\rho_j} + \sqrt{\rho_{j+1}}} \qquad (30)$$

The only remaining variables needed at the cell interface for the evaluation of the matricies are $c_{j+\frac{1}{2}}$, $\gamma_{j+\frac{1}{2}}$, and $D_{sj+\frac{1}{2}}$. The definition of these additional variables can be found in Appendix A. Since the choice of these values that satisfy the Roe criteria is not unique, some approximate quadratures are implemented. This proceeds as follows. First a good initial guess at these values is made.

$$\hat{c} = \frac{c_j + c_{j+1}}{2} \qquad (31)$$

$$\hat{\gamma} = \frac{\gamma_j + \gamma_{j+1}}{2} \qquad (32)$$

$$\hat{D}_s = \frac{D_{sj} + D_{sj+1}}{2} \qquad (33)$$

Next, a set of these values that satisfy Roe's criteria is determined. This is accomplished by projecting the initial values on to a hyperplane defined by the solution of Eq. 25.

$$D_{sj+\frac{1}{2}} = \frac{\hat{D}_s - \hat{c}^4\Delta\rho_s\delta p/\chi}{1 - \Delta p\delta p/\chi} \qquad (34)$$

$$\gamma_{j+\frac{1}{2}} = \frac{\hat{\gamma} - 1}{1 - \Delta p\delta p/\chi} + 1 \qquad (35)$$

where the Δ operator denotes $[(\cdot)_{j+1} - (\cdot)_j]$ and where,

$$\delta p = \Delta p + \sum_{s=1}^{n}\hat{D}_s\Delta\rho_s - (\hat{\gamma} - 1)(\Delta(\rho h) - \Delta p) \qquad (36)$$

$$\chi = \sum_{s=1}^{n}(\hat{c}^2\Delta\rho_s)^2 + (\Delta p)^2 \qquad (37)$$

and finally, the Roe-averaged frozen speed of sound is determined:

$$c_{j+\frac{1}{2}} = \sqrt{(\gamma_{j+\frac{1}{2}} - 1)h_{j+\frac{1}{2}} - \sum_{s=1}^{n}c_{sj+\frac{1}{2}}D_{sj+\frac{1}{2}}} \qquad (37)$$

For further details of this averaging procedure, see Reference 29. The inviscid fluxes on the families of cell interfaces are obtained in a similar manner by using the appropriate metric quantities.

3.2 Viscous Flux

The second-order viscous flux at the cell interface is obtained by realizing that all of the viscous elements have the form:

$$\phi_{j+\frac{1}{2}}(\psi_{j+1} - \psi_j) \qquad (38)$$

Note that central differencing about the corresponding cell interface is used for any derivatives that appear in the viscous flux. If the values of $\phi_{j+\frac{1}{2}}$ represent a simple average of ϕ in the neighboring cells then a second-order evaluation of the viscous term results. For example in the x-momentum equation, the quantity that depends on the neighboring

cells and hence needs to be averaged is $\left(\frac{\mu}{\mathcal{V}}\right)$. Note that the cell volume $\mathcal{V}$ is included in the averaging. The metric quantities m_x,m_y and m_z are known quantities on the cell wall and hence are not included in the averaging.

3.3 Linearization of the Fluxes

In order to obtain either the space-marching or time-iterative fully implicit numerical schemes discussed later in this paper, certain flux Jacobians must first be determined. These Jacobians arise from a simple linearization of the inviscid and viscous fluxes. For an implicit scheme, fluxes are evaluated at a location in space or time where the dependent variables are not readily known. Therefore, in order to evaluate these fluxes, a linearization with respect to the dependent variables is performed at a near by state thereby allowing a good approximation to this unknown flux. The first-order numerical flux on the $j+\frac{1}{2}$ cell interface, evaluated at the most recent step (whether it be a spatial step or time step), is represented as:

$$\begin{aligned}\hat{F}^{p+1}_{j+\frac{1}{2}} =& \frac{1}{2}[F^{p+1}_{j+1} + F^{p+1}_{j} \\ &+ (B^- - B^+)^{p+1}_{j+\frac{1}{2}}(\bar{Q}^{p+1}_{j+1} - \bar{Q}^{p+1}_{j})]\end{aligned} \tag{39}$$

An approximate linearization of this interface flux may be achieved by freezing the coefficient matrix $(B^- - B^+)$ at last step p and linearizing the remaining terms. Numerical experiments have shown that such an approximation is acceptable.[18] The linearized numerical flux is then written as:

$$\begin{aligned}\hat{F}^{p+1}_{j+\frac{1}{2}} =& \frac{1}{2}\left[B^p_{j+1} + (B^- - B^+)^p_{j+\frac{1}{2}}\right]\Delta\bar{Q}_{j+1} \\ &+ \frac{1}{2}\left[B^p_{j} - (B^- - B^+)^p_{j+\frac{1}{2}}\right]\Delta\bar{Q}_{j} + \hat{F}^p_{j+\frac{1}{2}} \\ =&(\hat{B}^R)^p_{j+\frac{1}{2}}\Delta\bar{Q}_{j+1} + (\hat{B}^L)^p_{j+\frac{1}{2}}\Delta\bar{Q}_{j} + \hat{F}^p_{j+\frac{1}{2}}\end{aligned} \tag{40}$$

where, $\Delta\bar{Q}_j$ is either a spatial or temporal increment in the dependent variables and p is the index corresponding to that increment.

$$\Delta\bar{Q}_j = \bar{Q}^{p+1}_j - \bar{Q}^p_j \tag{41}$$

The linearization of the viscous numerical flux, $\hat{S}_{j+\frac{1}{2}}$, is accomplished by freezing the value of viscosity and linearizing the remaining terms. Since these remaining terms are only a function of the dependent variables in the neighboring cells, the linearization is straightforward.

$$\begin{aligned}\hat{S}^{p+1}_{j+\frac{1}{2}} =& \hat{S}^p_{j+\frac{1}{2}} + \left(\frac{\partial\hat{S}_{j+1/2}}{\partial\bar{Q}_{j+1}}\right)\Delta\bar{Q}_{j+1} + \left(\frac{\partial\hat{S}_{j+1/2}}{\partial\bar{Q}_{j}}\right)\Delta\bar{Q}_{j} \\ =&\hat{S}^p_{j+\frac{1}{2}} + \hat{M}^R_{j+\frac{1}{2}}\Delta\bar{Q}_{j+1} + \hat{M}^L_{j+\frac{1}{2}}\Delta\bar{Q}_{j}\end{aligned} \tag{42}$$

A similar type of linearization for the meridional flux $\hat{G}$ and the streamwise numerical flux $\hat{E}$ can also be performed. However, a special linearization is reserved for the streamwise flux in the space-marching scheme. This will be addressed in that section.

3.4 Higher Order Flux

A higher order inviscid numerical flux can be produced by adding a corrective terms to the first-order flux. And in order to suppress any spurious oscillations that might occur, the correction terms must fulfill certain Total Variation Diminishing (TVD) criteria. Reference 24 outlines a class of flux-difference limiting schemes that meet this criteria. The higher order flux (denoted by the superscript ^{HO}) is written as:

$$\begin{aligned}\hat{F}^{HO}_{j+\frac{1}{2}} =& \hat{F}^{1^{st}}_{j+\frac{1}{2}} \\ &- \mathbf{R}_{j+\frac{1}{2}}\mathbf{\Lambda}^-_{j+\frac{1}{2}}\left\{\frac{(1-\phi)}{4}\left[\Delta\widetilde{\alpha_{j+\frac{3}{2}}}\right] + \frac{(1+\phi)}{4}\left[\Delta\widetilde{\widetilde{\alpha_{j+\frac{1}{2}}}}\right]\right\} \\ &+ \mathbf{R}_{j+\frac{1}{2}}\mathbf{\Lambda}^+_{j+\frac{1}{2}}\left\{\frac{(1+\phi)}{4}\left[\Delta\widetilde{\alpha_{j+\frac{1}{2}}}\right] + \frac{(1-\phi)}{4}\left[\Delta\widetilde{\widetilde{\alpha_{j-\frac{1}{2}}}}\right]\right\}\end{aligned} \tag{43}$$

This notation allows one to pick from a family of schemes with a choice of the parameter ϕ. For instance, two popular schemes are the fully upwind scheme ($\phi = -1$) and a third-order scheme ($\phi = \frac{1}{3}$). Note that the characteristic variable difference is the limited quantity in the present scheme. The characteristic variable difference is defined as:

$$\Delta\alpha_{j+\frac{1}{2}} = \mathbf{L}_{j+\frac{1}{2}}(\bar{Q}_{j+1} - \bar{Q}_j) \tag{44}$$

The limiting operators are defined with the "minmod" operator as,

$$\widetilde{(\cdot)}_{j+\frac{1}{2}} = \text{minmod}\left[(\cdot)_{j+\frac{1}{2}}, \beta(\cdot)_{j-\frac{1}{2}}\right] \tag{45}$$

$$\widetilde{\widetilde{(\cdot)}}_{j+\frac{1}{2}} = \text{minmod}\left[(\cdot)_{j+\frac{1}{2}}, \beta(\cdot)_{j+\frac{3}{2}}\right] \tag{46}$$

where the minmod operator is defined as

$$\text{minmod}[x, y] = \text{sign}(x) * \max[0, \min\{|x|, y * \text{sign}(x)\}] \tag{47}$$

and β is a compression parameter that is restricted to lie in the range

$$1 < \beta \leq \frac{3-\phi}{1-\phi}$$

4. TIME-MARCHING SCHEME

In this section, a time-marching scheme is presented that can either calculate an unsteady or time-asymptotic solutions to chemically reacting flow problems.

4.1 Numerical Scheme

If the high-order upwind, numerical fluxes described in the previous section are used at the cell faces, and an average set dependent variables are defined for each cell in

the computational mesh, the thin-layer formulation of the governing equations is written as:

$$\frac{\bar{Q}^{n+1}_{i,j,k} - \bar{Q}^{n}_{i,j,k}}{\Delta t}\mathcal{V}_{i,j,k} + (\hat{E}^{HO}_{i+\frac{1}{2},j,k} - \hat{E}^{HO}_{i-\frac{1}{2},j,k})^{n+1}$$
$$+(\hat{F}^{HO}_{i,j+\frac{1}{2},k} - \hat{F}^{HO}_{i,j-\frac{1}{2},k})^{n+1} + (\hat{G}^{HO}_{i,j,k+\frac{1}{2}} - \hat{G}^{HO}_{i,j,k-\frac{1}{2}})^{n+1}$$
$$= \frac{1}{Re}(\hat{S}_{i,j+\frac{1}{2},k} - \hat{S}_{i,j-\frac{1}{2},k})^{n+1} + \mathcal{V}_{i,j,k}\hat{D}^{n+1}_{i,j,k} \quad (48)$$

Note that only a first-order formula is used for the time term however, higher-order formulas are easily implemented for time-accurate computations. The numerical source term, $\hat{D}$, is evaluated using the cell averaged dependent variables.

For a fully implicit scheme, the fluxes and source term are evaluated at the $n+1$ time step. This is accomplished by linearizing these terms in the governing equations with respect to the time-change of the dependent variables. However, in order to limit the implicit stencil of dependent cells, only the first-order contribution to the inviscid fluxes is included in this linearization. This provides an implicit stencil of only three cells in each generalized coordinate direction. Now, to avoid the expense of inverting a large sparse matrix, three-dimensional approximate factorization is employed to break the banded matrix into three block-tridiagonal matrices. If the variables with asterisks denote intermediate variables, this is written in the following three steps. And finally, in an effort to reduce any errors that might occur in the scheme, such as linearization error and approximate factorization error, a modified Newton iteration process is employed. The entire implicit formula for the time-marching scheme is then written as,

$$\left(I - \hat{T}^{p}_{i,j,k}\right)\Delta\bar{Q}^{*}_{i,j,k} + \frac{\Delta t}{\mathcal{V}_{i,j,k}}\left[\left(\hat{A}^{R}\right)^{p}_{i+\frac{1}{2}}\Delta\bar{Q}^{*}_{i+1,j,k}\right.$$
$$\left.+\{\left(\hat{A}^{L}\right)^{p}_{i+\frac{1}{2}} - \left(\hat{A}^{R}\right)^{p}_{i-\frac{1}{2}}\}\Delta\bar{Q}^{*}_{i,j,k} - \left(\hat{A}^{L}\right)^{p}_{i-\frac{1}{2}}\Delta\bar{Q}^{*}_{i-1,j,k}\right]$$
$$= -\left(\bar{Q}^{p}_{i,j,k} - \bar{Q}^{n}_{i,j,k}\right) - \frac{\Delta t}{\mathcal{V}_{i,j,k}}\left[\left(\hat{E}^{HO}_{i+\frac{1}{2},j,k} - \hat{E}^{HO}_{i-\frac{1}{2},j,k}\right)\right.$$
$$+\left(\hat{F}^{HO}_{i,j+\frac{1}{2},k} - \hat{F}^{HO}_{i,j-\frac{1}{2},k}\right) + \left(\hat{G}^{HO}_{i,j,k+\frac{1}{2}} - \hat{G}^{HO}_{i,j,k-\frac{1}{2}}\right)$$
$$\left.-\frac{1}{Re}\left(\hat{S}_{i,j+\frac{1}{2},k} - \hat{S}_{i,j-\frac{1}{2},k}\right) - \mathcal{V}_{i,j,k}\hat{D}_{i,j,k}\right]^{p}$$

.....

$$\left(I - \hat{T}^{p}_{i,j,k}\right)\Delta\bar{Q}^{**}_{i,j,k} + \frac{\Delta t}{\mathcal{V}_{i,j,k}}\left[\left(\hat{B}^{R} - \frac{\hat{M}^{R}}{Re}\right)^{p}_{j+\frac{1}{2}}\Delta\bar{Q}^{**}_{i,j+1,k}\right.$$
$$+\left\{\left(\hat{B}^{L} - \frac{\hat{M}^{L}}{Re}\right)^{p}_{j+\frac{1}{2}} - \left(\hat{B}^{R} - \frac{\hat{M}^{R}}{Re}\right)^{p}_{j-\frac{1}{2}}\right\}\Delta\bar{Q}^{**}_{i,j,k}$$
$$\left.-\left(\hat{B}^{L} - \frac{\hat{M}^{L}}{Re}\right)^{p}_{j-\frac{1}{2}}\Delta\bar{Q}^{**}_{i,j-1,k}\right]$$
$$= \left(I - \hat{T}^{p}_{i,j,k}\right)\Delta\bar{Q}^{*}_{i,j,k}$$

.....

$$\left(I - \hat{T}^{p}_{i,j,k}\right)\Delta\bar{Q}_{i,j,k} + \frac{\Delta t}{\mathcal{V}_{i,j,k}}\left[\left(\hat{C}^{R}\right)^{p}_{k+\frac{1}{2}}\Delta\bar{Q}_{i,j,k+1}\right.$$
$$\left.+\left\{\left(\hat{C}^{L}\right)^{p}_{k+\frac{1}{2}} - \left(\hat{C}^{R}\right)^{p}_{k-\frac{1}{2}}\right\}\Delta\bar{Q}_{i,j,k} - \left(\hat{C}^{L}\right)^{p}_{k-\frac{1}{2}}\Delta\bar{Q}_{i,j,k-1}\right]$$
$$= \left(I - \hat{T}^{p}_{i,j,k}\right)\Delta\bar{Q}^{**}_{i,j,k}$$

The matrix, $\hat{T}_{i,j,k}$, appearing in the above expression represents the Jacobian of the chemical source terms that includes derivatives with respect to both temperature and species concentration. Note also that $\Delta\bar{Q}$ is defined as the iterative change of the cell averaged dependent variables, $\left(\bar{Q}^{p+1} - \bar{Q}^{p}\right)$. For the first iteration, the quantities at p are taken from those at the time level n. Ideally, all possible errors are eliminated as the residual of this iteration process is driven to zero. However, in practice, convergence is defined short of this with minimal loss in accuracy. This is done to reduce the number of Newton iteration steps and hence the expense of the calculation.

5. SPACE-MARCHING SCHEME

Space-marching schemes have been used extensively in the past to compute a variety of steady, supersonic flow fields. The numerical procedure differs from that described in the last section since the solution is marched in space rather than time. It is therefore much more efficient since the governing equations are only integrated once for any cell in the computational mesh. Further, for any cell in this mesh, only two (rather than three) block-tridiagonal inversions need be made. For these two reasons, it is easy to realize the benefits of having such a numerical scheme.

The space-marching solution procedure begins by first providing the solver with two slabs of cells (know as the initial starting planes), along with all of the dependent variables in these cells. There are various techniques for obtaining this information such as the use of a either time-dependent code(similar to the one described above) or a "conical step back" procedure,[30] or even by simply specifying freestream quantities for the entire slab. After the starting planes are initialized, the solution can be marched in the streamwise direction (ξ-direction) if the dependent variables meet a few criteria discussed in the next section.

5.1 Parabolizing Approximation

The mathematical nature of the governing equations prevents stable space-marching of the governing equations through subsonic or reversed flow regions of a flow field. It is therefore necessary to use a time-marching algorithm to locally obtain the solution in and around these portions of a hypersonic flow field. Since the viscous layer of a hypersonic flow field contains subsonic velocities, a spatially marched solution would be ill-posed and in some cases exponentially growing solutions (departure solutions) would be encountered. However, a number of different techniques have been developed to allow stable marching of a supersonic solution in the presence of a subsonic viscous layer. The technique used in this study is that proposed by Vigneron et al.[26]

The Vigneron technique first splits the inviscid flux vector on the streamwise cell interface into two parts.

$$\hat{E} = \hat{E}^{*} + \hat{P}^{*} \quad (49)$$

where,

$$\hat{E}^* = [\rho U, \rho U u + \omega l_x p, \rho U v + \omega l_y p, \rho U w + \omega l_z p, (e+p)U, \rho_1 U, \rho_2 U, \ldots, \rho_{n-1} U,]^T$$
$$\hat{P}^* = [0, (1-\omega) l_x p, (1-\omega) l_y p, (1-\omega) l_z p, 0, 0, 0, \ldots, 0]^T$$

The vector, $\hat{E}^*$ replaces the vector, $\hat{E}$ as the inviscid flux through the ξ-normal cell face and the vector, $\hat{P}^*$ can be treated as a source term which is evaluated at the nearest supersonic point, or it can be neglected entirely. For this discussion and for the results presented later, it was neglected.

The steady governing equations are now written by first eliminating the time term and by using the new streamwise flux presented above:

$$(\hat{E}^*_{i+\frac{1}{2},j,k} - \hat{E}^*_{i-\frac{1}{2},j,k}) + (\hat{F}^{HO}_{i,j+\frac{1}{2},k} - \hat{F}^{HO}_{i,j-\frac{1}{2},k}) + (\hat{G}^{HO}_{i,j,k+\frac{1}{2}} - \hat{G}^{HO}_{i,j,k-\frac{1}{2}}) = \frac{1}{Re}(\hat{S}_{i,j+\frac{1}{2},k} - \hat{S}_{i,j-\frac{1}{2},k}) + \mathcal{V}_{i,j,k}\hat{H}_{i,j,k} \quad (50)$$

For a first-order accuracy in the streamwise direction, the streamwise numerical fluxes are evaluated as follows,

$$\hat{E}^*_{i+\frac{1}{2},j,k} = \hat{E}^*\left(1_{i+\frac{1}{2},j,k}, \bar{Q}_{i,j,k}\right)$$
$$\hat{E}^*_{i-\frac{1}{2},j,k} = \hat{E}^*\left(1_{i-\frac{1}{2},j,k}, \bar{Q}_{i-1,j,k}\right) \quad (51)$$

In order to obtain a second-order streamwise flux, a second-order backward difference can be employed. For the results shown later in this paper, only a first-order difference of the streamwise flux was performed.

It has been shown with an eigenvalue analysis[11] that stable marching in the streamwise direction is possible if:

$$\omega = \min\left[1, \frac{\sigma\gamma M_\xi^2}{1+(\gamma-1)M_\xi^2}\right] \quad (52)$$

where M_ξ is the normal component of the frozen Mach number through the ξ-normal cell interface. The factor of safety, σ is typically set to 0.9

5.2 Numerical Scheme

Finally, with the use of approximate factorization, flux linearization, and a modified Newton iteration, the space-marching algorithm can be written in it's entirety.

$$\left(\hat{A}^*_{i+\frac{1}{2},j,k} - \mathcal{V}_{i,j,k}\hat{T}_{i,j,k}\right)^p \Delta\bar{Q}^*_{i,j,k} + \left(\hat{B}^R - \frac{\hat{M}^R}{Re}\right)^p_{j+\frac{1}{2}} \Delta\bar{Q}^*_{i,j+1,k} + \left\{\left(\hat{B}^L - \frac{\hat{M}^L}{Re}\right)^p_{j+\frac{1}{2}} - \left(\hat{B}^R - \frac{\hat{M}^R}{Re}\right)^p_{j-\frac{1}{2}}\right\} \Delta\bar{Q}^*_{i,j,k} - \left(\hat{B}^L - \frac{\hat{M}^L}{Re}\right)^p_{j-\frac{1}{2}} \Delta\bar{Q}^*_{i,j-1,k}$$
$$= -\left[\left(\hat{E}^*_{i+\frac{1}{2},j,k} - \hat{E}^*_{i-\frac{1}{2},j,k}\right) + \left(\hat{F}^{HO}_{i,j+\frac{1}{2},k} - \hat{F}^{HO}_{i,j-\frac{1}{2},k}\right) + \left(\hat{G}^{HO}_{i,j,k+\frac{1}{2}} - \hat{G}^{HO}_{i,j,k-\frac{1}{2}}\right) - \frac{1}{Re}\left(\hat{S}_{i,j+\frac{1}{2},k} - \hat{S}_{i,j-\frac{1}{2},k}\right) - \mathcal{V}_{i,j,k}\hat{D}_{i,j,k}\right]^p$$

.....

$$\left(\hat{A}^*_{i+\frac{1}{2},j,k} - \mathcal{V}_{i,j,k}\hat{T}_{i,j,k}\right)^p \Delta\bar{Q}_{i,j,k} + \left(\hat{C}^R\right)^p_{k+\frac{1}{2}} \Delta\bar{Q}_{i,j,k+1} + \left\{\left(\hat{C}^L\right)^p_{k+\frac{1}{2}} - \left(\hat{C}^R\right)^p_{k-\frac{1}{2}}\right\} \Delta\bar{Q}_{i,j,k} - \left(\hat{C}^L\right)^p_{k-\frac{1}{2}} \Delta\bar{Q}_{i,j,k-1} = \left(\hat{A}^*_{i+\frac{1}{2},j,k} - \mathcal{V}_{i,j,k}\hat{T}_{i,j,k}\right)^p \Delta\bar{Q}^*_{i,j,k}$$

The matrix $\hat{A}^*$ appearing in the above algorithm is the Jacobian of the Vigneron streamwise numerical flux. Similar to the time-marching scheme, $\Delta\bar{Q}$ is defined as the iterative change of the cell averaged dependent variables, $(\bar{Q}^{p+1} - \bar{Q}^p)$. For the first iteration, the quantities that are needed at i are taken as those from the last spatial step, $i-1$. Ideally, all possible errors are eliminated as the residual of the iteration process is driven to zero. However, as in the time-marching scheme, convergence is defined short of this with minimal loss in accuracy. This is done to reduce the number of Newton iteration steps and hence the expense of the calculation.

6. DECOMPOSITION

After either a time or spatial step has been taken, all of the dependent variables are known at the most recent step. From these variables, the internal energy of the mixture, ε can be calculated:

$$\varepsilon = \frac{e}{\rho} - \frac{1}{2}(u^2 + v^2 + w^2) \quad (53)$$

The temperature can then be obtained from the enthalpy curve fits with a Newton-Raphson iteration method. This Newton-Raphson iteration is written as,

$$T^{k+1} = T^k - \frac{g(T^k) - \varepsilon}{g'(T^k)} \quad (54)$$

where

$$g(T^k) = \sum_{s=1}^{n} c_s\left(h_s(T) - \beta_1 T/\mathcal{M}_s\right) \quad (55)$$

$$g'(T^k) = \sum_{s=1}^{n} c_s\left(C_{p,s}(T) - \beta_1/\mathcal{M}_s\right) \quad (56)$$

where the index k corresponds to the iteration index. The iterations are continued until convergence is reached. This rarely requires more than ten iterations to reduce the residual to machine accuracy. Once the temperature is known, the pressure is easily computed using Eq. 7. Values for γ and D_s are also computed at this point.

7. FINITE VOLUME METRICS

Before the numerical schemes detailed in previous sections can be employed, certain metric quantities that define the orientation and size of each cell in the computational mesh must first be evaluated. These metric quantities include three components of a surface-area vector for each cell interface and a volume for each cell. The generalized, six-sided cell shown in Fig. 1 is defined by eight verticies and any cell interface can be defined by the four coincident verticies of the neighboring cells. Reference 31 gives relatively simple formulas for computing these metric quantities. The surface-area vectors are given as:

$$\begin{aligned}
\mathbf{l}_{i+\frac{1}{2},j,k} &= \frac{1}{2}\left(\mathbf{r}_{i+\frac{1}{2},j+\frac{1}{2},k+\frac{1}{2}} - \mathbf{r}_{i+\frac{1}{2},j-\frac{1}{2},k-\frac{1}{2}}\right) \\
&\quad \times \left(\mathbf{r}_{i+\frac{1}{2},j+\frac{1}{2},k-\frac{1}{2}} - \mathbf{r}_{i+\frac{1}{2},j-\frac{1}{2},k+\frac{1}{2}}\right) \\
\mathbf{m}_{i,j+\frac{1}{2},k} &= \frac{1}{2}\left(\mathbf{r}_{i-\frac{1}{2},j+\frac{1}{2},k+\frac{1}{2}} - \mathbf{r}_{i+\frac{1}{2},j+\frac{1}{2},k-\frac{1}{2}}\right) \\
&\quad \times \left(\mathbf{r}_{i+\frac{1}{2},j+\frac{1}{2},k+\frac{1}{2}} - \mathbf{r}_{i-\frac{1}{2},j+\frac{1}{2},k-\frac{1}{2}}\right) \\
\mathbf{n}_{i,j,k+\frac{1}{2}} &= \frac{1}{2}\left(\mathbf{r}_{i-\frac{1}{2},j+\frac{1}{2},k+\frac{1}{2}} - \mathbf{r}_{i+\frac{1}{2},j-\frac{1}{2},k+\frac{1}{2}}\right) \\
&\quad \times \left(\mathbf{r}_{i-\frac{1}{2},j-\frac{1}{2},k+\frac{1}{2}} - \mathbf{r}_{i+\frac{1}{2},j+\frac{1}{2},k+\frac{1}{2}}\right)
\end{aligned}$$

where the vectors, $\mathbf{r}$ represent the position vectors of the cell vertices. The cell volume is then computed with the following formula,

$$\begin{aligned}
\mathcal{V}_{i,j,k} = \frac{1}{3}&\left(\mathbf{l}_{i-\frac{1}{2},j,k} + \mathbf{m}_{i,j-\frac{1}{2},k} + \mathbf{n}_{i,j,k-\frac{1}{2}}\right)\cdot \\
&\left(\mathbf{r}_{i+\frac{1}{2},j+\frac{1}{2},k+\frac{1}{2}} - \mathbf{r}_{i-\frac{1}{2},j-\frac{1}{2},k-\frac{1}{2}}\right)
\end{aligned}$$

There are two favorable properties of metric quantities evaluated in this manner. First, the sum of all the surface-area vectors associated with any cell is zero. This guarantees that the resulting algorithm is freestream preserving. Second, the sum of a region of cell volumes is equal to the volume of that region. In other words, the cell metrics allow no overlaping or spacing between the cells in the computational mesh.

8. BOUNDARY CONDITIONS

In the finite-volume philosophy, for any boundary in a computational mesh, a flux must be evaluated at that boundary that is consistent with any boundary conditions that might exist. The only types of boundaries in the computation of an entirely external, supersonic flow field are: 1) supersonic inflow(or far field), 2) supersonic outflow, 3) viscous boundary, and 4) symmetry conditions. Determination of an appropriate flux for the first two boundaries is trivial. For a supersonic inflow the flux is simply evaluated using freestream quantities. And for supersonic outflow, the numerical scheme provides the needed flux because of the nature of the flow. The other two boundary fluxes are a little more involved.

The symmetry condition is handled by generating fictitious cells out side of the computational domain so that the cell interface flux that coincides with the symmetry plane can be evaluated as if it were an interior face. Dependent variables of cells inside of the domain are reflected about the symmetry plane to produce a mirrored cell on the other side. The static dependent variables of the reflected cell acquire the identical quantity of their original. The reflected cell is depicted by a superscript ^{r}.

$$\begin{aligned}
\rho^r &= \rho \\
e^r &= e \\
\rho_s^r &= \rho_s \quad s = 1, 2, \ldots, n
\end{aligned}$$

The dynamic variables of the reflected cell are evaluated as follows.

$$\begin{aligned}
u^r &= u - 2\hat{n}_x(\hat{n}_x u + \hat{n}_y v + \hat{n}_z w) \\
v^r &= v - 2\hat{n}_y(\hat{n}_x u + \hat{n}_y v + \hat{n}_z w) \\
w^r &= w - 2\hat{n}_z(\hat{n}_x u + \hat{n}_y v + \hat{n}_z w)
\end{aligned}$$

The unit metrics in the above expression are those of a cell interface that is coincident with the symmetry condition. In order to evaluate the generalized higher-order flux at the symmetry condition, two reflected cells must be generated. This symmetry condition is easily made implicit by realizing that the reflected cells are related to interior cells through this simple transformation.

On a viscous boundary, both an inviscid and viscous flux must be evaluated. The inviscid flux is determined in a similar manner as the symmetry condition flux. The viscous flux is evaluated by first realizing that all of the velocity components are zero at the surface. Knowledge of either the wall temperature or heat flux must then be supplied. Evaluation of the heat flux term in the viscous flux is trivial if the heat flux is known a priori, however, if the wall temperature is known, the heat flux term is evaluated using a one-sided difference formula. If a catalytic wall is present, the mass fractions of each of the species are known at the wall, and the diffusion velocity terms are evaluated using a one-sided difference. If however, a non-catalytic wall is present, the diffusion velocities vanish at the wall and are dropped from the viscous flux entirely.

9. RESULTS

Two different types of geometries were chosen to validate the present techniques. The flow field about a simple 10 degree cone is first presented at zero angle of attack to demonstrate the accuracy of the current methods. Solutions about this same geometry at angles of attack are then included to show a three-dimensional capability. And finally, a blunt-body flow field about a sphere-cylinder geometry is presented to demonstrate the capability of the current techniques to predict such flow fields.

In this section, results obtained with both of the current techniques are presented. In order to distinguish the

results from one another, they are referenced by the names of their corresponding codes. The time-marching code has been given the name TUFF and the space-marching algorithm is referred to as STUFF. The first name stands for "A Three-Dimensional, Upwind-Differenced, Finite-Volume Flow Solver with Fully Coupled Chemistry". The additional character in the space-marching code's name, STUFF, stands for Space-Marching. The similarity of the names of these codes reflects the similarity in the techniques and hence the compatability of the techniques to compute a single flow field.

9.1 10° Cone Test Cases

The first sequence of results presented here are for the hypersonic, laminar flow of air in chemical nonequilibrium over a 10° half-angle cone at various angles of attack. The flow conditions were chosen to correspond to those of Prabhu.[11] The altitude considered was $60.96km$ and the free stream velocity was $8100m/s$. This altitude corresponds to an ambient temperature of $252.6K$ and pressure of $20.35N/m^2$ and the composition by mass was assumed to be 26.29% molecular oxygen and 73.71% molecular nitrogen. These flow conditions lead to a frozen Mach number of 25.4 and a Reynolds number of $127,300/m$. The cone wall was assumed to be noncatalytic with a constant temperature of $1200K$. For these computations, a Lewis number of 1.4 was assumed. The angles of attack that were considered are 0.0, 2.5 and 5.0 degrees.

For the 10° cone test cases presented here, results with both the time-marching and space-marching algorithms are included. The grid used for the time-marching results is shown in Fig. 3. The space-marching algorithm used this same grid as a base grid and interpolated between marching planes for any needed plane. This base grid measures 34 cells in the streamwise direction, 30 cells in the normal direction and 23 cells in the meridional direction. The length of the cone was $3.5m$. The axial cell size of this base grid started at $0.0002m$ near the nose and was increased to nearly $0.1m$ at the tail end of the cone. The normal size of the first cell away from the body was varied linearly from 3×10^{-5} to 2.3×10^{-4}. The grid was stretched from the body to the outer grid radius which also varied linearly from $0.01m$ at the nose to $0.5m$ at the tail. For these test cases, all of the cross flow planes were generated to be axis-normal.

The space-marching results were initiated by specifying free-stream quantities as initial data. Then at the onset of the computations, a maximum CFL number of 1 was used to determine the step size. This step size limitation was used until the bow shock emerged from the finely-spaced, viscous portion of the grid. The limiting CFL number was then increased to 30 for the remaining spatial steps. Using this limitation, a total of 660 spatial steps were required for the space-marching code. Three Newton iterations were performed for each spatial step. For the zero angle of attack test case, the required CPU-time was only 178 seconds on the Cray-2 computer. The time-marching results on the other hand needed much more computer time. The time-marching results were initiated with the space-marching solution and were assumed to converge after the maximum residual in the continuity equation decreased 3 orders of magnitude. A total of about 2100 iterations were required. It was found that this criteria was sufficient since no plotable differences in the results occurred by further reducing this residual. For these steady-state computations the Newton iteration process was not employed in the time-marching results since time-accuracy was not required. The resulting CPU-time needed for the zero angle of attack case was 3514 seconds using the time-marching technique. These CPU times reiterate the benefits of a space-marching algorithm for the computation of hypersonic flow fields.

For the zero angle of attack case, only a two-dimensional, axisymmetric result was obtained. This was done by considering only one of the meridional plane of cells in Fig. 3, and by assuming that the neighboring cells possess similar dependent variables. Figure 4 shows the axial variation of the surface pressure coefficient for the zero angle of attack case obtained with both TUFF and STUFF. Also shown in this figure are results of the central differencing scheme of Prabhu.[11] This surface pressure coefficient is defined as:

$$C_p = \frac{\tilde{p}_w - \tilde{p}_\infty}{\frac{1}{2}\tilde{\rho}_\infty \tilde{Q}^2_\infty}$$

All of the results predict a high pressure leading edge effect that then rapidly decays to a near-constant pressure region. Since the Reynolds number is relatively low for this test case, this leading edge effect is fairly strong. Reference 11 predicts a pressure in the later region that is about 10 percent lower than both of the current techniques. Since the governing equations, fluid properties and flow conditions of current results are identical, this discrepancy must be attributed to the difference in numerical procedures. Tannehill et al.[10] also found a discrepancy in the predicted shock shape of a central-differencing scheme with that of an upwind-differencing scheme. Therefore, the discrepancy in Fig. 4 can in part be explained by the strong dependence of the pressure inside a shock layer on the bow shock shape and by the enhanced ability of upwind schemes to capture the bow shock. Since Reference 11 employed a conical-stepback procedure, this discrepancy can further be explained by the difference in starting solution methods. Conical-stepback procedures make the assumption that the flow is locally conical however, with the specification of freestream at the point of the cone, this assumption is avoided entirely.

Although the differences mentioned above exist between the present results and those of Reference 11, the boundary layer profiles agree quite well. Figures 5-8 show the boundary layer profiles of various quantities at $x = 3.5m$. The abscissa of these plots corresponds to the normal distance, in meters, from the cone wall to the center of the cells. Velocity and temperature profiles are shown in Figures 5 and 6 respectively. Excellent agreement is observed between the two current results, however a small discrepancy is shown near the boundary layer edge where the grid is relatively coarse. The peak predicted temperatures agree very well in all of the computations. The mass fraction profile of atomic oxygen, O, at $x = 3.5$ is depicted in Fig. 7.

The values for mass fraction have been normalized with respect to the value at the wall to allow comparison with Reference 11. Agreement between these profiles is again excellent. Next, the profiles of the normalized electron density is shown in Fig. 8. Very good agreement is observed. Figure 9 shows the skin-friction coefficient(defined in Ref. 11) as a function of axial distance for the zero angle of attack case. Comparison of these quantities show good agreement with the existing data.

In order to validate the three-dimensional capability of the current techniques the solution about a 10° cone at angles of attack is presented. The angles chosen are 2.5 and 5.0 degrees. It was found that any greater angle required a refinement of the base grid shown in Fig. 3. The flow conditions for these computations were the same as for the zero angle of attack case. The solution procedure, including the step sizes, are also identical to the previous case with the exception that the entire three-dimensional grid shown in Fig. 3 was used instead of using only a single meridional plane. Space-marching solutions are shown for both cases and time-marching solutions are only shown for the 2.5 degree case because of the enormity of required computer time for a time-marching result.

The pressure contours in the crossflow plane at $x = 3.5$ for both angles of attack considered are shown in Figures 10a and 10b. The quality of upwind-differenced results is shown in these two figures by noting that the resulting shock thickness does not exceed two grid cells. These figures also depict two well known facts about cones at angles of attack. First, the shock layer gets thicker with greater angles of attack on the leeward side with a relatively small change in the thickness on the windward side. And second, it is also apparent that the pressure gradient around the cone becomes greater as the angle of attack is increased. In Figures 11a and 11b, the effect on temperature with angle of attack is depicted. These figures present the temperature profiles on both symmetry planes. These figures show that the boundary layer along with the shock layer thicken on the leeward side while they thin on the windward side with greater angles of attack. The peak temperatures however remain unchanged with these relatively small angles of incidence.

Figures 12a and 12b demonstrate the effect of angle of attack on chemical quantities. These figures show the O mass fraction profiles at an axial location of 3.5 for both angles of attack considered. Since the density is greater on the windward side of the cone, a greater degree of reaction can occur resulting in larger concentrations of atomic oxygen. And since the densities on the leeward side decreases with increasing angles of attack a reduction in the reactivity takes place resulting in less amounts of dissociation. These trends along with the thinning and thickening effects of the boundary layer discussed earlier are apparent in these two figures. Greater angles of attack are seen to only amplify these phenomena. Figures 13a and 13b show the effect on the axial variation of the heat transfer coefficient as the angle of attack is increased. The increase in the heat transfer rate on the windward side and a corresponding decrease on the leeward side with larger angles of attack is evident in these figures.

9.3 Sphere-Cylinder Test Case

This next test case is presented for two reasons. The first reason is to demonstrate the ability of the current techniques to predict blunt body flow fields including shock standoff distance. Shock standoff distance is a good measure of the accuracy of a numerical scheme since it is directly influenced by the distribution of dependent variables throughout the shock layer. The second reason that this test case is presented is to show how the two current techniques can be used in tandem to compute a single hypersonic flow field. The nose region of the flow field was computed with the time-marching technique, TUFF, and the after body was computed with the space-marching technique, STUFF.

The geometry and flow condition for this computation were chosen to allow comparison with an experiment by Lobb[32] in which spheres were fired at hypervelocities into air. The bow shock locations were defined by taking Schlieren photographs of the spheres in flight. These conditions were also considered by Candler[16] as a test case for a thermo-chemical nonequilibrium code validation. Comparison of the current techniques with both references is made below. The flow conditions are detailed below:

$$\tilde{Q}_\infty = 5280(m/s)$$
$$\tilde{T}_\infty = 293(K)$$
$$\tilde{p}_\infty = 664(N/m^2)$$

These flow conditions correspond to a frozen Mach number of 15.3 and a Reynolds number of $2,190,000/m$.

The grid used in the sphere-cylinder test case is shown in Fig. 14. The sphere radius was $0.635cm$ and the cylinder portion of the geometry measured two nose radii in length. This grid used 45 grid cells in each normal column of cells of which 9 are exponentially streatched near the body to allow for the presence of a boundary layer. The time-marching result used the first 24 columns of cells to obtain an axisymmetric solution in the nose region. The space-marching code used the remaining cells as a base grid in the computation of the afterbody region of the flow field. The computation proceeded by first obtaining a converged time-marching solution of the nose region. Machine accuracy was reached after 4700 iterations at a maximum CFL of 10 (see Fig. 15). This required 8650 seconds on the Cray-2 computer. The afterbody solution was then obtained using the nose region result for the starting planes and marching the solution down the body. By employing three Newton iterations in the space-marching algorithm and taking 220 steps to compute the afterbody flow field, only 82 seconds of CPU time were required.

Figure 16 depicts the resulting shock standoff distance in pressure contours about the sphere-cylinder geometry. Even though thermal nonequilibrium effects were neglected, the shock standoff distance compares very well in the entire nose region with the experiment of Lobb. The variation of

species concentration along the stagnation streamline are shown in Fig. 17. Comparison of the atomic oxygen profile with that of Candler shows good agreement. This figure also shows that the molecular oxygen almost completely dissociates in the stagnation region. Only about ten percent of the molecular nitrogen dissociates along the stagnation streamline and then recombines before the wall is reached. This recombination is caused by the cool wall temperature that drives the reactions backwards. The plot of temperature contours in Fig. 18 also demonstrates these phenomena. The initial temperature rise across the strong bow shock in the nose region then begins to decay as a result of the highly endothermic dissociation reactions. The thin thermal boundary layer is also seen in this figure. A contour plot of the resulting frozen Mach number contours, molecular oxygen contours and molecular nitrogen contours are shown in Figures 19, 20 and 21 respectively.

10. CONCLUDING REMARKS

A set of numerical schemes have been developed to compute the hypersonic flow of chemically reacting and weakly ionizing gases. These include a time-marching scheme and a cost effective, space-marching scheme. A fully implicit, strongly coupled, approximately factored method is employed in both techniques. The upwind, inviscid numerical fluxes are evaluated with an approximate Riemann solver that allows for the presence of a multicomponent mixture of calorically imperfect but thermally perfect gases. Stable higher order fluxes are obtained by utilizing a Total Variation Diminishing procedure. Two test cases were computed to validate the current techniques. Comparison with experimental data and with two existing numerical techniques shows very good agreement. Research is currently underway to incorporate a simple turbulence/transition model into the present codes. Further research includes adding the capability to predict hypersonic flow fields in various atmospheres.

11. ACKNOWLEDGEMENTS

This research was supported by NASA-Ames Research Center Grant NCC2-498. Computer time was provided by Pennsylvania State University and by the Numerical Aerodynamic Simulation (NAS) facility located at NASA-Ames Research Center.

12. REFERENCES

1) J. T. Howe, "Introductory Aerothermodynamics of Advanced Space Transportation Systems." *Journal of Spacecraft and Rockets*, Vol 22, No. 1, Jan.-Feb. 1985, pp. 104-111.

2) G. D. Walberg, "A Survey of Aeroassisted Orbit Transfer." *Journal of Spacecraft and Rockets*, Vol 22, No. 1, Jan.-Feb. 1985, pp. 3-18.

3) J. L. Shinn, J. N. Moss, and A. L. Simmonds, "Viscous Shock-Layer Heating Analysis for the Shuttle Windward-Symmetry Plane with Surface Finite Catalytic Recombination Rates," AIAA Paper 82-0842, June 1982.

4) K. V. Reddy, T. Fujiwara, T. Ogawa, and K. Arashi, "Computation of Three-Dimensional Chemically Reacting Viscous Flow Around Rocket Body" AIAA Paper 88-2616, June 1988.

5) C. P. Li, and T. C. Wey, "Numerical Simulation of Hypersonic Flow over an Aeroassist Flight Experiment Vehicle" AIAA Paper 88-2675, June 1988.

6) S. T. Yu, B. J. McBride, K. C. Hsieh, and J. S. Shuen, "Numerical Simulation of Hypersonic Inlet Flows with Equilibrium or Finite Rate Chemistry" AIAA Paper 88-0273, January 1988.

7) J. L. Shinn, H. C. Yee, and K. Uenishi, "Extension of a Semi-Implicit Shock-Capturing Algorithm for 3-D Fully Coupled, Chemically Reacting Flows in Generalized Coordinates." AIAA Paper 87-1577, June 1987.

8) P. A. Gnoffo, R. S. McCandless, and H. C Yee, "Enhancement to Program LAURA for Computation of Three-Dimensional Hypersonic Flow," AIAA Paper 87-0280, January 1987.

9) A. Balakrishnan, "Application of a Flux Split Algorithm to Chemically Relaxing, Hypervelocity Blunt-Body Flows," AIAA Paper 87-1578, June 1987.

10) J. C. Tannehill, J. O. Ievalts, D. K. Prabhu, and S. L. Lawrence, "An Upwind Parabolized Navier-Stokes Code for Chemically Reacting Flows," AIAA Paper 88-2614, June 1988.

11) D. K. Prabhu, J. C. Tannehill, and J. G. Marvin, "A New PNS Code for Three-Dimensional Chemically Reacting Flows." AIAA Paper 87-1472, June 1987.

12) B. A. Bhutta, C. H. Lewis, and F. A. Kautz II, "A Fast Fully-Iterative Parabolized Navier-Stokes Scheme for Chemically-Reacting Reentry Flows," AIAA Paper 85-0926, June 1985.

13) S. Swaminathan, N. C. Kim, and C. H. Lewis, "Nonequilibrium Viscous Shock-Layer Flows over Blunt Sphere-Cones at Angles of Attack," AIAA Paper 82-0825, June 1982.

14) G. Candler, and R. W. MacCormack, "The Computation of Hypersonic Ionized Flows in Chemical and Thermal Nonequilibrium" AIAA Paper 88-0511, January 1988.

15) C. Park, "Assessment of Two-Temperature Kinetic Model for Ionizing Air." AIAA Paper 87-1574, June 1987.

16) G. Candler, "The Computation of Weakly Ionized Hypersonic Flows in Thermo-Chemical Nonequilibrium," Ph.D. Thesis, Stanford University, June 1988.

17) G. Candler, and C. Park, "The Computation of Radiation from Nonequilibrium Hypersonic Flows." AIAA Paper 88-2678, June 1988.

18) G. A. Molvik, "Computation of Viscous Blast Wave Solutions with an Upwind, Finite Volume Method." AIAA Paper 87-1290, June 1987.

19) S. L. Lawrence, J. C. Tannehill, and D. S. Chaussee, "An Upwind Algorithm for the Parabolized Navier-Stokes Equations" AIAA Paper 86-1117, May 1986.

20) S. R. Chakravarthy, and S. Osher, "Numerical Experiments with the Osher Upwind Scheme for the Euler Equations." *AIAA Journal*, 21 (September 1983), pp. 1241-1248.

21) P. L. Roe, "Approximate Riemann Solvers, Parameter Vectors, and Difference Schemes." *Journal of Computational Physics*, 43 (1983), pp. 357-372.

22) S. K. Godunov, "A Finite-Difference Method for the Numerical Computation of Discontinuous Solutions of the Equations of Fluid Dynamics." Matematiceskii Sbornik, 47 (1959), pp. 271-290 (also Cornell Aeronautical Laboratory translation).

23) H. C. Yee, "Upwind and Symmetric Shock-Capturing Schemes," NASA-TM 89464, May 1987.

24) S. R. Chakravarthy, and S. Osher, "A New Class of High Accuracy TVD Schemes for Hyperbolic Conservation Laws." AIAA Paper 85-0363, January 1985.

25) M. M. Rai, "An Implicit Form for the Osher Upwind Scheme" AIAA Paper 84-0088, January 1984.

26) Y. C. Vigneron, J. C. Rakich, and J. C. Tannehill, "Calculation of Supersonic Viscous Flow over Delta Wings with Sharp Subsonic Leading Edges." AIAA Paper 78-1137, July 1978.

27) F. G. Blottner, M. Johnson, and M. Ellis, "Chemically Reacting Viscous Flow Program for Multi-Component Gas Mixtures," Report No. SC-RR-70-754, Sandia Laboratories, Albuquerque NM, December 1971.

28) C. R. Wilke, "A Viscosity Equation for Gas Mixtures," *J. Chem. Phys.*,Vol. 18, No. 4, April 1950, p. 517.

29) Y. Liu, and M. Vinokur, "Upwind Algorithms for General Thermo-Chemical Nonequilibrium Flows." AIAA Paper 89-0201, January 1989.

30) L. B. Schiff, and J. L. Steger, "Numerical Simulation of Steady Supersonic Viscous Flow," AIAA Paper 79-0130, January 1979 .

31) M. Vinokur, "An Analysis of Finite-Difference and Finite-Volume Formulations of Conservation Laws." NASA CR-177416, June 1986.

32) R. K. Lobb, "Experimental Measurement of Shock Distance on Spheres Fired in Air at Hypervelocities," *The High Temperature Aspects of Hypersonic flow*, ed. W. C. Nelson, Pergammon Press, MacMillan Co., New York, 1964.

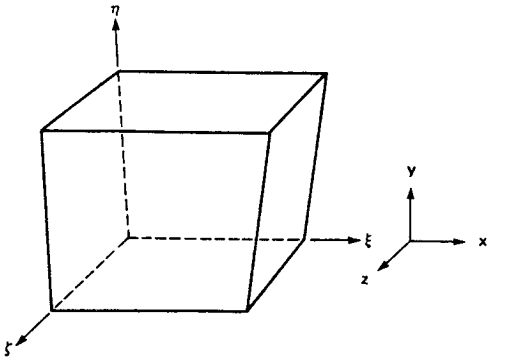

Fig. 1 Three-dimensional Finite-Volume Cell

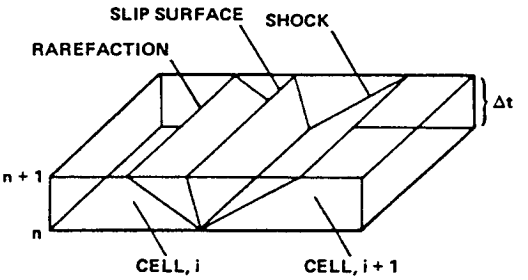

Fig. 2 Illustration of a Riemann Problem

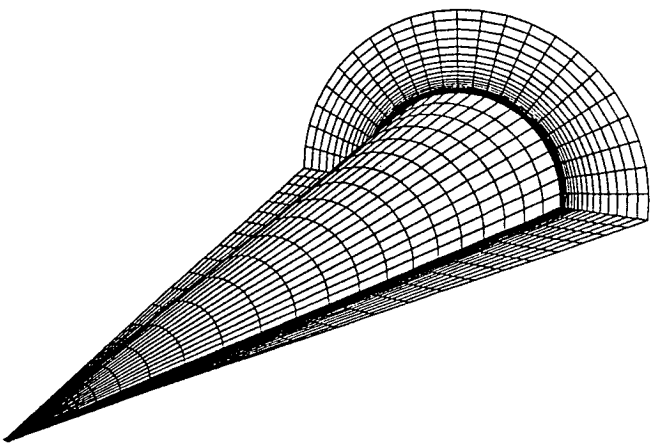

Fig. 3 Grid Used in all Cone Computations

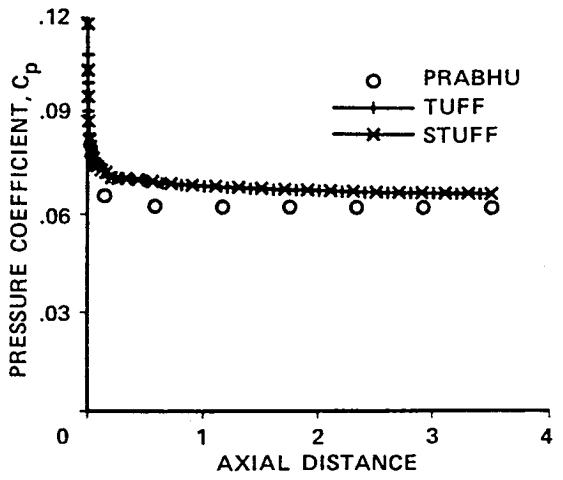

Fig. 4 Wall Pressure Coefficients

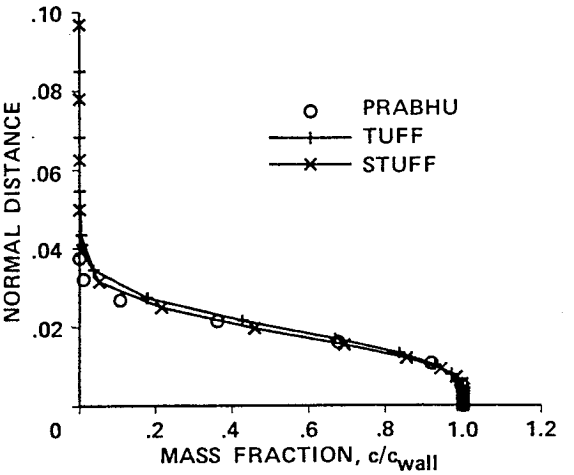

Fig. 7 O Mass Fraction Profiles at $x = 3.5$

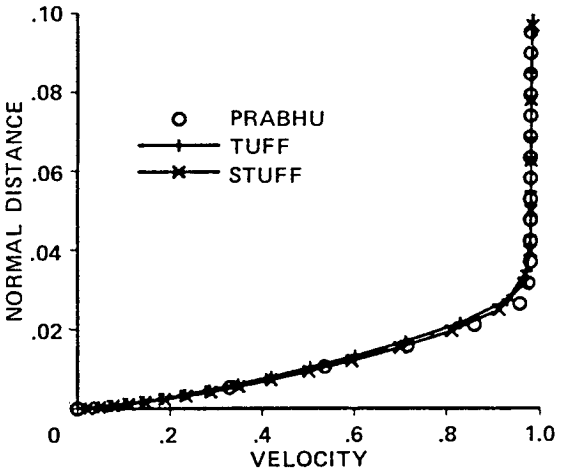

Fig. 5 Velocity Profiles at $x = 3.5$

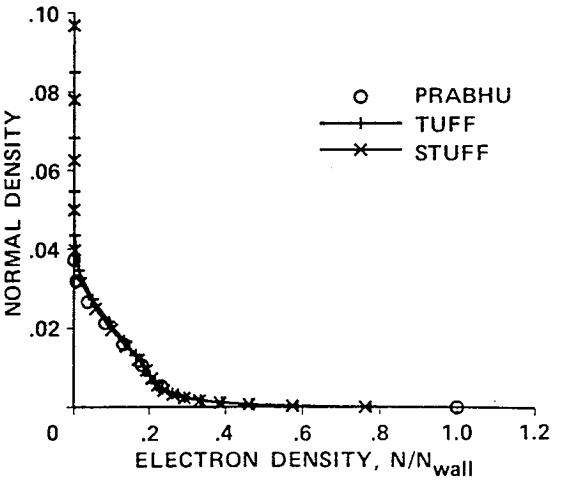

Fig. 8 Electron Molar Density Profiles at $x = 3.5$

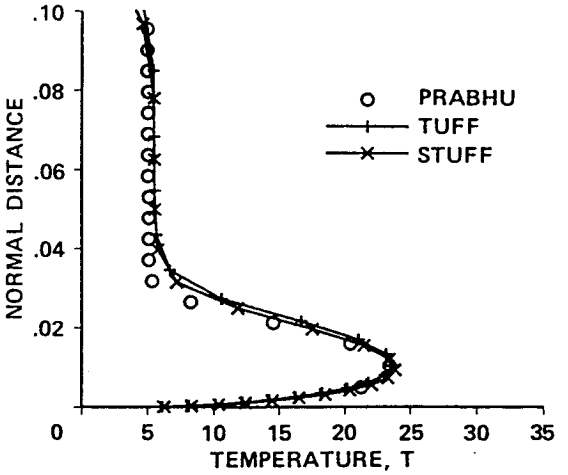

Fig. 6 Temperature Profiles at $x = 3.5$

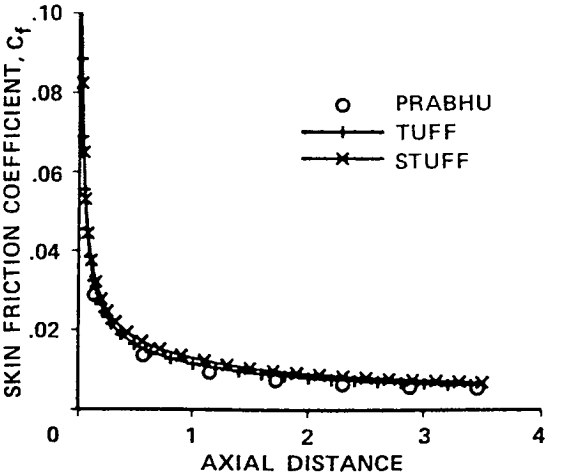

Fig. 9 Skin Friction Coefficients

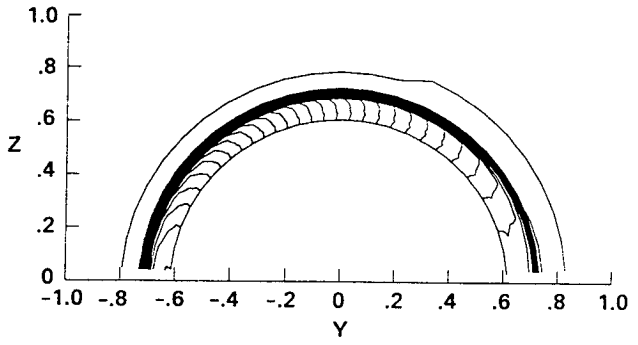

Fig. 10a Pressure Contours at $x = 3.5$ ($\alpha = 2.5$)

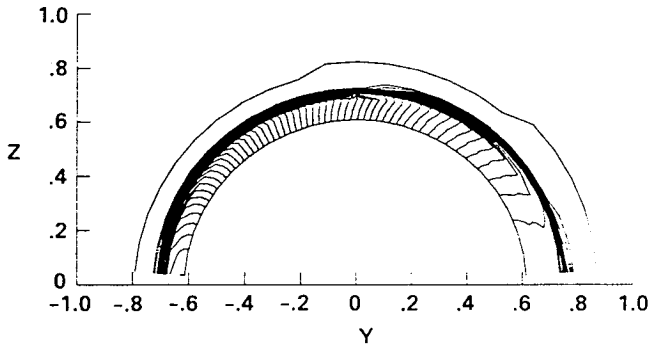

Fig. 10b Pressure Contours at $x = 3.5$ ($\alpha = 5.0$)

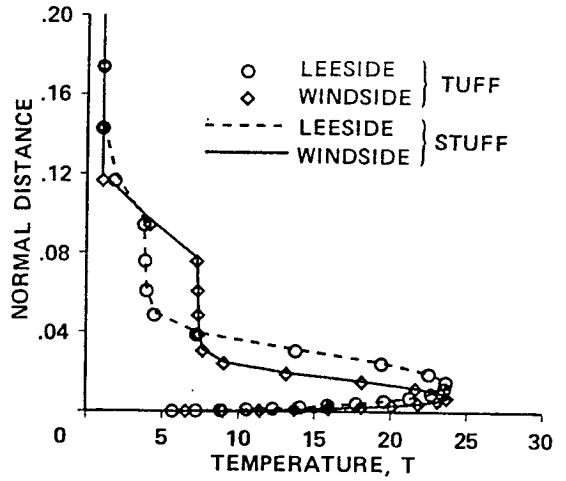

Fig. 11a Temperature Profiles at $x = 3.5$ ($\alpha = 2.5$)

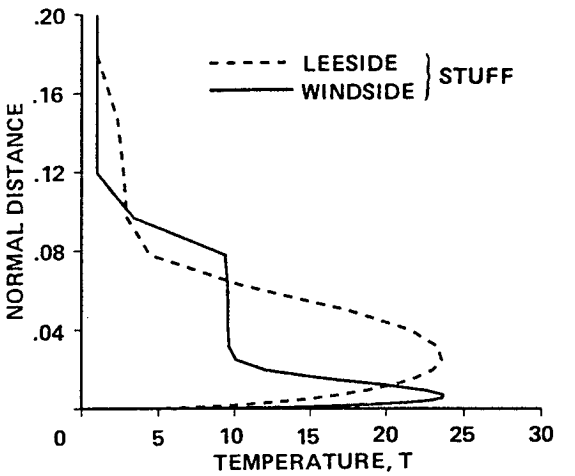

Fig. 11b Temperature Profiles at $x = 3.5$ ($\alpha = 5.0$)

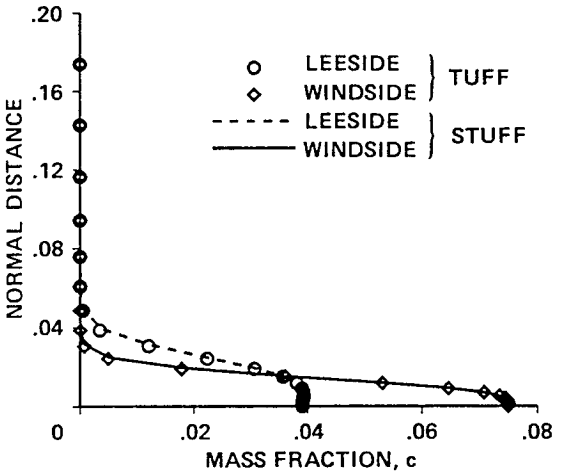

Fig. 12a O Mass Fraction Profiles at $x = 3.5$ ($\alpha = 2.5$)

Fig. 11a Temperature Profiles at $x = 3.5$ ($\alpha = 2.5$)

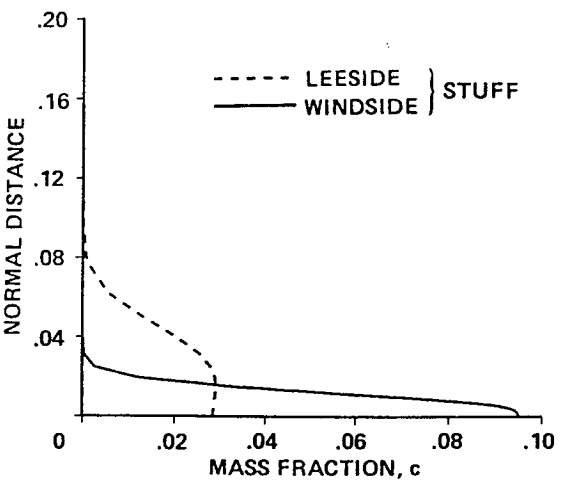

Fig. 12b O Mass Fraction Profiles at $x = 3.5$ ($\alpha = 5.0$)

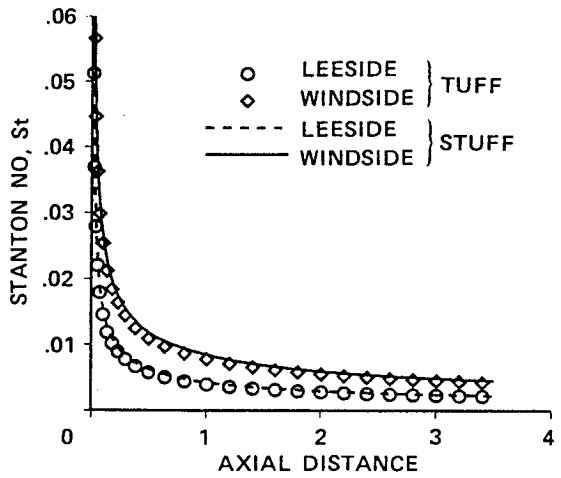

Fig. 13a Heat Transfer Coefficients ($\alpha = 2.5$)

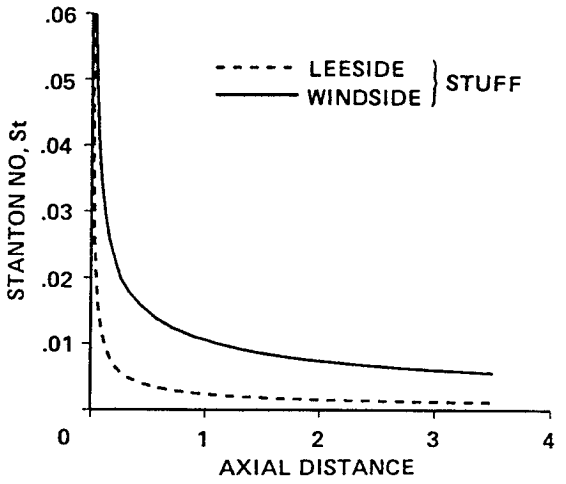

Fig. 13b Heat Transfer Coefficients ($\alpha = 5.0$)

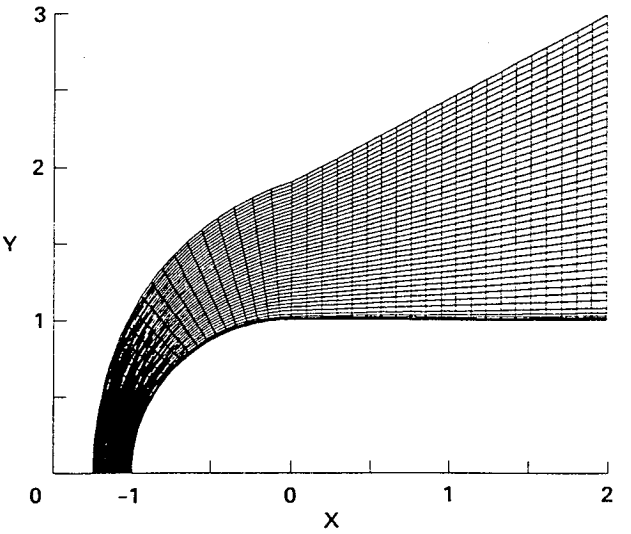

Fig. 14 Grid Used in Sphere-Cylinder Test Case

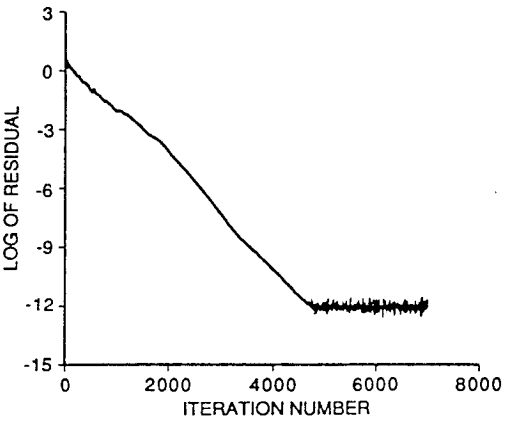

Fig. 15 Convergence Plot for CFL = 10

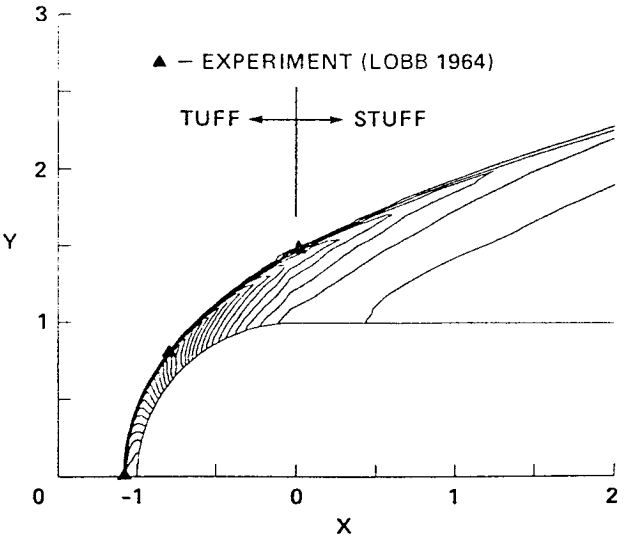

Fig. 16 Pressure Contours with Shock Standoff Comparison

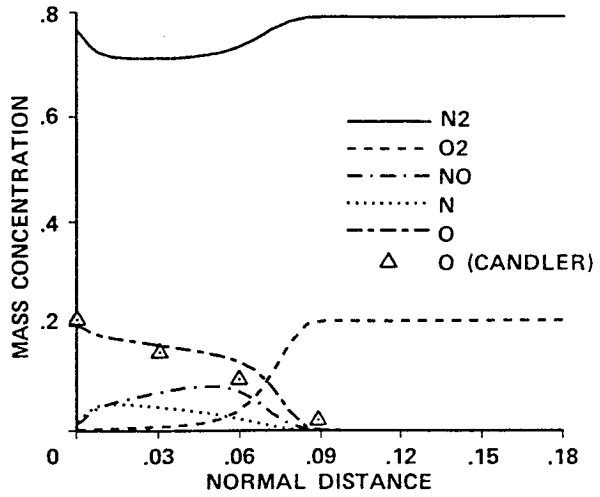

Fig. 17 Mass Concentrations on Stagnation Streamline

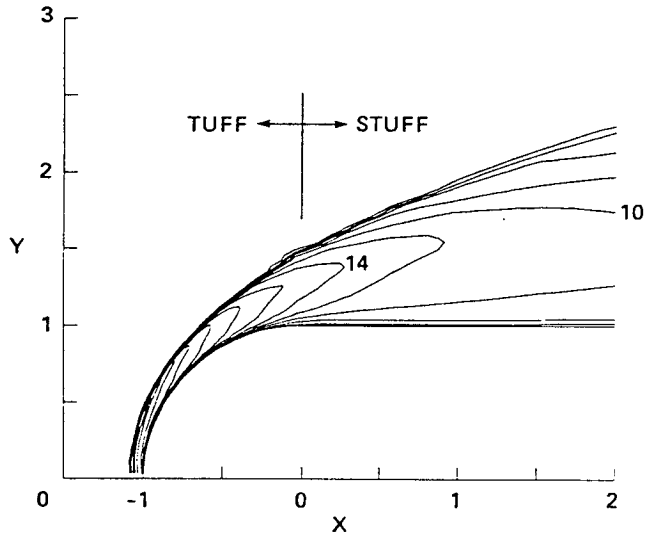

Fig. 18 Temperature Contours

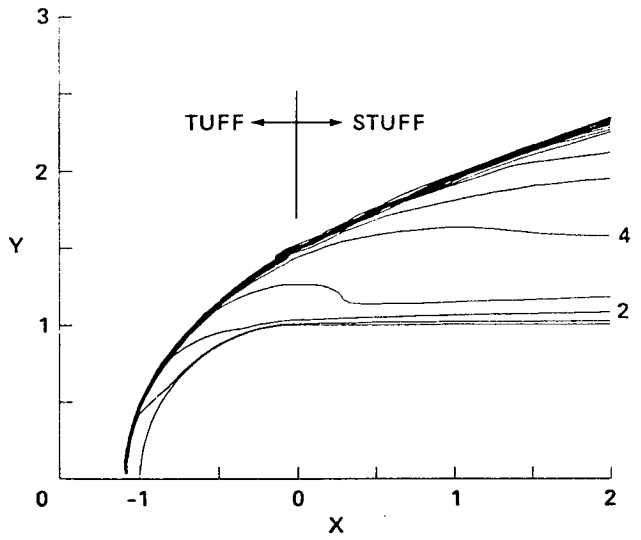

Fig. 19 Frozen Mach Number Contours

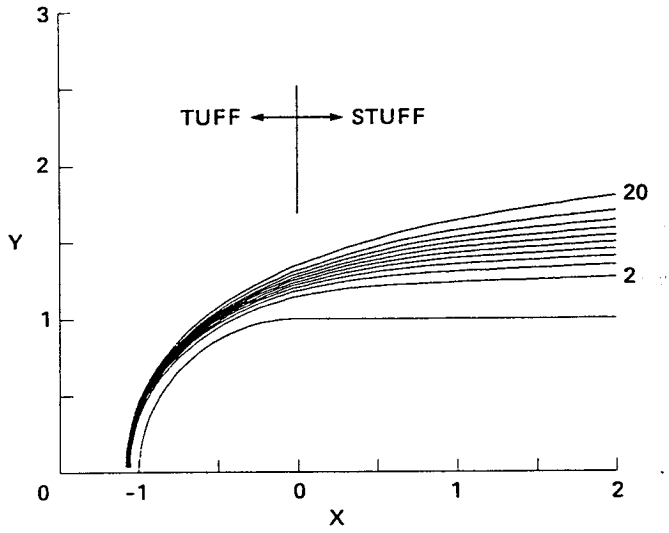

Fig. 20 Percent O_2 Mass Concentration Contours

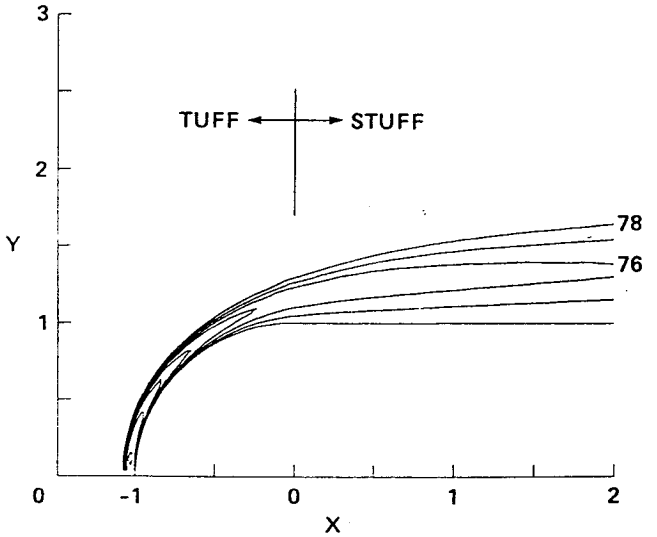

Fig. 21 Percent N_2 Mass Concentration Contours

APPENDIX A
Inviscid Flux Jacobian

The inviscid flux Jacobian, $\hat{\mathbf{A}}$, is given below:

$$\hat{\mathbf{A}} = \begin{bmatrix}
0 & l_x & l_y & l_z & 0 & 0 & 0 & \dots & 0 \\
-Uu + l_x\frac{\partial p}{\partial \rho} & U + l_x u + l_x\frac{\partial p}{\partial \rho u} & l_y u + l_x\frac{\partial p}{\partial \rho v} & l_z u + l_x\frac{\partial p}{\partial \rho w} & l_x\frac{\partial p}{\partial e} & l_x\frac{\partial p}{\partial \rho_1} & l_x\frac{\partial p}{\partial \rho_2} & \dots & l_x\frac{\partial p}{\partial \rho_{n-1}} \\
-Uv + l_y\frac{\partial p}{\partial \rho} & l_x v + l_y\frac{\partial p}{\partial \rho u} & U + l_y v + l_y\frac{\partial p}{\partial \rho v} & l_z v + l_y\frac{\partial p}{\partial \rho w} & l_y\frac{\partial p}{\partial e} & l_y\frac{\partial p}{\partial \rho_1} & l_y\frac{\partial p}{\partial \rho_2} & \dots & l_y\frac{\partial p}{\partial \rho_{n-1}} \\
-Uw + l_z\frac{\partial p}{\partial \rho} & l_x w + l_z\frac{\partial p}{\partial \rho u} & l_y w + l_z\frac{\partial p}{\partial \rho v} & U + l_z w + l_z\frac{\partial p}{\partial \rho w} & l_z\frac{\partial p}{\partial e} & l_z\frac{\partial p}{\partial \rho_1} & l_z\frac{\partial p}{\partial \rho_2} & \dots & l_z\frac{\partial p}{\partial \rho_{n-1}} \\
-UH + \frac{\partial p}{\partial \rho}U & l_x H + U\frac{\partial p}{\partial \rho u} & l_y H + U\frac{\partial p}{\partial \rho v} & l_z H + U\frac{\partial p}{\partial \rho w} & (1+\frac{\partial p}{\partial e})U & \frac{\partial p}{\partial \rho_1}U & \frac{\partial p}{\partial \rho_2}U & \dots & \frac{\partial p}{\partial \rho_{n-1}}U \\
-c_1 U & c_1 l_x & c_1 l_y & c_1 l_z & 0 & U & 0 & \dots & 0 \\
c_2 U & c_2 l_x & c_2 l_y & c_2 l_z & 0 & 0 & U & \dots & 0 \\
\vdots & \vdots & \vdots & \vdots & \vdots & \vdots & \vdots & \ddots & \vdots \\
-c_{n-1}U & c_{n-1}l_x & c_{n-1}l_y & c_{n-1}l_z & 0 & 0 & 0 & \dots & U
\end{bmatrix}$$

where, the metrics are evaluated at the cell face and the dependent variables are those of a neighboring cell. The Inviscid flux Jacobians, $\hat{\mathbf{B}}$ and $\hat{\mathbf{C}}$, are obtained by substituting the cell interface metrics $\mathbf{m}$ and $\mathbf{n}$ respectively in the above matrix.

The pressure derivatives appearing in this matrix can be written as:

$$\begin{aligned}
\frac{\partial p}{\partial \rho} &= -D_n + \frac{(\gamma-1)(u^2+v^2+w^2)}{2} \\
\frac{\partial p}{\partial \rho u} &= -(\gamma-1)u \\
\frac{\partial p}{\partial \rho v} &= -(\gamma-1)v \\
\frac{\partial p}{\partial \rho w} &= -(\gamma-1)w \\
\frac{\partial p}{\partial e} &= (\gamma-1) \\
\frac{\partial p}{\partial \rho_s} &= D_n - D_s \qquad s = 1,2,\dots,n-1
\end{aligned}$$

Two convenient terms that are used in the above expressions are γ and D_s. For a mixture of calorically imperfect but thermally perfect gases, these terms are written as:

$$\begin{aligned}
D_s &= (\gamma-1)h_s - \gamma\frac{\beta_1 T}{\mathcal{M}_s} \quad s = 1,2,\dots,n \\
\gamma &= \frac{\mathcal{M}C_{pf}}{\mathcal{M}C_{pf} - \beta_1}
\end{aligned}$$

Here, C_{pf} is the frozen specific heat of the mixture. For a single, perfect gas, D_s becomes zero and γ becomes the ratio of specific heats of that gas. For convenience, the temperature derivatives that appear in the viscous and source term Jacobians are also given.

$$\begin{aligned}
\frac{\partial T}{\partial \rho} &= \frac{\mathcal{M}}{\beta_1 \rho}\left(\frac{(\gamma-1)(u^2+v^2+w^2)}{2} - D_n - \frac{\beta_1 T}{\mathcal{M}_n}\right) \\
\frac{\partial T}{\partial \rho u} &= -\frac{\mathcal{M}}{\beta_1 \rho}(\gamma-1)u \\
\frac{\partial T}{\partial \rho v} &= -\frac{\mathcal{M}}{\beta_1 \rho}(\gamma-1)v \\
\frac{\partial T}{\partial \rho w} &= -\frac{\mathcal{M}}{\beta_1 \rho}(\gamma-1)w \\
\frac{\partial T}{\partial \rho v} &= \frac{\mathcal{M}}{\beta_1 \rho}(\gamma-1) \\
\frac{\partial T}{\partial \rho_s} &= \frac{\mathcal{M}}{\beta_1 \rho}\left(D_n - D_s + \frac{\beta_1 T}{\mathcal{M}_n} - \frac{\beta_1 T}{\mathcal{M}_s}\right) \quad s = 1,2,\dots,n-1
\end{aligned}$$

APPENDIX B
Eigenvectors

Consider the similarity transformation between the inviscid flux Jacobian,**A**, and the diagonal matrix, **Λ**, consisting of the eigenvalues of **A**. This transformation is written as:

$$\mathbf{\Lambda} = \mathbf{L}\mathbf{A}\mathbf{R}, \qquad \mathbf{L} = \mathbf{R}^{-1}$$

where,

$$\mathbf{\Lambda} = \mathrm{diag}(U + C, U - C, U, U, \ldots, U)$$

For this discussion, the metrics for the ξ-normal cell face are used. However, the other faces are considered by simply using those metrics instead. The terms appearing in the eigenvalues are then defined as:

$$U = l_x u + l_y v + l_z w$$
$$C = c\sqrt{l_x^2 + l_y^2 + l_z^2}$$

where, c is the frozen speed of sound:

$$c = \sqrt{\gamma \frac{p}{\rho}}$$

A set of left and right eigenvectors providing this similarity transformation are given below. The Left eigenvectors are:

$$\mathbf{L} = \begin{bmatrix}
\frac{(u^2+v^2+w^2)}{2} - \frac{c\hat{U}}{(\gamma-1)} - \frac{D_n}{(\gamma-1)} & -u + \frac{c\hat{l}_x}{(\gamma-1)} & -v + \frac{c\hat{l}_y}{(\gamma-1)} & -w + \frac{c\hat{l}_z}{(\gamma-1)} & 1 & \frac{D_n - D_1}{(\gamma-1)} & \frac{D_n - D_2}{(\gamma-1)} & \cdots & \frac{D_n - D_{n-1}}{(\gamma-1)} \\
\frac{(u^2+v^2+w^2)}{2} + \frac{c\hat{U}}{(\gamma-1)} - \frac{D_n}{(\gamma-1)} & -u - \frac{c\hat{l}_x}{(\gamma-1)} & -v - \frac{c\hat{l}_y}{(\gamma-1)} & -w - \frac{c\hat{l}_z}{(\gamma-1)} & 1 & \frac{D_n - D_1}{(\gamma-1)} & \frac{D_n - D_2}{(\gamma-1)} & \cdots & \frac{D_n - D_{n-1}}{(\gamma-1)} \\
-\hat{V} & \hat{m}_x & \hat{m}_y & \hat{m}_z & 0 & 0 & 0 & \cdots & 0 \\
-\hat{W} & \hat{n}_x & \hat{n}_y & \hat{n}_z & 0 & 0 & 0 & \cdots & 0 \\
\frac{(u^2+v^2+w^2)}{2} - h & -u & -v & -w & 1 & 0 & 0 & \cdots & 0 \\
-c_1 & 0 & 0 & 0 & 0 & 1 & 0 & 0 & 0 \\
-c_2 & 0 & 0 & 0 & 0 & 0 & 1 & 0 & 0 \\
\vdots & \vdots & \vdots & \vdots & \vdots & \vdots & \vdots & \ddots & \vdots \\
-c_{n-1} & 0 & 0 & 0 & 0 & 0 & 0 & 0 & 1
\end{bmatrix}$$

And the Right eigenvectors are:

$$\mathbf{R} = \begin{bmatrix}
\frac{(\gamma-1)}{2c^2} & \frac{(\gamma-1)}{2c^2} & 0 & 0 & \frac{-(\gamma-1)}{c^2} & \frac{(D_1 - D_n)}{c^2} & \frac{(D_2 - D_n)}{c^2} & \cdots & \frac{(D_{n-1} - D_n)}{c^2} \\
\frac{(\gamma-1)u}{2c^2} + \frac{(\gamma-1)\hat{l}_x}{2c} & \frac{(\gamma-1)u}{2c^2} - \frac{(\gamma-1)\hat{l}_x}{2c} & \hat{m}_x & \hat{n}_x & \frac{-(\gamma-1)u}{c^2} & \frac{(D_1 - D_n)u}{c^2} & \frac{(D_2 - D_n)u}{c^2} & \cdots & \frac{(D_{n-1} - D_n)u}{c^2} \\
\frac{(\gamma-1)v}{2c^2} + \frac{(\gamma-1)\hat{l}_y}{2c} & \frac{(\gamma-1)v}{2c^2} - \frac{(\gamma-1)\hat{l}_y}{2c} & \hat{m}_y & \hat{n}_y & \frac{-(\gamma-1)v}{c^2} & \frac{(D_1 - D_n)v}{c^2} & \frac{(D_2 - D_n)v}{c^2} & \cdots & \frac{(D_{n-1} - D_n)v}{c^2} \\
\frac{(\gamma-1)w}{2c^2} + \frac{(\gamma-1)\hat{l}_z}{2c} & \frac{(\gamma-1)w}{2c^2} - \frac{(\gamma-1)\hat{l}_z}{2c} & \hat{m}_z & \hat{n}_z & \frac{-(\gamma-1)w}{c^2} & \frac{(D_1 - D_n)w}{c^2} & \frac{(D_2 - D_n)w}{c^2} & \cdots & \frac{(D_{n-1} - D_n)w}{c^2} \\
\frac{(\gamma-1)\hat{U}}{2c} + \frac{(\gamma-1)H}{2c^2} & -\frac{(\gamma-1)\hat{U}}{2c} + \frac{(\gamma-1)H}{2c^2} & \hat{V} & \hat{W} & 1 - \frac{(\gamma-1)H}{c^2} & \frac{(D_1 - D_n)H}{c^2} & \frac{(D_2 - D_n)H}{c^2} & \cdots & \frac{(D_{n-1} - D_n)H}{c^2} \\
\frac{c_1(\gamma-1)}{2c^2} & \frac{c_1(\gamma-1)}{2c^2} & 0 & 0 & \frac{-c_1(\gamma-1)}{c^2} & 1 + \frac{c_1(D_1 - D_n)}{c^2} & \frac{c_1(D_2 - D_n)}{c^2} & \cdots & \frac{c_1(D_{n-1} - D_n)}{c^2} \\
\frac{c_2(\gamma-1)}{2c^2} & \frac{c_2(\gamma-1)}{2c^2} & 0 & 0 & \frac{-c_2(\gamma-1)}{c^2} & \frac{c_2(D_1 - D_n)}{c^2} & 1 + \frac{c_2(D_2 - D_n)}{c^2} & \cdots & \frac{c_2(D_{n-1} - D_n)}{c^2} \\
\vdots & \vdots & \vdots & \vdots & \vdots & \vdots & \vdots & \ddots & \vdots \\
\frac{c_{n-1}(\gamma-1)}{2c^2} & \frac{c_{n-1}(\gamma-1)}{2c^2} & 0 & 0 & \frac{-c_{n-1}(\gamma-1)}{c^2} & \frac{c_{n-1}(D_1 - D_n)}{c^2} & \frac{c_{n-1}(D_2 - D_n)}{c^2} & \cdots & 1 + \frac{c_{n-1}(D_{n-1} - D_n)}{c^2}
\end{bmatrix}$$

The vector, $\hat{\mathbf{l}} = \hat{l}_x i + \hat{l}_y j + \hat{l}_z k$ is the unit cell normal, and the vectors $\hat{\mathbf{m}}$ and $\hat{\mathbf{n}}$ are two arbitrary, perpendicular unit vectors that are in turn perpendicular to $\hat{\mathbf{l}}$. The terms $\hat{U}$, $\hat{V}$ and $\hat{W}$ are the velocities in each of these directions and can be written as:

$$\hat{U} = \hat{l}_x u + \hat{l}_y v + \hat{l}_z w$$
$$\hat{V} = \hat{m}_x u + \hat{m}_y v + \hat{m}_z w$$
$$\hat{W} = \hat{n}_x u + \hat{n}_y v + \hat{n}_z w$$

APPENDIX C
Chemical Source Terms

The chemical source term appearing in Eq. 1 is written as:

$$D = (0, 0, 0, 0, 0, \dot{w}_1, \dot{w}_2, \ldots, \dot{w}_{n-1})^T$$

where $\dot{w}_s$ is the mass production of species s resulting from any number of chemical reactions involving that species. Consider a mixture of gases with n species undergoing m simultaneous reactions. Each chemical reaction is represented symbolically as:

$$\sum_{l=1}^{n_t} \nu'_{kl} A_l \rightleftharpoons \sum_{l=1}^{n_t} \nu''_{kl} A_l$$

where ν'_{kl} and ν''_{kl} are the stoichiometric coefficients and A_l is the chemical symbol for the l^{th} species. n_t is the total number of reactants including third bodies and electrons. The mass production rate of species s is determined by the law of mass action. It is stated as:

$$\dot{w}_s = \mathcal{M}_s \sum_{l=1}^{m} (\nu''_{l,s} - \nu'_{l,s}) \left[k_{f,l} \prod_{r=1}^{n_t} [\gamma_r]^{\nu'_{l,r}} - k_{b,l} \prod_{r=1}^{n_t} [\gamma_r]^{\nu''_{l,r}} \right]$$

The molar concentrations, γ_r, of the species are defined as:

$$\gamma_r = \rho_r / \mathcal{M}_r \qquad r = 1, 2, \ldots, n$$

and the molar concentrations of the catalytic third bodies are expressed in terms of their third body efficiencies as:

$$\gamma_r = \sum_{s=1}^{n} Z_{(r-n),s} \gamma_s \qquad r = n+1, n+2, \ldots, (n + n_{tb})$$

where n_{tb} is the number of third bodies considered. If electrons are considered, their molar concentration is evaluated by assuming the molar concentration of electrons is equal to the molar concentration of ions. This is stated as,

$$\gamma_{n_t} = \sum_{s=1}^{n} I_s \gamma_s$$

where, I_s is the charge of species s and the subscript n_t represents the last considered species which in this case is the electron.

The forward and backward reaction rates of any reaction considered are assumed to be solely a function of temperature and are expressed in the modified Arrhenius form as

$$k_{f,l}(T) = \exp(\log_e C_{1,l} + \frac{C_{2,l}}{T} + C_{3,l} \log_e T)$$
$$k_{b,l}(T) = \exp(\log_e D_{1,l} + \frac{D_{2,l}}{T} + D_{3,l} \log_e T)$$

These reaction rate coefficients have been nondimensionalized with the following expressions.

$$C_{1,l} = \frac{\tilde{L}}{\tilde{Q}_\infty} \left(\frac{\tilde{\rho}_\infty}{\tilde{\mathcal{M}}_\infty} \right)^{\alpha_l - 1} 10^{3-3\alpha_l} \tilde{T}_\infty^{\tilde{C}_{3,l}} \tilde{C}_{1,l}$$
$$D_{1,l} = \frac{\tilde{L}}{\tilde{Q}_\infty} \left(\frac{\tilde{\rho}_\infty}{\tilde{\mathcal{M}}_\infty} \right)^{\beta_l - 1} 10^{3-3\beta_l} \tilde{T}_\infty^{\tilde{D}_{3,l}} \tilde{D}_{1,l}$$
$$C_{2,l} = \frac{\tilde{C}_{2,l}}{\tilde{T}_\infty}, \qquad C_{3,l} = \tilde{C}_{2,l}$$
$$D_{2,l} = \frac{\tilde{D}_{2,l}}{\tilde{T}_\infty}, \qquad D_{3,l} = \tilde{D}_{2,l}$$

$$\alpha_l = \sum_{r=1}^{n_t} \nu'_{l,r}, \qquad \beta_l = \sum_{r=1}^{n_t} \nu''_{l,r}$$

The terms $\tilde{C}_{1,l}$, $\tilde{C}_{2,l}$, $\tilde{C}_{3,l}$, $\tilde{D}_{1,l}$, $\tilde{D}_{2,l}$ and $\tilde{D}_{3,l}$ are constants for a particular reaction l.

EXPERIMENTAL AND COMPUTATIONAL RESULTS FOR 5 DEGREE BLUNT CONES WITH SHOCK GENERATORS AT HIGH VELOCITY

by

A. W. Strawa*, G. A. Molvik**, L. A. Yates† , and C. Cornelison‡
NASA Ames Research Center, Moffett Field, California

ABSTRACT

Experiments and computations have been performed under laminar conditions in air on 5° blunt cones at velocities of 5 km/s and 6 km/s and at Reynolds numbers of 10^5 and 10^6. The experiments were conducted in the Ames' ballistic range. The computations were performed using ideal-, equilibrium- and nonequilibrium-chemistry models for air. At the conditions of the tests, the aerodynamic coefficients are sensitive to the real-gas effects present, and both experimental and computational aerodynamic coefficients show real-gas and non-linear effects. The nonequilibrium computations show that a large amount of oxygen is dissociated in the blunt nose region of the flow and much of the oxygen remains dissociated over the entire length of the body, providing an insight into the source of the observed effects in the aerodynamic coefficients. The experimental and computational shock-shapes are in good agreement.

NOMENCLATURE

A	model base area
C_D	drag coefficient
C_L	lift coefficient
C_M	pitching moment coefficient
C_{M_d}	combined damping coefficient $C_{M_d} = C_{M_q} + C_{M_{\dot{\alpha}}}$
d	model base diameter
M_∞	free-stream Mach number
m	model mass
Re_l	free-stream Reynolds number based on model length
T	temperature
(u, v, w)	model velocity with respect to body axis
V	velocity $V = \sqrt{u^2 + v^2 + w^2}$
(x, y, z)	model position in Cartesian system
α	pitch angle
α_T	thermal diffusivity
β	yaw angle
ϵ	estimated error in aerodynamic coefficients
γ	ratio of specific heats
κ	thermal conductivity
q	rate of pitch
q_s	surface heat flux
ρ	density
σ	resultant angle-of-attack; $\sin(\sigma) = \sqrt{v^2 + w^2}/V$

subscripts

b	base
n	nose
s	surface value
∞	freestream value

INTRODUCTION

Future missions of national interest require the design of vehicles that will fly at hypervelocities and at high altitudes.[1,2] New mission profiles will subject these future vehicles to harsh environments where not all of the relevant physical phenomenon are completely understood. Since no ground based facility can completely simulate the flight environment, computational solutions will become increasingly important in vehicle design and in predicting vehicle performance. To this end, it is essential that our ground based facilities and computer codes be used together to understand the relevant phenomenon and to insure that they are properly modeled. Experiments that can better isolate the effects of certain physical phenomena can be designed with the aid of computational aerothermodynamics, and experimental results can be used to verify the computational models and methods. The process of code verification is discussed in Ref. 3.

The objective of this research was to conduct an experiment which would produce non-linear and real-gas effects in the aerodynamic coefficients for a generic model, to use a state-of-the-art computer code to compute the flowfields, and to compare the results. Past experience with the Apollo vehicle and the Space Shuttle (STS) indicate that real-gas effects can have a significant influence on pitching moments.[4-6] Computational

*Research Scientist, Aerothermodyamics Branch. Member AIAA.
**MCAT Institute, NASA Ames Research Center. Member AIAA.
†Eloret Institute, Sunnyvale, Ca. AIAA Member.
‡Test Engineer, NASA Ames Research Center.

methodology at that time was unable to predict the full extent of these effects. Computational methods today have matured to the point were complex hypersonic flowfields can be calculated. However, experimental data demonstrating real-gas effects on slender bodies which are suitable for code verification are very limited. Welsh et al. conducted tests on 10° blunt cones at $V = 4.8\,km/s$ in nitrogen and air in a ballistic range.[7] They attributed changes in C_M to real-gas effects. Kruse obtained drag data for 6° blunt cones at $V = 5.2\,km/s$ and Re_l = 300,000 in the Ames' ballistic range.[8] Malcolm and Rakich showed the effect of nose bluntness on 12.5° cones at Mach 17.[9] All of these tests showed nonlinearity and real-gas effects in the aerodynamic coefficients. Real-gas effects were observed by Strawa et al. on sharp cones.[10] Additionally, real-gas effects have been simulated by matching γ in the Langley CF_4 tunnel (see, for example, ref. 11).

In the present study, a 5° half-angle cone with a bluntness ratio, d_n/d_b, of .3 was selected. Two small shock generators were included to show the effects of real-gas chemistry on the shape of internal shocks. The velocities were 5 and $6\,km/s$ and the Mach numbers were 14.5 and 17.6. The computations were conducted using a combination of time- and space- marching algorithms which included fully-coupled chemistry models. The strong shock produced by the blunt nose at these speeds generated temperatures high enough to dissociate a significant amount of oxygen. The Reynolds numbers (based on model length) were varied from 10^6 to 10^5, which should result in a increase in skin friction by a factor of three for laminar flow conditions. Viscous interactions between the boundary layer and the outer inviscid flow can have important effects on the surface pressure distribution and, hence, on the drag, lift, and moment coefficients.[12] The moment coefficient of the present model should be sensitive to real-gas effects on the pressure and skin friction.

THE BALLISTIC RANGE EXPERIMENTS

The experimental data presented in this paper were obtained in the the Hypervelocity Free-Flight Aerodynamic Facility (HFFAF) ballistic range at Ames Research Center. The HFFAF ballistic range is shown schematically in Fig. 1. The facility consists of: a two-stage light-gas gun, a tank in which the sabot is separated from the model, and a test section where the major portion of the instrumentation is located. Gun bore sizes range from 1.1 cm to 3.75 cm (the 2.5 cm gun was used in these tests) and the test section is about 1 m across and 25 m long. The test section can be evacuated to achieve the proper Reynolds number for the model size and velocity. In the HFFAF a model of about 50 gm mass can be accelerated up to $7\,km/s$.

The ballistic range can simultaneously simulate the Mach number and Reynolds number of a high-speed vehicle in an undisturbed, clean, and well-characterized ambient gas. Additionally, there is no sting to effect the aerodynamics of the model. As the model flys through the test section its position, orientation, and time-of-flight are recorded at 16 test stations that consist of orthogonal, focused-shadowgraph systems. In the HFFAF the position of the model can be measured to ± 0.006 cm, its orientation to $\pm 0.1°$, and time-of-flight to ± 40 ns.

In the present study, cones with a bluntness ratio, d_n/d_b, of .3 and shock generators were launched in the ballistic range for the purpose of measuring the aerodynamic coefficients and shock shapes. A drawing of the model is shown in Fig. 2. Fig. 3 is a photograph of the model and its four piece sabot and pusher plug. The sabot protects the model during the high-g's encountered during launch. After launch, aerodynamic forces separate the sabot pieces and the model proceeds downrange in free flight. The nose of all models was fabricated of tantalum to avoid nose-tip ablation and the afterbody was fabricated of aluminum. The test conditions for the experimental data are listed in Table 1. The runs were divided into three groups based on freestream conditions. In case 1, $V = 5\,km/sec.$ and $Re_l = 10^5$; in case 2, $V = 5\,km/sec$ and $Re_l = 10^6$; in case 3, $V = 6\,km/s$ and $Re_l = 10^5$. The test gas was air. For all conditions tested, the flow over the models remained laminar. When test runs were made at $V = 6\,km/s$ and $Re_l = 10^6$, the nose tip temperature became so high that the tantalum nose began to spall. These runs are not included in this report.

A new data reduction routine is used to fit the calculated trajectory to the measured trajectory using a least-squares analysis. The routine assumes a 5 degree-of-freedom model of the equations of motion (roll rate is assumed constant), written in terms of the aerodynamic coefficients. The aerodynamic coefficients are approximated by Taylor series expansion in $\sin\sigma$:

$$C_M = (C_{M_1} + C_{M_3}\sin^2\sigma + C_{M_5}\sin^4\sigma)\sin\sigma \quad (1)$$

$$C_L = (C_{L_1} + C_{L_3}\sin^2\sigma + C_{L_5}\sin^4\sigma)\sin\sigma \quad (2)$$

$$C_D = C_{D_0} + C_{D_2}\sin^2\sigma \quad (3)$$

The routine can fit raw data from several test runs simultaneously improving the accuracy of the method. The equations and method used are described in more detail in the Appendix.

The data reduction routine provides estimates of the error, ϵ, in the aerodynamic coefficients; for example,

$$\epsilon_D = \sqrt{Var(C_D)} \quad (4)$$

The error estimates take into account the uncertainty in measuring model trajectory and freestream conditions and the quality of the least-squares fit. However, they are sensitive to the number of terms taken in the Taylor series expansions used to approximate the aerodynamic coefficients. During data reduction, the number of terms in the expansions is varied and the set which produces the smallest estimated error is reported. The minimum estimated error occurs in the region where the experimental data is concentrated. For the present tests, the data is concentrated at resultant angles between 5° and 10°.

FLOWFIELD COMPUTATIONS

Two numerical algorithms were used to obtain the computed results.[13,14] The baseline conditions for these computations are listed in Table 2. The first algorithm, TUFF, is a time-marching scheme and was used to compute the axisymmetric, blunt-body results from the stagnation point to 70° on the spherical nose. The second algorithm, STUFF, is a space-marching scheme and was used to compute the remaining afterbody flow field. Both codes employ a finite-volume philosophy to ensure that the algorithms (including boundary conditions) are fully conservative. Further, they obtain upwind inviscid fluxes by employing a Riemann solver that fully accounts for the gas model used. Either a ideal-, equilibrium-, or nonequilibrium-chemistry model can be used.[14] Thermal equilibrium is assumed in all gas models. The algorithms are total variation diminishing (TVD) which allows the computation of flowfields with strong discontinuities without introducing any spurious oscillations. They employ a strong coupling between the fluid dynamic and species conservation equations and are made fully implicit to eliminate the step size restriction of explicit schemes. Finally, the Vigneron approximation is used in the STUFF algorithm to allow stable space-marching in the presence of a subsonic viscous layer.[15]

This combination of a time- and space-marching algorithms was chosen since it allowed the solution to be obtained on a rather fine grid in a reasonable amount of computer time. The blunt body grid measured 29 cells from the stagnation point to the terminator and 49 cells of exponentially increasing size in the normal direction. The first cell was $0.25 \times 10^{-6} m$ off the body surface for the lower Reynolds number computations and was decreased by a factor of three for the higher Reynolds number cases. The after-body grid used the same normal spacing as the blunt body grid. The three-dimensional, space-marching computations were performed with 29 meridonal planes of cells. Nonequilibrium computations at zero angle-of-attack required about 1.4 CPU-hours on the Cray Y-MP, while computations at 5° angle-of-attack required over 6.1 CPU-hours.

The surface temperature as a function of flight-time was computed with a one-dimensional, heat-transfer model. The surface heat flux was taken to be

$$\dot{q}_s(t_f) = \frac{\kappa(T_s(t_f) - T_i)}{\sqrt{\pi t_f \alpha_T}}. \qquad (5)$$

An iteration was performed to obtain the wall temperature, T_s, along the model surface and the time-of-flight, t_f, was taken to be 5 msec. The initial temperature of the cone, T_i, was assumed to be room temperature and the cone's multiple composition was modeled. A fully catalytic wall boundary condition was used. Wall temperature profiles show that, except at the nose, the wall temperature is approximately that of the free-stream.

RESULTS AND DISCUSSION

The experimentally determined coefficients of the aerodynamic functions are tabulated in Table 3. The aerodynamic coefficients at a specific angle-of-attack can be obtained from equations 1, 2, and 3. Included with the values for the aerodynamic coefficient are values for the estimated error. Computations were performed at 0 angle-of-attack for all cases and at 5° angle-of-attack for cases 1 and 2. For case 2, three gas models were used. The computed aerodynamic coefficients at 0° and 5° angle-of-attack are tabulated in Table 4. The experimental and computational values are also presented graphically for comparison. In these figures, the experimental data are plotted as lines and the computed results are plotted as points. The number of terms included in the expansions of the aerodynamic coefficients and the domain in which these expansions are valid are determined by the total angular range of the data. For case 2, the angular range extended to $\sigma = 8°$, and the data is plotted only over this range. For cases 1 and 3 the angular range extended to $\sigma = 15°$.

Computed and experimental shock shapes are in reasonable agreement. Fig. 4 shows a comparison of the computed and experimental outer shock structure for case 2. The computed shock is the white line superimposed on a shadowgraph from the range test. An outline of the body shape used in the computation is also included. Unfortunately, the ambient densities at the conditions of the tests were too low to produce shadowgraphs of sufficient quality to discern the internal shock structure produced by the shock generators. As will become apparent in the discussion that follows, however, the shock generators did have some effects on the aerodynamics of the test model.

Drag

Experimental and computed drag coefficient versus resultant angle-of- attack, σ, is plotted in Fig. 5

for all three cases and are tabulated in Tables 3 and 4. The pressure at the base was assumed to be a vacuum for the computational results. Actually, the base pressure is estimated to be about half that of ambient, resulting in an increase in the computed drag coefficient of less than 3%. This correction to the computational result is approximately equal to the estimated experimental error. Values of C_D calculated at 0° and 5° using modified Newtonian theory are also included for comparison. Newtonian theory considers only pressure drag and should provide a value close to but slightly below the higher Reynolds number case (case 2) as is observed. The drag for case 2 is due mostly to the pressure drag generated by the blunt nose. The drag due to viscous effects is much more important in cases 1 and 3, where the Reynolds number is 10^5. From case 1 to case 2 the Reynolds number has increased from $Re_l = 10^5$ to $Re_l = 10^6$ while the velocity has remained constant at 5 km/s. Since skin friction is proportional to Reynolds number to the -0.5 power, the viscous drag should be three times greater in case 1 than in case 2. This effect can be seen in the shift of the experimental drag curve. For example, C_{D_0}, equal to 0.170 in case 1, decreased to 0.112 in case 2(see Table 3). This shift is reflected in the computed nonequilibrium-chemistry drag coefficient which was 0.1617 for case 1 and 0.1241 for case 2. Little real-gas effects are observed in the computed values of C_D. This is in agreement with earlier data for blunt cones.

The velocity has increased from V = 5 km/s in case 1 to V = 6 km/s in case 2 while the Reynolds number has remained constant at 10^5. There is negligible effect of this velocity increase as can be seen in Table 3, where the differences in C_{D_0} and C_{D_2} are less than the sum of their estimated errors.

Computational results are in generally good agreement with experimental results. Computed drag for cases 1 and 3 fall slightly below but within the estimated error of the experimental values. The computed value for C_{D_0} in case 2 is higher than the experimental value by about 10%. This is outside the estimated error for that case. The shape of the drag curve with respect to angle-of-attack is caused by drag due to lift, thus, C_{D_2} is expected to be proportional to C_L. Tables 3 and 4 show that experimental values for C_{D_2} are virtually the same for cases 1 and 2 as are values for C_L in the computed results. The computed value of C_{D_2} for case 1 is 3.46, in good agreement with the experimental data; the computed value for C_{D_2} for case 2 is 2.42, which is not in agreement with the experimental data. The reasons for this discrepancy are presently unknown.

Moment

Experimental and computed values of the moment coefficient are plotted in Figure 6 with the values listed in Tables 3 and 4, respectively. The experimental data shows much non-linearity in agreement with the results reported by Welsh et al.[7] and Malcolm and Rakich[9] for blunt cones with different cone half-angles. The non-linearity can also be seen in the values for C_M listed in Table 3. For cases 1 and 3, three moment coefficient terms were needed to adequately fit the model trajectory. In case 2 only two terms were needed to describe the model trajectory due to a smaller range of angular motion. Table 3 shows little difference between the values for C_{M_1} and C_{M_3} over the measured range of motion for cases 1 and 2 showing little Reynolds number effect. This is reflected in the nonequilibrium-air values of C_M computed at 5° reported in Table 4. While the computed viscous contribution to the moment coefficient decreased markedly from 0.0090 in case 1 to 0.0028 in case 2, the pressure contribution increased from 0.0339 in case 1 to 0.0375 in case 2, offsetting the decrease in viscous effects. Table 4 shows a difference in the moment coefficient in case 2 of 32% between the computed ideal-gas value to that of the nonequilibrium-air value, demonstrating that the real-gas effects for this case made the model more stable. Welsch et al. found that while real-gas effects made models with a bluntness ratio of less than 0.2 unstable, models with a bluntness ratio greater than 0.2 were stabilized.[7] This agrees with the current computational result. The calculations for case 2 show little change in the viscous contribution to moment coefficient between the nonequilibrium-air model (-0.0028) and the ideal-gas model (-0.0024). The pressure contribution changes from -0.0375 for the nonequilibrium air case to -0.0249 for the ideal gas case, a change of 66%. The estimated errors for experimental moment coefficient for case 3 are too large to attribute any effect to the change in velocity.

Figs. 7 a through c show computed mass fractions of atomic oxygen for the three cases, respectively, at three locations measured from the nose and at 0° angle-of-attack. The mass fraction of oxygen in the ambient stream is 26%. The oxygen is fully dissociated in the stagnation region of all of the cases, and the figures show that significant amounts of atomic oxygen are present in the flow along the after body where it has the most effect on the aerodynamics. The mass fraction of atomic oxygen for all cases decreases to zero at the wall reflecting the wall boundary conditions. In case 1 the mass fraction is lower than in the other two cases and decreases quickly downstream reflecting the lower temperatures generally present in the flow in that case. The calculations for case 2 show little change in the viscous contribution to the moment between the nonequilibrium air chemistry model (-0.0028) and the ideal-gas chemistry model (-0.0024). The pressure contribution to the

moment, on the other hand, changes from -0.0375 for the nonequilibrium air model to -0.0249 for the ideal gas model, a change of 66%. This suggests that real-gas effects are important in the pressure field rather than in the viscous boundary layer as one might expect.

Fig. 8 shows simulated oilflow patterns for cases 1 and 2 at $\sigma = 5°$. The simulated oilflow patterns were generated by taking the velocity vector of the first gridpoint off the surface. These figures show that most of the dissociated fluid from the nose of the body is swept to the lee side of the body concentrating atomic oxygen on the lee side. Fluid in the boundary layer on the windward surface has traversed a weak oblique shock and will contain little dissociated oxygen while fluid on the lee surface will contain a large amount of dissociated oxygen. This partially explains the difference between the moment coefficients calculated using the ideal gas and nonequilibrium air chemistry models. The computations suggest the start of a separation region with reverse flow near the second shock generator at $\sigma = 5°$. While the PNS code used to compute the flow on this portion of the body can indicate the presence of a separated region, it cannot compute flow details in that region or the effects on the aerodynamics. This separation region is quite small and will have little effect on the drag but may effect the lift and moment coefficients somewhat.

The computed solutions are, of course, steady state solutions, and the question arises whether the dynamics of the model in free-flight in the ballistic range will allow the separation to set up at this angle-of-attack. The models went through between one and two cycles of motion during their 5 msec flight down the range. By contrast, the flow time (the time fluid at the nose takes to reach the tail) is on the order of 6 μsec. This corresponds to a reduced frequency of about 0.002. There will be enough time for the separation to set up and, hence, the trajectory and experimentally determined aerodynamic coefficients will reflect the effects of the separation.

Lift

Figure 9 shows the experimental and computed values for C_L for case 2. The model motion is less sensitive to the lift coefficient than to the other coefficients reported in this paper, and in ballistic range testing 1.5 to 2 wavelengths of motion is required in a given run to determine the lift coefficient. About half a wavelength of motion was obtained for cases 1 and 3. While this was enough for the determination of drag and moment, it did not allow sufficient confidence in values for the lift coefficient. Therefore, lift coefficients are reported only for case 2. Computed values of C_L for all cases are reported in Table 4. Since our confidence in the experimental lift coefficients for cases 1 and 3 was low, the effect of variations in the lift coefficient on the other aerodynamic coefficients was investigated. A linear lift coefficient was assumed, i.e. C_{L_3} and C_{L_5} were set to zero while C_{L_1} and the drag and moment coefficients were allowed to vary. Values of C_L equal to 1.5 times the computed value were input into the reduction routine and the moment and drag coefficients were recalculated. This resulted in changes in C_D and C_M on the order of 0.05%. These variations are much smaller than the expected accuracy of the drag and moment coefficients themselves.

Agreement between the computed and experimental values of lift coefficient at 5° for case 2 are acceptable. A value obtained using modified Newtonian theory is included for comparison. This value is very high as is expected. The computed nonequilibrium air value of 0.0927 is greater than the ideal gas value of 0.0778 showing a significant real-gas effect. The real-gas effects for the 5° cones are much greater than that reported by Welsh et al. for 10° cones.

The calculated value of C_L for case 1 (see Table 4) was 0.0908, only 2% below the value for case 2. This suggests that Reynolds number effects are not as important in the lift coefficient as was suspected.

Damping

Damping is due to 1) a slightly different angle-of-attack from forebody to afterbody due to the curved flight path, and 2) a time lag before a translation in nose position can result in a translation of the shear flow on the afterbody. The first order damping coefficient, $C_{M_d} = C_{M_q} + C_{M_\dot{\alpha}}$, is extremely difficult to obtain in most facilities. Since all of the aerodynamics are reflected in the motion of the model, the damping coefficient must be included in the data reduction routine. When there are onlu a few cycles of motion, the trajectory of the model is not very sensitive to the damping coefficient, thus, the estimated errors obtained for these coefficient are typically large. However, designers often need only know the sign and order of magnitude of these coefficients to properly design a vehicle. The damping coefficient obtained for all three cases are included in Table 3. Note the large differences in damping coefficient between the three cases. Unsteady codes are needed to compute the damping coefficient; hence, none were computed for this model.

CONCLUSIONS

Experiments and computations have been performed on 5° half-angle cones with a bluntness ratio of 0.3 and with shock generators at 5 and 6 km/s and at Reynolds numbers of 10^5 and 10^6 in air. Experimentally derived aerodynamic coefficients have been

determined for drag, moment, lift, and damping with estimated errors. The computations employed ideal-, equilibrium-, and nonequilibrium-gas chemistry models for air and realistic boundary conditions at the wall. The calculated moment and lift coefficients demonstrate real-gas effects. These effects increase the stability of this test model, in agreement with previous results. The strong shock produced by the at these speeds generates temperatures high enough to dissociate all of the oxygen in the blunt nose region. The computations show that significant amounts of atomic oxygen persist in the flow along the after body where it can effect the aerodynamic performance of the model. The presence of the atomic oxygen is seen to have a large effect on the pressure contribution to the moment coefficient and little effect on the viscous contribution. The experimental results have been compared with the computations. With few exceptions, there is good agreement between experimental and computed shock shapes and aerodynamic coefficients. The computations can provide detailed information about the state of the gas. While measurement techniques have been developed which can provide experimental confirmation of these details, they have only recently begun to be applied in hypervelocity facilities.

APPENDIX

A Five-Degree of Freedom Routine for Determining Aerodynamic Coefficients from Free-Flight Experiments

Aerodynamic coefficients can be obtained from free-flight experiments with a least-squares procedure that fits functions describing the motion of a projectile to experimental data.[16] The procedure has been modified to a weighted least-squares procedure. The motion of the model is described by twelve first-order differential equations.[17] For a five-degree of freedom system, the roll rate is assumed constant and the system reduces to eleven first-order differential equations:

$$\dot{V} = -\frac{D}{m} - g \sin \theta_w \tag{6}$$

$$\dot{x} = V \cos \theta_w \cos \psi_w \tag{7}$$

$$\dot{y} = -V \cos \theta_w \sin \psi_w \tag{8}$$

$$\dot{z} = -V \sin \theta_w \tag{9}$$

$$\dot{\alpha} = q - q_w \sec \beta - p \cos \alpha \tan \beta - r \sin \alpha \tan \beta \tag{10}$$

$$\dot{\beta} = r_w + p \sin \alpha - r \cos \alpha \tag{11}$$

$$\dot{q} = \frac{M}{I_y} + \frac{I_y - I_x}{I_y} pr \tag{12}$$

$$\dot{r} = \frac{N}{I_y} - \frac{I_y - I_x}{I_y} pq \tag{13}$$

$$\dot{\phi}_w = P_w + Q_w \sin \phi_w \tan \theta_w + R_w \cos \phi_w \tan \theta_w \tag{14}$$

$$\dot{\theta}_w = Q_w \cos \phi_w - R_w \sin \phi_w \tag{15}$$

$$\dot{\psi}_w = (Q_w \sin \phi_w + R_w \cos \phi_w) \sec \theta_w \tag{16}$$

where

$$p_w = p \cos \alpha \cos \beta + (q - \dot{\alpha}) \sin \beta + r \sin \alpha \cos \beta + \text{coriolis and gravity terms} \tag{17}$$

$$q_w = \frac{L}{mV} + \text{coriolis and gravity terms} \tag{18}$$

$$r_w = -\frac{Y}{mV} + \text{coriolis and gravity terms} \tag{19}$$

and $(P_w, Q_w, R_w) = (p_w, q_w, r_w)$ plus additional terms due to a rotating earth. In these equations, V is the velocity of the projectile, (x, y, z) is the location of the projectile in reference to an earth fixed coordinate system, α and β are the pitch and yaw angles relative to the wind axes, p, q, and r are the roll, pitch, and yaw rates, and ϕ_w, θ_w, and ψ_w give the orientation of the wind axes to the earth fixed axes. The model specific parameters m, I_y, and I_x are, respectively, the mass, the moment of inertia about a transverse axis through the center of gravity, and the moment of inertia about the axis of symmetry. The aerodynamic information is contained in the functions describing the pitching and yawing moments, M and N, the functions describing the lift and yawing forces, L and Y, and the function describing the drag, D.

For an axially symmetric projectile, these aerodynamic functions can be approximated by the expansions:

$$M = \frac{\rho A d V^2}{2} (C_{M_0} + C_{M_\sigma} \cos \beta \sin \alpha) + C_{M_q} q + C_{M_{\dot{\alpha}}} \dot{\alpha} \tag{20}$$

$$N = -\frac{\rho A d V^2}{2} (C_{N_0} + C_{M_\sigma} \sin \beta) + C_{M_q} r \cos \alpha - C_{M_{\dot{\beta}}} \dot{\beta} \tag{21}$$

$$L = \frac{\rho A V^2}{2} (C_{L_0} + C_{L_\sigma} \cos \beta \sin \alpha) \tag{22}$$

$$Y = \frac{\rho A V^2}{2} (C_{Y_0} + C_{L_\sigma} \sin \beta) \tag{23}$$

$$D = \frac{\rho A V^2}{2} C_D \tag{24}$$

where ρ is the density of the fluid, A is the base area of the model, and d is the diameter of the base. The coefficients C_{M_0}, C_{N_0}, C_{L_0}, and C_{Y_0} are the moments and lifts at zero angle-of-attack and are caused by small asymmetries in machining. The aerodynamic coefficients C_{M_σ}, C_{L_σ}, and C_D are assumed to be functions of σ (the resultant angle-of-attack), the Mach number, and the Reynolds number. The aerodynamic damping terms, C_{M_q} and $C_{M_{\dot{\alpha}}}$ are assumed to be constant. For the test conditions reported in this paper, $\dot{\beta} \approx -r \cos \alpha$ and $\dot{\alpha} \approx q$. It is therefore impossible to determine C_{M_q} and

C_{M_σ} separately; only the sum of these two coefficients can be determined. The other aerodynamic coefficients are approximated by

$$C_{M_\sigma} = C_{M_1} + C_{M_3} \sin^2 \sigma + C_{M_5} \sin^4 \sigma \quad (25)$$

$$C_{L_\sigma} = C_{L_1} + C_{L_3} \sin^2 \sigma + C_{L_5} \sin^4 \sigma \quad (26)$$

$$C_D = C_{D_0} + C_{D_2} \sin^2 \sigma \quad (27)$$

The estimated errors for the aerodynamic coefficients and for functions of these aerodynamic coefficients are readily available from the least squares analysis. For instance, if the angle-of-attack is known exactly, the variance for C_D is equal to

$$\mathrm{Var}(C_D) = \mathrm{Var}(C_{D_0}) + 2\,\mathrm{Cov}(C_{D_0}, C_{D_2}) \sin^2 \sigma + \mathrm{Var}(C_{D_2}) \sin^4 \sigma \quad (28)$$

where the variances and covariance are given by

$$\mathrm{Var}(C_{D_0}) = A^{-1}_{C_{D_0}, C_{D_0}} \mathrm{Var}(x) \quad (29)$$

$$\mathrm{Var}(C_{D_2}) = A^{-1}_{C_{D_2}, C_{D_2}} \mathrm{Var}(x) \quad (30)$$

$$\mathrm{Cov}(C_{D_0}, C_{D_2}) = A^{-1}_{C_{D_0}, C_{D_2}} \mathrm{Var}(x) \quad (31)$$

The variance and, hence, the predicted error for the drag are functions of the variances for each coefficient, their covariance, and the angle-of-attack. Since the covariances are often negative, the minimum predicted error can occur at non-zero angles-of-attack; it typically occurs in the region where the angular data is clustered. Similar results can be obtained for both the lift and moment coefficients.

REFERENCES

1. Walberg, G.D., "A survey of aeroassisted orbital transfer," *J. Spacecraft*, vol. 22, no. 1, 1985.
2. William, R.M., "National Aero-Space Plane: technology for America's future," *Aerospace America*, Nov. 1986.
3. Marvin, J.G., "Accuracy requirements and benchmark experiments for CFD validation," AGARD Symposium on Validation of Computational Fluid Dynamics, Lisbon, Portugal, May 2-5, 1988.
4. Crowder, R.S., and Moote, J.D., "Apollo entry aerodynamics," *J. Spacecraft*, vol. 6, no. 3, March, 1969.
5. Griffith, B.J., Maus, J.R., and Best, J.T., "Explaination of the hypersonic longitudinal stability problem - lessons learned," in *Shuttle Performance: Lessons Learned*, NASA Conference Publication 2283, 1983.
6. DeRose, C.E., "Trim attitude, lift, and drag of the Apollo comand module with offset center-of-gravity positions at Mach numbers to 29", NASA TN D-5276.
7. Welsh, C.J., Lawrence, W.R., and Watt, R.M., "Real-gas effects on the aerodynamics of blunt cones as measured in a hypervelocity range," AEDC- TR-79-33, Oct. 1979.
8. Kruse, R.L., "Comparison of the aerodynamic characteristics of an ablating and nonablating blunted conical body," NASA TN D-7196, Mar. 1973.
9. Malcolm, G. N., and Rakich, J. V., "Comparison of Free-flight experimental results with theory on the nonlinear aerodynamic effects of bluntness for slender cones at Mach number 17," AIAA Paper No. 70-554.
10. Strawa, A.W., and Prabhu, D.K., "A comparison of experimental and computational results for 5 and 10 degree cones at high Mach numbers," AIAA paper no. 88-2705.
11. Hunt, J.L., Jones, R.A., and Midden, R.E., "Simulation of Real-gas effects for Mars entry", *J. Spacecraft*, Vol. 11, no. 1, Jan. 1974.
12. Anderson, J.D., **Hypersonic and High Temperature Gas Dynamics**, McGraw-Hill, 1989.
13. Molvik, G.A., Merkle, C.L., "A set of strongly coupled, upwind algorithms for computing flows in chemical nonequilibrium." AIAA Paper 89-0199, January 1989.
14. Molvik, G.A., "A computational model for the prediction of hypersonic, reacting flows," Ph.D. Thesis, Pennsylvania State University, August 1989.
15. Vigneron, Y.C., Rakich, J.C., and Tannehill,J.C., "Calculation of supersonic viscous flow over delta wings with sharp subsonic leading edges." AIAA Paper 78-1137, July 1978.
16. Chapman, G.T., and Kirk, D.B., "A method for extracting aerodynamic coefficients from free-flight data," *AIAA Journal*, vol 8,no. 4, Apr. 1970, pp. 753-758.
17. Etkin, B., **Dynamics of Atmospheric Flight**, Wiley, 1972.

Table 1. Experimental Conditions

	Shot #	$V_{(km/s)}$	Re_l	$P_{(kPa)}$	Temp(K)	Mass(gm)	Length(cm)	Base diam(cm)	$X_{c.g.(cm)}$
Case 1	1785	4.99	0.10×10^6	0.878	297.4	1.84	3.62	0.886	1.79
	1788	4.98	0.10×10^6	0.884	297.8	1.82	3.62	0.886	1.79
	1790	4.95	0.10×10^6	0.884	297.7	1.84	3.62	0.886	1.79
Case 2	1750	5.06	1.10×10^6	9.443	298.7	1.91	3.63	0.889	1.87
	1752	5.02	1.11×10^6	9.443	296.7	1.91	3.64	0.889	1.87
	1756	5.00	1.07×10^6	9.373	300.3	1.89	3.63	0.886	1.85
Case 3	1823	6.08	0.11×10^6	0.793	294.2	2.09	3.64	0.889	1.88
	1826	6.05	0.11×10^6	0.800	294.2	2.08	3.64	0.889	1.88

Table 2. Baseline Conditions for Computations

	$V_{(km/s)}$	density$_{(kg/m^3)}$	Temp(K)	$X_{c.g.(cm)}$
Case 1	5.0	0.0103	298	1.813
Case 2	5.0	0.1126	298	1.813
Case 3	6.0	0.0103	298	1.813

Table 3. Experimental Aerodynamic Coefficients

	$V_{(km/s)}$	M_∞	Re_l	C_{D_0}	C_{D_2}	C_{L_1}	C_{L_3}	C_{M_1}	C_{M_3}	C_{M_5}	C_{M_d}*
Case 1	5	14.4	10^5	0.1700 ±0.0065	3.532 ±0.184			−0.204 ±0.028	−30.7 ±1.7	309. ±20.	−2.24 ±0.36
Case 2	5	14.5	10^6	0.1124 ±0.0011	3.537 ±0.140	0.715 ±0.054	38.0 ±4.6	−0.243 ±0.017	−30.0 ±1.6		−0.30 ±0.04
Case 3	6	17.6	10^5	0.1627 ±0.0104	3.269 ±0.152			0.043 ±0.051	−46.5 ±5.6	410. ±54.	−11.45 ±2.90

* $C_{M_d} = C_{M_c} + C_{M_b}$

Table 4. Computed Aerodynamic Coefficients

	$V_{(km/s)}$	Re_l	$\sigma_{(deg)}$	gas model	C_D	C_L	C_M
Case 1	5	10^5	0	non-eq. air	0.1617		
			5	non-eq. air	0.1880	0.0908	-0.0430
Case 2	5	10^6	0	non-eq. air	0.1241		
			5	non-eq. air	0.1425	0.0927	-0.0404
			0	ideal gas	0.1272		
			5	ideal gas	0.1413	0.0778	-0.0275
			0	eq. air	0.1263		
Case 3	6	10^5	0	non-eq. air	0.1592		

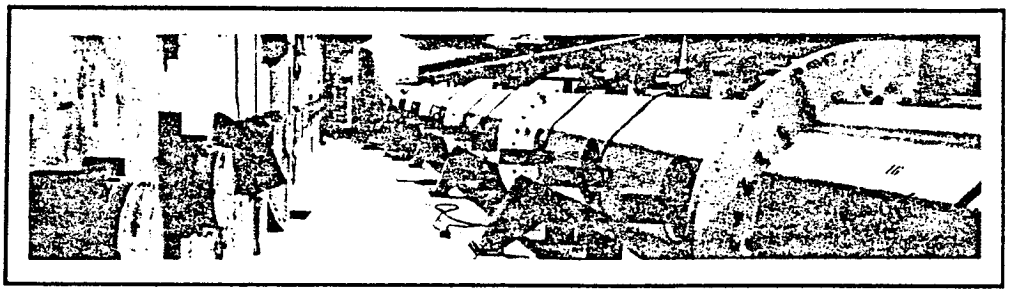

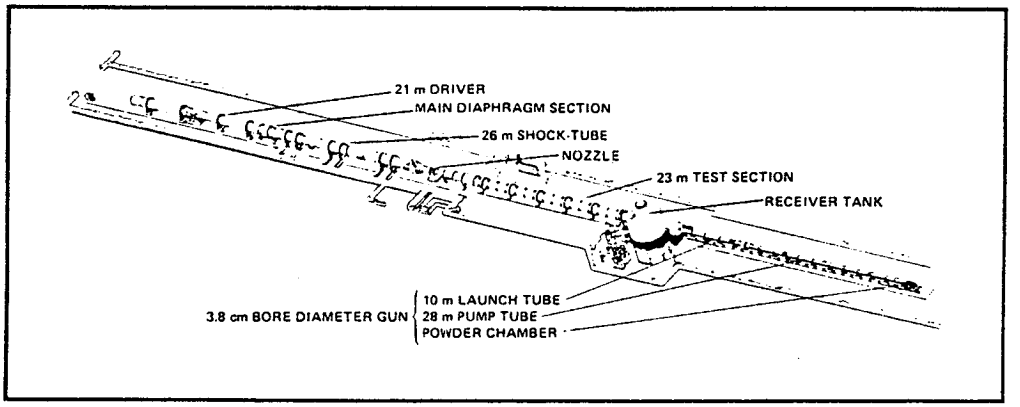

1. Photograph and schematic of Ames' Hypervelocity Free-Flight Aerodynamic Facility.

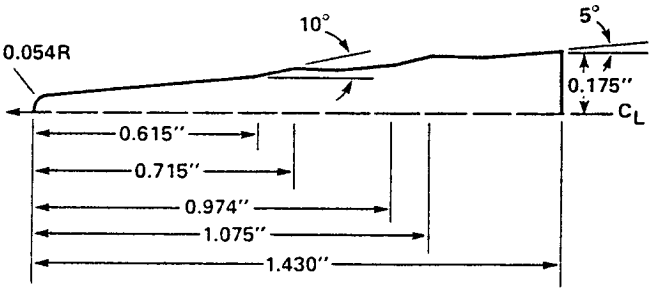

2. Drawing of 5° half-angle cone model with shock generators.

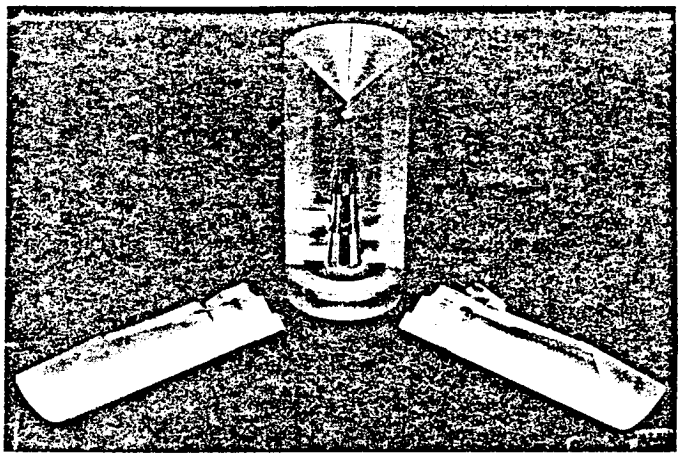

3. Photograph of model with sabot pieces.

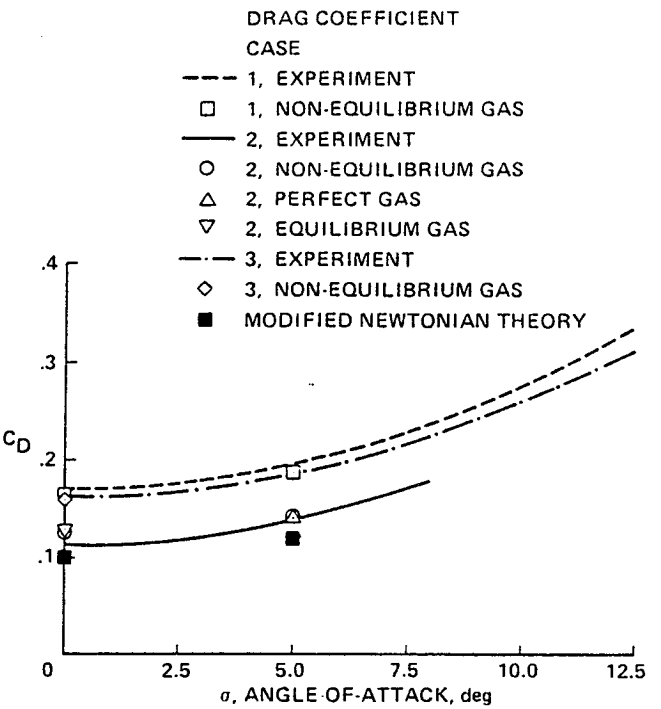

5. Experimental and computed C_D vs angle-of-attack.

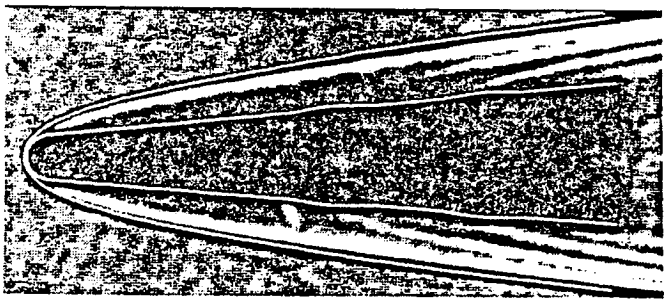

4. Shadowgraph of 5° model in free-flight at $V = 5\,km/s$ and $Re = 10^6$ (case 2). The white lines superimposed on the photograph are the computed shock shape and body outline.

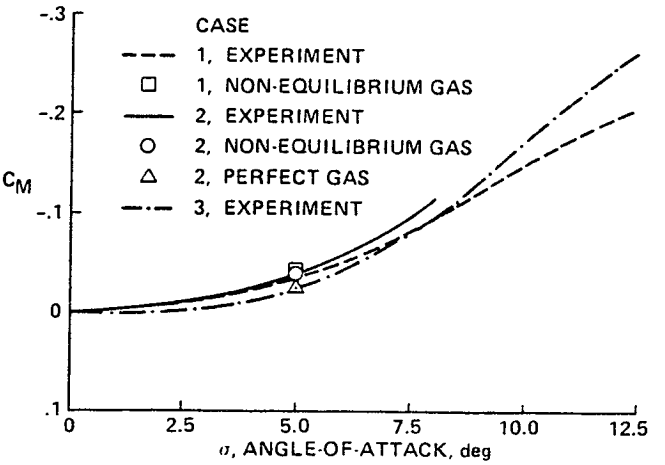

6. Experimental and computed C_M vs angle-of-attack.

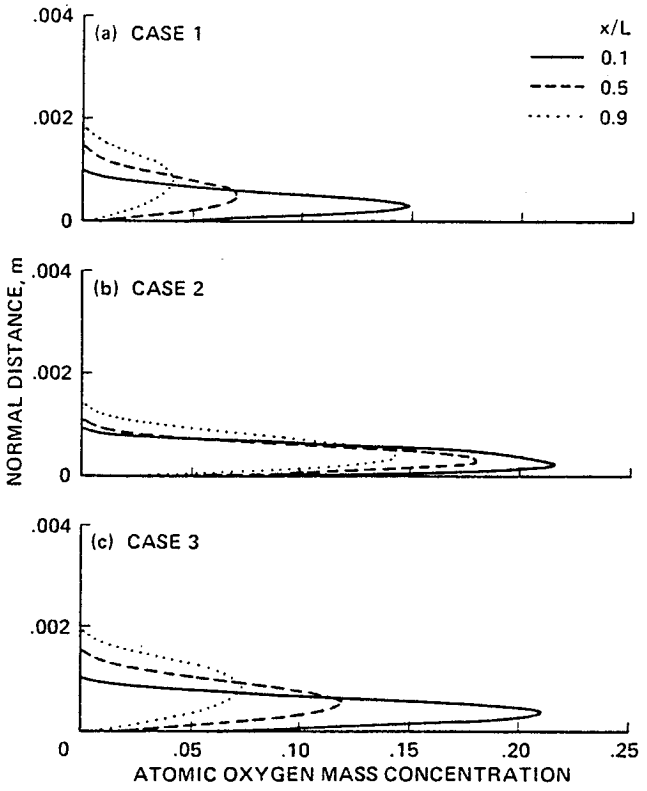

7. Mass concentration of atomic oxygen for
   a) case 1 ($V = 5\,km/s$; $Re = 10^5$),
   b) case 2 ($V = 5\,km/s$; $Re = 10^6$),
   c) case 3 ($V = 6\,km/s$; $Re = 10^5$).

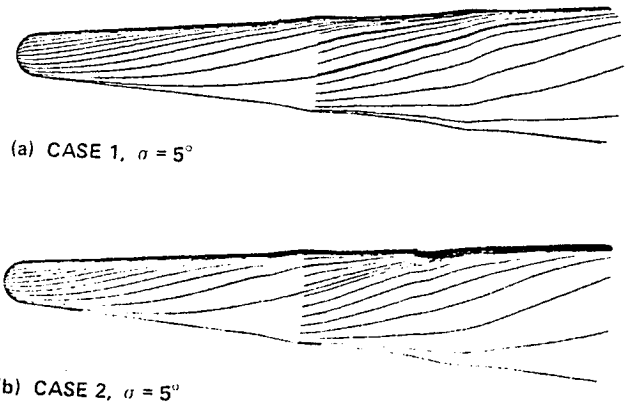

8. Computed oilflow lines
   a) for case 1 ($V = 5\,km/s$; $Re = 10^5$)
   b) for case 2 ($V = 5\,km/s$; $Re = 10^6$).

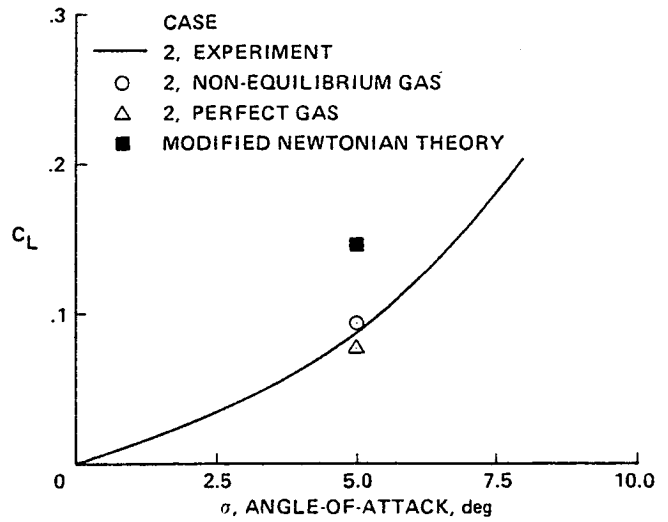

9. Experimental and computed C_L vs angle-of-attack for case 2 ($V = 5\,km/s$; $Re = 10^6$).

Preprint of AIAA Paper 91-1601, AIAA 10th Computational Fluid Dynamics Conf., 24-27 June 1991, Honolulu, Hawaii.

Conservative Multizonal Interface Algorithm for the 3-D Navier-Stokes Equations

G. H. Klopfer* and G. A. Molvik*
NASA Ames Research Center
Moffett Field, CA 94035

Abstract

One method of solving the Navier-Stokes equations about complex and realistic aerodynamic configurations is to use a zonal method. In this method the overall flow field domain is subdivided into smaller blocks or zones. In each of these zones, the flow field is solved separately of the other zones. The boundary data for each zone is provided by the neighboring zones. The major difficulty of the zonal methods has been how to maintain overall conservation for arbitrarily shaped zones. A new method of conservative patched zones has been developed. It uses structured meshes in the individual zones. The interface between the zonal block faces is defined by the union of the face points of adjoining blocks. An unstructured grid is generated upon which the interface fluxes can be determined. Flux balancing of the interface fluxes is then easily achieved to obtain global conservation. The method has been implemented into two Navier-Stokes codes. The use of the procedure is easily implemented into other finite volume codes. There are no topological restrictions on the zonal boundaries; e.g. the zonal interfaces can be curved surfaces for ease in constructing structured meshes in each of the zones. Several examples are presented to demonstrate the viability of the interfacing procedure.

Introduction

There are two basic approaches of numerically simulating the Navier-Stokes equations about complex and realistic aerodynamic configurations. One is based on structured meshes in which the neighbors of a mesh point are known implicitly. The other approach is based on an unstructured mesh in which the neighbors of a mesh point are not known implicitly and this information must be stored for each point. Numerical methods based on structured meshes are well developed, but suffer limitations when dealing with complex configurations in that it is difficult, if not impossible, to generate a single mesh about such a configuration and still have the required mesh qualities for stable and accurate numerical solutions. The generation of unstructured grids about complex configurations is, in principle, much easier; however, the numerical methods for such grids are not yet mature enough to compete against structured grid numerical methods.

The structured grid generation problem for complex configurations can be alleviated by zonal methods. In this method the overall domain is subdivided into smaller blocks or zones. In each of these zones, a grid is generated and the flow field is solved independently of the other zones. The boundary data for each zone is provided by the neighboring zones. The major difficulty of the zonal methods has been how to maintain overall conservation for arbitrarily shaped zones. The resolution of this difficulty is the purpose of this paper.

There are two types of zonal methods in common usage today. One is the overlaid zones in which both zones share a common interface region, as used in the Chimera [1] approach. The other is the patched zonal technique where the two zones share only a common boundary. Examples of this approach are the zonal method of Rai [2] and Thomas [3]. Both methods have advantages and disadvantages depending on the application. With patched grids it is much easier to maintain conservation since there is only one boundary across which the two zones communicate. On the other hand for moving multiple bodies the overlaid grid approach has certain advantages if conservation is not important, i.e., the flow field is continuous with no shock waves or shear surfaces. If conservation is important, as it is in this investigation, then we are restricted to patched zones.

Most methods using conservative patching methods are restricted to interface surfaces which are planar surfaces due to the minor gaps and overlaps that occur at a curved interface if the two zones are not mesh continuous. Furukawa et al [4] attempted to resolve this problem by using only one of the zones to determine the zonal boundary for both zones. The open question that remains is which zone determines the interface boundary. Furukawa et al chose to use the zone which has the better resolution. This can result in loss of accuracy if the mesh ratio changes in the interface, for example at a viscous boundary layer.

In this paper the zonal interface boundary is determined by the union of all the face mesh points of both adjoining zones. The interface surface is now unique and determined much more accurately than either one of the individual face surfaces. The collection of interface points is in general no longer structured and readily available unstructured grid generation techniques can be used to construct (triangulate) an interface grid. With the triangulated interface grid, the metrics (i.e., surface area normals) and cell volumes can be determined for each of the interface cells.

The development of the interface algorithm is discussed in the following sections. The procedure has been implemented into two finite volume three-dimensional Navier-Stokes codes, namely TUFF [5] and a finite volume version of CNS [6] henceforth called CNSFV. We will limit the exposition to the diagonal version of the Beam and Warming scheme [7] as used in the CNSFV code, but results from the TUFF code will also be presented.

---

* Research Scientist, MCAT Institute, San Jose, CA 95127

Numerical Scheme

Navier-Stokes Equations

The three-dimensional thin-layer Navier-Stokes equations in strong conservation law form in curvilinear coordinates are

$$\partial_\tau \hat{V} Q + \partial_\xi F + \partial_\eta G + \partial_\zeta H = Re^{-1} \partial_\zeta S \qquad (1)$$

where

$$Q = \begin{pmatrix} \rho \\ \rho u \\ \rho v \\ \rho w \\ e \end{pmatrix}, F = \begin{pmatrix} \rho U \\ \rho u U + \xi_x \hat{V} p \\ \rho v U + \xi_y \hat{V} p \\ \rho w U + \xi_z \hat{V} p \\ (e+p)U - \xi_t \hat{V} p \end{pmatrix},$$

$$G = \begin{pmatrix} \rho V \\ \rho u V + \eta_x \hat{V} p \\ \rho v V + \eta_y \hat{V} p \\ \rho w V + \eta_z \hat{V} p \\ (e+p)V - \eta_t \hat{V} p \end{pmatrix}, H = \begin{pmatrix} \rho W \\ \rho u W + \zeta_x \hat{V} p \\ \rho v W + \zeta_y \hat{V} p \\ \rho w W + \zeta_z \hat{V} p \\ (e+p)W - \zeta_t \hat{V} p \end{pmatrix} \qquad (2)$$

The contravariant velocity components are defined as

$$\begin{aligned} U &= \hat{V}(\xi_t + \xi_x u + \xi_y v + \xi_z w), \\ V &= \hat{V}(\eta_t + \eta_x u + \eta_y v + \eta_z w), \\ W &= \hat{V}(\zeta_t + \zeta_x u + \zeta_y v + \zeta_z w) \end{aligned} \qquad (3)$$

and the viscous flux is given by

$$S = \mu \hat{V} \begin{pmatrix} 0 \\ m_1 u_\zeta + m_2 \zeta_x / 3 \\ m_1 v_\zeta + m_2 \zeta_y / 3 \\ m_1 w_\zeta + m_2 \zeta_z / 3 \\ m_1 m_3 + m_2 (\zeta_x u + \zeta_y v + \zeta_z w)/3 \end{pmatrix} \qquad (4)$$

with

$$\begin{aligned} m_1 &= {\xi_x}^2 + {\xi_y}^2 + {\xi_z}^2, \\ m_2 &= \zeta_x u_\zeta + \zeta_y v_\zeta + \zeta_z w_\zeta, \\ m_3 &= (u^2 + v^2 + w^2)/2 + (Pr(\gamma - 1))^{-1} (a^2)_\zeta \end{aligned} \qquad (5)$$

The pressure is given by the equation of state

$$p = (\gamma - 1)(e - \rho(u^2 + v^2 + w^2)/2) \qquad (6)$$

Metric Terms

The metrics used above have a different meaning for a finite volume formulation compared to the finite difference formulation of [6]. Referring to a typical finite volume cell as shown in figure 1, the finite volume metrics are defined (see, for example, Vinokur [8]) as

$$\mathbf{s}_{j+\frac{1}{2}} = s_{x,j+\frac{1}{2}} \mathbf{i} + s_{y,j+\frac{1}{2}} \mathbf{j} + s_{z,j+\frac{1}{2}} \mathbf{k}$$

$$= \frac{1}{2}[(\mathbf{r}_7 - \mathbf{r}_4) \times (\mathbf{r}_8 - \mathbf{r}_4) + (\mathbf{r}_3 - \mathbf{r}_4) \times (\mathbf{r}_7 - \mathbf{r}_4)]$$

$$\mathbf{s}_{k+\frac{1}{2}} = s_{x,k+\frac{1}{2}} \mathbf{i} + s_{y,k+\frac{1}{2}} \mathbf{j} + s_{z,k+\frac{1}{2}} \mathbf{k}$$

$$= \frac{1}{2}[(\mathbf{r}_7 - \mathbf{r}_2) \times (\mathbf{r}_3 - \mathbf{r}_2) + (\mathbf{r}_6 - \mathbf{r}_2) \times (\mathbf{r}_7 - \mathbf{r}_2)]$$

$$\mathbf{s}_{l+\frac{1}{2}} = s_{x,l+\frac{1}{2}} \mathbf{i} + s_{y,l+\frac{1}{2}} \mathbf{j} + s_{z,l+\frac{1}{2}} \mathbf{k} \qquad (7)$$

$$= \frac{1}{2}[(\mathbf{r}_7 - \mathbf{r}_5) \times (\mathbf{r}_6 - \mathbf{r}_5) + (\mathbf{r}_8 - \mathbf{r}_5) \times (\mathbf{r}_7 - \mathbf{r}_5)]$$

The finite volume metrics represent the cell face area normals in each of the curvilinear coordinates (ξ, η, ζ). They are related to the metrics introduced in equations (1 - 5) as follows

$$\begin{aligned} \xi_x \hat{V} &= s_{x,j+\frac{1}{2}} \\ \xi_y \hat{V} &= s_{y,j+\frac{1}{2}} \\ \xi_z \hat{V} &= s_{z,j+\frac{1}{2}} \\ \eta_x \hat{V} &= s_{x,k+\frac{1}{2}} \\ \eta_y \hat{V} &= s_{y,k+\frac{1}{2}} \\ \eta_z \hat{V} &= s_{z,k+\frac{1}{2}} \\ \zeta_x \hat{V} &= s_{x,l+\frac{1}{2}} \\ \zeta_y \hat{V} &= s_{y,l+\frac{1}{2}} \\ \zeta_z \hat{V} &= s_{z,l+\frac{1}{2}} \end{aligned} \qquad (8)$$

The volume of the computational cell is given by

$$\hat{V} = \frac{1}{6}[(\mathbf{r_4} - \mathbf{r_1}) \times (\mathbf{r_3} - \mathbf{r_1}) \cdot (\mathbf{r_7} - \mathbf{r_3})$$

$$+(\mathbf{r_8} - \mathbf{r_1}) \times (\mathbf{r_4} - \mathbf{r_1}) \cdot (\mathbf{r_7} - \mathbf{r_8})$$

$$+(\mathbf{r_3} - \mathbf{r_1}) \times (\mathbf{r_2} - \mathbf{r_1}) \cdot (\mathbf{r_7} - \mathbf{r_3})$$

$$+(\mathbf{r_2} - \mathbf{r_1}) \times (\mathbf{r_6} - \mathbf{r_1}) \cdot (\mathbf{r_7} - \mathbf{r_6})$$

$$+(\mathbf{r_6} - \mathbf{r_1}) \times (\mathbf{r_5} - \mathbf{r_1}) \cdot (\mathbf{r_7} - \mathbf{r_6})$$

$$+(\mathbf{r_5} - \mathbf{r_1}) \times (\mathbf{r_8} - \mathbf{r_1}) \cdot (\mathbf{r_7} - \mathbf{r_8})] \quad (9)$$

and is the finite volume equivalent of the inverse Jacobian of the coordinate transformation in the finite difference formulation of [6].

Diagonal Beam-Warming Algorithm

The implicit Beam-Warming scheme for the finite volume formulation is given by

$$[I - \hat{V}^{-1}\hat{h}(\delta_\xi A^n + \delta_\eta B^n + \delta_\zeta C^n - Re^{-1}\delta_\zeta M^n)]\delta Q^{-1} = R^n \quad (10)$$

where

$$R^n = -\hat{V}^{-1}\hat{h}[\delta_\xi F^n + \delta_\eta G^n + \delta_\zeta H^n - Re^{-1}\delta_\zeta S^n] \quad (11)$$

The convective three-dimensional flux Jacobians A, B, C and the viscous flux Jacobian are defined in the appendix of [5]. With the use of approximate factorization and diagonalization of the flux Jacobian matrices, a scalar pentadiagonal algorithm [7] can be derived as

$$T_\xi[I + \hat{V}^{-1}\hat{h}\delta_\xi\Lambda_\xi]N[I + \hat{V}^{-1}\hat{h}\delta_\eta\Lambda_\eta]P\cdot$$

$$[I + \hat{V}^{-1}\hat{h}\delta_\zeta\Lambda_\zeta]T_\zeta{}^{-1}\Delta Q^n = R^n \quad (12)$$

where δ_ξ is a central difference operator and $\Delta Q^n = Q^{n+1} - Q^n$ with $Q^{n+1} = Q(t^n + \hat{h})$. The viscous terms are not included in the left-hand (implicit) side. The artificial dissipation is included in both sides and is derived below.

The inviscid flux Jacobians are diagonalized as follows:

$$\partial_Q F = A = T_\xi \Lambda_\xi T_\xi{}^{-1}$$

$$\partial_Q G = B = T_\eta \Lambda_\eta T_\eta{}^{-1}$$

$$\partial_Q H = C = T_\zeta \Lambda_\zeta T_\zeta{}^{-1}$$

The T_ξ, T_η, T_ζ are the eigenvector matrices of A, B, C, respectively with $\Lambda_\xi, \Lambda_\eta, \Lambda_\zeta$ as the respective eigenvalues.

We also have

$$N = T_\xi{}^{-1}T_\eta$$

$$P = T_\eta{}^{-1}T_\zeta$$

Each of the factors of the implicit operator of equation (12) has an artificial term added to stabilize the central difference operator. The dissipation is based on Jameson's nonlinear second and fourth order dissipation and for the $\xi-$ operator takes the form

$$\hat{h}\hat{V}^{-1} \nabla_\xi [\bar{\sigma}_{j+\frac{1}{2}}(\epsilon^{(2)} \Delta_\xi \cdot - \epsilon^{(4)} \Delta_\xi \nabla_\xi \Delta_\xi \cdot)]\Delta Q^n \quad (13)$$

with

$$\epsilon^{(2)} = \kappa_2 max(\gamma_{j+1}, \gamma_j, \gamma_{j-1}) \quad (14)$$

$$\gamma_j = \frac{|p_{j+1} - 2p_j + p_{j-1}|}{|p_{j+1} + 2p_j + p_{j-1}|} \quad (15)$$

$$\epsilon^{(4)} = max(0, \kappa_4 - \epsilon^{(2)}) \quad (16)$$

where κ_2, κ_4 are constants of o(1), and Δ_ξ, ∇_ξ are the forward and backward difference operators. $\bar{\sigma}_{j+\frac{1}{2}}$ is a modified spectral radius defined as

$$\bar{\sigma}_{j+\frac{1}{2}} = \bar{\sigma}_j + \bar{\sigma}_{j+1}$$

$$\bar{\sigma}_j = \sigma_j\left(1 + \sqrt{max(\sigma_k/\sigma_j, \sigma_l/\sigma_j)}\right), \quad (17)$$

$$\sigma_j = \left[|U| + a\sqrt{s_x{}^2 + s_y{}^2 + s_z{}^2}\right]_j \quad (18)$$

and where cell centered surface areas are used, e.g.

$$s_{x,j} = \frac{1}{2}(s_{x,j+\frac{1}{2}} + s_{x,j-\frac{1}{2}})$$

The modified form of the spectral radius, equation (17), is suggested by Turkel [9] to account for large aspect

ratio computational cells as for example in a viscous layer. Similar dissipation terms are obtained for the $\eta-$ and $\zeta-$ operators. The dissipation terms added to the right hand side of equation (10) are identical to those given above except that ΔQ^n is replaced by Q^n.

To show that the above scheme is conservative and has the telescoping property, the right hand side of (12) can be written as

$$R^n = -\hat{h}\hat{V}^{-1}[\hat{F}^n_{j+\frac{1}{2}} - \hat{F}^n_{j-\frac{1}{2}} + \hat{G}^n_{k+\frac{1}{2}} - \hat{G}^n_{k-\frac{1}{2}}$$

$$+\hat{H}^n_{l+\frac{1}{2}} - \hat{H}^n_{l-\frac{1}{2}} - Re^{-1}\hat{S}^n_{l+\frac{1}{2}} + Re^{-1}\hat{S}^n_{l-\frac{1}{2}}] \qquad (19)$$

where $\hat{F}, \hat{G}, \hat{H}, \hat{S}$ are the numerical fluxes and are defined, for example for $\hat{F}$, as

$$\hat{F}^n_{j+\frac{1}{2}} = \bar{F}^n_{j+\frac{1}{2}} + \bar{\sigma}_{j+\frac{1}{2}}(\epsilon^{(2)}\,\Delta_\xi\, Q^n - \epsilon^{(4)}\,\Delta_\xi\,\nabla_\xi\,\Delta_\xi\, Q^n)_{j+\frac{1}{2}} \qquad (20)$$

with

$$\bar{F}^n_{j+\frac{1}{2}} = \frac{1}{2}[s_{x,j+\frac{1}{2}}(f_{j+1} + f_j)^n + s_{y,j+\frac{1}{2}}(g_{j+1} + g_j)^n$$

$$+s_{z,j+\frac{1}{2}}(h_{j+1} + h_j)^n] \qquad (21)$$

Similar terms are obtained for the numerical fluxes in the other two coordinate directions.

Boundary Conditions

To complete the equation set, boundary conditions must be specified. With the use of curvilinear coordinates, the physical boundaries have been mapped into computational boundaries, which simplifies the application of boundary conditions. The boundary conditions to be implemented for external viscous or inviscid flows include (1) inflow or far field, (2) outflow, (3) inviscid and (4) viscous impermeable wall, and (5) symmetry conditions. For external three-dimensional flow fields about closed bodies, the topology of the grid usually introduces (6) grid singularities which require special boundary conditions. The use of zonal methods can avoid the generation of grid singularities, but requires (7) special zonal interface boundary conditions. For compressible flows these zonal boundary conditions should be conservative to maintain global conservation.

In the finite volume approach, the specification of boundary conditions reduces to specifying the appropriate numerical fluxes at the boundaries. The details of implementing boundary conditions (1) through (5) are well known and are given in [5] and [10]. The grid singularity boundary condition is described below and the interface boundary conditions are given in the next section.

The grid singularity boundary condition is similar to the symmetry boundary condition for the inviscid and viscous fluxes in that there is no flux through that boundary. If, however, that is all that is done the results shown in figure 2a are obtained. These results are the density contours of a Mach 8 viscous blunt body flow. As shown in the figure, a nonphysical behavior appears at the singular line. The nonphysical results are due to a local violation of the entropy condition [11]. For central difference schemes, the artificial dissipation is the only stabilizing (entropy producing) mechanism available. At the grid singularity, the spectral radius, and hence the artificial dissipation, vanishes due to the vanishing of the metrics. The introduction of Harten's entropy correction [12] resolves the difficulty and the results are shown in figure 2b.

Interface Method

Most methods using conservative patching methods are restricted to interface surfaces which are planar due to the minor gaps and overlaps that occur at a curved interface if the two zones are not mesh continuous. This is demonstrated in figure 3a. Furukawa et al [4] attempted to resolve this problem by using only one of the zones to determine the zonal boundary for both zones. This is shown for the two-dimensional example in figure 3b. The open question that remains is which zone determines the interface boundary. Furukawa et al chose to use the zone with the better resolution. This, however, can result in loss of accuracy if the mesh ratio changes in the interface as for example at a viscous boundary layer.

In this paper the zonal interface boundary is determined by the union of all the face mesh points of both adjoining zones as shown in figure 3c for the two-dimensional case. The interface surface is now unique and determined much more accurately than by either one of the individual face surfaces. This presumes that the individual points from both zones lie in the interface surface and that the interface surface is itself smooth and continuous. The collection of interface points is, in general, no longer structured, and readily available unstructured grid generation techniques can be used to construct (triangulate) an interface grid. With the triangulated interface grid, the metrics (i.e., surface area normals) and cell volumes can be determined for each of the interface cells, i.e., the computational cells that touch the interface surface.

The redefinition of the interface surface has modified all the interface cells and they are no longer hexahedral, but rather multifacetted. Determining the surface area normals and cell volumes now becomes more complicated. There are three types of interface cells, namely, face cells, edge cells, and corner cells. The face cells have only one face bordering other zones, whereas the edge and corner cells have two or three faces in contact with other zones, respectively. A typical cell at the interface is shown in figure 4.

The modification introduced by the interface surface requires that the metrics and cell volumes of the interface cells be corrected to account for the changed shape of the interface cells. Corrections are required for the area normals of the cell face touching the interface surface, the four sidewalls, which may no longer be quadrilaterals, and the cell volume. For inviscid steady flows, the cell volume corrections are not needed since the volume has no effect on the steady solution as shown by equation (11). However,

for all viscous flows and inviscid unsteady flows the volume corrections are necessary.

There are two ways that the interface grids can be triangulated. The first involves eliminating all the grid lines from the structured grid cell faces and constructing the triangulated mesh. Since in general the new grid lines will not be aligned with the original grid lines, a clipping algorithm is used to clip those triangles which lie outside a particular individual face cell of either zone. An example of this triangulation procedure is shown in figure 5. Here two zones have square faces each consisting of a Cartesian grid of 15×15 uniformly spaced points. The two faces are oriented at an angle of 45° to each other (see figure 5a). The union of both sets of face points results in an unstructured collection of points which are then triangulated with an advancing front unstructured mesh generation procedure [13]. The resulting mesh is shown in figure 5b.

The second procedure retains the original grid lines and triangulates any set of points which form a polygon of more than three sides. This approach avoids the use of a clipping algorithm since each face cell contains an integral number of interface triangular cells. An example of this procedure is shown in figure 10b for two zones with polar grids.

The unstructured interface grid requires that a set of pointers be defined. These pointers indicate which two interface cells share a common interface area or section. These sections need not be triangular even though the surface has been triangulated. A common section (or polygon) may be composed of several triangles if the surface is triangulated by the second procedure described above or it may be composed of several clipped triangles if the first procedure is used. For a more efficient interface flux computation it is convenient to define another set of cross-reference pointers. These cross-reference pointers identify which interface polygons are in contact with each of the interface cells.

Numerical Interface Flux

The final step required for the conservative interface algorithm is to determine the numerical fluxes at the interface. Originally it was anticipated that the interface flux could be determined by any stable numerical scheme, not necessarily the one used in the interior of the zone. However, it was found that if the numerical schemes differ, then "glitches" always appear at the zonal interface. It was also necessary to maintain the same order of accuracy for the interface scheme as for the interior scheme. An example of this case is shown in figure 6. Here the interface flux is determined by a first order upwind scheme and the interior by a second order upwind scheme. The unfortunate results are the discrepancies at the interface boundary as shown by the pressure contours. The use of the same second order upwind scheme for the interface flux eliminates these discrepancies.

The above example shows that it is not possible to completely generalize a conservative interface algorithm. The numerical flux must be determined by the same numerical scheme as used in the interior of the zone. The geometric aspects of the interface algorithm can be generalized, which is essentially the most difficult part of the interface procedure. The numerical fluxes at the interface must (and should) be computed by the particular flow solver involved.

The computation of the interface numerical flux is relatively straightforward. Since it is scheme dependent it is given is general form first, valid for many schemes up to second-order accuracy. A specific form will be given for the CNSFV code. Figure 7 shows two zones, j1 and j2, and the interface with the individual surface polygons labelled by "i". The flux at the interface section "i" is given by

$$\vec{F}_{j1,j2=\frac{1}{2}} = \Phi[\vec{s}^i, \vec{q}_{j1=1}, \vec{q}_{j1=2}, \vec{q}_{j2=1}, \vec{q}_{j2=2}]$$

where Φ is the function defining the particular scheme under consideration, $\vec{s}^i$ is the area normal of the interface section "i", and the $\vec{q}_{j1}$ and $\vec{q}_{j2}$ are the cell-centered values in zones 1 and 2, respectively.

The numerical flux at the opposite face of the interface cell is slightly more complicated. It is

$$\vec{F}_{j2=\frac{3}{2}} = \Phi[\vec{s}_{j2=\frac{3}{2}}, \vec{q}_{j2=1}, \vec{q}_{j2=2}, \vec{q}_{j2=3}, \vec{q}_{j1=1}]$$

where $\vec{q}_{j1=1}$ is the area (i.e., $|\vec{s}^i|$) weighted average of all the interface cells of the zone "1" sections that comprise the face cell of zone "2" touching the interface surface. If higher order schemes are considered, then special care must also be taken for the fluxes at the next level of cell faces, ie. $\vec{F}_{j2=\frac{5}{2}}$. The above formulation is valid for all cell-centered finite volume schemes.

For the particular case of the CNSFV code, the interface numerical fluxes are

$$\hat{F}^n_{\frac{1}{2}} = \bar{F}^n_{\frac{1}{2}} + \bar{\sigma}_{\frac{1}{2}}(\epsilon^{(2)} \triangle_\xi Q^n - \epsilon^{(4)} \triangle_\xi \nabla_\xi \triangle_\xi Q^n)_{\frac{1}{2}}$$

where

$$\bar{F}^n_{\frac{1}{2}} = \frac{1}{2}\left[s^i{}_x(f_{j2=1} + f_{j1=1})^n + s^i{}_y(g_{j2=1} + g_{j1=1})^n \right.$$

$$\left. + s^i{}_z(h_{j2=1} + h_{j1=1})^n\right]$$

and

$$\bar{\sigma}_{\frac{1}{2}} = \bar{\sigma}_{j1=1} + \bar{\sigma}_{j2=1}$$

The flux at $j2 = \frac{3}{2}$ is similarily determined, taking care to use the appropriate area averaged values of all cell-centered values.

Results

To validate the interface algorithm, several tests were conducted. The first test is the freestream preserving test.

In this test, the inflow and and permeable wall boundary conditions (ie. conditions (1),(3) or (4) from the boundary conditions section) are set to the freestream conditions and the solution is converged. If the initial conditions were also set to the freestream condition, then the residual should be at machine zero (R= $O(10^{-14})$) and remain there for all subsequent iterations provided that the flow field is discretized properly with no gaps or overlaps in any of the computational cells and interface boundaries. Indeed, for the CNSFV code, this was the case.

However, the freestream test is not a good indication of the accuracy of the scheme. Because of the telescoping property of the scheme, the surface area normals can be computed inaccurately (even erroneously) and the scheme will still pass the freestream test. To test for accuracy, a single cell residual, equation (19), is computed with the same freestream conditions imposed as above. In this case, the maximum residual was of the $O(10^{-8})$ on a 64 bit machine (Cray YMP). If the grid and the metric terms are computed in double precision (ie. 128 bits), then the maximum residual reduces to $O(10^{-12})$. This indicates that machine roundoff errors are not yet a problem, but can be if the meshes are refined much further.

Three different flow cases covering the entire Mach regime from incompressible, to supersonic, and to hypersonic flows with finite rate chemistry were computed with the TUFF code. The same basic conservative interface algorithm described above was used in all three cases, however the conservation law equations differed for each of the three cases.

The first case involved an incompressible inviscid flow about a cylinder. The two zone mesh is shown in figure 8a. The pressure contours are given in figure 8b and the surface pressures in 8c. The results across the zonal boundaries are smooth and continuous.

The second set of results are for supersonic blunt body flow. This case is an inviscid Mach 2, axisymmetric blunt body flow computed on the four-zone mesh shown in figure 9a. Figure 9b shows the solution and the bow shock position. For these results, the analytic shock location at steady state [14] is shown by the solid squares. The solution is shown in terms of mach contours on a background grid which is cell centered for plotting purposes only. As can be seen the multizonal computed and analytic shock shapes compare quite well.

The final flow results obtained are for a viscous hypersonic flow about a hemisphere at $M_\infty = 15.3$ and $Re = 2.2 \times 10^5/m$. The interface triangulation for the two zones containing the grid polar singularity is depicted in figure 10b. The flow results in terms of Mach and atomic oxygen concentration contours are shown in figures 10c and d, respectively. Again, the results indicate that the solution contours are smooth and continuous across the zonal boundaries. Although not shown, the computed shock stand-off distance agreed well with the experimental data of reference 15.

Closing Remarks

A conservative zonal interface algorithm has been presented. It uses some of the best features of both the structured and unstructured mesh CFD technology. The interface surface grid is unstructured from which the metrics and interface fluxes can be readily constructed to obtain the proper conservative interface algorithm. For efficiency and rapid convergence, the flow solver within each of the zones is based on structured mesh CFD technology. The ordering between the zones can be unstructured for maximum flexibility in constructing zones and grids about complex and arbitrary configurations. The interface algorithm has been implemented into two three-dimensional Navier-Stokes finite volume codes (TUFF and CNSFV) and has shown to yield good results. Further testing is being conducted for more complex and realistic aerodynamic configurations. The procedure is general and can be easily implemented into other finite volume codes.

References

1. Benek, J.A., Buning, P.G., and Steger, J.L.; "A 3-D Chimera Grid Embedding Technique", AIAA Paper No. 85-1523CP, 1985.

2. Rai, M. M.; "A Conservative Treatment of Zonal Boundaries for Euler Equations Calculations", Journal of Computational Physics, Vol. 62, No. 2, Feb. 1986, pp. 472-503.

3. Walters, R.W., Reu,T., McGregory, W., Thomas, J. L., and Richardson, P.F.; "A Longitudinally-Patched Grid Approach with Applications to High Speed Flows", AIAA Paper No. 85-0295, 1985.

4. Furukawa, M., Yamasaki, M., and Inoue, M.; "A Zonal Approach for Solving the Navier-Stokes Equations Using a TVD Finite Volume Method", International Symposium on Computational Fluid Dynamics - Nagoya, Nagoya Trade & Industry Center, Nagoya, Japan, August 28-31, 1989.

5. Molvik, G. and Merkle, C. L.; "A Set of Strongly Coupled Algorithms for Computing Flows in Chemical Nonequilibrium", AIAA Paper 89-0199, Jan. 1989.

6. Ryan, J.S., Flores, J., and Chow, C.-Y.; "Development and Validation of a Navier-Stokes Code for Hypersonic External Flow", Journal of Spacecraft and Rockets, Vol. 27, No. 2, March-April 1990, pp. 160-166.

7. Pulliam, T.H. and Chaussee, D.S.; "A Diagonal Form of an Implicit Approximate Factorization Algorithm", Journal of Computational Physics, Vol. 39, 1981, p. 347.

8. Vinokur, M.; "An Analysis of Finite-Difference and Finite-Volume Formulations of Conservation Laws", NASA CR-177416, June 1986.

9. Turkel, E. and Vatsa, V.N.; "Effect of Artificial Viscosity on Three Dimensional Flow Solutions", AIAA Paper 90-1444, AIAA 21st Fluid Dynamics, Plasma Dynamics and Lasers Conference, Seattle, WA, June 1990.

10. Atwood, C. A.; "An Upwind Approach to Unsteady Flowfield Simulation", AIAA Paper 90-3100, AIAA 8th Applied Aerodynamics Conference, August 1990.

11. Merriam, M.L.; "An Entropy-Based Approach to Nonlinear Stability", NASA TM-101086, March 1989.

12. Harten, A.; "On a Class of High Resolution Total-Variation-Stable Finite-Difference Schemes", SIAM

J. Num. Anal., Vol. 21, pp. 1-23, 1984.

13. Merriam, M.L.; "A Fast Robust Algorithm For Delaunay Triangulation", Unpublished Paper, NASA Ames Research Center, Moffett Field, CA, October 1989.

14. Lyubimov, A.N. and Rusanov, V.V.; "Gas Flows Past Blunt Bodies", NASA TT-F 715, 1973.

15. Lobb, R. K.;"Experimental Measurements of Shock Distance on Spheres Fired in Air at Hypervelocities", The High Temperature Aspects of Hypersonic Flow, ed. W. C. Nelson, Pergammon Press, McMillan Co., New York, 1964.

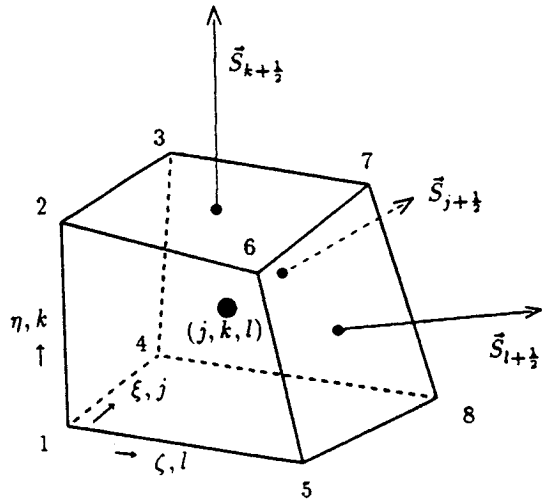

Figure 1. Finite volume cell nomenclature.

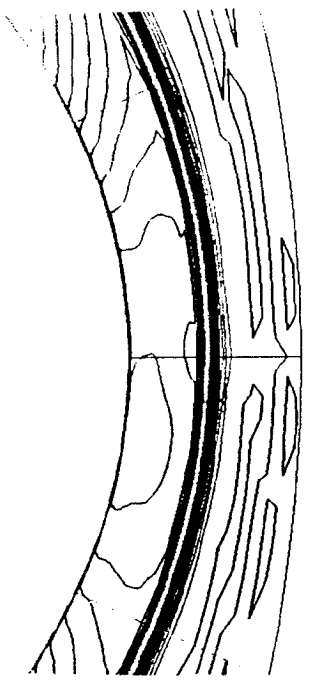

a) grid singularity problem.

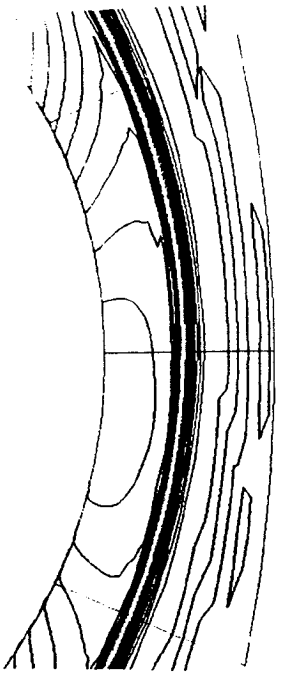

b) grid singularity problem resolved by Harten's entropy correction [12].

Figure 2. Density contours for a viscous blunt body flow
$M_\infty = 8.0, Re_D = 2.19 \times 10^5, \alpha = 5.0^o$

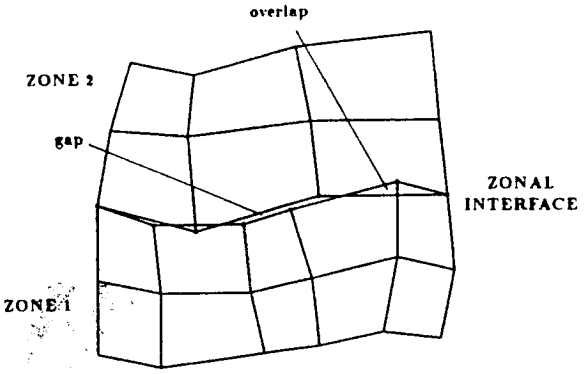

a) "classical"
works only for planar interfaces,
otherwise conservation errors occur.

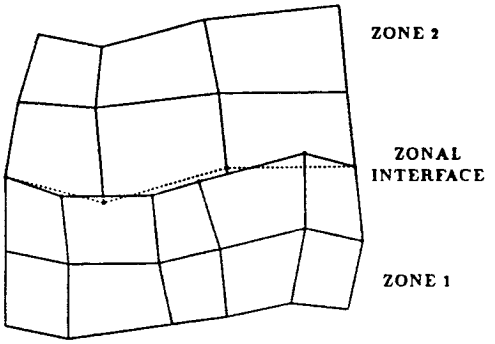

b) Furukawa et al [4] method
uses boundary of finer mesh
zone to determine the interface boundary.

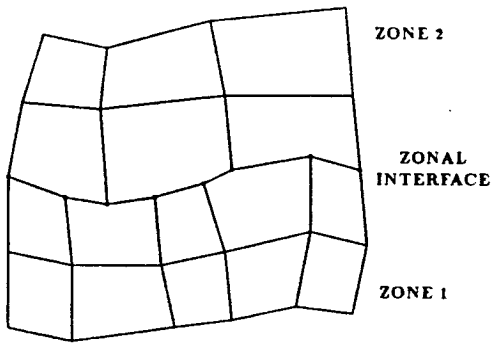

c) present procedure
uses all the interface points
to define the interface boundary.

Figure 3. Zonal Boundary on a Curved Interface

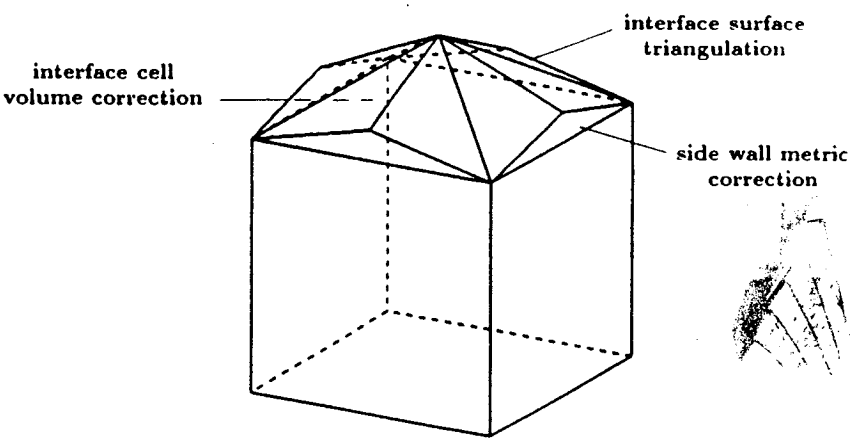

Figure 4. A typical zonal interface finite volume cell.

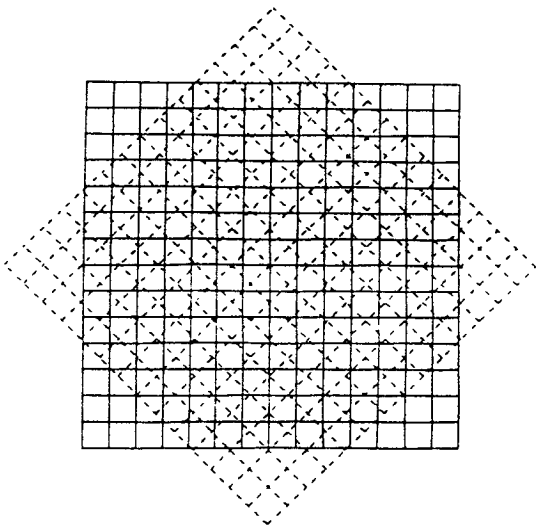

Figure 5a. The two structured face grids
of a typical interface surface.

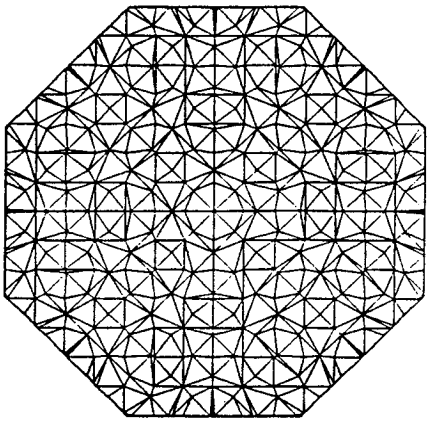

Figure 5b. The unstructured grid
of a typical interface surface.

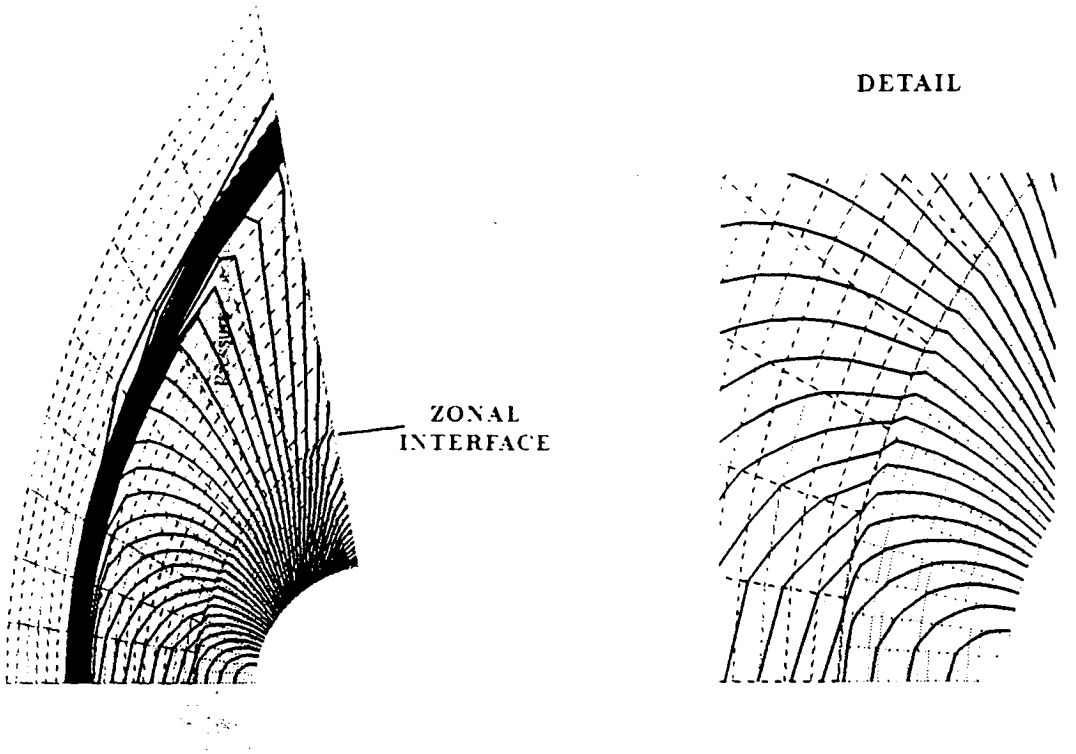

Figure 6. Pressure contours for inviscid blunt body flow at $M_\infty = 2.0$.

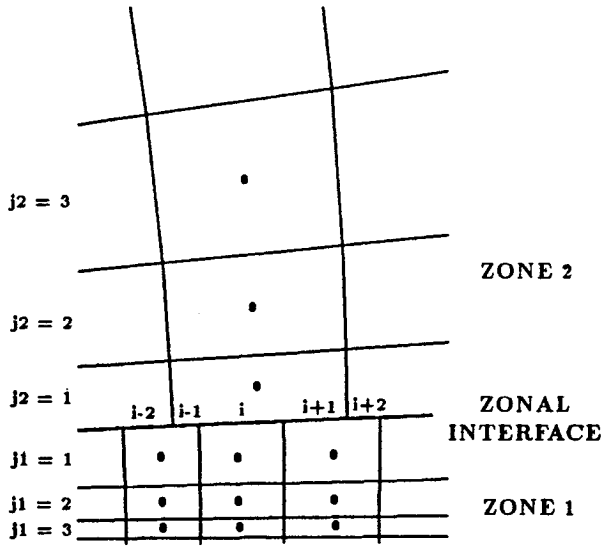

Figure 7. Mesh and nomenclature for numerical flux computation at zonal interface.

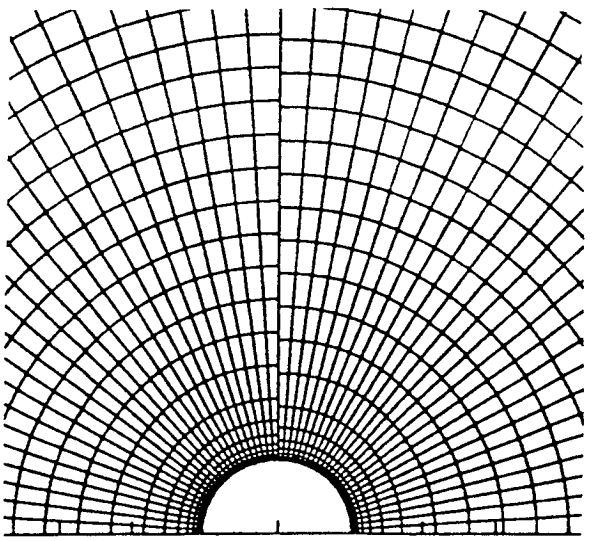

a) Two zone grid.

Figure 8. Inviscid incompressible flow about a cylinder.

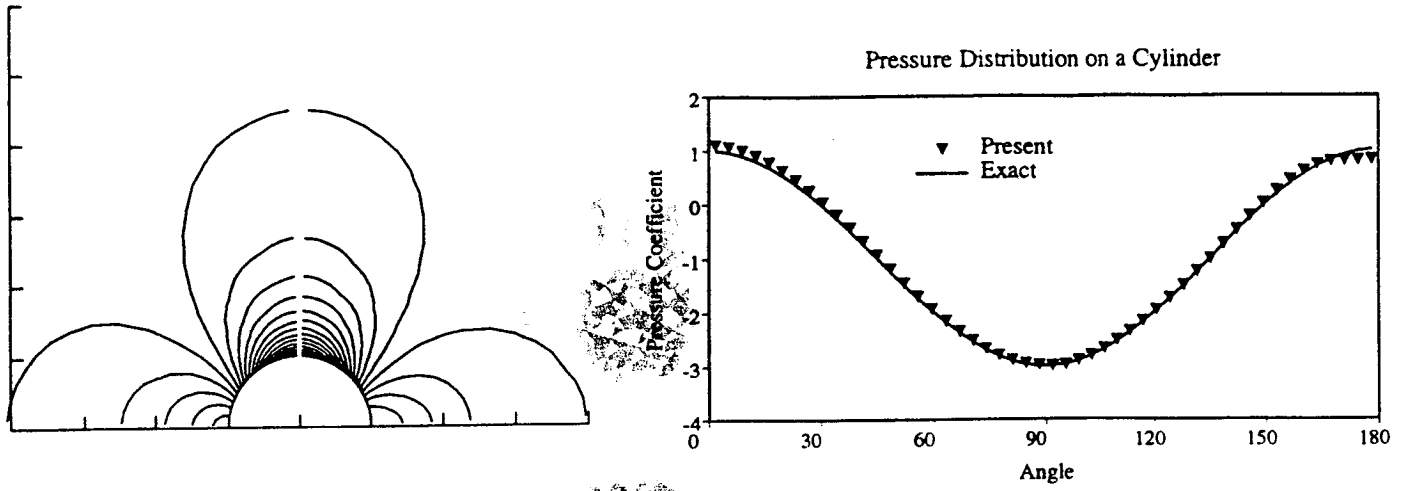

b) Pressure contours

c) Comparison with analytic data.

Figure 8. Inviscid incompressible flow about a cylinder.

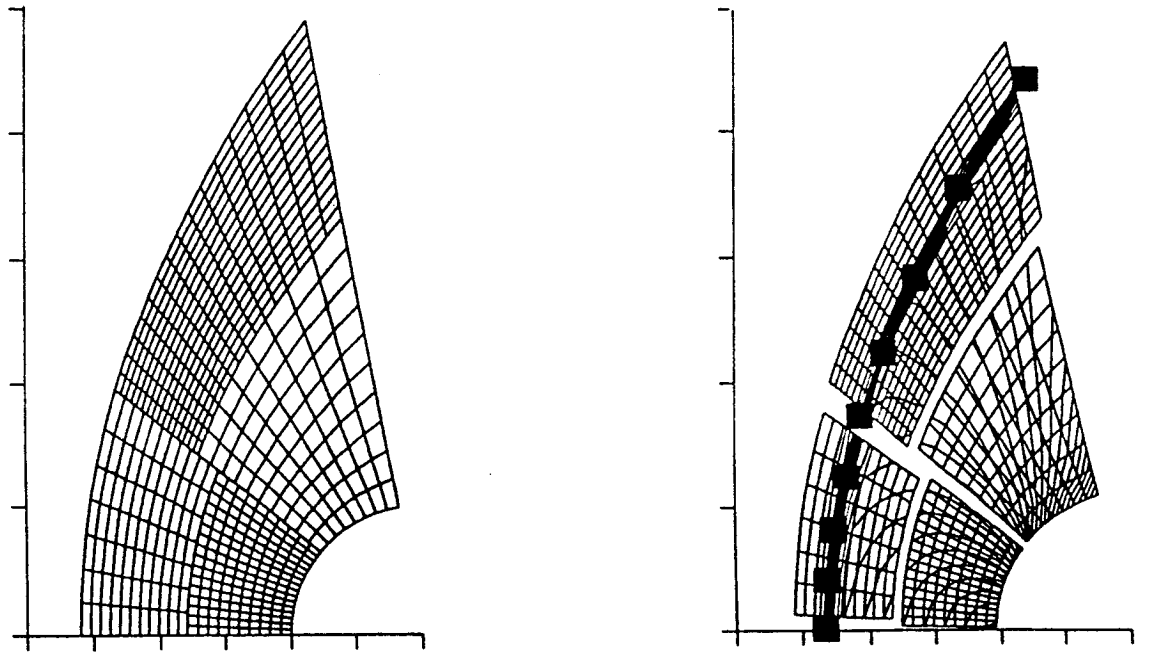

a) Four zone grid.

b) Mach contours.
■ - analytic bow shock location
(Lyubimov, NASA TT-F715, 1973).

Figure 9. Axisymmetric inviscid blunt body flow at $M_\infty = 2.0$.

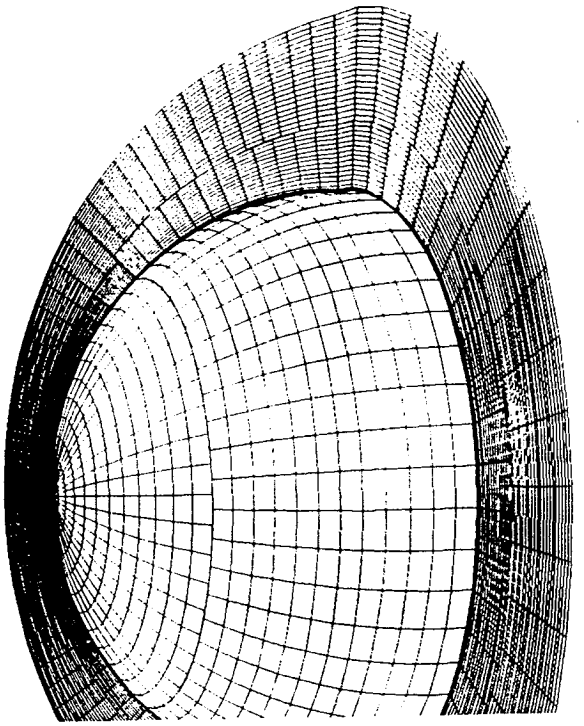

(a) Four Zone Grid

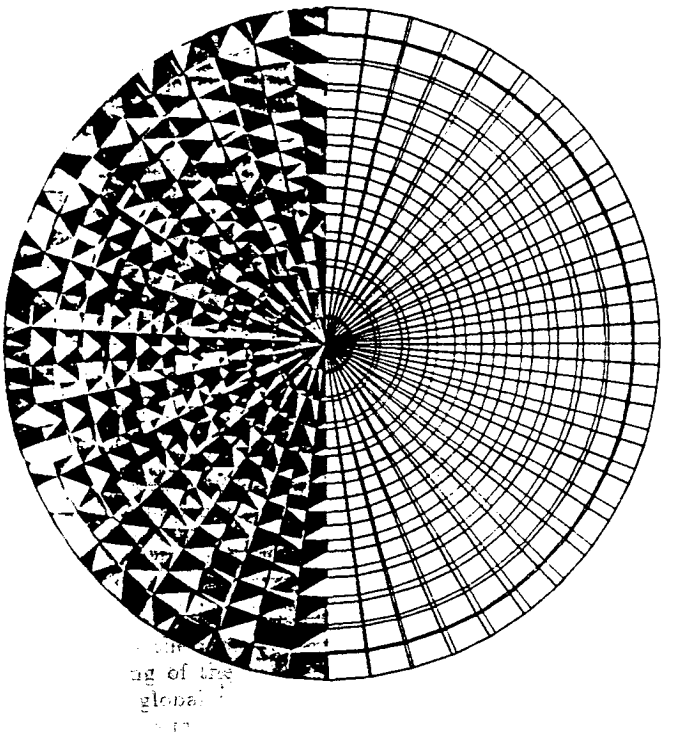

(b) The Two Face Grids and Triangulation

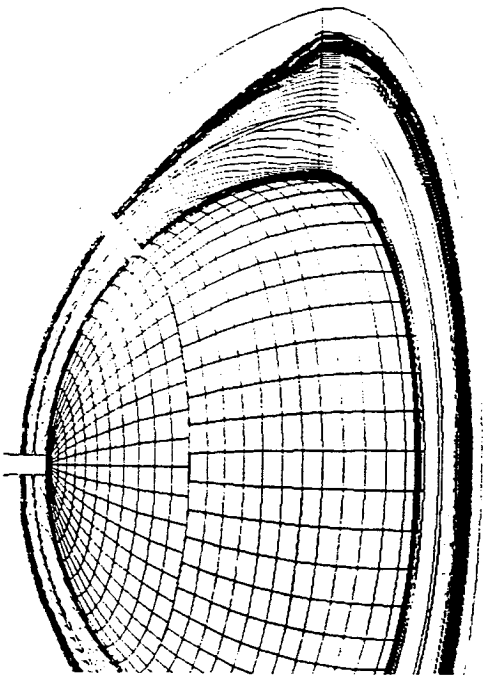

(c) Mach Contours

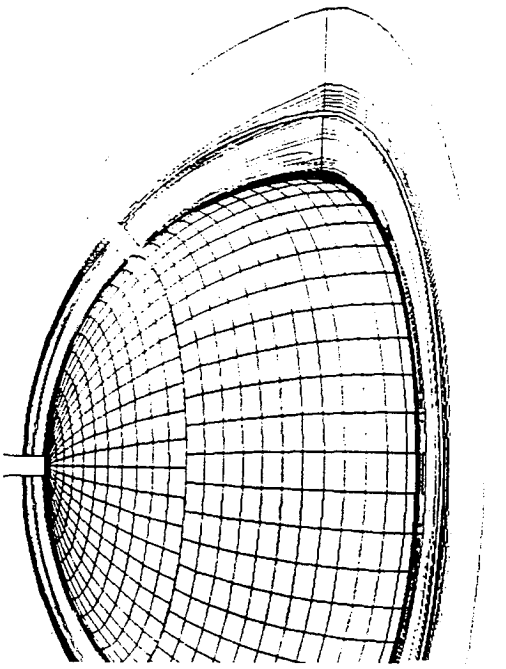

(d) Atomic Oxygen Concentration Contours

Figure 10. Viscous Hypersonic Blunt Body Flow with Finite Rate Chemistry $M_\infty = 15.3$, $Re = 2.2 \times 10^6/m$.

CALCULATION OF HIGH SPEED BASE FLOWS*

*R. H. Nichols, J. R. Maus,** and R. L. Spinetti†*
Calspan Corporation/AEDC Operations
Arnold Engineering Development Center
Arnold Air Force Base, Tennessee 37389
and
G. A. Molvik
MCAT Corporation
Moffett Field, California 94035

Abstract

A computational approach for high-speed base flows of reentry shapes is demonstrated. The approach is based on solving the thin-layer Navier-Stokes equations for perfect gas, equilibrium air, or chemical nonequilibrium air. An efficient space-marching algorithm is used whenever possible on the body and in the far wake. A blocked time-marching algorithm is used to calculate the embedded subsonic flow in the base region. A two-equation turbulence model which includes compressibility effects is used to extend the approach to Reynolds numbers above the transition to turbulent flow. Comparisons with data are made for both laminar and turbulent base flows, with good agreement in all cases.

Introduction

Base flows and their effect on the wakes of reentry vehicles have long been a subject of both experimental and theoretical research. The signature of a reentry vehicle is to a large extent determined by the character of its wake, which extends hundreds of base diameters behind the body. The properties of the far wake of a slender body at high speed are, in turn, strongly dependent on the near-wake flow field. Only limited theoretical models currently exist for the flow in the near-wake region. Computational tools are needed to aid in the analysis of these types of flows.

The flow field about a slender reentry vehicle can be divided into four regions as is illustrated schematically in Fig. 1. Because of the strong dependency of the near-wake flow field on the flow over the body, calculation of the base flow must begin with a computation over the body itself. Many techniques are available to calculate the flow field over the body. Space-marching parabolized Navier-Stokes (PNS) codes can be used to efficiently solve for the flow field over the body. The intermediate and far wake, the most downstream region of Fig. 1, can also be efficiently computed using a PNS code, provided initial conditions can be specified. The near wake, or base region, encompasses the separated flow region, the recompression, and the acceleration to supersonic flow. This region is difficult to model. A time-marching Navier-Stokes (TNS) computation is usually required to model the flow field in this area. This paper is primarily directed toward base-flow and near-wake computations. The overall objective of the effort, however, is directed toward prediction of flow quantities, chemical species, and electron concentrations in the intermediate and far wake.

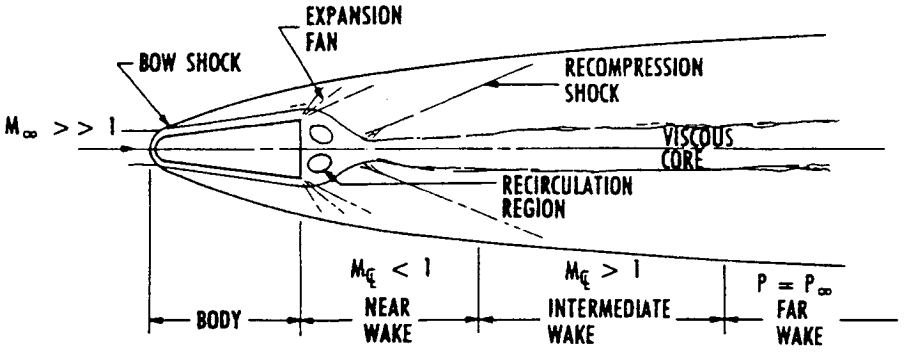

Fig. 1. Wake flow regions.

*The research reported herein was performed by the Arnold Engineering Development Center (AEDC), Air Force Systems Command. Work and analysis for this research were done by personnel of Calspan Corporation/AEDC Operations, operating contractor for the AEDC aerospace flight dynamics facilities. Further reproduction is authorized to satisfy needs of the U. S. Government.

** Senior Member, AIAA.

† Member, AIAA.

High-speed base flows are extremely rich in fluid dynamic and thermochemical complexities. Separation and reverse flow are the principal features in the base region that complicate flow-field predictions. The local Mach number may vary from above 10 to less than one across the shear layer. Strong shocks and expansions produce large temperature gradients in the flow. Temperatures which are high enough to produce dissociation and ionization in air occur. If transition to turbulence occurs, the location of transition will greatly affect the character of the wake. A detailed discussion of transition to turbulence is beyond the scope of this paper.

Near-wake flow data which are free from support interference effects are difficult to obtain. Sting or strut mounting of a model in a wind tunnel clearly interferes with the base-flow development. Ballistic ranges, which have been the premier facilities for studying the characteristics of wakes, can provide little detail in the base-flow region. Some data acquired in magnetic suspension tunnels or with wire-supported models exist, but these data are generally limited to relatively low temperatures and Reynolds numbers. As a result, computational techniques assume greater importance for providing information about this class of flows. On the other hand, very little data exist with which to test the validity of the computations.

Computation of high-speed base and near-wake flows has received increased attention recently. Much of the activity is focused in the area of plumes associated with propulsive systems for hypersonic flight vehicles. However, nonthrusting base flows have received renewed attention. Of particular interest are the recent papers of Conti and MacCormack,[1] Kim, Loellbach, and Lee[2] and Gnoffo, Price, and Braun.[3] In each of these papers, the authors numerically solve the Navier-Stokes equations in a time-marching manner to obtain a steady-state solution for the near-wake flow field. Different algorithms are being applied, different gridding techniques used, and different gas models employed, but the overall solution strategy is the same. The same general technique is used in the present paper.

This work extends the current state of near-wake calculations to Reynolds numbers above transition to turbulent flow by adding a two-equation turbulence model to the equation set. The turbulence model includes a correction to account for compressibility effects. To the authors' knowledge these are the first near-wake computational results including both turbulence and nonequilibrium chemistry effects. The paper contains several comparisons with perfect gas data for base flows and near-wake flows.

Approach

The three-dimensional thin-layer Navier-Stokes equations are solved using the set of strongly coupled, upwind algorithms developed by Molvik and Merkle.[4] Both algorithms use upwind differencing, Total Variation Diminishing (TVD) techniques in a finite-volume framework. The first algorithm is a time-marching scheme, and is generally used to obtain solutions in the subsonic portions of the flow field. The second algorithm is a much less expensive space-marching scheme which can be applied in the supersonic portion of the flow field. The time-marching code has been given the name TUFF (A **T**hree-Dimensional, **U**pwind-Differenced, **F**inite-Volume Flow Solver with **F**ully Coupled Chemistry), and the space-marching algorithm is referred to as STUFF. The time-marching scheme uses the zonal interfaces described in Ref. 5 to decompose the domain into more computationally and geometrically efficient blocks.

The codes currently include perfect gas, equilibrium air, and chemical nonequilibrium air capability. The equilibrium air model uses the curve fits of Srinivasan, Tannehill, and Weilmuenster. [6] The species considered in the nonequilibrium air model are oxygen (O_2), atomic oxygen (O), nitrogen (N_2), atomic nitrogen (N), nitric oxide (NO), nitric oxide ion (NO^+), and electrons (e^-). It is assumed that the gas mixture possesses a zero net local charge, allowing the conservation of electron mass equation to be eliminated from the equation set. The reactions that are considered are

$$
\begin{array}{lllllllll}
(1) & O_2 & + & M_1 & = & 2O & + & M_1 & \\
(2) & N_2 & + & M_2 & = & 2N & + & M_2 & \\
(3) & N_2 & + & N & = & 2N & + & N & \\
(4) & NO & + & M_3 & = & N & + & O + M_3 & (1) \\
(5) & NO & + & O & = & O_2 & + & N & \\
(6) & N_2 & + & O & = & NO & + & N & \\
(7) & N & + & O & = & NO^+ & + & e^- &
\end{array}
$$

where M_1 , M_2 , and M_3 are catalytic third bodies. Reaction rates and transport properties are obtained from Blottner, Johnson, and Ellis.[7] Wilke's mixing rule[8] is used to compute the mixture viscosity and thermal conductivity from those of the individual species. Each algorithm is strongly coupled and fully implicit, including the chemical source terms. The Vigneron, et al.[9] approximation is used in the space-marching algorithm to allow stable marching in the presence of a subsonic viscous wall layer.

Two turbulence models are included in the code, the Baldwin-Lomax[10] algebraic model and a two-equation k-ε model of Nichols, et al.[11]. The two-

equation model was incorporated for flows with multiple turbulent length scales or flows in which convection of turbulent quantities is important. The low Reynolds number two-equation model is derived from the model of Speziale, et al.[12] The model includes compressibility effects on turbulence through the compressible dissipation correction of Sarker and Balakrishnan[13] and through the compressiblity transformation of Mager[14] in the calculation of y+ for wall effects. The turbulence equations are solved fully coupled with the mean flow equations.

Results

Rearward Facing Step

The code was initially applied to the rearward facing step configuration of Smith.[15] The model consisted of a 4-in. forward plate and a 12-in. aft plate with a 0.443-in. step height. Two cases representing the highest and lowest Reynolds numbers tested were computed in order to evaluate the code's performance in both laminar and turbulent separated flow. Two-dimensional calculations were performed for both cases assuming a perfect gas and adiabatic walls. A 101 × 71 mesh divided into three zones was used for both calculations. The spacing at the wall was chosen to correspond to a y+ of one.

The laminar flow case was defined by a Mach number of 5.0, a Reynolds number of 1 × 10^5 per in., and a total temperature of 680°R. Calculated and experimental pressure distributions along the lower surface are shown in Fig. 2. Both the base pressure and the recompression along the reattachment surface are well predicted by the code.

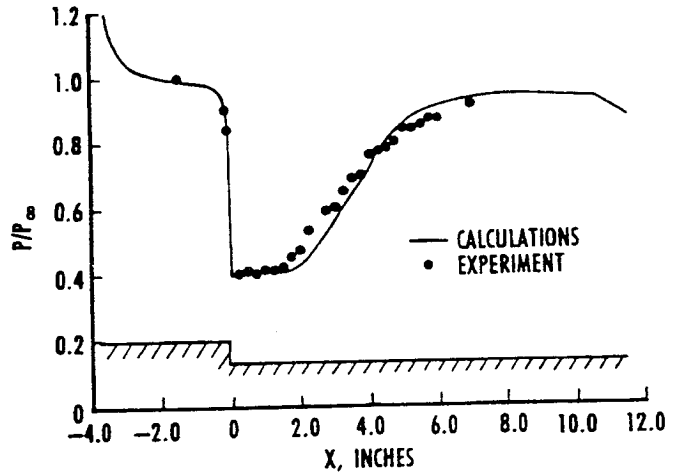

Fig. 2. Surface static pressure distribution for a laminar rearward facing step at M_∞ = 5.

The turbulent flow case was defined by a Mach number of 2.5, a Reynolds number of 4.6 × 10^5 per in., and a total temperature of 620°R. Boundary-layer transition location was not measured in the test, so the two-equation model was allowed to transition naturally. The turbulence model generally causes boundary-layer transition to occur prematurely. Based on the short length of the upper plate and the relatively low Reynolds number of the experiment, the boundary layer on the upper step is probably transitional in nature. Calculated and experimental pressure distributions along the lower surface are shown in Fig. 3. The calculated base pressure is slightly greater than the experimental result, probably due to the improper treatment of the state of the boundary layer on the upper plate, but in general the agreement is quite good.

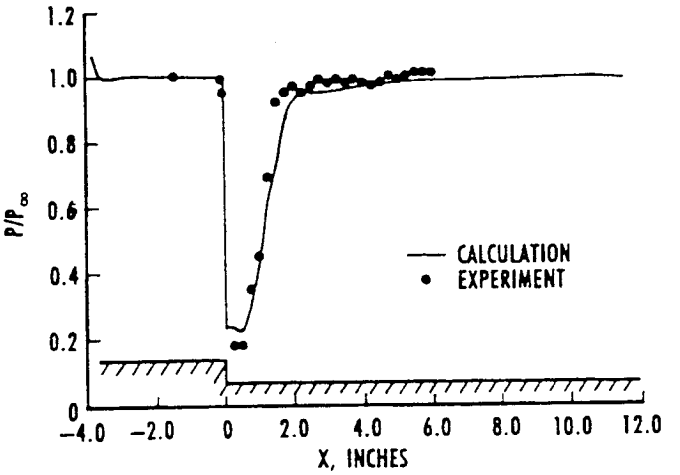

Fig. 3. Surface static pressure distribution for a turbulent rearward facing step at M_∞ = 2.5.

Laminar Sharp Cone

Perfect gas calculations of the laminar wake behind a sharp, 10-deg half-angle cone in helium at Mach 16.35 were performed and compared to the experimental data of Murman, et al.[16] and of Peterson.[17] The cone had a 1-in. base diameter. The tests were performed in the magnetic suspension wind tunnel at Princeton and thus are free of support interference effects. The Reynolds number was 1.21 × 10^5 per in. and the total temperature was 560°R. The cone was at 0-deg angle of attack. The solutions were found to be sensitive to the viscosity model used for the helium gas. The model used for the results presented here was

$$\mu = 0.1\exp[-12.365 + 0.1732\ln(T) - 0.006473\ln^2(T)] \quad (2)$$

Adiabatic no-slip boundary conditions were applied on all walls. The PNS code was used to calculate the flow over most of the forebody. A 91 × 101 computational mesh composed of three zones

was used for the TNS code in the near-wake region. Calculated density and Mach number distributions across the wake are compared to experimental results at two stations behind the cone in Figs. 4 and 5. The calculations are in excellent agreement with the data. Features such as the corner expansion and the recompression shock can clearly be seen. The centerline static pressure distribution is shown in Fig. 6. The peak recompression pressure is underpredicted, causing the pressures downstream of the recompression region to be underpredicted. These results for the centerline static pressure distribution agree well with the calculations of Tassa and Conti.[18] The cone base pressure distribution is shown in Fig. 7. The calculated results agree with the data. The base pressure is not constant as is generally the case for lower speed base flows. The base pressure is low near the corner due to the extremely strong expansion of the flow around the corner of the model. The base pressure rises towards the model centerline because of the recompression which occurs when the flow is turned near the wake centerline.

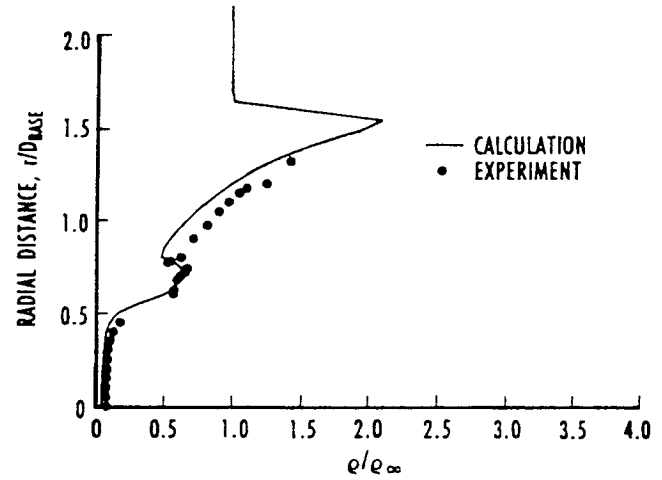

a. Density

b. Mach number

Fig. 4. Distributions across the wake at x/D = 5.0 for a sharp cone at M_∞ = 16.35.

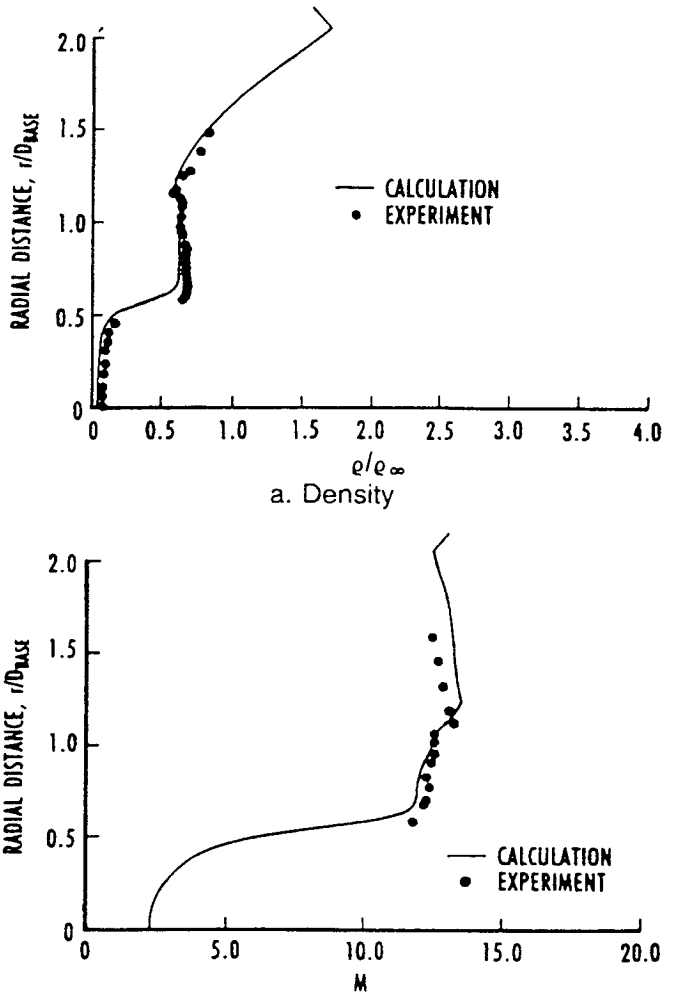

a. Density

b. Mach number

Fig. 5. Distributions across the wake at X/D = 10.0 for a sharp cone at M_∞ = 16.35.

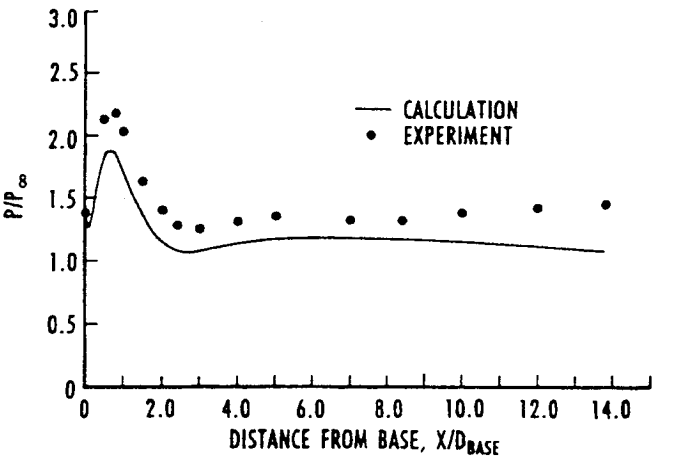

Fig. 6. Centerline static pressure distribution in the wake of a sharp cone at M_∞ = 16.35.

Laminar Blunt Cone

Calculations of the laminar wake behind a 10-percent blunt cone with a 10-deg half-angle were performed for the same test conditions as the

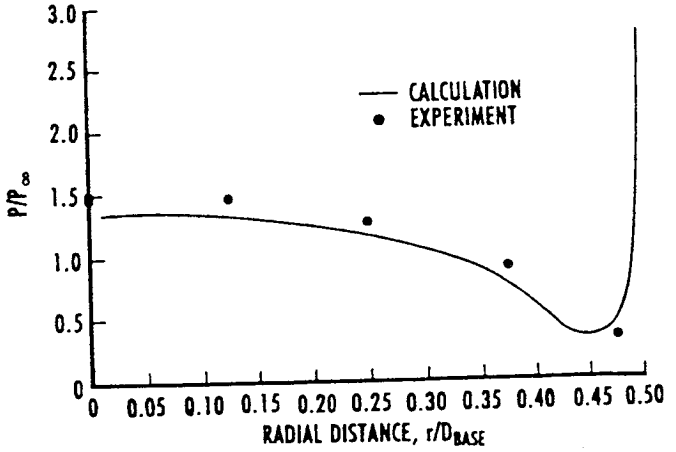

Fig. 7. Base pressure distribution for a sharp cone at M_∞ = 16.35.

previous case and compared to the data of Peterson.[17] The blunt cone also had a base diameter of one in. The flow over the nose was calculated with the time-marching code. This solution was used to initialize a space-marching solution over most of the forebody. The time-marching code was then run for the near-wake region. The space-marching code was then initialized in the intermediate wake at an x/D of four downstream of the base and marched to an x/D of twenty. This was done to demonstrate the space-marching capability in the intermediate and far wake. Calculated density and Mach number profiles at two stations in the wake are compared with experimental data at two stations behind the cone in Figs. 8 and 9. Both the time-marching (TUFF) and space-marching (STUFF) calculated results are shown in Fig. 8. The results agree well with the data. Centerline static pressure results for both algorithms are compared with experimental results in Fig. 10. While calculated results overpredict the peak pressure in the recompression region, there is generally good agreement between the calculations and experiment. The calculations of Tassa and Conti[18] underpredicted the peak recompression pressure for this case. Base pressure results are shown in Fig. 11. The peak base pressure is overpredicted, but the trends in the experimental results are reproduced by the calculations.

Turbulent Sharp Cone

Perfect gas calculations were performed on the turbulent wake behind the sharp, 5.9-deg half-angle cone with a rounded corner shown in Fig. 12. The flow conditions were for a Mach number of 7.4, a Reynolds number of 3.9 × 10^5 per in., and a total temperature of 1,400°R. The computations were compared to data obtained in a magnetic suspension tunnel at AEDC. The cone was at 0-deg angle of attack. The computational grid blocking strategy employed with the time-marching code is also shown in Fig. 12.

Boundary-layer transition on the cone was assumed to occur following the correlation for sharp cones in AEDC tunnels A, B, C, and F

$$X_{tb} = 4.6(Re \times 10^{-6})^{-5/7} \quad (3)$$

$$X_{te} = 7.5(Re \times 10^{-6})^{-5/7} \quad (4)$$

where X_{tb} is the beginning of transition, X_{te} is the end of transition, and Re is the unit Reynolds number per inch. Transition was simulated on the forebody with the PNS code by damping the eddy viscosity (μ_t) calculated with the algebraic turbulence model using the following:

$$\mu_t = 0 \quad (5)$$

for $x < X_{tb}$ and

$$\mu_t = \{1-\exp[-0.5476(XB - 4.6)^2]\}\ \mu_{tFT} \quad (6)$$

for $x > X_{tb}$, where XB is defined as

$$XB = x(Re \times 10^{-6})^{5/7} \quad (7)$$

μ_{tFT} is the fully turbulent eddy viscosity calculated by the algebraic turbulence model. The two-equation

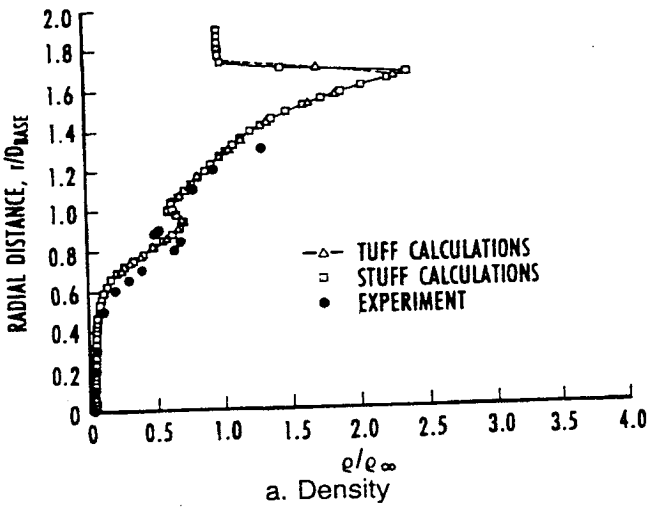

a. Density

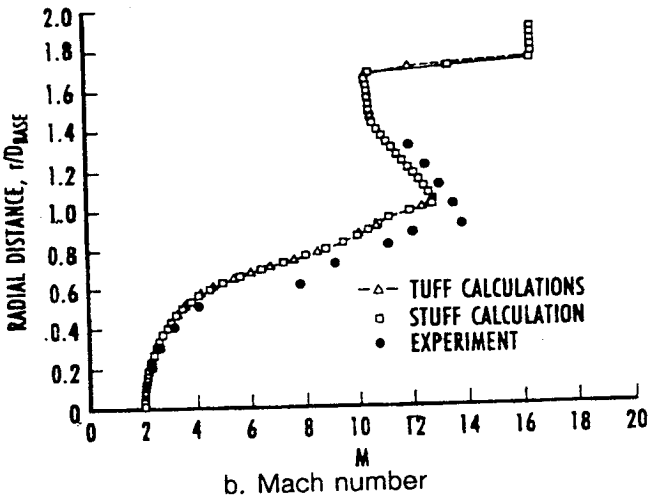

b. Mach number

Fig. 8. Distributions across the wake at X/D = 5.0 for a blunt cone at M_∞ = 16.35.

turbulence model was used after boundary-layer transition was completed. The PNS code was used to compute the flow over most of the cone forebody. A 121 × 91 computational mesh composed of six zones (Fig. 12) was used to calculate the flow in the near-wake region with the TNS code. The calculated and experimental pressure distributions along the wake centerline are shown in Fig. 13. The calculations accurately predict the cone base pressure and overpredict the recompression. Calculated pitot pressure distributions across the wake are compared to the experimental results in Fig. 14. The major features of the computed wake flow field are in excellent agreement with the measurements. The corner expansion and recompression shock are clearly seen.

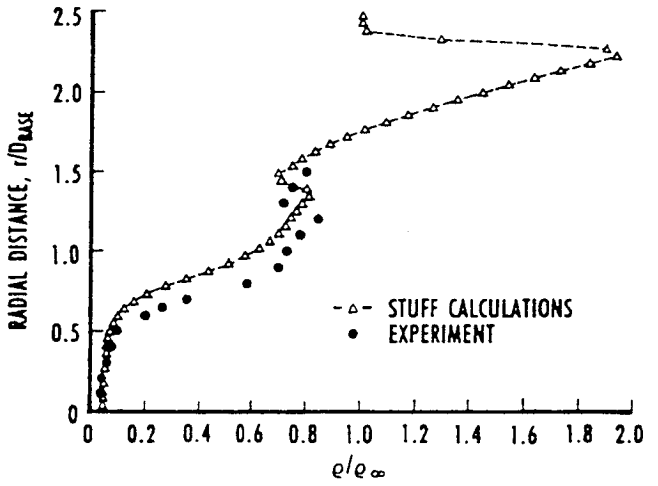

a. Density

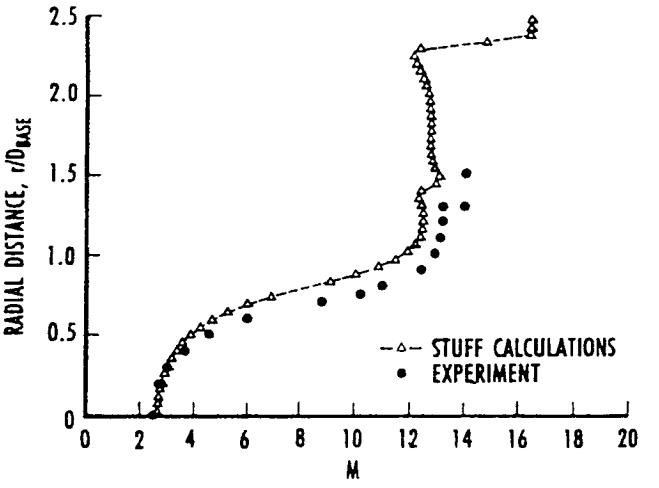

b. Mach number

Fig. 9. Distributions across the wake at X/D = 10.0 for a blunt cone at M_∞ = 16.35.

Blunt Cone with Three Gas Models

Computational results were obtained for the near wake of an 8-deg spherically blunt cone, 127 mm long, flying at a velocity of 5,200 m/sec at 0-deg angle of attack. Ambient static pressure and temperature conditions of 100 torr and 300K were chosen as typical of AEDC Hypervelocity Range G. A uniform cone surface temperature of 2,000K was assumed. Computational results were obtained with perfect gas, equilibrium air, and chemical nonequilibrium air models to assess the effects of chemistry on the near-wake flow field. A sketch of the computational geometry and solution domain is presented in Fig. 15.

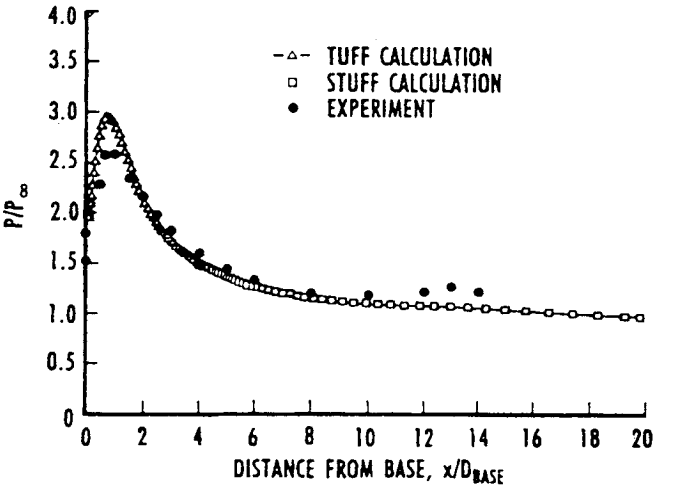

Fig. 10. Centerline static pressure distribution in the wake of a blunt cone at M_∞ = 16.35.

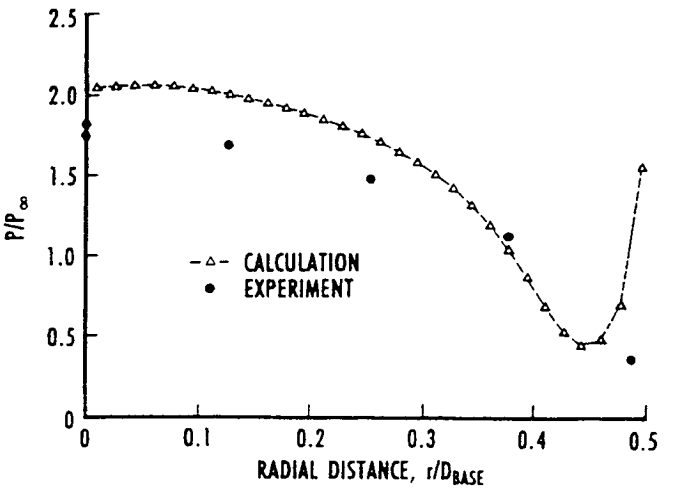

Fig. 11. Base pressure distribution for a blunt cone at M_∞ = 16.35.

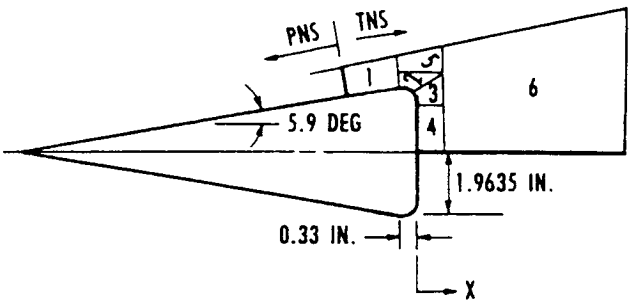

Fig. 12. 5.9-degree sharp cone geometry.

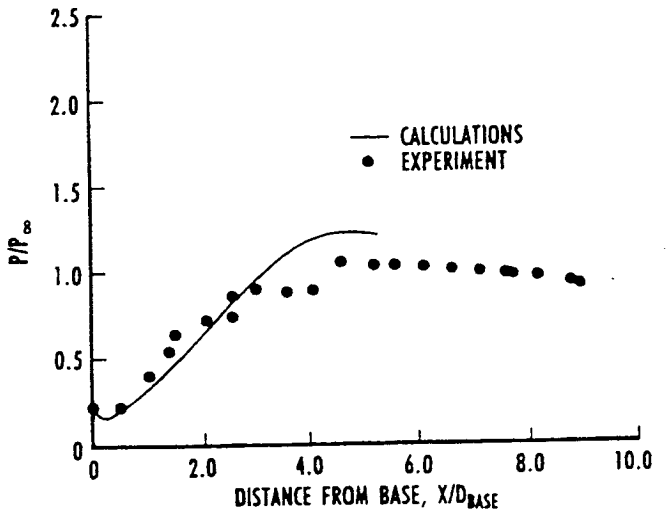

Fig. 13. Wake centerline static pressure distribution for a 5.9-deg cone at M_∞ = 7.4.

The laminar flow-field solution for the spherical nose was obtained with the time-marching code. Computation of the flow-field solution over most of the afterbody (up to x = 100 mm) was obtained with the space-marching code. Instantaneous transition to turbulence was assumed to occur at x = 15mm. The algebraic eddy viscosity model of Baldwin and Lomax[10] was used to approximate the effects of turbulence for the first 45 mm after transition, and then the k-ε model was used for the remainder of the calculation over the body and in the wake.

The near-wake flow field was obtained with the time-marching code. The computational domain started at x = 100mm and extended 10 base diameters downstream from the end of the cone. The perfect-gas computation used an 81 × 71 mesh divided into two zones. The equilibrium air and chemical nonequilibrium air computations used a 121 × 101 mesh composed of two zones. The two zones used for the afterbody and near-wake computation are shown in Fig. 15. Constant temperature, no-slip wall boundary conditions were specified along the base. For the nonequilibrium computation, a non-catalytic wall boundary condition was used on all body surfaces. Local time-stepping was used for all of the cases considered.

Pressure contours, normalized by the free-stream static pressure, and velocity vectors for the perfect-gas case are presented in Figs. 16 and 17, respectively. The principal features of the near-wake flow are apparent. The corner expansion, recompression shock, primary recirculation region, and viscous boundary layer on the base all are clearly discernible. In addition, secondary and tertiary recirculation regions can be seen near the corner of the cone. An embedded shock can be seen near the

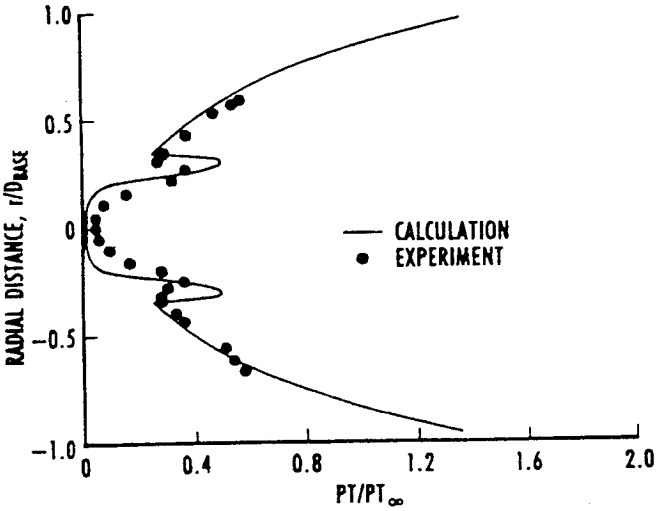

a. X/D_{BASE} = 2.06

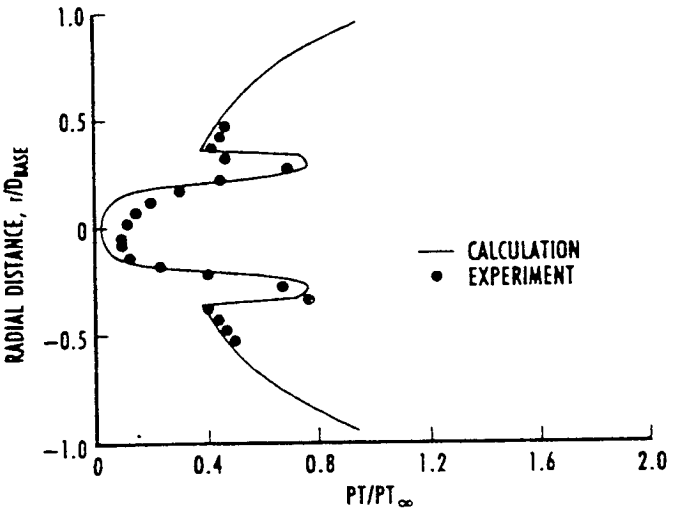

b. X/D_{BASE} = 3.03

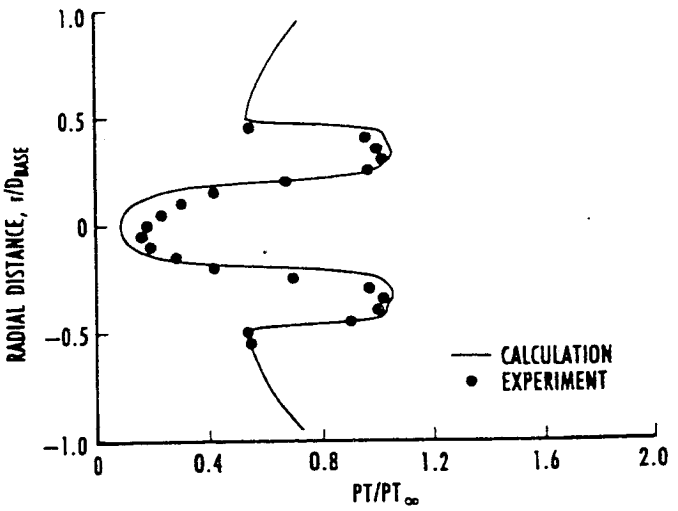

c. X/D_{BASE} = 5.02

Fig. 14. Pitot pressure distributions across the wake for a 5.9-degree cone at M_∞ = 7.4.

body axis and close to the base. The primary recirculation region is locally supersonic near the body axis

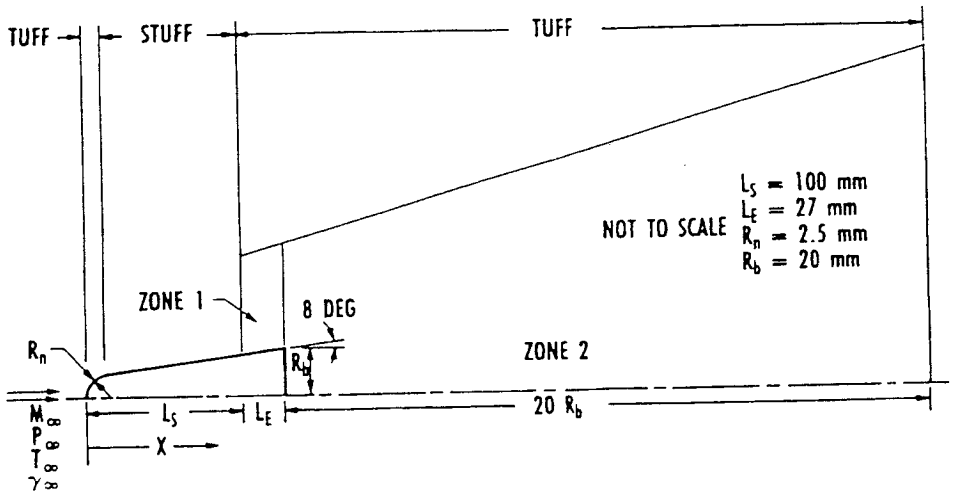

Fig. 15. Eight degree spherically blunt cone.

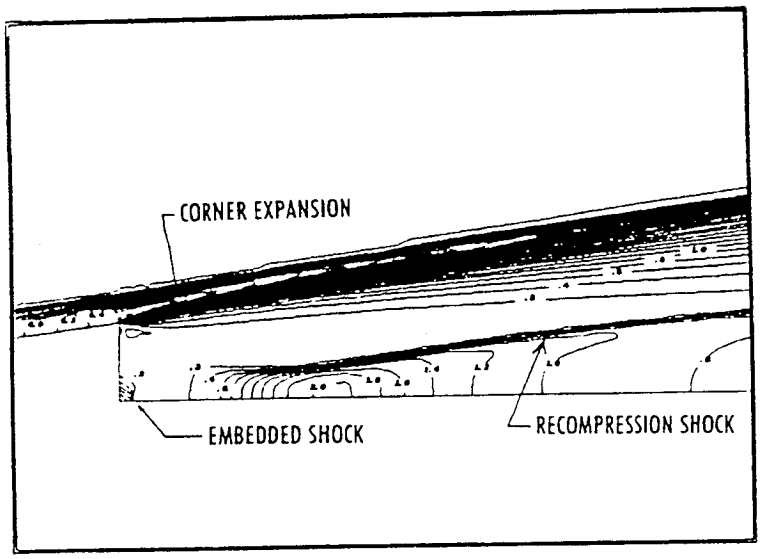

Fig. 16. Pressure contours (P/P_∞) for a blunt cone with a perfect gas model.

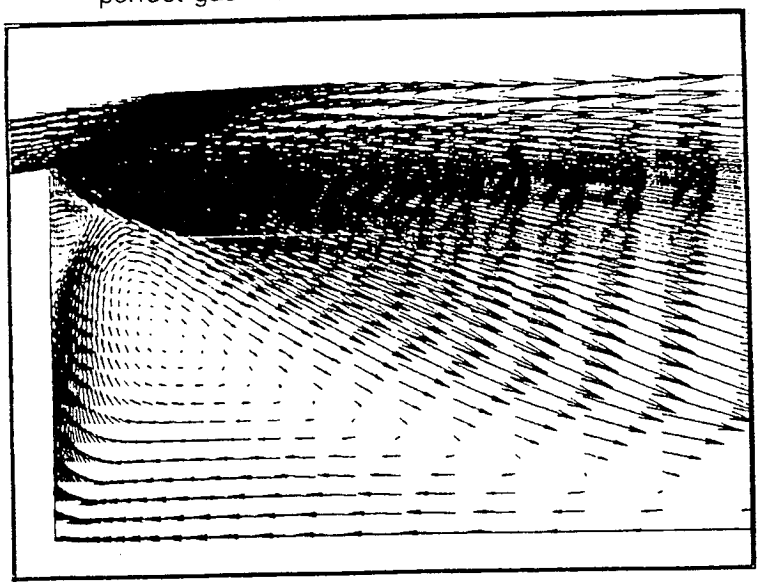

Fig. 17. Velocity vectors for a blunt cone with a perfect gas model.

and is compressed through the embedded shock from the presence of the base. Conti and MacCormack[1] and Kovenya and Lebedev[19] reported similar features. Comparisons of the wake centerline pressure and temperature distributions obtained with the different gas models are presented in Figs. 18 and 19. The x coordinate is measured from the base of the cone. The wake stagnation point occurs approximately 1.0 to 1.5 base diameters downstream from the base of the cone depending on the gas model used. Downstream of the wake stagnation point the flow expands to a pressure below the free-stream pressure. Equilibration of the pressure with the free stream will occur over a downstream distance of many base diameters. Compression of the flow through the embedded shock also generates centerline temperatures that are well above the specified cone surface value. Additionally, the choice of the gas model greatly influences the peak centerline temperature. The perfect-gas model predicts a peak temperature of approximately 19 times the free-stream value, the nonequilibrium model predicts a peak temperature that is approximately 13.5 times the free-stream value, and the equilibrium model predicts a peak temperature that is approximately 20 percent less than the nonequilibrium value. These trends are expected because of the large amounts of energy absorbed by the chemical reactions. After 10 base diameters, the temperature is 10 to 12 times greater than the free-stream value. The wake centerline electron density distribution, an important parameter to the radar signature, is presented in Fig. 20. The peak electron density occurs in the hot core of the wake and decreases as the flow accelerates

and cools downstream of the wake stagnation point. The calculated effects of the various gas models agree with the trends reported by Kim, Loellbach, and Lee.[2]

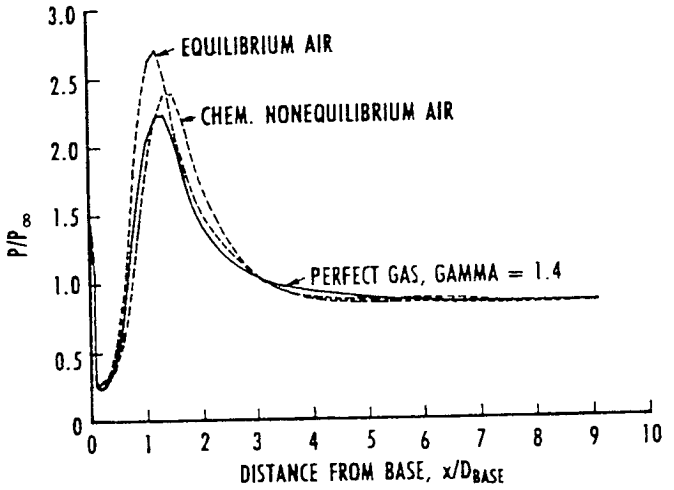

Fig. 18. Wake centerline pressure distributions for a blunt cone with three gas models.

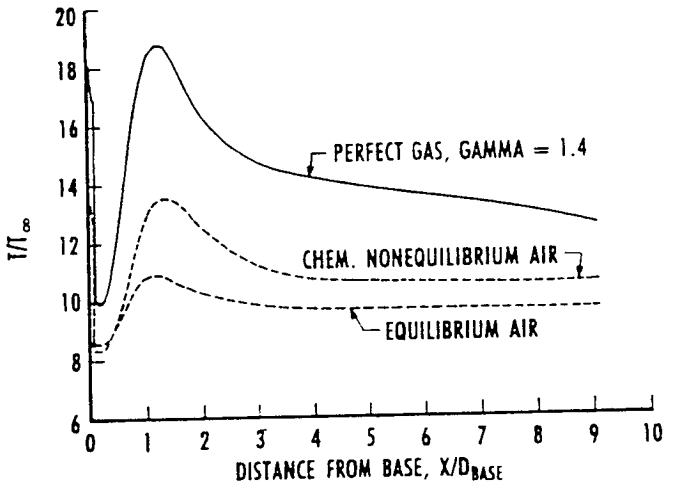

Fig. 19. Wake centerline temperature distributions for a blunt cone with three gas models.

Summary

A computational technique applicable to high-speed base flows has been demonstrated. The technique is based on solving the three-dimensional thin-layer Navier-Stokes equations for either a perfect gas, equilibrium air, or a chemical nonequilibrium air model. An efficient space-marching algorithm is used whenever possible on the body and in the far wake. A blocked time-marching algorithm is used to calculate the embedded subsonic flow in the base region. A two-equation turbulence model which includes compressibility effects is used to extend the approach to high Reynolds numbers.

A series of computations has been made to compare with base-flow and near-wake flow data. These test cases have free-stream Mach numbers ranging from 2.5 to 16.35 and encompass both laminar and turbulent flow conditions. The experimental data used for comparison were obtained in wind tunnels with stagnation temperatures low enough that no dissociation of the test gas was present. Good agreement with the data was obtained in all cases.

Further demonstration of the computational capability has been accomplished by carrying out calculations for a blunt cone configuration with free-stream conditions typical of those encountered in a ballistic range. The Reynolds number was assumed to be high enough to cause boundary-layer transition on the cone frustrum. These computations were performed assuming a perfect gas, equilibrium air and chemical nonequilibrium air.

References

1. Conti, R. J. and MacCormack, R. W. "Navier-Stokes Computations of Hypersonic Near Wakes with Foreign Gas Injection." AIAA-92-0838, January 1992.

2. Kim, M. S., Loellbach, M. M., and Lee, K. D. "Effects of Gas Models on Hypersonic Base Flow Calculations." AIAA-92-0641, January 1992.

3. Gnoffo, P. A., Price, J. M., and Braun, R. D. "On the Computation of Near Wake, Aerobrake Flowfields," AIAA-91-1371, June 1991.

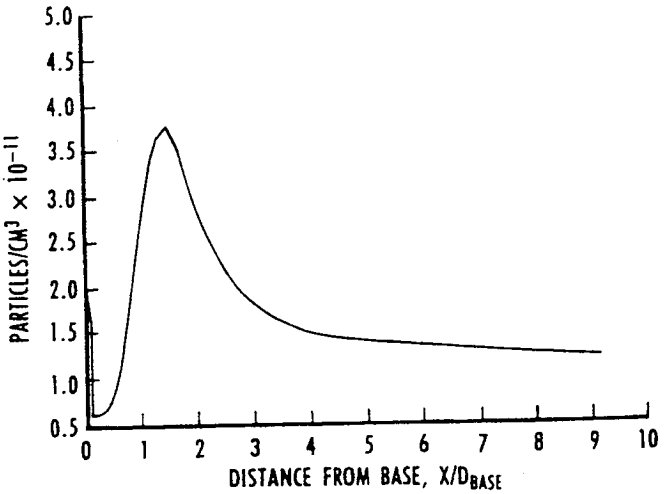

Fig. 20. Wake centerline electron density distribution for a blunt cone with a chemical non-equilibrium gas model.

4. Molvik, G. A. and Merkle, C. L. "A Set of Strongly Coupled, Upwind Algorithms for Computing Flows in Chemical Nonequilibrium." AIAA-89-0199, January 1989.

5. Klopfer, G. H. and Molvik, G. A. "Conservative Multizonal Interface Algorithm for the 3-D Navier-Stokes Equations." AIAA-91-1601, June 1991.

6. Srinivasan, S., Tannehill, J. C., and Weilmuenster, K. J. "Simplified Curve Fits for the Thermodynamic Properties of Equilibrium Air." NASA RP 1181, August 1987.

7. Blottner, F. G., Johnson, M., and Ellis, M. "Chemically Reacting Viscous Flow Program for Multi-Component Gas Mixtures." Report No. SC-RR-70-754, Sandia Laboratories, Albuquerque, New Mexico, December 1971.

8. Wilke, C. R. "A Viscosity Equation for Gas Mixtures." J. Chem. Phys., Vol. 18, No. 4, April 1950, p. 517.

9. Vigneron, Y. C., Rakich, J. C., and Tannehill, J. C. "Calculation of Supersonic Viscous Flow over Delta Wings with Sharp Subsonic Leading Edges." AIAA-78-1137, July 1978.

10. Baldwin, B. S., and Lomax, H. "Thin Layer Approximation and Algebraic Model for Separated Turbulent Flows." AIAA-78-257, January 1978.

11. Nichols, R. H., Jacocks, J. L., and Rist, M. J. "Calculation of the Carriage Loads of Tandem Stores on a Fighter Aircraft." AIAA-92-0283, January 1992.

12. Speziale, C. G., Ridha, A., and Anderson, E. C. "A Critical Evaluation of Two-Equation Models for Near Wall Turbulence." ICASE Report No. 90-46, June 1990.

13. Sarker, S. and Balakrishnan, L. "Application of a Reynolds Stress Turbulence Model to the Compressible Shear Layer." ICASE Report No. 90-18, February 1990.

14. Mager, A. "Transformation of the Compressible Turbulent Boundary Layer." Journal of the Aeronautical Sciences, Vol. 25, No. 5, May 1958, pp. 305-311.

15. Smith, H. E. "The Flow Field and Heat Transfer Downstream of a Rearward Facing Step in Supersonic Flow." ARL 67-0056, March 1967.

16. Murman, E. M., Peterson, C. W., and Bogdonoff, S. M. "Diagnostic Studies of Laminar Hypersonic Cone Wakes." AGARD CP No. 19, Vol. 1, May 1967.

17. Peterson, C. W. "An Experimental Study of Laminar Hypersonic Blunt Cone Wakes." Astronautica Acta, Vol. 15, No. 2, 1969, pp. 67-76.

18. Tassa, Y. and Conti, R. "Numerical Navier-Stokes Modeling of Hypersonic Laminar Wakes Behind Blunt Cones With Real-Gas Effects." AIAA-87-0374, January 1987.

19. Kovenya, V. M. and Lebedev, A. S. "Numerical Modeling of Viscous Separated Flow in the Near Wake." J. Applied Mech. and Tech. Phys., Vol. 30, No. 5, September-October 1989, pp. 718-724.

AIAA-92-3425

Analysis of a Hydrocarbon Scramjet with Augmented Preburning

Gregory A. Molvik, Jeffrey V. Bowles
and Loc C. Huynh,
NASA Ames Research Center,
Moffett Field, CA

AIAA/SAE/ASME/ASEE
28th Joint Propulsion Conference and Exhibit
July 6-8, 1992 / Nashville, TN

Analysis of a Hydrocarbon Scramjet with Augmented Preburning

Gregory A. Molvik*, Jeffrey V. Bowles† and Loc C. Huynh‡
NASA Ames Research Center
Moffett Field, CA

ABSTRACT

This paper presents the results of a feasibility study of a hydrocarbon scramjet design utilizing an augmented preburner upstream of the main fuel injector locations. The combustor design evaluated here is for a small hypersonic research vehicle. It consists of a preburner into which a small amount of fuel is burned with on-board liquid oxygen and injected into the main airflow, upstream of the main fuel injector locations, thus ensuring that combustion is present and uninterrupted. Two degrees of analysis are presented including a one-dimensional cycle analysis and a complete computational fluid dynamic analysis with finite-rate chemistry and a two-equation turbulence model. Comparison of these analyses show good agreement when the CFD-predicted fuel consumption schedule is used in the cycle analysis.

INTRODUCTION

The advent of the National Aero-Space Plane (NASP) has generated renewed interest in hypersonics research. The U. S. Air Force and NASA are pursuing the design and development of a single-stage-to-orbit (SSTO) vehicle in the NASP X-30. Both Europe and Japan have also proposed hypersonic vehicle design activities. Applications of hypersonic vehicle concepts to high-speed missions, both military and civilian, are also underway in government and industry. There exists an increasing need for hypersonic research vehicles (HRV) to demonstrate integrated aerodynamic, propulsion, and structural technologies for hypervelocity design and to develop a research database for reducing the risk involved in the development of operational hypersonic vehicles. Conceptual design activities are currently under way at NASA Ames Research Center to determine the feasibility of such a research vehicle utilizing near-term technology (Fig. 1).

The research goals of this activity are to provide an understanding of the underlying physics, verification of design tools, and validation of the technologies and systems needed. The research requirements are classified into two areas: 1) basic research, and 2) systems technology demonstration, which addresses programmatic research issues and overall vehicle system integration and performance. The disciplinary research requirements include aerodynamics and aero-thermodynamics of hypersonic flight, hypersonic air-breathing propulsion system performance, structures and materials characteristics, and finally instrumentation requirements for hypersonic vehicles.

The propulsion system for this HRV study is a hydrocarbon supersonic combustion ramjet (scramjet). Both NASA and DoD are currently reviewing a wide range of missions requiring a high-speed performance capability [1-3]. For a Mach number range of 4 to 10, hydrocarbon fuels provide sufficient engine specific impulse (Isp) performance, heat sink capability, and offer the potential of reduced vehicle size compared with hydrogen-powered designs. In addition, the handling and infrastructure requirements for the hydrocarbon fuels have a distinct advantage compared to cryogenic hydrogen.

The slow reaction rates of a hydrocarbon/air mixture in a supersonic stream can have a significant impact on the inlet/combustor design. Because of the size limitation of an engine on a small research vehicle, a mechanism is required to provide sufficient fuel/air temperatures for burning within the combustor. The concept of employing an in-stream, embedded ramjet as a pilot light has been proposed [3-4] and appears to be a promising technique for maintaining combustion. An alternative is to use a liquid oxygen (LOX) augmented pre-burner located

---

* Senior Research Scientist, MCAT Institute, Member AIAA
† Aerospace Engineer, Member AIAA
‡ Aerospace Engineer, Eloret Institute

upstream of the main fuel injectors to promote burning in the combustor. Because the LOX would be stored onboard the research vehicle, the required pre-burning should be kept to a minimum to reduce the impact on the vehicle design and gross weight. For the relatively short hypersonic research mission cruise times (5 to 10 minutes), the impact of this additional onboard mass will not have a significant impact on the HRV design.

In this paper, the feasibility of a hydrocarbon scramjet engine utilizing a LOX/preburner concept is addressed. An engine design for a small hypersonic vehicle is proposed and then analyzed. Two degrees of analysis are presented in this paper. A one-dimensional cycle code is first used to define a baseline configuration and the operating conditions of the engine. A computational fluid dynamic (CFD) analysis is then performed to predict the details of the engine flow field. The results of the CFD analysis are then fed back into the cycle code for the purpose of further refining the design and computing an overall vehicle performance. Comparisons between the cycle and CFD results are also included.

CYCLE ANALYSIS

As opposed to accelerator-type missions (e.g. SSTO) where the mass capture characteristics of the vehicle are most important, cruise configurations place an emphasis on the aerodynamic performance of the design. Hence vehicle lift-to-drag ratio (L/D) or the product of L/D and engine Isp (a parameter proportional to Brequet range factor) becomes more important. A waverider configuration, with high hypersonic L/D potential, was selected as the baseline configuration for the present study of the HRV. The configuration/engine installation was numerically optimized to maximize (L/D) x Isp, using forebody shape, ramp angles and cowl position as optimization parameters. For this analysis, the forebody is a Mach 8, waverider configuration and the ramp angles and cowl position were designed to produce shock-on-lip and shock-on-shoulder[5]. The engine geometry and operating parameters were held fixed in the optimization procedure. The HRV conceptual design analysis and sizing was computed using the hypersonic vehicle synthesis code (HAVOC) of Ref. 6. The numerical optimization was performed using the methods of Ref. 7.

As part of the HRV vehicle synthesis, the nose-to-tail propulsion module of the HAVOC code was used to predict installed engine performance of the hydrocarbon scramjet. The forebody and nozzle flow fields are computed using an inviscid 2-D real gas, weak wave/oblique shock analysis. In addition, the nozzle flow field was computed assuming frozen flow (mole fractions taken at the combustor exit plane). The combustor flow is solved using the one-dimensional mass, momentum, and energy equations for the fuel/air mixture, and marching through the combustor with a specified number of steps. Multiple fuel injection stations and LOX-augmented preburning injection are accounted for. Overall engine heat balance is computed using an input combustor skin friction coefficient as a function of freestream Mach number. For the initial analysis, the combustion efficiency was taken from Ref. 8, which accounts only for mixing efficiency, with no reaction delay time effects included. Modeling the combustion efficiency as a function of location in the combustor (i.e. a heat release schedule) enables the one-dimensional code to predict flow properties and engine performance using a multi-step approach. The combustor efficiency model must come from either experimental data or more detailed calculations. For results presented later, an improved combustor efficiency was computed with CFD and then implemented in the cycle analysis code.

CFD ANALYSIS

The design of future high-speed propulsion systems such as those for NASP and the HRV will for the most part be based on CFD. The need for CFD in scramjet propulsion design stems from the fact that scramjet propulsion is difficult to test in ground-based facilities and has yet to be demonstrated in flight. Therefore, CFD will continue to play a major role in the design of scramjet propulsion systems.

The requirements of a flow solver for hypersonic scramjet computations are very demanding. The flow solver must be capable of predicting the three-dimensional flow of a highly-turbulent mixture of reacting gasses with separated regions and strong flow field discontinuities. Upwind-differenced schemes offer an appealing approach to solutions of scramjet flow fields because of their ability to capture strong flow field discontinuities without user-specified smoothing terms. Further, multi-equation turbulence models become a requirement for accurately computing the turbulent shear layers

and boundary layers in a scramjet engine. Finally, a strongly coupled, nonequilibrium chemistry capability is required to compute the highly-reactive combustion processes that are present in a hydrocarbon scramjet engine.

Numerous unsteady numerical methods have recently been developed [9-18] that address chemical nonequilibrium effects in both internal and external flows. The numerical scheme chosen for this study is the time-marching flow solver, TUFF, originally developed by Molvik and Merkle[9] for external hypersonic, reacting flow fields. Even though the TUFF code was originally developed for external hypersonic computations, it has many of the characteristics required for internal, scramjet computations. It employs a finite-volume philosophy to ensure that the scheme is fully conservative. The inviscid fluxes are obtained by employing a temporal Riemann solver that fully accounts for the presence of a multicomponent mixture of gasses. A total-variation-diminishing (TVD) technique of the type outlined by Chakravarthy [19] allows extension to higher orders of accuracy without introducing spurious oscillations. The scheme employs strong coupling between the fluid-dynamic and chemistry equations. It solves the thin-layer, Reynolds-averaged, Navier-Stokes equations with viscous terms in all directions and has generalized boundary conditions. The scheme is made implicit with full linearization, approximate factorization and by employing a modified Newton iteration process to reduce linearization and approximate factorization errors. The turbulence model included in the original code is the algebraic model of Baldwin and Lomax [20]. Recently, a zonal scheme was incorporated [21] that utilizes patched interfaces to maintain conservation and spatial accuracy. For a complete description of the governing equations and numerical scheme, the reader is referred to Ref. 9.

Several modifications were required to the original TUFF code for scramjet computations. It was necessary to change the kinetics model from pure air to hydrocarbon / air including the reaction rates and mass action coefficients. Similar changes to the thermodynamic and transport data were also required. Further, a higher-order turbulence model with compressibility effects was added to improve the prediction of the many viscous phenomena. Finally, a boundary condition procedure was added to model the injection ports. These modifications are detailed below.

Kinetics Model

Flow field analysis of complete finite-rate chemical kinetics for hydrocarbon based fuels with air can be very complex and resource exhaustive. Hydrocarbon/air models have been proposed with tens of species and hundreds of reactions. CFD codes that include these complete models are currently limited to 1-D simply because of the exhaustive computer resource requirements for extension to higher dimensions. Simplified reaction mechanisms for the hydrocarbon combustion process offer a solution to this problem by foregoing the details of the combustion process. In this approach, various species and reactions are combined and simplified while preserving the net effect of the reaction processes. Since kinetic details are not required in the present study, a simplified reaction mechanism was sufficient.

For the scramjet propulsion system analysis, the two-step reaction mechanism of Westbrook and Dryer [22] was employed to simulate the combustion of fuel with air. For hydrocarbon scramjet propulsion, the liquid fuel can be used as a coolant on various portions of the aircraft. This results in an endothermic reaction that can vaporize and dissociate the liquid fuel. Gaseous ethylene was used in this analysis, as a surrogate fuel intended to represent the products of this endothermic reaction. The kinetics model for ethylene is outlined below.

$$C_2H_4 + 2O_2 \leftrightarrow 2CO + 2H_2O \qquad (1)$$

$$CO + \frac{1}{2}O_2 \leftrightarrow CO_2 \qquad (2)$$

The first reaction represents the combustion of ethylene with oxygen. The second reaction is included to complete the combustion process and to serve as an equilibrium mechanism for the products that then improves the predicted heat of reaction and adiabatic flame temperature. This equilibrium step is especially necessary since substantial amounts of CO and H_2 can exist in the combustion products along with CO_2 and H_2O.

The values of the forward and backward reaction rate constants are evaluated with Arrhenius fits to existing laminar flame data. These take the form:

$$k = A T^n \exp(-E_a/RT) \qquad (3)$$

where the pre-exponential factor, A, and the activation energy, E_a, are constants for a particular reaction. The temperature-dependence exponent, n, was set to zero for all of the reaction rate fits. The reaction rate constants recommended by Ref. 22 are tabulated below:

Table 1 Reaction Rates

Equation	A	Ea
1f	2.4×10^{12}	30
1b	0.0	-
2f	4.0×10^{14}	40
2b	5.0×10^{8}	40

The backward reaction rate for equation 1 was set to zero. The units for the pre-exponential constant and for the activation energy are cm-sec-mole-kcal-kelvins.

The mass production rate of each species is determined with a modified law of mass action in this simplified model. The reaction rates evaluated with the modified law, are shown below:

$$R_1 = [C_2H_4]^{0.1}\,[O_2]^{1.65}\,k_{1f} \qquad (4)$$

$$R_2 = [CO]^{1.0}[H_2O]^{0.5}\,[O_2]\,k_{2f} - [CO_2]^{1.0}\,k_{2b} \qquad (5)$$

with the bracketed terms representing the molar concentrations of each indicated species. The mass production rate for each species, s, can now be determined with the following:

$$\dot{\omega}_s = \mathcal{M}_s\left[\left(\nu''_{1s} - \nu'_{1s}\right)R_1 + \left(\nu''_{2s} - \nu'_{2s}\right)R_2\right] \qquad (6)$$

where, $\nu''_k s$ and $\nu'_k s$ are the reactant and product stoichiometric coefficients and $\mathcal{M}_s$ is the molecular weight of species s. Throughout this kinetics model, molecular nitrogen, N_2, has been treated as an inert species.

Thermodynamic/Transport Properties

The thermodynamic and transport properties for the individual species in the hydrocarbon/air mixture were obtained from Ref. 23. For these curve fits, the properties are expressed solely as functions of temperature. The temperature range for this data is typically limited to 300-5000°K. However, research is currently underway at NASA Lewis Research Center to expand this range [24]. For details on the computation of mixture properties in the TUFF code, see Ref. 9.

Turbulence Modeling

Modeling scramjet flow fields with CFD requires an advanced turbulence model capable of accurately accounting for compressible turbulent shear layers and jets. This was accomplished in the present study with the incorporation of the low Reynolds number K-ε turbulence model originally developed by Jones and Launder [25]. The compressibility correction of Zeman [26] was also included in the two-equation formulation to improve the computation of compressible shear layers. The modified numerical constants were suggested by Ref. 26 to produce better boundary layer results as well as improve shear layer growth rates. The entire turbulence model was transformed to a generalized finite-volume coordinate system and strongly coupled with the existing flow solver, including the viscous and inviscid flux computation and the source term treatment.

Injector Boundary Condition Procedure

For the engines studied in this paper, all of the injectors (including preburner and main) were designed to be supersonic in the boundary-normal direction. This simplifies the boundary condition procedure since merely specifying of the injector variables is required for a supersonic inflow boundary condition. This type of injector is also quite practical in a scramjet since injector pressures are typically high enough to choke the injector flow. The supersonic inflow boundary condition was imposed only on those cell faces that correspond to an injector exit. No-slip, viscous boundary conditions were imposed on the cell faces adjacent to the injector exit. This led to the use of rectangular injectors to avoid further complication of the boundary condition procedure and the grid generation process.

RESULTS

Three sets of results are included in this paper: a shear layer test case, and two- and three-dimensional scramjet results. Because of the absence of high-speed, hydrocarbon combustion data, a validation case for the combustion model of Ref. 22, under scramjet conditions, is not possible. Validation for this

model is therefore limited to the laminar flame comparisons with shock tunnel data by the originators of the model. High quality, CFD validation experiments in the area of high-speed hydrocarbon combustion are therefore greatly needed.

Shear Layer Test Case

The first test case is that of two parallel streams of perfect gasses that are initially separated by a splitter plate with boundary layers of zero thickness (Fig. 2). This test case is intended to validate the Jones and Launder turbulence model, with the Zeman compressibility correction, for high-speed shear layers. The flow conditions were chosen to correspond with the computation of Viegas [27] in which a comparison with experiment was conducted. In this test case, the total temperature and static pressure of the two air streams were matched and set to 833°K and 1 atmosphere, respectively. The Mach numbers of the two streams were 4.92 and 1.1. Strong compressibility effects are expected for these flow conditions.

The results of the shear layer test case are shown in Figs. 3-5. Note that for the figures presented in this section, the high Mach number stream is on the top (positive y direction). Results using the standard Jones and Launder K-ε turbulence model with no compressibility correction are presented first. A direct comparison of results with those of Viegas are shown in Figs. 3 and 4. These figures present profiles of velocity and turbulent kinetic energy profiles at five axial stations in the shear layer, plotted as a function of distance across the shear layer normalized by the local vorticity thickness of the shear layer. These results indicate a linear growth of the shear layer with axial distance and also suggest that a profile similarity exists for a shear layer with zero boundary layer thickness at the end of the splitter plate. These figures also show that the shear layer penetration is much greater into the low Mach number stream. There is also a general turning of the high-speed stream into the low-speed stream. This is in agreement with the results of Viegas.

Comparison of these results with those of Viegas are excellent except for a slight vertical drift that can be seen in both Figs. 3 and 4. This difference is attributed to the far-field boundary conditions used by Viegas. Those boundary conditions produced a small vertical velocity throughout the flow field that tended to further turn the shear layer into the low Mach number stream. Comparisons of the profiles are otherwise in direct agreement including the peak turbulent kinetic energy, the velocity profile and shear layer thickness.

The linearity of the growth rate is easily seen in Fig. 5. This figure shows the vorticity thickness as a function of the axial distance from the splitter plate. Vorticity thickness is defined as follows:

$$\delta_w = (U_1 - U_2) / \left(\frac{\partial U}{\partial y}\right)_{max} \qquad (7)$$

Comparison of the standard Jones and Launder two-equation turbulence model with that of Viegas shows very good agreement. The predicted growth rate for the two-equation model with the compressibility correction is also plotted here. This plot shows a reduction in the growth rate from the standard model which has been shown by Refs. 26 and 27 to be in better agreement with experiment.

Two-Dimensional Scramjet Result

As a first attempt to determine the feasibility of a hydrocarbon scramjet engine with augmented preburning, a two-dimensional analysis was conducted. The initial geometric definition for the scramjet engine, including throat height, shock isolator length, and combustor length, and combustor area ratio were taken from Ref. 4. The embedded ramjet section was removed and a hydrocarbon/LOX preburner was added. A mixing section aft of the preburner station was also added to allow mixing of the preburner exhaust gasses with the oncoming air so as not to suffocate the main burner jets of oxygen. A schematic showing the scramjet concept is presented in Fig. 6. Backward facing steps, prior to the main fuel injection station were included to act as flame holders and mixing enhancement mechanisms. Finally, for the purpose of comparison, a preburner was only employed on the top of the engine leaving the lower main burners exposed to just the oncoming air stream.

Preliminary HAVOC design results at a Mach number of 8 and a dynamic pressure of 1500psf for the waverider HRV with two ramps and with both shock on shoulder and on cowl lip indicated that a contraction ratio of roughly 14 was achievable. Details of this inlet design are included in Ref. 5. Using a guideline of approximately 1000°K as auto-ignition of a gaseous ethylene/oxygen mixture, the 1-D cycle code was run with the LOX augmentation

preburning option to compute parametrically, the required fuel and oxygen flow to achieve an equivalent mixed 1-D temperature at the main fuel injector station equal to the auto-ignition value(Fig. 7). For an engine with an equivalence ratio of 1 (stoichiometric) this resulted in roughly 2.5% of the fuel being directed to the preburner which was then burned stoichiometricaly with onboard LOX. A heat balance on the vehicle and engine was used to compute the fuel total temperature. The preburner and main burner pressure and velocity were then selected to produce supersonic normal injection and the required exit areas were also computed. The resulting operating conditions of this engine are given in Table 2.

Table 2. Engine Operating Conditions

	Inlet	Preburner	Main
Gas	Air	Products	C_2H_4
Mach No.	3.84	2.5	2.5
T(°K)	795	2897	403
P(atm)	.95	1.76	1.73
Area(in)	2.0000	0.0268	0.0820
Angle	-	90°	90°

The area in the above table is based on a one inch width section.

The CFD results for this two-dimensional approximation are shown in Figs. 8-12. Throughout the CFD simulation process, the ingestion of a thick boundary layer formed on the forebody of the hypersonic vehicle by the scramjet was neglected. The grid for this computation spanned 150 cells in the axial direction and 74 cells in the cross flow direction and was generated algebraically. For this turbulent computation, the grid spacing at the wall was set to 2.5×10^{-5}m. The pressure contours for the entire scramjet engine are shown in Fig. 8 and indicate a somewhat smooth pressure variation throughout the engine except in the vicinity of the injectors and steps. The preburner exhaust gasses produce a shock that traverses the entire height of the scramjet. The pressure rise of this shock is then quickly suppressed by a weak expansion that is caused by a slight geometric expansion region starting just after the preburner location. These preburner gasses then are convected downstream and seem to adhere to the upper surface for this two-dimensional computation.

The upper and lower step flows exhibit entirely different behavior, because the upper step was exposed to the hot preburner exhaust gasses and the lower step was not. The lower step flow field exhibits a steady behavior and contains many of the features that are typical of a reward facing step flow field. A recirculating region located aft of the step is present but is slightly enhanced by the existence of the normal fuel injector placed one quarter of a step height downstream of the step. The gas behind this step is entirely comprised of fuel. A recompression shock is also clearly visible in the pressure contours of Fig. 8. Combustion of the lower gasses begins about five step heights aft of the step and is visibly enhanced by the recompression shock. This enhancement effect can be seen about 8 step heights aft of the step in the temperature contours of Figs. 9 and 10.

The upper step on the other hand produces a violently unsteady flow field. The hot preburner exhaust gasses on the upper surface interact with the air and fuel to produce intermittent periods of combustion aft of the step. The predicted flow field is highly irregular and no cyclic behavior was observed. It should be noted that a local time-stepping routine was used and a time-accurate scheme could produce an entirely different solution. At the point in the computation that these figures were generated, a pure fuel jet was observed that penetrated well into the oncoming air stream. This phenomenon can be seen both in the fuel contours of Fig. 11 and the velocity vectors of Fig. 12.

Several deficiencies emerged in this two-dimensional analysis of a clearly three-dimensional problem. First, the geometry required modification to accommodate a two-dimensional computation. This consisted of considerably shortening the injection port lengths to maintain a constant injection area as the ports were changed from series of individual ports to a single slot. Second, the jet penetration and mixing efficiency are significantly reduced in a two-dimensional computation. This is the most prevalent effect and can significantly affect the predicted performance of the scramjet engine. And finally, any side wall effects are entirely neglected in a 2-D computation. For these reasons, a three-dimensional analysis was performed. The three-dimensional CFD analysis presented in the following discussion addresses the first two issues stated here, although it still neglects any side wall effects.

Three-Dimensional Scramjet Result

Several modifications were made to the two-dimensional scramjet engine design before the three-dimensional computation was performed. First, the forebody geometry was further optimized with the HAVOC code, resulting in slightly different inlet conditions. These new inlet conditions are included in Table 3. Next, the two-dimensional results indicated that the steps filled up entirely with fuel and did not serve the purpose of a flame holder. Further, they produced a negligible effect on mixing, and cycle analysis indicated that engine performance is better served with this aft-facing area distributed in the main combustion region. For these reasons, the steps were eliminated in the three-dimensional scramjet design. The flow of LOX was then reduced to the preburner resulting in a fuel-rich preburner. This reduced the required amount of onboard LOX with only a minimal effect on temperature distribution prior to main fuel injection. This is because the fuel-rich preburner exhaust gasses continue to react with the air after injection. Finally, preburning was employed both on the top and bottom of the scramjet to improve engine efficiency. Fig. 13 shows a schematic of the modified scramjet engine.

As in the two-dimensional design, the preburner and main burner injectors were designed to produce supersonic injection. A further consideration in the three-dimensional design was the penetration distance of the injectors. Reference 28 gives a relationship for the jet penetration distance as a function of the jet and freestream Mach numbers, the momentum ratio of the two streams, the angle of injection and the jet diameter, d_j. This relationship is given below:

$$\frac{h}{d_j} = \frac{9.05}{1+\cos(\alpha_j)} \sqrt{\frac{\rho_j u_j}{\rho_\infty u_\infty}} \frac{1+\frac{\gamma_\infty - 1}{2} M_\infty^2}{M_\infty \left(1+\frac{\gamma_j - 1}{2} M_j^2\right)} \qquad (8)$$

The preburner injection was designed to only penetrate through the boundary layer , whereas the main injection was designed to reach well into the air stream for better mixing. This resulted in a guideline of h=0.5cm for the preburner and h=2.0cm on the main burner. Because of the large amounts of fuel being injected through the main injectors at stoichiometric conditions, the main fuel injectors were designed with a streamwise length-to-width aspect ratio of 5 and an angle of injection of 30 degrees to help reduce blockage. The injectors were laterally spaced one inch apart on both the top and bottom of the scramjet. The top injectors were then offset one-half inch to a produce a staggered injection for the purpose of increasing jet penetration and to avoid the additional losses of impacting jets. The preburners were aligned with the main fuel injectors to ensure that the hot preburner gasses fell in near vicinity of the main fuel. The HAVOC code was run with this new engine and produced the following engine operating conditions.

Table 3. Engine Operating Conditions

	Inlet	Preburner	Main
Gas	Air	Products and C_2H_4	C_2H_4
Mach No.	3.83	1.1	2.2
T(°K)	833	3395	801
P(atm)	.86	13.39	2.49
Area(in)	2.0000	0.005	0.166
Angle	-	90°	30°

A three-dimensional CFD analysis of this engine was performed. Because of the periodicity of the engine in the absence of any side walls, only the flow between the centerline of the top injectors and the centerline of the bottom injectors was actually solved. The grid for this computation was generated algebraically and contained 119 cells in the axial direction, 60 cells from top to bottom, and 16 cells laterally. The grid spacing on the walls was set to 4.0×10^{-5}m. All of the injector exits were modeled as rectangles containing 8 cells in each of the axial and lateral directions. This three-dimensional computation required 1850 iterations leading to 102 hours on a Cray-YMP. The computation was halted after no plotable difference was seen with further iteration.

The results of the three-dimensional CFD analysis are shown in Figs. 14-26. The pressure contours on both the symmetry plane containing the top injector and the one containing the lower injector are shown in Fig. 14. As in the two-dimensional results, the pressures are smoothly varying except in the vicinity of the injectors. The large influence of these injectors is clearly visible in these figures and affects the entire flow path. Shocks emanating from both the preburner and main fuel injectors traverse the height and width of the computational space. These shocks can significantly affect the

efficiency of the engine, and any further refinement of this design will address the losses associated with these large structures. The temperature contours (Fig. 15) show the injector penetration and the temperature rise caused by combustion. This figure indicates that the penetration of the combustion region is slightly more than half the height of the scramjet. A significant degree of penetration is present, yet avoids adverse effects such as jet-jet interactions and jet-wall interactions.

The depth of penetration and degree of combustion are better seen in the fuel and oxygen mass fraction contours of Figs. 16 and 17. The fuel contours clearly show the regions of unburned gaseous fuel and the oxygen contours show the locations that are deficient in oxygen indicating the penetration distance of fuel and products. These oxygen contours show that the injector gasses do indeed penetrate far into the flow path. Also shown in the fuel contours are the fuel-rich preburner gasses The depletion of the fuel and oxygen in the preburner gasses indicates that combustion is present and exhausts nearly all of the fuel in the preburner gasses.

The velocity vectors of Figs. 18 and 19 show some details of the injector flow fields. The velocity vectors in the immediate vicinity of the preburner exit exhibit a spreading behavior that is typical of an under-expanded jet. This phenomenon is also present in the main injector region but is less visible because of the inclination of the vectors. A separation region is present in the preburner injector region that reaches seven jet diameters upstream of the injector. This phenomenon is absent near the main fuel injectors because of the reduced angle of injection. Also shown in this figure is the increased penetration that can be achieved with normal injection.

Figures 20,21 and 22 contain crossflow contour plots of temperature, fuel and water respectively, at various axial locations. The axial locations correspond to the following: 1) the back of the preburner station, 2) just upstream of the main fuel injection, 3) the back of the main injector station, 4) within the combustion chamber, and 5) the combustor exit. The exact axial locations are indicated on the plots.

The temperature contours of Fig. 20 clearly show the mechanism that is studied in this paper. Fig. 20(a) shows the hot preburner gasses that emerge from the preburner injector ports. These gasses mix and react with the oncoming air stream but still contain a very hot core just before main fuel injection (Fig. 20(b)). This hot core, falling just above the main fuel injection, serves as a "pilot light" for main fuel injectors causing combustion of the main fuel to instantaneously occur (Fig. 20(c)). The main fuel injectors were designed to produce a significant amount of penetration without traversing the entire height of the scramjet. This was accomplished and is clearly shown in the combustion chamber temperature contours (Figs. 20(d&e)). These figures indicate that the concept of preburning does indeed accomplish the task of maintaining combustion at the main fuel injection station and that an injector can be designed to provide significant flow path penetration without unstarting the engine.

The effect of the upper surface corner on combustion is shown in Figs. 21 and 22. An expansion wave emanating from this corner causes the density and temperature to decrease having an adverse effect on the rate of combustion and mixing. This wave affects the upper gasses before reaching the lower gasses. Therefore the expansion has a greater effect on the upper gasses. For this reason, there are more unburned and unmixed gasses present in the upper region of the scramjet.

The ability of the 3-D CFD finite-rate model to provide the equivalent 1-D combustor efficiency (i.e. the heat release schedule) allows the 1-D cycle analysis code to predict thermodynamic flow properties through the combustor, and hence compute engine and vehicle performance. Sensitivity analysis using the cycle code indicates that at Mach 8 a 1% change in overall combustion efficiency represents approximately 1% change in cowl-to-tail Isp and 0.8% change in axial thrust coefficient. Hence having a good combustor efficiency model permits the use of a 1-D cycle code to model engine performance with sufficient accuracy for conceptual design analysis.

The remaining figures present a comparison of the CFD results with those of a 1-D cycle analysis. The combustor efficiency computed by the CFD solution was implemented in the cycle code since no other schedule was available for this engine design. This was accomplished by curve fitting the average fuel fraction schedule (Fig. 23) and using this schedule in the 1-D cycle code. Both the CFD predicted schedule and the curve fit are shown in Fig. 23. Also shown on Fig. 23 is the

predicted amount of carbon monoxide from both the CFD and 1-D cycle analysis. The CFD analysis predicts a higher amount than the 1-D cycle code. This is caused by the difference in the equilibrium mechanisms of the two codes and suggests an improvement to the simplified kinetics employed in the CFD solver for scramjet computations. Comparison of the average temperature, the momentum-averaged pressure and the mass-averaged velocity from the CFD analysis with the results of the cycle code show general agreement (Figs. 24-26). The discrepancies can be attributed to the improved ability of the CFD method to account for detail and the difference in the equilibrium mechanisms.

CONCLUSIONS

As a result of this effort, two methods for the conceptual design and analysis of hydrocarbon fueled scramjets were developed and demonstrated: a cycle code with a simplified nose-to-tail flow field analysis capability, and a complete 3-D CFD code with finite-rate chemistry for hydrocarbon/air combustion. Utilizing the heat release schedule predicted by the CFD analysis in the cycle code, the combustor flow field properties and level of combustion product constituents computed by the two respective methods agree. Verification of the 1-D cycle code results by the CFD analysis encourages further application of the cycle code to a broader range of engine design parameters. Promising configurations can then be analyzed in detail using CFD. However, there is currently a void of high-quality, CFD validation-type data for high-speed hydrocarbon combustion, leaving an uncertainty in any predicted results.

The CFD results for the 2-D engine configuration indicated the need for full 3-D analysis of the combustor flow field to properly predict the three-dimensional penetration and mixing inherent in the combustion process. An accurate modeling of the mixing process, especially for diffusion-controlled combustion, is required in order to adequately predict overall engine performance, with either a 1-D cycle code or a full-CFD analysis code. The forebody flow field boundary layer should also be included in any nose-to-tail analysis. The presence of this boundary layer can have a significant effect on the efficiency of the scramjet and on the performance of the entire vehicle.

The analysis of the liquid oxygen-augmented preburning hydrocarbon scramjet indicated that the concept does indeed produce combustion of the main fuel within the scramjet engine. The preburning process provides a sufficiently-elevated temperature flow into the main fuel injector region to support immediate combustion of the gaseous ethylene fuel. However, because of the significant amount of unburned fuel at the combustor exit, there is a need for better mixing efficiency within the combustor. For the current fuel injector configuration, improved engine cycle performance could also be achieved at a lower overall engine equivalence ratio, limited by engine cooling requirements.

ACKNOWLEDGEMENTS

This work was partially supported by NASA Ames Research Center under grants NCC2-498 and NCC2-746. The authors would like to acknowledge Chuck Carlson and Robert Schnurstein of Rockwell International / Rocketdyne Division for their technical advice on injector sprays and Thomas E. Whitaker of Sterling Software for graphics and technical support.

REFERENCES

[1] Beach, H. L. and Blankson, I. M., "Prospects for Future Hypersonic Air-Breathing Vehicles," Proceedings, Vol. 1, 10th ISABE, Sept 1991.

[2] Blankson, I. M., "Airbreathing Hypersonic Cruise: Prospects for a Mach 4 to 7 Waverider Aircraft," ASME-92-GT-437, June, 1992.

[3] Kay, I. W., Peschke, W.T. and Guile, R. N., "Hydrocarbon-Fueled Scramjet Combustor Investigation," AIAA Paper 90-2337, July 1990.

[4] Arena, A. V. and Grant, M., "The Technical Design and Integration Issues of Hydrocarbon-Fueled Scramjet Missiles," JANNAF Report, Feb. 1991.

[5] Molvik, G. A., Bowles, J.V. and Huynh, L. C., "Analysis of a Hypersonic Research Vehicle with a Hydrocarbon Scramjet Engine," proposed paper at the AIAA 31st Aerospace Sciences Meeting, Reno NV, Jan. 1993.

[6] Bowles,J. V. Conceptual Studies Activities. Proceedings of the Second

National Aerospace Plane Symposium. Applied Physics Laboratory, Laurel, MD, Nov. 1986.

[7] Vanderplaats, G. N. and Hansen, S. R.,"DOC Users Manual", Version 1.00, VMA Engineering, Goleta, CA, 1989.

[8] Anderson, G. Y. and Rogers, R. C., A "Comparison of Experimental Supersonic Combustor Performance with an Empirical Correlation of Nonreactive Mixing Results", NASA TM X-2429, October, 1971.

[9] Molvik, G. A. and Merkle, C. L., "A Set of Strongly- Coupled Upwind Algorithms for Computing Flows in Chemical Nonequilibrium," AIAA Paper 89-0199. Jan. 1989.

[10] Gnoffo, P. A. and McCandless, R. S., "Three Dimensional AOTV Flowfields in Chemical Nonequilibrium," AIAA Paper 86-0230, Jan. 1986.

[11] Candler, G. V. and MacCormack, R. W., "The Computation of Hypersonic Ionized Flows in Chemical and Thermal Nonequilibrium," AIAA Paper 88-0511, Jan. 1988.

[12] Palaniswamy, S., Chakravarthy, S. R. and Ota, D. K., "Finite-Rate Chemistry for USA-Series Code: Formulation and Applications," AIAA Paper 89-0200, Jan 1989.

[13] Shuen, J. S. and Liou, M. S., "Flux-Splitting Algorithms for Two-Dimensional Viscous Flows with Finite-Rate Chemistry," AIAA Paper 89-0388. Jan. 1989.

[14] Yu, S. T., Tsai, Y. L. P. and Shuen, J. S., "Three-Dimensional Calculation of Supersonic Reacting Flows Using an Lu Scheme," AIAA Paper 89-0391, Jan 1989.

[15] Palmer, G., "An Efficient, Explicit Finite-Rate Algorithm to Compute Flows in Chemical Nonequilibrium," AIAA Paper 89-0522. Jan. 1989.

[16] Hoffman, J. J.,. "Development of an Algorithm for the Three-Dimensional Fully-Coupled Navier-Stokes Equations with Finite-Rate Chemistry," AIAA Paper 89-0670, Jan.1989.

[17] Imlay, S. T., Roberts, D. W., Soetrisno, M. and Eberhardt, S., "Nonequilibrium Thermo-Chemical Calculations using a Diagonal Implicit Scheme," AIAA Paper 91-0468, Jan. 1991.

[18] Withington, J. P., Shuen, J. S. and Yang, V., "A Time Accurate Implicit Method for Chemically Reacting Flows at All Mach Numbers," AIAA Paper 91-0581, Jan, 1991.

[19] Chakravarthy, S. R. and Osher, S., "Numerical Experiments with the Osher Upwind Scheme for the Euler Equations," *AIAA Journal*, 21 (Sept. 1983), pp. 1241-1248.

[20] Baldwin, B. S. and Lomax, H., "Thin Layer Approximation and Algebraic Model for Separated Turbulent Flows." AIAA Paper 78-257, Jan. 1978.

[21] Klopfer, G. H. and Molvik G. A., "Conservative Multizonal Interface Algorithm for the 3-D Navier-Stokes Equations," AIAA Paper 91-1601, June 1991.

[22] Westbrook, C. K. and Dryer, F. L., "Simplified Reaction Mechanisms for the Oxidation of Hydrocarbon Fuels in Flames,", *Combustion Science and Technology*, Vol. 27, 1981, pp. 31-43.

[23] Gordon, S. and McBride, B. J., "Computer Program for Calculation of Complex Chemical Equilibrium Compositions, Rocket Performance, Incident and Reflected Shocks, and Chapman-Jouguet Detonations," NASA SP-273, 1976.

[24] McBride, B. J., NASA-Lewis Research Center, Personal Communication, 1991.

[25] Jones, W. P. and Launder, B. E., "The Prediction of Laminarization with a Two-Equation Model of Turbulence," *International Journal of Heat and Mass Transfer*, Vol. 15, 1972, pp. 303-314.

[26] Zeman, O., "Compressible Turbulence Subjected to Shear and Rapid Compression," Eighth Symposium on Turbulent Shear Flows, Munich, Germany, Sept, 1991.

[27] Viegas, J. R. and Rubesin, M. W., "A Comparative Study of Several Compressibility Corrections to Turbulence Models Applied to High-Speed Shear Layers," AIAA Paper 91-1783, June 1991.

[28] McClinton, C. R., "Effect of Injection Angle on the Interaction Between Sonic Secondary Jets and Supersonic Free Stream," NASA TN D-6669, Feb. 1972.

Fig. 1 Hypersonic vehicle concept with an integrated hydrocarbon scramjet engine.

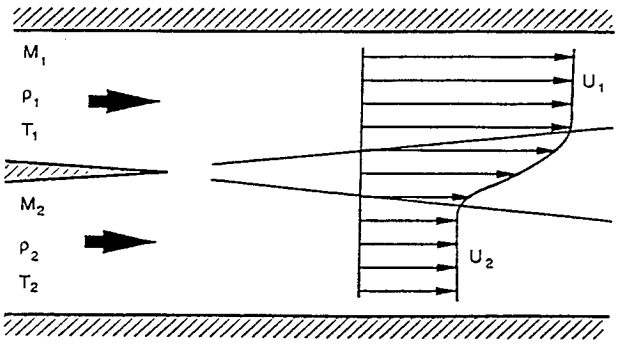

Fig. 2 Schematic diagram of free-shear layer.

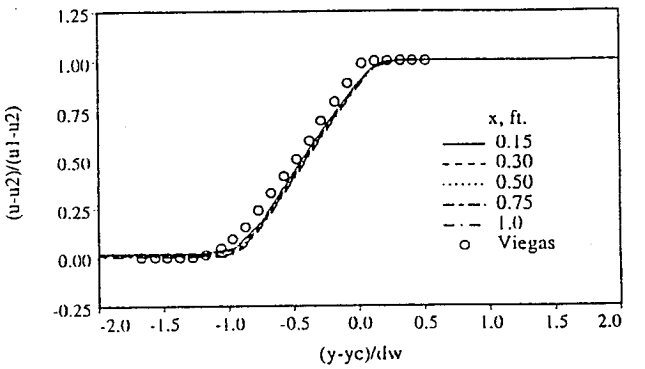

Fig. 3 Velocity profiles

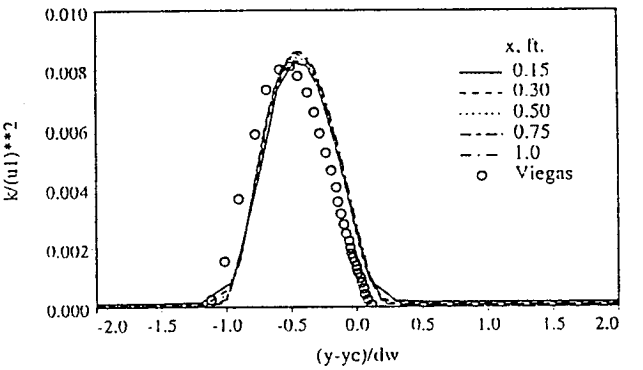

Fig. 4 Turbulent kinetic energy profiles

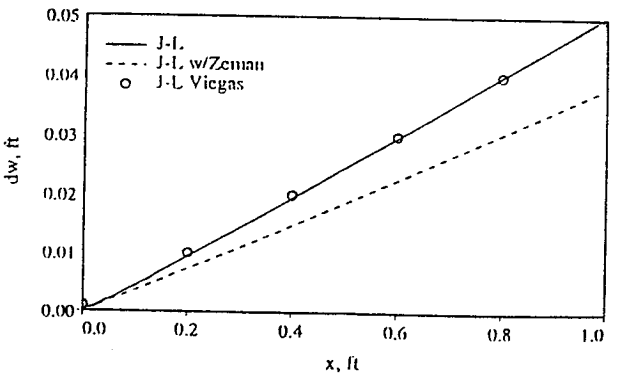

Fig. 5 Shear layer growth rate (vorticity thickness)

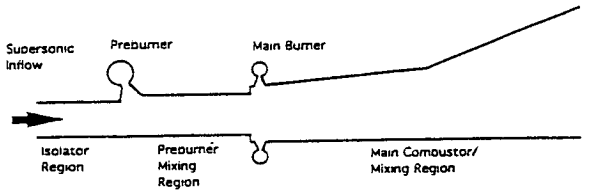

Fig. 6 Schematic diagram of the 2-D scramjet engine geometry

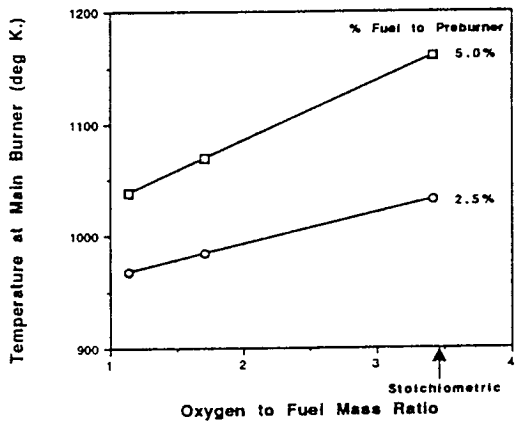

Fig. 7 Main burner temperature as a function of oxygen to fuel mass ratio

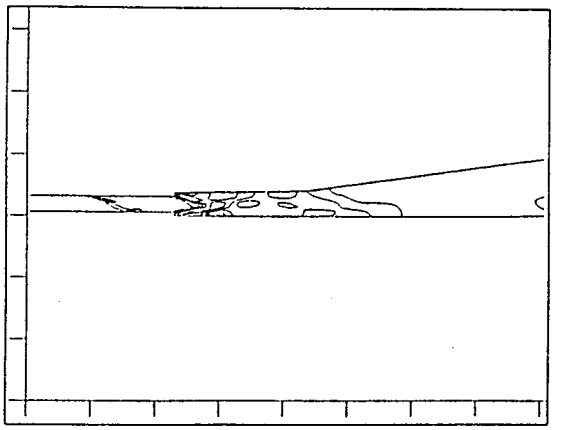

Fig. 8 Pressure contours

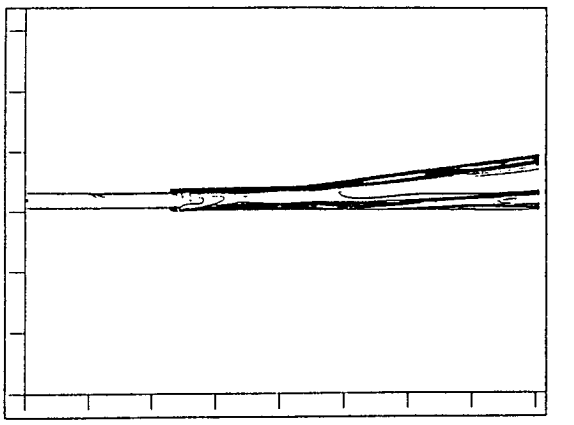

Fig. 9 Temperature contours

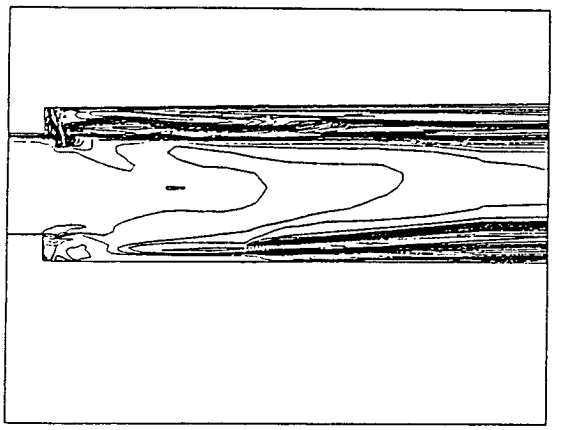

Fig. 10 Temperature contours (Zoom view)

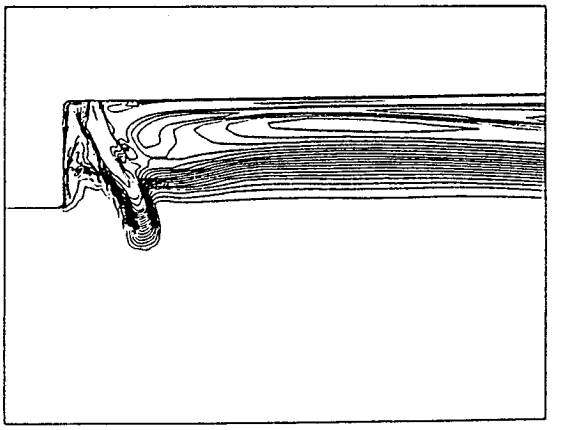

Fig. 11 Fuel mass fraction contours

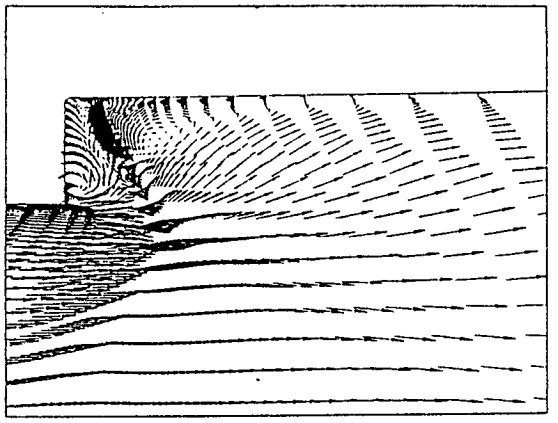

Fig. 12 Velocity vectors

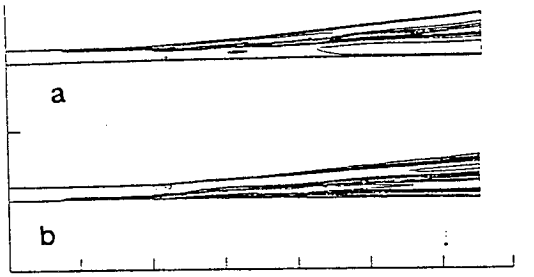

Fig. 15 Temperature contours at a) symmetry plane of top injectors, b) symmetry plane of bottom injectors.

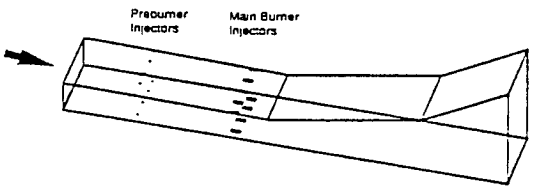

Fig. 13 Schematic diagram of the 3-D scramjet engine geometry

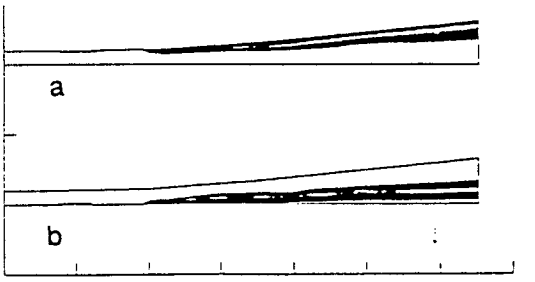

Fig. 16 C_2H_4 mass fraction contours at a) symmetry plane of top injectors, b) symmetry plane of bottom injectors.

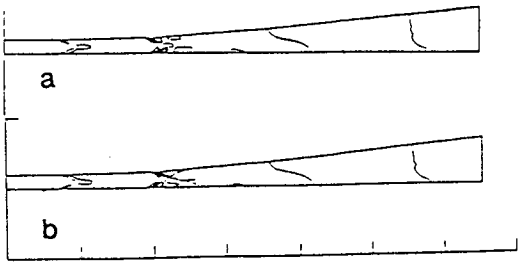

Fig. 14 Pressure contours at a) symmetry plane of top injectors, b) symmetry plane of bottom injectors.

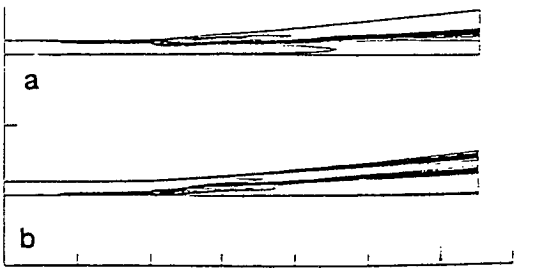

Fig. 17 O_2 mass fraction contours at a) symmetry plane of top injectors, b) symmetry plane of bottom injectors.

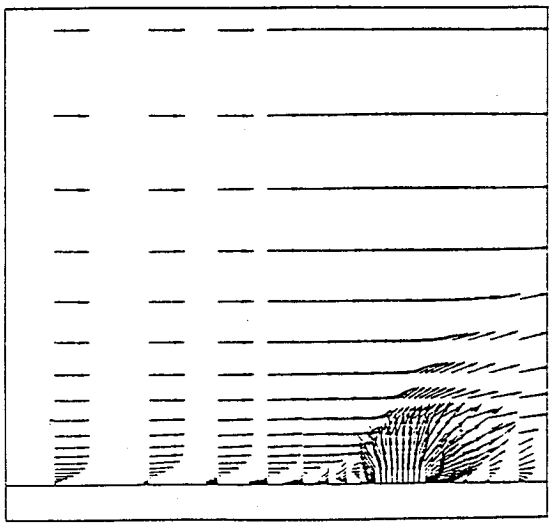

Fig. 18 Velocity vectors in vicinity of preburner injector

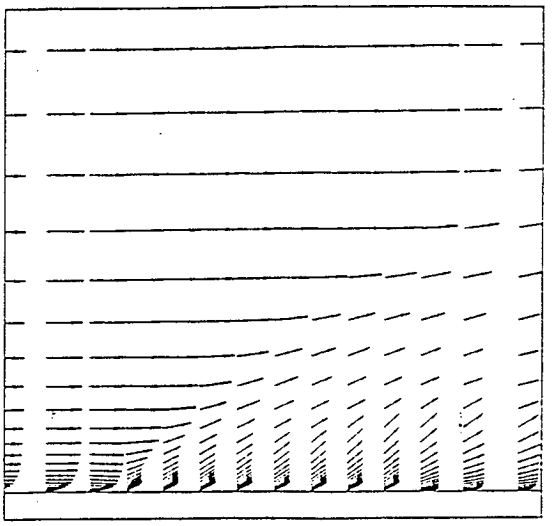

Fig. 19 Velocity vectors in vicinity of main burner injector

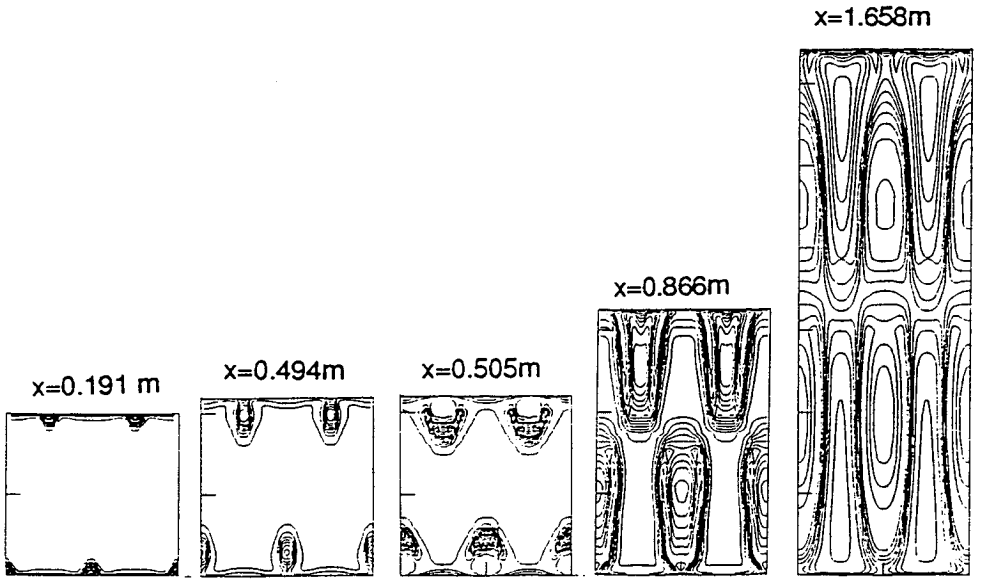

Figure 20: Temperature Contours at Indicated Axial Locations

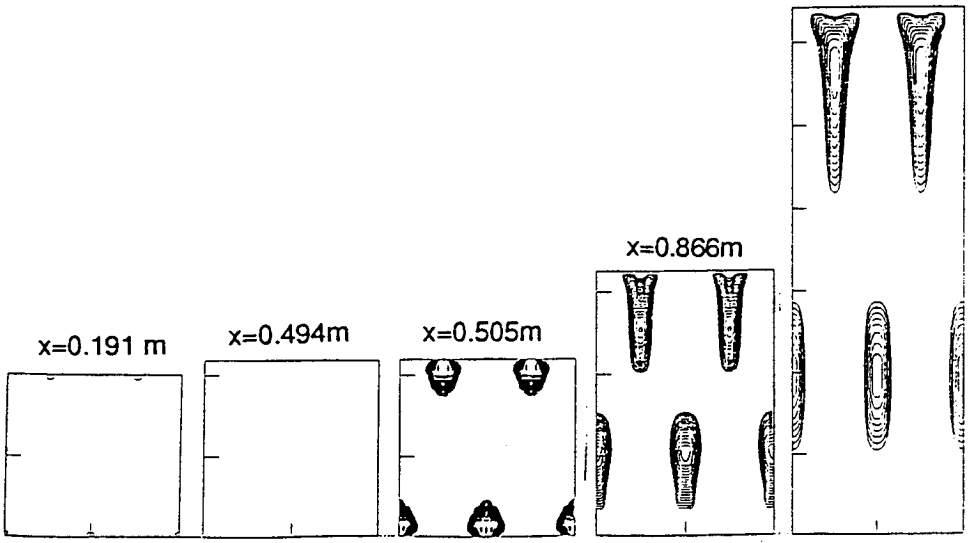

Figure 21: C_2H_4 Mass Fractions Contour at Indicated Axial Locations

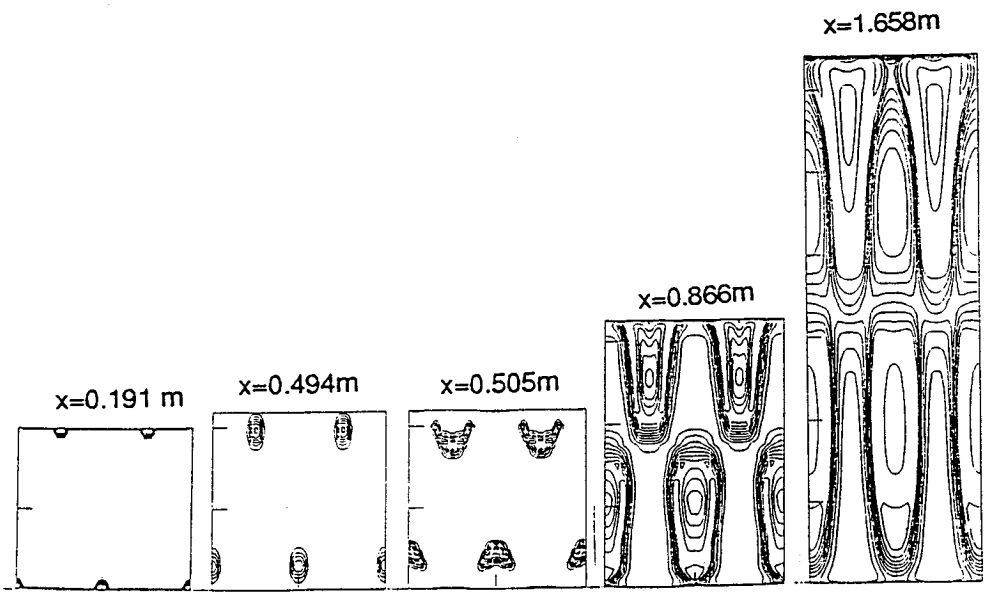

Figure 22: H_2O Mass Fraction Contours at Indicated Axial Locations

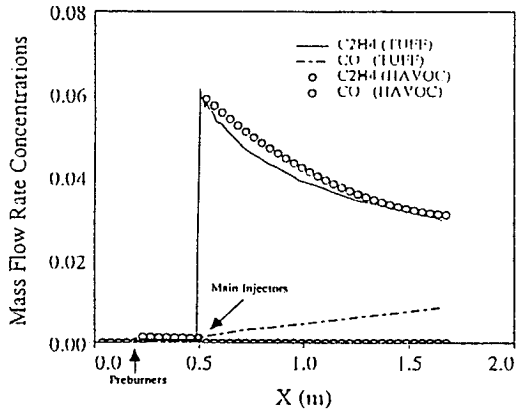

Fig. 23 C_2H_4 and CO mass concentrations as a function of axial locatio

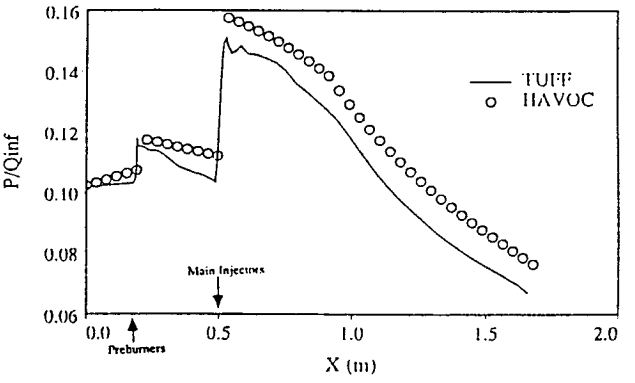

Fig. 25 Pressure as a function of axial location

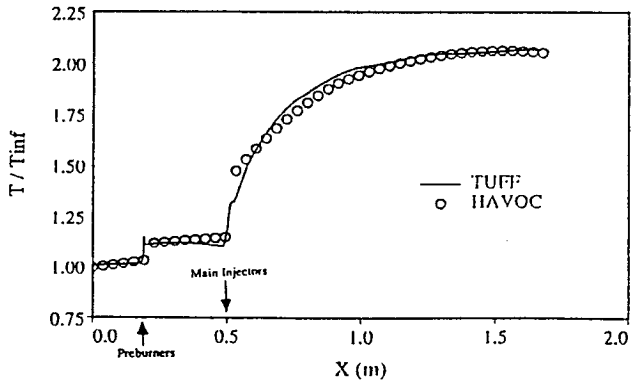

Fig. 24 Temperature as a function of axial location

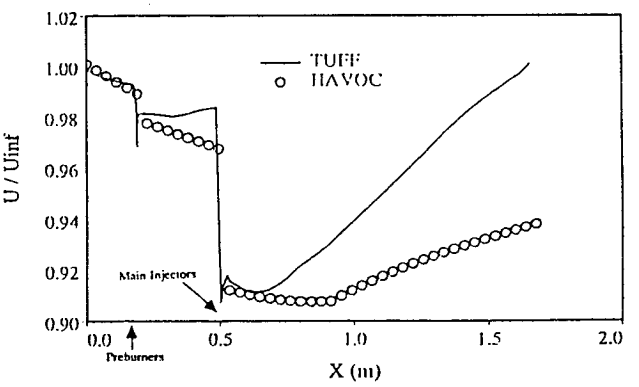

Fig. 26 Axial velocity as a function of axial location

AIAA

AIAA-93-0509
Analysis of a Hypersonic Research Vehicle with a Hydrocarbon Scramjet Engine

Gregory A. Molvik, Jeffrey V. Bowles
and Loc C. Huynh,
NASA Ames Research Center,
Moffett Field, CA

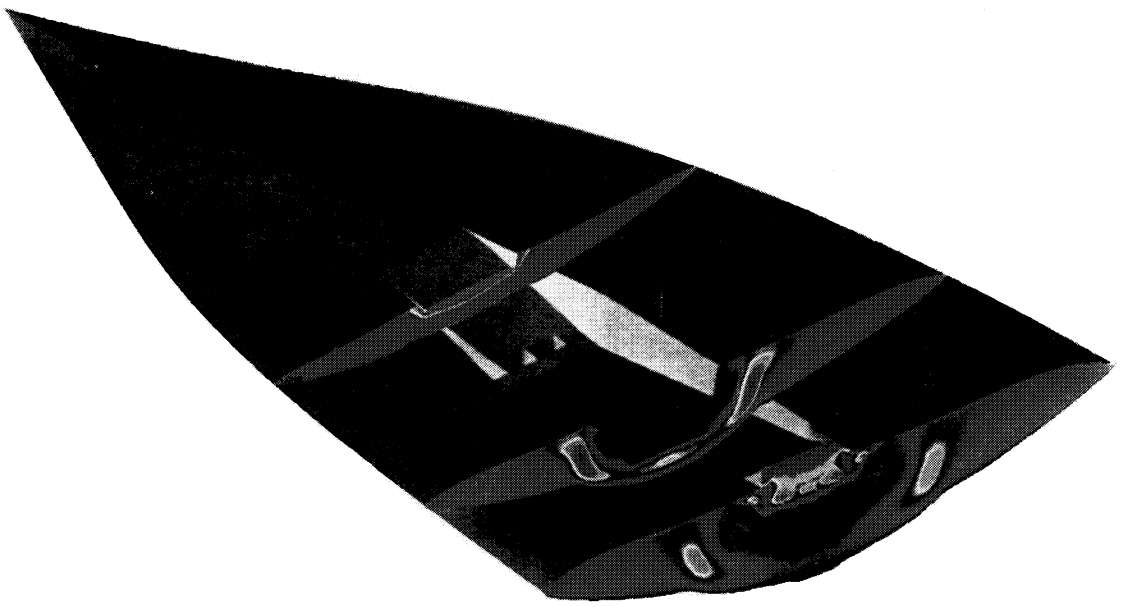

31st Aerospace Sciences Meeting & Exhibit
January 11-14, 1993 / Reno, NV

Analysis of a Hypersonic Waverider Research Vehicle with a Hydrocarbon Scramjet Engine

Gregory A. Molvik*, Jeffrey V. Bowles† and Loc C. Huynh‡
NASA Ames Research Center
Moffett Field, CA

ABSTRACT

The results of a feasibility study of a hypersonic waverider research vehicle with a hydrocarbon scramjet engine are presented. The integrated waverider/scramjet geometry is first optimized with a vehicle synthesis code to produce a maximum product of the lift-to-drag ratio and the cycle specific impulse, hence cruise range. Computational fluid dynamics (CFD) is then employed to provide a nose-to-tail analysis of the system at the on-design conditions. Some differences are noted between the results of the two analysis techniques. A comparison of experimental, engineering analysis and CFD results on a waverider forebody are also included for validation.

INTRODUCTION

Interest in the development of various types of hypersonic vehicles has recently seen a resurgence. There exists an increasing need for hypersonic research vehicles (HRV) to demonstrate integrated aerodynamic, propulsion, and structural technologies for hypervelocity design and to develop a research database for reducing the risk involved in the development of operational hypersonic vehicles. Conceptual design activities are currently under way at NASA Ames Research Center to determine the feasibility of such a research vehicle utilizing near-term technology (Fig. 1). The objective of this research is to define an integrated hypersonic cruise vehicle that demonstrates sustained air-breathing hypersonic propulsion.

The research goals of this activity are to provide an understanding of the underlying physics, verification of design tools, and validation of the technologies and systems needed. The research requirements are classified into two main areas: 1) basic research, and 2) systems technology demonstration, which addresses programmatic research issues and overall vehicle system integration and performance. The disciplinary research requirements include aerodynamics and aero-thermodynamics of hypersonic flight, hypersonic air-breathing propulsion system performance, structures and materials characteristics, and finally instrumentation requirements for hypersonic vehicles.

In order to accomplish these research goals, the mission of the HRV requires sustained cruise at various Mach numbers to address numerous hypersonic research requirements, including vehicle performance, real gas effects, boundary layer transition, shock-boundary layer interaction, turbulence modeling, propulsion integration, and structures / material performance. These requirements lead to the need for a high lift-to-drag ratio (L/D) to achieve the desired test times and to maximize the payload fraction to allow greater degrees of instrumentation. Waverider configurations have received a high degree of interest for their potentially high lift-to-drag ratios and their flow quality at the inlet plane [1]. These characteristics of waveriders are very desirable for cruise missions with integrated engines, hence HRV's. However, the (L/D)max of the propulsion-integrated configuration may be much lower than that of the pure waverider shape.

For the HRV, most of the research requirements dictate a need for a hydrocarbon scramjet and/or ramjet operating between Mach numbers of 6 to 8. For a Mach number range of 4 to 10, hydrocarbon fuels provide sufficient engine specific impulse (Isp) performance, heat sink capability, and offer the potential of reduced vehicle size compared with hydrogen-powered designs. In addition, the handling and infrastructure requirements for the hydrocarbon

* Senior Research Scientist, MCAT Institute, Member AIAA
† Aerospace Engineer, Member AIAA
‡ Aerospace Engineer, Eloret Institute

fuels have a distinct advantage compared to cryogenic hydrogen.

A common factor among all hypersonic vehicles is the need to effectively integrate the propulsion system with the airframe structure to maximize vehicle performance. The design must account for the aerodynamic heating, stability and control, and materials and structures. This poses a significant challenge to the designer of air-breathing aircraft since the problem becomes multidisciplinary.

In this paper, the conceptual design and analysis of an air-breathing, Mach 8, waverider-configured, hypersonic testbed vehicle is performed. A comprehensive vehicle synthesis and design code is first used to define an optimal baseline configuration and CFD methods are then employed to refine the accuracy of the predicted performance. A nose-to-tail analysis is performed for the power-on flight condition at the design Mach number.

CONCEPTUAL DESIGN TOOLS

For the results presented later in this paper, two levels of analysis were performed. They include engineering analysis methods and computational fluid dynamics. The simplified engineering codes have been traditionally used in the conceptual design process to predict representative vehicle performance but have degraded accuracy in regions where the simplified assumptions break down. These regions can be numerous in a complex hypersonic vehicle design with integrated propulsion systems. Further, these simplified methods lack the capability to predict any unforeseen physics associated with a particular design. CFD, on the other hand, can significantly improve the accuracy and detail, but not without penalty. Significant computer resources can be required for a complete CFD analysis of the design. This section of the paper describes both analysis tools used in the overall design process.

Hypersonic Vehicle Synthesis Code

The HAVOC hypersonic vehicle synthesis code [2] can be used to design, analyze and optimize hypersonic waverider configurations with or without an integrated hydrocarbon scramjet. The optimization methodology is that of Ref. 3. The aero/aerothermal and propulsion flow path techniques are briefly discussed below.

The geometric definition of a hypersonic waverider configuration is computed by assuming that the lower surface of the waverider is a stream surface in an axisymmetric shock layer. Inverse design techniques are employed to determine this stream surface from a previously computed shock layer. The upper surface of the waverider is simply defined as the free-stream surface containing the waverider leading edge. The generating surface can be defined in either the free-stream (hence upper vehicle surface), or on the lower vehicle surface at an arbitrary longitudinal location. A sixth-order polynomial is used to describe the surface geometry. Solution of the real-gas Taylor-Macoll equations gives the inviscid flow properties throughout the shock layer. A simplified compressible boundary layer reference enthalpy method [4] is used to compute the local skin friction coefficient, which is used in turn to compute equilibrium radiation surface temperatures. No viscous-inviscid interactions are modeled in this engineering analysis approach. Leading-edge temperatures are computed using a swept-cylinder model [5]. Pressure lift and drag are computed by integration of the pressure coefficient over the surface of the vehicle. Base drag is computed using 70% vacuum pressure coefficient in the vehicle base region.

The simplified, nose-to-tail propulsion model consists of an inviscid, 2-D, real gas, shock/weak-wave flow code coupled to a 1-D subsonic/supersonic combustor analysis code. The shock/weak-wave code solves the inviscid inlet flow field as a function of vehicle forebody/ramp geometry, including cowl position, angle of attack and free stream Mach number. Equivalent 1-D flow properties are then computed at the inlet throat, and the 1-D combustor mass, momentum and energy equations with wall skin friction and heat transfer are solved stepwise through the burner. Combustor efficiency (i.e., heat release schedule as a function of combustor station) is input and was taken from Ref. 6 for the present results. The nozzle flow field is then computed from the combustor exit solution using the real-gas shock/weak-wave 2-D code, including nozzle and cowl flap geometry. First order estimates of axial and normal forces and pitching moment are thus computed as a function of vehicle geometry and flight condition. Overall propulsion system heat loads are then used to determine fuel inlet temperature or to compute required engine cooling equivalence ratio.

CFD Codes

Computational fluid dynamics has and will continue to play an important role in the design and analysis of hypersonic systems. This is because ground based facilities are expensive to operate and in many cases cannot duplicate the exact flight conditions of such vehicles. Simplified methods such as that described above have limitations and cannot predict any unforeseen physics. Although studies have been performed that use CFD to investigate various components of hypersonic vehicles including waverider forebodies [7-9], complete power-on, nose-to-tail studies are scarce in the open literature. However with recent advances in both numerical algorithms and computer technology, such solutions are becoming possible.

Requirements of a numerical algorithm are very demanding for hypersonic, nose-to-tail computations. The algorithm must be capable of predicting the three-dimensional flow of a highly turbulent mixture of reacting gasses with separated regions and strong flow field discontinuities. Multi-equation turbulence models become a requirement to accurately compute the numerous shear layers and boundary layers that are present. Further, upwind algorithms offer an appealing approach to solutions of hypersonic flow fields because of the ability to capture strong flow field discontinuities without user-specified smoothing terms. Finally, a strongly coupled, nonequilibrium chemistry model is required to compute the highly reactive combustion processes within a scramjet engine.

For the present numerical analysis, the TUFF and STUFF codes of Ref. 10 were employed. The TUFF code is a time-marching code. It is generally used to obtain solutions in the subsonic or separated regions of the hypersonic flow field. Large run-times can prohibit the computation of an entire hypersonic flow field with a scheme of this nature. Hence, the second algorithm, STUFF, was developed. It employs a space-marching algorithm that can obtain a solution in relatively little computer time. For the nose-to-tail solution presented later, the STUFF code was employed to obtain nozzle and external solutions. The TUFF code was employed in Ref. 6 to obtain the solution of the current combustor. The combustor results in this paper were computed with the HAVOC code by employing the CFD-predicted heat release schedule of Ref. 6.

The TUFF and STUFF codes offer many of the required features for accurate hypersonic flow field computations. Both codes employ nonequilibrium, equilibrium and perfect gas models. They employ a finite-volume philosophy to ensure that the schemes (including the boundary conditions) are fully conservative. Further, they obtain their upwind inviscid fluxes by employing a Riemann solver that fully accounts for the gas model used. This property allows the flow field discontinuities, such as shocks and shear layers, to be captured without significant amounts of smearing. Total variation diminishing (TVD) techniques are included to allow extension of the schemes to higher orders of accuracy without introducing spurious oscillations. The schemes employ a strong coupling between the fluid dynamic and chemistry equations and are made fully implicit to eliminate the step-size restriction of explicit schemes. A fully conservative zonal scheme [11] has been implemented to allow solutions of geometrically complex problems. Turbulence models include both a zero [12] and two-equation [13] model with a correction for compressibility [14]. Finally, a sublayer approximation [15] is used in the space-marching algorithm to allow stable marching in the presence of a subsonic viscous layer. For the computations with hydrocarbon-air chemistry presented later, the thermodynamic data of Ref. 16 and kinetics data of Ref. 17 were used. These codes have been validated on many classes of hypersonic flows including internal and external flow fields.

For the waverider forebody validation case presented later in this paper, a modification to the viscosity model was required. Because of the very low temperatures experienced in the hypersonic test facilities, Sutherland's law for viscosity is no longer valid. The viscosity model of Ref. 18 was therefore employed in the CFD codes. This model was designed for hypersonic wind tunnel analysis and can be used to temperatures at which condensation begins. Also, base drag was computed assuming a 70% vacuum pressure coefficient, as in the engineering analysis above.

Grid generation was accomplished by employing an interactive surface grid generator, S3D [19], and an interactive volume grid generator, HYPGEN-UI [20], for the external grids. Cross-section geometry obtained from the engineering analysis was directly used in the surface grid generation process. For the internal engine grid generation, an algebraic solver was employed.

The combination of these grid generation techniques proved to be quite effective in this current analysis.

RESULTS

Two sets of results are included in this paper: a pure waverider forebody test case and an integrated waverider/scramjet result. The first test case serves as a validation case for both the CFD and engineering analysis techniques on waverider geometries. The second case consists of the results of a conceptual design and analysis of a hypersonic waverider research vehicle with a hydrocarbon scramjet engine.

Waverider Forebody Result

The first set of results presented here are for a pure waverider forebody at on-design conditions. The geometry and flow conditions are those defined by Reuss[21] at Ohio State University (OSU). In Ref. 21 a viscous-optimized waverider design was developed and tested. The MAXWARP code [22] was employed to generate a conical waverider geometry with a maximum lift-to-drag ratio at the OSU supersonic tunnel conditions. For this analysis, the free stream properties were those of the OSU supersonic facility and the geometry was restricted to a conical shock waverider resulting from a 12 degree cone. The freestream properties are listed in Table 1. The optimization procedure accounted for both pressure and viscous forces including base drag. Throughout the optimization procedure, the coupling between the boundary layer and inviscid flow field was neglected. For this reason, the boundary layer displacement thickness was removed from the experimental model on both the upper and lower surfaces. The resulting waverider model was then installed in the OSU supersonic facility to provide surface pressure measurements only. The experimental model is 0.1651 meters in length and is shown in Fig. 2.

Property	Value
Mach	8.00
Reynolds No.	1140000/m
U_∞	1227 m/s
ρ_∞	.00377 kg/m^3
T_∞	58.6 K
Gas	Air

Table 1. OSU tunnel operating conditions.

The HAVOC code and both the TUFF and STUFF CFD codes were used to obtain flow field solutions of the OSU waverider at on-design conditions. The HAVOC results were obtained on the unaltered geometry since the effect of boundary layer displacement is neglected as in the MAXWARP code. However, the modified geometry was used in the CFD analysis since there is a direct coupling of the inviscid and viscous phenomena in a full numerical analysis.

As mentioned earlier, the S3D and HYPGEN-UI codes were used for the grid generation procedure for the CFD results. Grid points were clustered near the leading edge of the waverider since high gradients can exist in that region. The grid spacing at the surface was set to 7.6×10^{-6}m. The outer boundary of the grid was placed well beyond the upper and lower bow shocks to a distance of 0.076m from the body. The surface grid and volume grid are shown in Fig. 3. The space-marching code, STUFF, was then used to obtain a solution about the entire geometry. This was possible since the nose was pointed allowing the Mach number in the marching direction to remain supersonic. This condition is required for stable marching. TUFF results were also obtained for comparison. Because the test time of the experiment was on the order of a minute, adiabatic boundary conditions were used in the CFD analyses. A perfect gas was assumed for these computations.

Density contours of the CFD results at the last axial cross-section are shown in Fig. 4. This figure clearly shows the bow shock and boundary layer that are present in both the upper and lower flow fields. The boundary layers on both the top and bottom of the waverider are quite thick and comprise nearly one-third of the shock-layers. The effect of the relatively thick boundary layers on the inviscid flow field becomes apparent with the slightly detached shock wave from the waverider leading edge. Further, the inviscid portion of the flow field no longer exhibits a conical nature because of the influence of the boundary layer.

The pressure contours at 95% of the body length are shown in Fig. 5 for all of the analysis techniques and the OSU experiment. All of the analysis results agree quite well at on-design conditions including TUFF and STUFF and engineering analysis. A grid refinement analysis was also performed to determine any grid dependency and very little was observed. The experimental results, on the other hand, show a 14 percent higher pressure on the waverider

forebody than any of the analysis results. Comparison of STUFF results at a one-degree angle of attack agree much better with experiment. This seems to point to an uncertainty in the experimental angle of attack. For the experimental results presented here, a one-degree error in the experimental angle of attack was possible and falls within the experimental uncertainty range [21]. Further experiments are planned to resolve this discrepancy.

Figure 5 also shows the enhanced ability of the CFD techniques to predict viscous, waverider forebody flow fields. This is apparent in the large pressure rise predicted at the waverider leading edge by the CFD techniques. This pressure rise is caused by compression waves emanating from the rapidly growing boundary layer in the vicinity of the leading edge. This effect is entirely neglected in the engineering code results since no coupling is allowed between the viscous and inviscid analysis. This effect, however, is also present in the experimental results.

	MAXWARP	HAVOC	STUFF
C_L	0.0870	0.0885	0.0844
C_D	0.0241	0.0257	0.0313
L/D	3.62	3.45	2.69

Table 2. Comparison of predicted aerodynamic coefficients.

Table 2 shows the predicted aerodynamic coefficients of both engineering codes and of the CFD analysis. Since only very little difference was observed between the TUFF and STUFF aerodynamic coefficients, only the STUFF results are included in this table. All of the predicted lift coefficients agree quite well even though the leading edge pressure rise was present in the CFD results. The increased lift caused by the pressure rise on the lower surface is counteracted by a similar pressure rise on the upper surface in the CFD results. The drag coefficient predicted by the CFD analysis however is slightly larger. This is simply explained by increased pressure drag on the forebody resulting from the boundary layer displacement especially at the leading edge.

Hypersonic Waverider Research Vehicle Design and Analysis

Design Optimization

As opposed to accelerator-type missions (e.g., SSTO) where the mass capture characteristics of the vehicle are most important, cruise configurations place an emphasis on the aerodynamic performance of the design. Hence vehicle lift-to-drag ratio (L/D) or the product of L/D and engine Isp (a parameter proportional to Brequet range factor) becomes more important. A waverider configuration, with high hypersonic L/D potential, was selected as the baseline configuration for the present study of the HRV. The configuration/engine installation was numerically optimized to maximize (L/D) x Isp, using forebody shape, ramp angles and cowl position as optimization parameters. For this analysis, the forebody is a Mach 8 waverider configuration and the ramp angles and cowl position were designed to produce first and second ramp shock-on-lip and cowl shock-on-shoulder. The engine geometry and operating parameters were held fixed in the optimization procedure. The numerical optimization was performed using the HAVOC cycle code.

The design parameters and constraint functions used for optimization are listed below. There were 15 design parameters used in the optimization process. Six parameters defined the waverider generating surface (hence the vehicle shape); eight parameters defined the ramps, cowl, nozzle geometries, and leading-edge radius; the last design parameter was free stream dynamic pressure. Eight constraints were used in the optimization process, including engine throttle greater than or equal to the required cooling equivalence ratio, leading edge equilibrium radiation temperature limited to 3200°F, wing tip closure angle limited to 10 degrees, and the vehicle structural thickness limit at vehicle aft end, accounting for nozzle integration. The volume was constrained to 1.7% of vehicle length cubed. Finally, the vehicle width to length ratio was less than or equal to 0.75.

For the Mach 8 design, a generating shock angle of 12 degrees was arbitrarily selected. The waverider shape optimization process involved planform shape changes to sweep the leading edge in order to alleviate high heating rates at the higher free stream dynamic pressures, traded off against leading edge radius and associated leading edge bluntness drag. The design

optimization process of the inlet (ramp positions and ramp angles) resulted in the two ramp shocks converging on the cowl lip (shock-on-lip) then reflected to the shoulder of the combustor entrance (shock-on-shoulder). The geometric contraction ratio was approximately 14, with a resulting pressure at the combustor inlet of about one atmosphere. Preliminary performance estimates indicated a required vehicle length of 23 ft, with an overall vehicle body density of 20 lbs/ft**3. A lift-to-drag ratio of 4.3 was achieved, with a cowl-to-tail Isp of 746 seconds at an assumed combustor efficiency of 95% and at an equivalence ratio of 1.0, with a free stream dynamic pressure of 900 psf, resulting in an initial cruise altitude of 92,500 ft. An engine width of roughly 0.762m. produced a net thrust that is equal to the net drag of the vehicle at the design point. For the results presented below, the engine combustion efficiency of 55% was taken from Ref. 6

Scramjet Engine Concept

The slow reaction rates of a hydrocarbon/air mixture in a supersonic stream can have a significant impact on the inlet/combustor design. Because of the size limitation of an engine on a small research vehicle, a mechanism is required to provide sufficient fuel/air temperatures for burning within the combustor. The design concept of Ref. 6 is employed here and uses a liquid oxygen (LOX) augmented pre-burner located upstream of the main fuel injectors to promote burning in the combustor. Because the LOX would be stored onboard the research vehicle, the required pre-burning should be kept to a minimum to reduce the impact on the vehicle design and gross weight. For the relatively-short hypersonic research mission cruise times (5 to 10 minutes), this additional on-board mass should not have a significant impact on the HRV design.

Preliminary HAVOC design results at a Mach number of 8 for the waverider HRV indicated that the air throat temperature was 833°K. Given that the spontaneous ignition temperature of an ethylene/oxygen mixture is roughly 780°K[23], a guideline of 1000°K was used as the design temperature at the mainburner station to insure that combustion was indeed present. The required preburner fuel flow and preburner O/F ratio were then computed. To achieve the design temperature at the main fuel injector station, approximately 2.5% of the overall stoichiometric engine fuel flow with a preburner O/F ratio of 1.71 (twice preburner stoichiometric) is required. The CFD results of Ref. 6 confirmed that burning was present at the main burner station under these conditions. A heat balance on the vehicle and engine was used to compute the fuel total temperature at injection. Detailed engine operating conditions and geometry are presented in Ref. 6.

Nose-to-Tail Analysis

Nose-to-tail analyses utilizing both CFD and cycle codes were performed. The geometries for both analyses, however, were somewhat different. The ramp sidewalls in the cycle analysis were assumed to have zero thickness and were aligned with the forebody flow. They therefore resulted in zero pressure drag with only a nominal addition to the viscous drag. The CFD geometry, on the other hand, contained ramp sidewalls with an included angle of 21 deg. Because the sidewall attaches to the cowl lip and because the cowl protruded far below the lower surface of the waverider, the sidewall contained a significant amount of additional volume. This added volume was exposed to the forebody flow and produced additional drag to the vehicle.

The grid generation for the CFD nose-to-tail analysis is described below. The grid generation tools used for the external grids are the S3D and HYPGEN-UI codes mentioned previously. The external portion was divided into three axial sections: nose-to-inlet, inlet-to-exit, and exit-to-end sections. Grid generation was performed separately on each of these portions. For the surface grid, points were clustered on the waverider leading edge, on the sidewall leading edge and on all of the other convex corners of the vehicle. The lower surface grid is shown in Fig. 6. The outer boundary of the volume grid was placed well beyond the anticipated bow shock to a distance of roughly three meters from the vehicle surface. The spacing of the first point from the surface was set to 1.0×10^{-5}m. The grid dimensions for the three external grids measured 102x70x144, 60x70x129 and 12x70x130 from nose to tail. The values of these dimensions correspond to the number of grid points in the streamwise direction, circumferential direction, and radial direction.

For the internal grids, the engine was divided into three separate flow paths starting at the inlet face. These flow paths then merged at the internal nozzle entrance. An algebraic grid generation routine was used to generate all of the interior grids. The internal grids measured 7x79x50 for the inboard engine, 7x79x99 for the

outboard engines and 3x79x79 for the internal nozzle section. The number of grid points in the streamwise direction is small since the space-marching scheme interpolates for additional grid planes as they are needed.

The space-marching scheme, STUFF, was employed to obtain the nozzle and external CFD results for the waverider HRV. A space-marching solution is possible if the flow field is void of streamwise subsonic and separated areas. The space-marching solution began at the nose of the vehicle by setting the dependent variables in all of the cells to be freestream. The solution progressed by marching downstream through each of the grids until the aft end of the vehicle was reached. A fully conservative patching scheme [11] was employed to transfer the solution from one grid to the next. The frozen chemistry option was employed for the CFD results including the nozzle portion. This was sufficient since combustion is slowed considerably at the combustor exit [6].

For the nose-to-tail results presented here, the HAVOC cycle code was used to provide the solution within the inlets and combustor. This was done to avoid the computational expense of obtaining time-marching solutions of both the outboard and inboard engines with 48 fuel injection ports in each. A time-marching solution is required in portions of the engine because the presence of axially-subsonic and axially-separated regions prohibits space-marching. The CFD forebody results were averaged at the inlet face to provide one-dimensional inlet conditions for the cycle code. The presence of an oblique cowl shock was accounted for and provided the mechanism to turn the flow parallel to the engine cowl. The CFD-predicted heat release schedule of Ref. 6 was used in the one-dimensional cycle analysis of the combustor. CFD then picked up again at the exit of the combustor.

The two-dimensional, shock/weak wave results of the HAVOC analysis are plotted in Fig. 7. This figure shows the shock, contact surface, and expansion wave arrangement for the current integrated design on the vehicle symmetry plane. The intent of the forebody/ ramp design is clearly shown in this figure. Both of the ramp shocks impinge on the cowl leading edge and the cowl shock impinges on the shoulder. The bow shock, however, lies outside of the inlet. This is because at Mach 8, with a fixed throat height, having the bow shock on the cowl lip can produce shock-on-ramp with possible boundary layer separation and engine unstart. The nozzle geometry was restricted to two planar sections and the corresponding expansion and shock are shown in Fig. 7.

Figure 8 is a plot of the surface pressure on the keel line of the vehicle. Both the CFD and cycle results are plotted. Agreement is excellent except in the vicinity of inviscid/viscous interactions. Comparison of the pressure on the waverider forebody are within 2 percent except at the leading edge where CFD predicts a pressure spike resulting from boundary layer displacement. The ramp pressures also agree quite well except for the asymptotic behavior of the CFD results that is typical of shock/boundary layer interactions. Other reasons for this slight discrepancy are three-dimensional effects. One such effect is encountered as the planar ramp emerges from the curved waverider forebody. The intersection line bends downstream from the vehicle symmetry plane. This three-dimensional effect reduces the pressure near the intersection region. Figure 8 also shows very good agreement on the outer surface of the cowl and on the nozzle surface. Comparison of surface pressure on the upper surface showed that the CFD predicted pressures were 3-10% higher than the engineering predictions. This is also explained by viscous/inviscid interactions.

The pressure contours in Fig. 9 show the shock and expansion waves that are predicted with CFD. The location and strength of these waves are in very good agreement with those predicted by the cycle code (Fig. 7). The CFD results, however, predict that the ramp shocks lie slightly outside of the inlet instead of on the cowl lip. This difference is attributed to shock/boundary layer interactions and to three-dimensional effects. The boundary layers on the upper and lower surface are visible in the density contours of Fig. 10.

Figures 11 and 12 show the CFD predicted pressure and density contours, respectively, on crossflow planes at various axial stations. These stations correspond to the following locations: a) beginning of the second ramp, b) at the inlet, c) at the middle of the cowl, d) at the engine exit and e) at the vehicle end. The two ramp shocks are visible in the pressure contours of Fig. 11a and clearly exhibit a 3-dimensional behavior. The bow shock is attached to the leading edge of the waverider and produces a very clean flow field on the forebody absent of the ramp geometry.

Figures 11b and 12b show that the flow into the inlet is fairly clean except for a weak shock that emanates from the ramp sidewall and interacts with the forebody boundary layer. Also evident in Fig. 12b is a thickening of the ramp boundary layer thickness nearer the ramp sidewall. This is caused by the tendency of the flow to spill off of the first ramp resulting in a sideways velocity component. This effect washes the boundary layer away from the symmetry plane of the vehicle. It is then stopped before the inlet station by the sidewalls on the second ramp. Another feature that should be noted in Figs. 11b and 12b is the shock emanating from the outer surface of the ramp sidewall. This feature is absent in the cycle analysis since the sidewalls were assumed to have zero thickness. The resulting high pressure region adds considerably to the net drag of the vehicle since the outer sidewall has an area component in the streamwise direction. This effect resulted in a negative net-thrust predicted by the nose-to-tail analysis. This therefore leads to a need to reduce the thickness of the sidewalls. The pressure and density contours on the external portion of the engine at the midpoint of the cowl are plotted in Figs 11c and 12c. The ramp shocks have clearly merged with the bow shock at this point and an expansion fan emanating from the lower surface of the cowl is evident.

Figures 11(d-e) and 12(d-e) depict the CFD predicted flow field on the aft portion of the vehicle. This flow field region is very complex due to the presence of the engine, although a significant portion of the waverider flow field remains unaffected. The bow shock remained attached to the leading edge for the entire length of the vehicle. This feature is desirable since any spillage of the high pressure gasses onto the upper surface would reduce the performance of the vehicle. Two flow field features that are clearly visible in the nozzle portion of the flow are the initial nozzle expansion and the shock caused by the second nozzle plane. These features appear to be nearly two-dimensional, leading to the good agreement with the cycle analysis (Fig. 8).

Figure 13 shows the pressure contours on the lower surface of the vehicle. The impact on the surface pressure by the presence of the integrated scramjet is visible in this figure. The lower surface is comprised of a large region of undisturbed flow with a fairly constant pressure. The remaining surface is exposed to the numerous shocks and expansion fans that originate from the integrated propulsion system. These include the ramp shocks, the sidewall shocks, the exterior cowl expansions, the engine shroud expansion, and the numerous nozzle waves.

Of particular interest in the current design is the forebody ramp system and the resulting flow field. Due to the curvature of the waverider forebody, an oblique intersection results between it and the first ramp. This intersection is visible in the pressure contours of Fig. 13. The strong pressure gradients that are present in this vicinity cause the flow to be diverted away from the vehicle symmetry plane beginning at the origin of the first ramp. This effect tends to reduce the amount of mass provided to the inlet. An intersection that is less oblique would reduce the spillage since the pressure gradient would be aligned more with the flow direction. This can be accomplished by reducing the curvature of the waverider forebody at the symmetry plane. In the current design, this spillage was effectively halted at the second ramp by using sidewalls. This is shown in the surface streamlines of Fig. 14.

CONCLUSIONS

Two methods were demonstrated for the conceptual design and analysis of a hypersonic waverider research vehicle: an engineering analysis code with a simplified nose-to-tail flow field analysis capability and a complete 3-D CFD code with a hydrocarbon/air capability. The methods have been shown to agree well for waverider forebodies except in the vicinity of the leading edge where CFD exhibits a superior capability to predict the strong viscous/inviscid interaction. Comparison with the OSU waverider experimental results were inconclusive since the angle of attack of the experiment was questionable. The coupling of the cycle code with CFD to compute a single flow field was also demonstrated. Even though the cycle code has a significantly degraded ability to predict detail, this coupling proved to be useful because of the reduced computer resources required.

The nose-to-tail analysis of the waverider HRV clearly showed benefits of the current design and also revealed areas for improvement. The waverider forebody combined with the current ramp system provided a uniform flow to the inlet of the scramjet. Further, the forebody shock remained attached to the leading edge for the entire length of the vehicle. This avoided spillage of the high pressure air onto the upper surface which could significantly reduce lift. The

analysis also showed that the ramp sidewalls need to be thinner since they protrude far into the forebody flow field and cause unnecessary drag to the vehicle.

FUTURE RESEARCH

Future research includes addressing the issues found in the analysis of the HRV design. These include the engine performance, nozzle performance, side-wall drag and inlet efficiency. Further studies also include structural analysis/weight estimation, power-on/power-off stability and control analysis and off-design performance studies.

ACKNOWLEDGMENTS

This work was partially supported by NASA Ames Research Center under grants NCC2-498 and NCC2-746. The authors would like to acknowledge Dr. Hirokazu Miura at NASA Ames Research Center for providing a waverider model deformation analysis and Mr. Thomas Whitaker of Sterling Software for graphics and technical support.

REFERENCES

[1] O'Neill, M. K., and Lewis, M. J., "Optimized Scramjet Integration on a Waverider," AIAA Paper 91-1693, June 1991.

[2] Bowles, J. V. Conceptual Studies Activities. Proceedings of the Second National Aerospace Plane Symposium. Applied Physics Laboratory, Laurel, MD, Nov. 1986.

[3] Vanderplaats, G. N. and Hansen, S. R.,"DOC Users Manual", Version 1.00, VMA Engineering, Goleta, CA, 1989.

[4] Schlichting, H., "Boundary-Layer Theory", Seventh Edition, McGraw-Hill Book Co., New York, 1979.

[5] Anderson, J. D., "Hypersonic and High Temperature Gas Dynamics," First Edition, McGraw-Hill Book Co., New York, 1989.

[6] Molvik, G. A., Bowles, J.V. and Huynh, L. C., "Analysis of a Hydrocarbon Scramjet with Augmented Preburning," AIAA Paper 92-3425, July, 1992.

[7] Jones, K. D., "Application of a Supersonic Full Potential Method for Analysis of Waverider Configurations," NASA TP-2608, 1986.

[8] Takashima, N., and Lewis, M. J., "Navier Stokes Computation of a Viscous Optimized Waverider," AIAA Paper 92-0305, Jan. 1992.

[9] Jones, K. D., Bauer, S. X. S., and Dougherty, F. C., "Hypersonic Waverider Analysis: A Comparison of Numerical and Experimental Results," AIAA Paper 91-1696, June 1991.

[10] Molvik, G. A. and Merkle, C. L., "A Set of Strongly- Coupled Upwind Algorithms for Computing Flows in Chemical Nonequilibrium," AIAA Paper 89-0199. Jan. 1989.

[11] Klopfer, G. H. and Molvik G. A., "Conservative Multizonal Interface Algorithm for the 3-D Navier-Stokes Equations," AIAA Paper 91-1601, June 1991.

[12] Baldwin, B. S. and Lomax, H., "Thin Layer Approximation and Algebraic Model for Separated Turbulent Flows." AIAA Paper 78-257, Jan. 1978.

[13] Jones, W. P. and Launder, B. E., "The Prediction of Laminarization with a Two-Equation Model of Turbulence," *International Journal of Heat and Mass Transfer*, Vol. 15, 1972, pp. 303-314.

[14] Zeman, O., "Compressible Turbulence Subjected to Shear and Rapid Compression," Eighth Symposium on Turbulent Shear Flows, Munich, Germany, Sept, 1991.

[15] Vigneron, Y. C., Rakich, J. C. and Tannehill, J. C., "Calculation of supersonic Viscous Flow over Delta Wings with Sharp Subsonic Leading Edges," AIAA Paper 78-1137, July 1978.

[16] Gordon, S. and McBride, B. J., "Computer Program for Calculation of Complex Chemical Equilibrium Compositions, Rocket Performance, Incident and Reflected Shocks, and Chapman-Jouguet Detonations," NASA SP-273, 1976.

[17] Westbrook, C. K. and Dryer, F. L., "Simplified Reaction Mechanisms for the

Oxidation of Hydrocarbon Fuels in Flames,", *Combustion Science and Technology*, Vol. 27, 1981, pp. 31-43.

[18] Reinecke, W. G., "Charts for Use with Hypersonic Air Wind Tunnels," Aerospace Research Laboratories Report, ARL 64-56, April, 1964.

[19] Luh, R. C., Pierce, L. E., Yip, D., "Interactive Surface Grid Generation," AIAA Paper 91-0796, Jan. 1991.

[20] Chan, W. M. and Steger, J. L., "Enhancements of a Three-Dimensional Hyperbolic Grid Generation Scheme," *Applied Mathematics and Computation*, Vol 51, pp. 181-205, 1992.

[21] Reuss, R. L., "Experimental Study of Hypersonic Waveriders," Masters Thesis, Ohio State University, 1993.

[22] Corda, S., and Anderson, J. D. Jr., "Viscous Optimized Hypersonic Waveriders Designed from Axisymmetric Flow Fields," AIAA Paper 88-0369, Jan. 1988.

[23] Barnett, H. C. and Hibbard, R. R., "Basic Considerations in the Combustion of Hydrocarbon Fuels with Air," NACA Report 1300, 1959.

FIGURES

Fig. 1 Hypersonic vehicle concept with an integrated hydrocarbon scramjet engine.

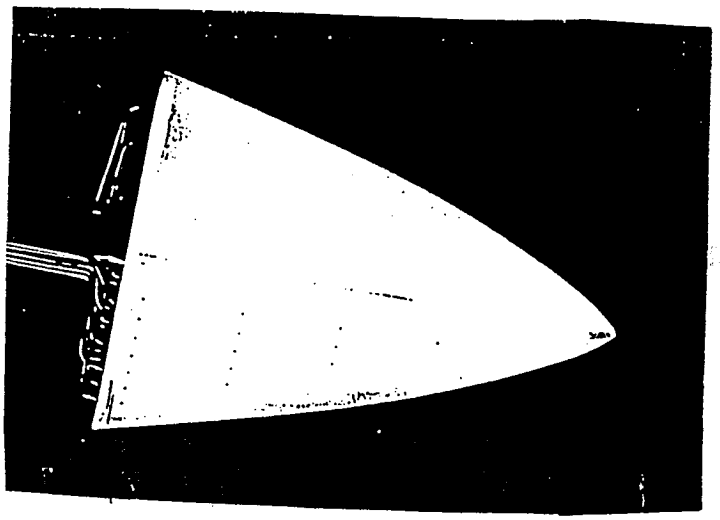

Fig. 2 OSU waverider model.

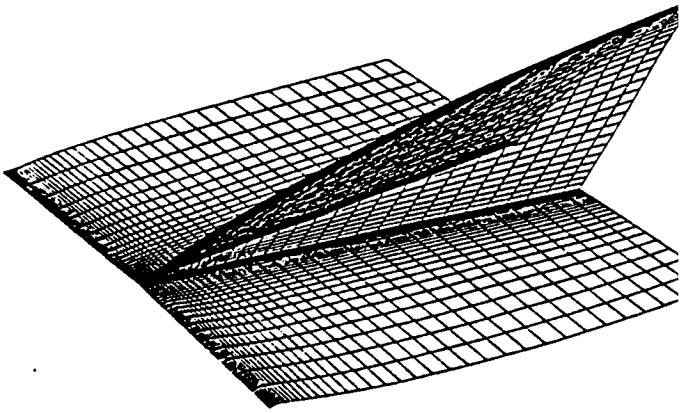

Fig. 3 Grid used for the CFD analysis of the OSU waverider.

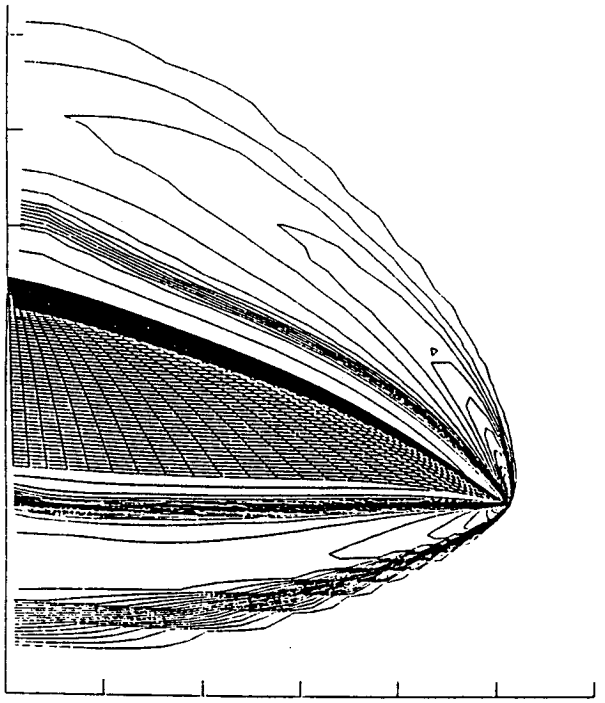

Fig. 4 CFD predicted density contours at the aft end of the OSU waverider.

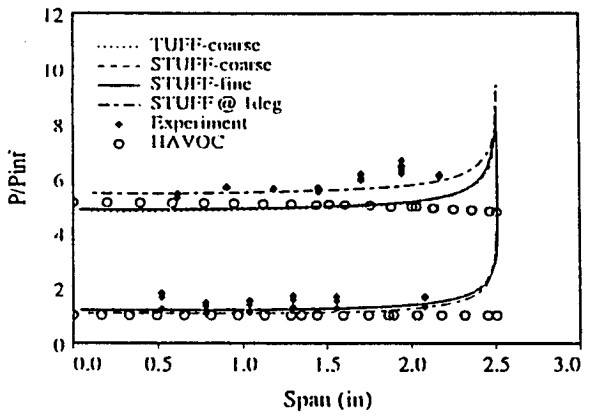

Fig. 5 Pressure comparison at x=0.156845m

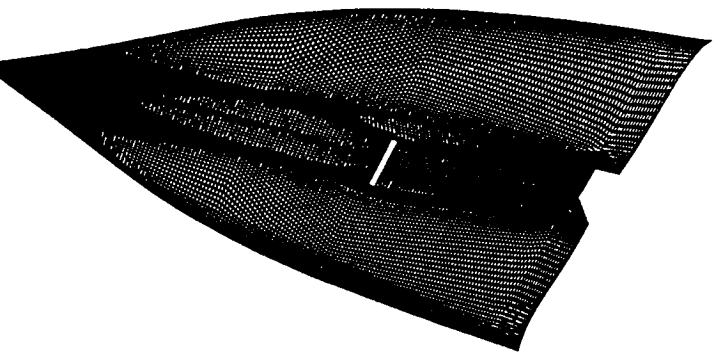

Fig. 6 Lower surface grid for the current waverider HRV design.

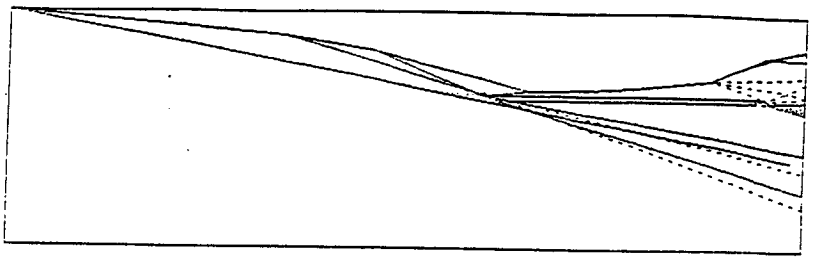

Fig. 7 HAVOC predicted flow field on the lower symmetry plane.

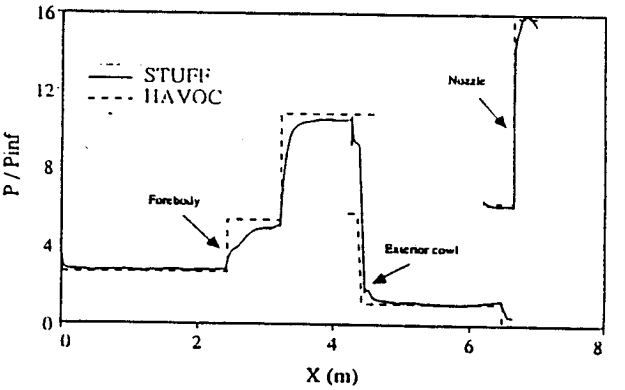

Fig. 8 Keel line pressure comparison.

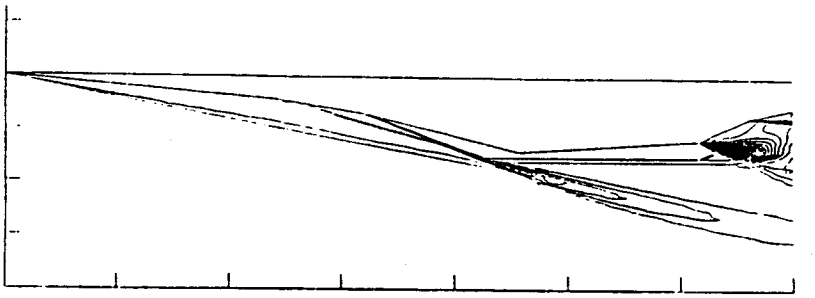

Fig. 9 CFD predicted pressure contours on vehicle symmetry plane.

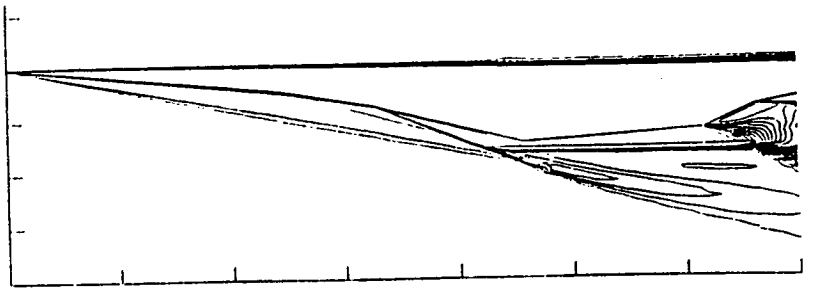

Fig. 10 CFD predicted density contours on vehicle symmetry plane.

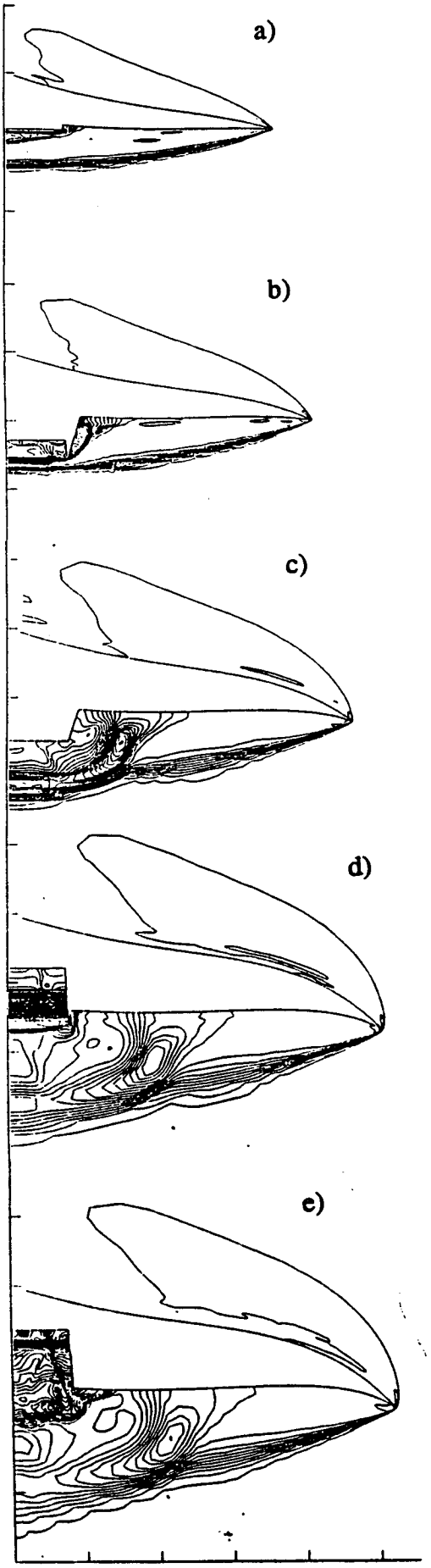

Fig. 11 CFD predicted pressure contours at various axial locations.

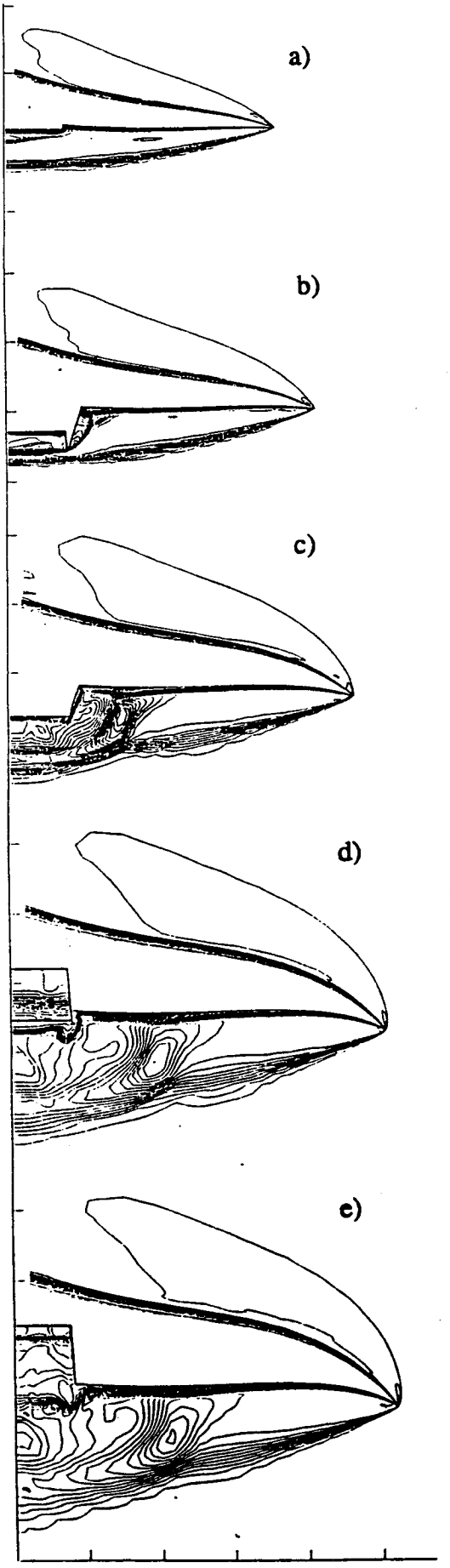

Fig. 12 CFD predicted density contours at various axial locations.

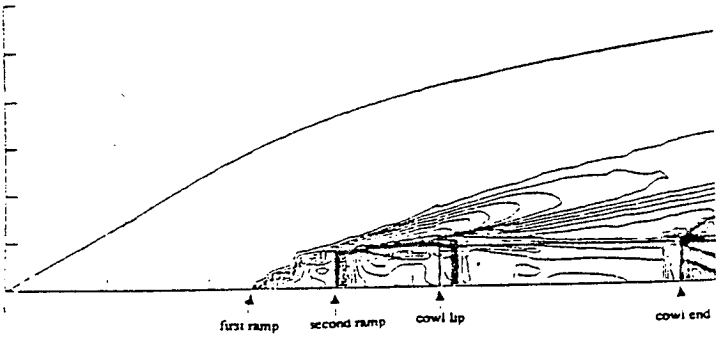

Fig. 13 CFD predicted surface pressure plot.

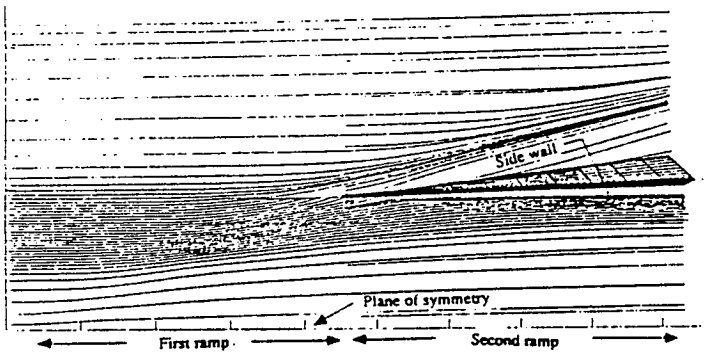

Fig. 14 CFD predicted surface streamlines on the forebody ramp system.

AIAA-93-5097

A Hypersonic Research Vehicle with Hydrocarbon Scramjet Propulsion: Design and Analysis

Gregory A. Molvik, Jeffrey V. Bowles and Loc C. Huynh
NASA Ames Research Center,
Moffett Field, California USA

AIAA/DGLR Fifth International Aerospace Planes and Hypersonics Technologies Conference
November 30 - December 3, 1993
Munich, Germany

A Hypersonic Waverider Research Vehicle with Hydrocarbon Scramjet Propulsion: Design and Analysis

Gregory A. Molvik*, Jeffrey V. Bowles† and Loc C. Huynh‡
NASA Ames Research Center
Moffett Field, CA

ABSTRACT

The results of a feasibility study of a hypersonic waverider research vehicle with a hydrocarbon scramjet engine are presented. The scramjet engine concept consists of a preburner into which a small amount of fuel is burned with on-board liquid oxygen and injected into the airflow, upstream of the main fuel injector locations, thus ensuring that main fuel combustion is present and uninterrupted. The integrated waverider/scramjet geometry is optimized with a vehicle synthesis code to produce a maximum product of the lift-to-drag ratio and the cycle specific impulse, hence cruise range. Computational fluid dynamics is employed to provide engine performance and a nose-to-tail analysis of the vehicle at the on-design conditions. Comparisons are made between the results of the two analysis techniques and some differences are noted.

INTRODUCTION

Interest in the development of various types of hypersonic vehicles has recently seen a resurgence. There exists an increasing need for hypersonic research vehicles (HRV) to demonstrate integrated aerodynamic, propulsion, and structural technologies for hypervelocity design and to develop a research database for reducing the risk involved in the development of operational hypersonic vehicles. Conceptual design activities are currently under way at NASA Ames Research Center to determine the feasibility of such a research vehicle utilizing near-term technology (Fig. 1). The objective of this research is to define an integrated hypersonic cruise vehicle that demonstrates sustained air-breathing hypersonic propulsion.

The research goals of this activity are to provide an understanding of the underlying physics, verification of design tools, and validation of the technologies and systems needed. The research requirements are classified into two main areas: 1) basic research, and 2) systems technology demonstration, which addresses programmatic research issues and overall vehicle system integration and performance. The disciplinary research requirements include aerodynamics and aero-thermodynamics of hypersonic flight, hypersonic air-breathing propulsion system performance, structures and materials characteristics, and finally instrumentation requirements for hypersonic vehicles.

In order to accomplish these research goals, the mission of the HRV requires sustained cruise at various Mach numbers to address numerous hypersonic research requirements, including vehicle performance, real gas effects, boundary layer transition, shock-boundary layer interaction, turbulence modeling, propulsion integration, and structures/material performance. These requirements lead to the need for a high lift-to-drag ratio (L/D) to achieve the desired test times and to maximize the payload fraction to allow greater degrees of instrumentation. Waverider configurations have received a high degree of interest for their potentially high lift-to-drag ratios and their flow quality at the inlet plane [1]. These characteristics of waveriders are very desirable for cruise missions with integrated engines, hence HRV's. However, the $(L/D)_{max}$ of the propulsion-integrated configuration may be much lower than that of the pure waverider shape.

For the HRV, most of the research requirements dictate a need for a hydrocarbon scramjet and/or ramjet operating between Mach numbers of 6 to 8. For a Mach number range of 4 to 10, hydrocarbon fuels provide sufficient engine specific impulse (Isp) performance, heat sink capability, and offer the potential of reduced vehicle size compared with hydrogen-powered designs. In addition, the handling and infrastructure requirements for the hydrocarbon

---

* Senior Research Scientist, MCAT Institute, Member AIAA
† Aerospace Engineer, Member AIAA
‡ Aerospace Engineer, Eloret Institute

fuels have a distinct advantage compared to cryogenic hydrogen.

The slow reaction rates of a hydrocarbon/air mixture in a supersonic stream can have a significant impact on the inlet/combustor design. Because of the size limitation of an engine on a small research vehicle, a mechanism is required to provide sufficient fuel/air temperatures for burning within the combustor. The concept of employing an in-stream, embedded ramjet as a pilot light has been proposed [2-3] and appears to be a promising technique for maintaining combustion. An alternative is to use a liquid oxygen (LOX) augmented pre-burner located upstream of the main fuel injectors to promote burning in the combustor. Because the LOX would be stored onboard the research vehicle, the required pre-burning should be kept to a minimum to reduce the impact on the vehicle design and gross weight. For the relatively short hypersonic research mission cruise times (5 to 10 minutes), the impact of this additional onboard mass will not have a significant impact on the HRV design.

A common factor among all hypersonic vehicles is the need to effectively integrate the propulsion system with the airframe structure to maximize vehicle performance. The design must account for the aerodynamic heating, stability and control, and materials and structures. This poses a significant challenge to the designer of air-breathing aircraft since the problem becomes multidisciplinary.

In this paper, the conceptual design and analysis of an air-breathing, Mach 8, waverider-configured, hypersonic testbed vehicle is performed. The feasibility of a hydrocarbon scramjet engine utilizing a LOX/preburner concept is first addressed[4] and then a comprehensive vehicle synthesis and design code is used to define an optimal baseline configuration[5]. Computational Fluid Dynamic (CFD) methods were employed throughout the design process to refine the accuracy of the predicted performance. CFD results are included of the current scramjet engine concept and of the integrated vehicle at on design conditions.

CONCEPTUAL DESIGN TOOLS

For the results presented later in this paper, two levels of analysis were performed including: engineering analysis and computational fluid dynamics. Engineering codes have been traditionally used in the conceptual design process to predict representative vehicle performance but have degraded accuracy in regions where simplifying assumptions break down. These regions can be numerous in a complex hypersonic vehicle design with integrated propulsion systems. Further, these simplified methods lack the capability to predict any unforeseen physics associated with a particular design. CFD, on the other hand, can significantly improve the accuracy and detail, but not without penalty. Significant computer resources can be required for a complete CFD analysis of the design. This section of the paper describes both analysis tools used in the present design process.

Hypersonic Vehicle Synthesis Code

The HAVOC hypersonic vehicle synthesis code [6] can be used to design, analyze and optimize a hypersonic waverider configuration including an integrated scramjet engine. The optimization methodology utilized in the HAVOC code is detailed in Ref. 7. The aero/aerothermal and propulsion flow path techniques are briefly discussed below.

The geometric definition of a hypersonic waverider configuration is computed by assuming that the lower surface of the waverider is a stream surface in an axisymmetric shock layer. Inverse design techniques are employed to determine this stream surface from a previously computed shock layer. The upper surface of the waverider is simply defined as the free-stream surface containing the waverider leading edge. The generating surface can be defined in either the free-stream (hence upper vehicle surface), or on the lower vehicle surface at an arbitrary longitudinal location. A sixth-order polynomial is used to describe the surface geometry. Solution of the real-gas Taylor-Macoll equations give the inviscid flow properties throughout the shock layer. A simplified compressible boundary layer reference enthalpy method [8] is used to compute the local skin friction coefficient, which is used in turn to compute equilibrium radiation surface temperatures. No viscous-inviscid interactions are modeled in this engineering analysis approach. Leading-edge temperatures are computed using a swept-cylinder model [9]. Pressure lift and drag are computed by integration of the pressure coefficient over the surface of the vehicle. Base drag is computed using 70% vacuum pressure coefficient in the vehicle base region.

The simplified, nose-to-tail propulsion model consists of an inviscid, 2-D, real gas, shock/weak-wave flow code coupled to a 1-D subsonic/supersonic combustor analysis code. The shock/weak-wave code solves the inviscid inlet flow field as a function of vehicle forebody/ramp geometry, including cowl position, angle of attack and free stream Mach number. Equivalent 1-D flow properties are then computed at the inlet throat, and the 1-D combustor mass, momentum and energy equations with wall skin friction and heat transfer are solved stepwise through the burner. Combustor efficiency (i.e., heat release schedule as a function of combustor station) was taken from the engine CFD results for the present analysis. The nozzle flow field is then computed from the combustor exit solution using the real-gas shock/weak-wave 2-D code, including nozzle and cowl flap geometry. First order estimates of axial and normal forces and pitching moment are thus computed as a function of vehicle geometry and flight condition. Overall propulsion system heat loads are then used to determine fuel inlet temperature or to compute required engine cooling equivalence ratio.

CFD Codes

For the present numerical analysis, the TUFF and STUFF codes of Ref. 10 were used since they offer many of the features required for accurate hypersonic flow field computations including upwind fluxes and fully coupled chemistry. The TUFF code is a time-marching code. It is generally used to obtain solutions in the subsonic or separated regions of the hypersonic flow field. The STUFF code employs a space-marching algorithm that can obtain a solution in relatively little computer time. For the results presented later, the STUFF code was employed to obtain nozzle and external solutions. The TUFF code was used to obtain the solution within the combustor.

Simplified reaction mechanisms for the hydrocarbon combustion process offer an appealing alternative to exhaustive computations with large chemistry systems. In this approach, various species and reactions are combined and simplified while preserving the net effect of the reaction processes. Since kinetic details are not required in the present study, a simplified reaction mechanism was sufficient. For the scramjet propulsion system analysis, the two-step reaction mechanism of Westbrook and Dryer [11] was employed to address the combustion of fuel with air. For hydrocarbon scramjet propulsion, the liquid fuel can be used as a coolant on various portions of the aircraft. This results in an endothermic reaction that can vaporize and dissociate the liquid fuel. Gaseous ethylene was used in this analysis, as a surrogate fuel intended to represent the products of this endothermic reaction. The thermodynamic and transport properties for the individual species in the hydrocarbon/air mixture were obtained from Ref. 12.

Modeling scramjet flow fields with CFD requires an advanced turbulence model capable of accurately accounting for compressible turbulent shear layers and jets. This was accomplished in the present study with the incorporation of the low Reynolds number K-ε turbulence model originally developed by Jones and Launder [13]. The compressibility correction of Zeman [14] was also included in the two-equation formulation to improve the computation of compressible shear layers. The turbulence model was transformed to a generalized finite-volume coordinate system and strongly coupled with the existing flow solver, including the viscous and inviscid flux computation and the source term treatment.

Grid generation was accomplished by employing an interactive surface grid generator, S3D [15], and an interactive volume grid generator, HYPGEN-UI [16], for the external grids. Cross-section details determined by the HAVOC code were used in the surface grid generation process. For the internal engine grid generation, an algebraic solver was employed. The combination of these grid generation techniques proved to be quite effective and timely.

RESULTS

Two sets of results are included in this paper. The first set of results addresses the design and performance of a single hydrocarbon scramjet utilizing an augmented preburner upstream of the main fuel injectors. The second set consists of the results of a conceptual design and analysis of a hypersonic waverider research vehicle(HWRV) with a hydrocarbon scramjet engine. The conceptual design of the HWRV relied heavily on the CFD results of the scramjet engine.

Hydrocarbon Scramjet Result

The initial geometric definition for the scramjet engine, including throat height, shock isolator length, and combustor length, and combustor

area ratio was taken from Ref. 3. The embedded ramjet section was removed and a hydrocarbon/LOX preburner was added. A mixing section aft of the preburner station was also added to allow mixing of the preburner exhaust gasses with the oncoming air so as not to suffocate the main burner jets of oxygen. A schematic showing the scramjet concept is presented in Fig. 2.

Preliminary HAVOC design results at a Mach number of 8 and a dynamic pressure of 1500psf for the waverider HRV with two ramps and with both shock on shoulder and on cowl lip indicated that a contraction ratio of roughly 14 was achievable. Given that the spontaneous ignition temperature of an ethylene/oxygen mixture is roughly 780°K[17], a guideline of 1000°K was used as the design temperature at the mainburner station to insure that combustion was indeed present. The 1-D cycle code was run with the LOX augmentation preburning option to compute parametrically, the required fuel and oxygen flow to achieve an equivalent mixed 1-D temperature at the main fuel injector station equal to the auto-ignition value. For an engine with an equivalence ratio of 1 (stoichiometric) this resulted in roughly 2.5% of the fuel being directed to the preburner that was then burned stoichiometricaly with onboard LOX. The flow of LOX was then reduced to the preburner resulting in a fuel-rich preburner. This reduced the required amount of onboard LOX with only a minimal effect on temperature distribution prior to main fuel injection. This is because the fuel-rich preburner exhaust gasses continue to react with the air after injection. A heat balance on the vehicle and engine was used to compute the fuel total temperature. The resulting operating conditions of this engine are given in Table 1.

Table 1. Engine Operating Conditions

	Inlet	Preburner	Main
Gas	Air	Products and C_2H_4	C_2H_4
Mach No.	3.83	1.1	2.2
T(°K)	833	3395	801
P(atm)	0.86	13.39	2.49
Area(in)	2.0000	0.005	0.166
Angle	-	90°	30°

The area in the above table is based on a one inch width section.

An important consideration in the design of a scramjet is the penetration distance of the injectors. Reference 18 gives a relationship for the jet penetration distance as a function of the jet and free stream Mach numbers, the momentum ratio of the two streams, the angle of injection and the jet diameter. The preburner injection was designed to only penetrate through the boundary layer, whereas the main injection was designed to reach well into the air stream for better mixing. This resulted in a guideline of h=0.5cm for the preburner and h=2.0cm on the main burner. Because of the large amounts of fuel being injected through the main injectors at stoichiometric conditions, the main fuel injectors were designed with a streamwise length-to-width aspect ratio of 5 and an angle of injection of 30 degrees to help reduce blockage. The injectors were laterally spaced one inch apart on both the top and bottom of the scramjet. The top injectors were then offset one-half inch to a produce a staggered injection for the purpose of increasing jet penetration and to avoid the additional losses of impacting jets. The preburners were aligned with the main fuel injectors to ensure that the hot preburner gasses fell in near vicinity of the main fuel.

A three-dimensional CFD analysis of this engine was performed. Because of the periodicity of the engine in the absence of any side walls, only the flow between the centerline of the top injectors and the centerline of the bottom injectors was actually solved. The grid for this computation was generated algebraically and contained 119 cells in the axial direction, 60 cells from top to bottom, and 16 cells laterally. The grid spacing on the walls was set to 4.0×10^{-5}m. All of the injector exits were modeled as rectangles containing 8 cells in each of the axial and lateral directions. This three-dimensional computation required 1850 iterations leading to 102 hours on a Cray-YMP. The computation was halted after no plotable difference was seen with further iteration. Throughout the CFD simulation process, the ingestion of a thick boundary layer formed on the forebody of the hypersonic vehicle by the scramjet was neglected.

For the current engine design, all of the injectors (including preburner and main) were designed to be supersonic in the boundary-normal direction. This simplifies the CFD boundary condition procedure since merely specification of the injector variables is required for a supersonic inflow boundary condition. This type of injector is also quite practical in a scramjet since injector pressures are typically high enough to choke the injector flow. The supersonic inflow boundary

condition was imposed only on those cell faces that correspond to an injector exit. No-slip, viscous boundary conditions were imposed on the cell faces adjacent to the injector exit. This led to the use of rectangular injectors to avoid further complication of the boundary condition procedure and the grid generation process.

The results of the CFD analysis are shown in Figs. 3-13. The pressure contours on both the symmetry plane containing the top injector and the one containing the lower injector are shown in Fig. 3. The pressures are smoothly varying except in the vicinity of the injectors. Shocks emanating from both the preburner and main fuel injectors traverse the height and width of the computational space. These shocks can significantly affect the efficiency of the engine, and any further refinement of this design will address the losses associated with these structures. The temperature contours (Fig. 4) show the injector penetration and the temperature rise caused by combustion. This figure indicates that the penetration of the combustion region is more than half the height of the scramjet. A significant degree of penetration is present, without adverse effects such as jet-jet interactions and jet-wall interactions.

The velocity vectors of Figs. 5 and 6 show details of the injector flow fields. The velocity vectors in the immediate vicinity of the preburner exit exhibit a spreading behavior that is typical of an under-expanded jet. This phenomenon is also present in the main injector region but is less visible because of the inclination of the vectors. A separation region is present in the preburner injector region that reaches seven jet diameters upstream of the injector. This phenomenon is absent near the main fuel injectors because of the reduced angle of injection.

Figures 7, 8 and 9 contain crossflow contour plots of temperature, fuel and water respectively, at various axial locations. The axial locations correspond to the following: 1) just aft of the preburner station, 2) just upstream of the main fuel injection, 3) the back of the main injector station, 4) within the combustion chamber, and 5) the combustor exit. The exact axial locations are indicated on the plots.

The temperature contours of Fig. 7 clearly show the mechanism that is studied in this paper. Fig. 7(a) shows the hot preburner gasses that emerge from the preburner injector ports. These gasses mix and react with the oncoming air stream but still contain a very hot core just before main fuel injection (Fig. 7(b)). This hot core, falling just above the main fuel injection, serves as a "pilot light" for main fuel injectors causing combustion of the main fuel to instantaneously occur (Fig. 7(c)). The main fuel injectors were designed to produce a significant amount of penetration without traversing the entire height of the scramjet. This was accomplished and is clearly shown in the combustion chamber temperature contours (Figs. 7(d&e)). These figures indicate that the concept of preburning does indeed accomplish the task of maintaining combustion at the main fuel injection station and that an injector can be designed to provide significant flow path penetration without unstarting the engine.

The effect of the upper surface corner on combustion is shown in Figs. 8 and 9. An expansion wave emanating from this corner causes the density and temperature to decrease having an adverse effect on the rate of combustion and mixing. This wave affects the upper gasses before reaching the lower gasses. Therefore the expansion has a greater effect on the upper gasses. For this reason, there are more unburned and unmixed gasses present in the upper region of the scramjet.

The remaining figures present a comparison of the CFD results with those of a 1-D cycle analysis. The combustor efficiency computed by the CFD solution was implemented in the cycle code since no other schedule was available for this engine design. This was accomplished by curve fitting the average fuel fraction schedule (Fig. 10) and using this schedule in the 1-D cycle code. Both the CFD predicted schedule and the curve fit are shown in Fig. 10. Also shown on Fig. 10 is the predicted amount of carbon monoxide from both the CFD and 1-D cycle analysis. The CFD analysis predicts a higher amount than the 1-D cycle code. This is caused by the difference in the equilibrium mechanisms of the two codes and suggests an improvement to the simplified kinetics employed in the CFD solver for scramjet computations. Comparisons of the average temperature, the momentum-averaged pressure and the mass-averaged velocity from the CFD analysis with the results of the cycle code show general agreement (Figs. 11-13). The discrepancies can be attributed to the improved ability of the CFD method to account for detail and the difference in the equilibrium mechanisms. Finally, a sensitivity analysis using

the cycle code indicates that, at Mach 8, a 1% change in overall combustion efficiency represents approximately 1% change in cowl-to-tail Isp and 0.8% change in axial thrust coefficient.

Hypersonic Waverider Research Vehicle Design and Analysis

Unlike accelerator-type missions (e.g., SSTO) where the mass capture characteristics of the vehicle are most important, cruise configurations place an emphasis on the aerodynamic performance of the design. Hence vehicle lift-to-drag ratio (L/D) or the product of L/D and engine Isp (a parameter proportional to Brequet range factor) becomes more important. A waverider configuration, with high hypersonic L/D potential, was selected as the baseline configuration for the present study of the HRV. The configuration/engine installation was numerically optimized to maximize (L/D) x Isp, using forebody shape, ramp angles and cowl position as optimization parameters. For this analysis, the forebody is a Mach 8 waverider configuration and the ramp angles and cowl position were designed to produce first and second ramp shock-on-lip and cowl shock-on-shoulder. The engine geometry and operating parameters were held fixed in the optimization procedure. The numerical optimization was performed using the HAVOC cycle code.

The design parameters and constraint functions used for optimization are listed below. There were 15 design parameters used in the optimization process. Six parameters defined the waverider generating surface (hence the vehicle shape); eight parameters defined the ramps, cowl, nozzle geometries, and leading-edge radius; the last design parameter was free stream dynamic pressure. Eight constraints were used in the optimization process, including engine throttle greater than or equal to the required cooling equivalence ratio, leading edge equilibrium radiation temperature limited to 3200°F, wing tip closure angle limited to 10 degrees, and the vehicle structural thickness limit at vehicle aft end, accounting for nozzle integration. The volume was constrained to 1.7% of vehicle length cubed. Finally, the vehicle width to length ratio was less than or equal to 0.75.

For the Mach 8 design, a generating shock angle of 12 degrees was arbitrarily selected. The waverider shape optimization process involved planform shape changes to sweep the leading edge in order to alleviate high heating rates at the higher free stream dynamic pressures, traded off against leading edge radius and associated leading edge bluntness drag. The design optimization process of the inlet (ramp positions and ramp angles) resulted in the two ramp shocks converging on the cowl lip (shock-on-lip) then reflecting on the shoulder of the combustor entrance (shock-on-shoulder). The geometric contraction ratio was approximately 14, with a resulting pressure at the combustor inlet of about one atmosphere. Preliminary performance estimates indicated a required vehicle length of 23 ft, with an overall vehicle body density of 20 lbs/ft**3. A lift-to-drag ratio of 4.3 was achieved, with a cowl-to-tail Isp of 746 seconds at an assumed combustor efficiency of 95%, and at an equivalence ratio of 1.0, with a free stream dynamic pressure of 900 psf, resulting in an initial cruise altitude of 92,500 ft. An engine width of roughly 0.762m produced a net thrust that is equal to the net drag of the vehicle at the design point. For the results presented below, the engine combustion efficiency of 55% was taken from the scramjet engine CFD results.

Nose-to-tail analyses utilizing both CFD and cycle codes were performed. The geometries for both analyses, however, were slightly different. The ramp sidewalls in the cycle analysis were assumed to have zero thickness and were aligned with the forebody flow. They therefore resulted in zero pressure drag with only a nominal addition to the viscous drag. The CFD geometry, on the other hand, contained ramp sidewalls with an included angle of 21 degrees Because the sidewall attaches to the cowl lip and because the cowl protruded far below the lower surface of the waverider, the sidewall contained a significant amount of additional volume. This added volume was exposed to the forebody flow and produced additional drag to the vehicle.

The grid generation for the CFD nose-to-tail analysis is described below. The grid generation tools used for the external grids are the S3D and HYPGEN-UI codes mentioned previously. The external portion was divided into three axial sections: nose-to-inlet, inlet-to-exit, and exit-to-end sections. Grid generation was performed separately on each of these portions. For the surface grid, points were clustered on the waverider leading edge, on the sidewall leading edge and on all of the other convex corners of the vehicle. The lower surface grid is shown in Fig. 14. The outer boundary of the volume grid was placed well beyond the anticipated bow shock to a distance of roughly three meters from

the vehicle surface. The spacing of the first point from the surface was set to 1.0×10^{-5}m. The grid dimensions for the three external grids measured 102x70x144, 60x70x129 and 12x70x130 from nose to tail. The values of these dimensions correspond to the number of grid points in the streamwise direction, circumferential direction, and radial direction. An internal nozzle grid measuring 3x79x79 was generated algebraically for the CFD solution.

The space-marching scheme, STUFF, was employed to obtain the nozzle and external CFD results for the waverider HRV. The space-marching solution began at the nose of the vehicle by setting the dependent variables in all of the cells to be free stream. The solution progressed by marching downstream through each of the grids until the aft end of the vehicle was reached. A fully conservative patching scheme [19] was employed to transfer the solution from one grid to the next. The frozen chemistry option was employed for the CFD results including the nozzle portion. This was sufficient since combustion is slowed considerably at the combustor exit.

For the CFD nose-to-tail results presented here, the HAVOC cycle code was used to provide the solution within the inlets and combustor. This was done to avoid the computational expense of obtaining time-marching solutions of both the outboard and inboard engines with 48 fuel injection ports in each. The CFD forebody results were averaged at the inlet face to provide one-dimensional inlet conditions for the cycle code. The presence of an oblique cowl shock was accounted for and provided the mechanism to turn the flow parallel to the engine cowl. The CFD-predicted heat release schedule presented above was used in the one-dimensional cycle analysis of the combustor.

The two-dimensional, shock/weak wave results of the HAVOC analysis are plotted in Fig. 15. This figure shows the shock, contact, and expansion wave arrangement for the current integrated design on the vehicle symmetry plane. The intent of the forebody/ ramp design is clearly shown in this figure. Both of the ramp shocks impinge on the cowl leading edge and the cowl shock impinges on the shoulder. The bow shock, however, lies outside of the inlet. This is because at Mach 8, with a fixed throat height, having the bow shock on the cowl lip can produce shock-on-ramp with possible boundary layer separation and engine unstart. The nozzle geometry was restricted to two planar sections and the corresponding expansion and shock are shown in Fig. 15.

Figure 16 is a line plot of the surface pressure on the keel line of the vehicle. Both the CFD and cycle results are plotted. Agreement is excellent except in the vicinity of inviscid/viscous interactions. Comparison of the pressure on the waverider forebody is within 2 percent except at the leading edge where CFD predicts a pressure spike resulting from boundary layer displacement. The ramp pressures also agree quite well except for the asymptotic behavior of the CFD results that is typical of shock/boundary layer interactions. Another reason for this discrepancy can be attributed to the three-dimensional intersection of the first ramp with the curved waverider forebody. The intersection line bends downstream from the vehicle symmetry plane. This three-dimensional effect reduces the pressure near the intersection region. Figure 16 also shows very good agreement on the outer surface of the cowl and on the nozzle surface. Comparison of surface pressure on the upper surface showed that the CFD predicted pressures were 3-10% higher than the engineering predictions. This is explained by viscous/inviscid interactions.

The pressure contours in Fig. 17 show the keel line shock and expansion waves that are predicted with CFD. The location and strength of these waves are in very good agreement with those predicted by the cycle code (Fig. 15). The CFD results, however, predict that the ramp shocks lie slightly outside of the inlet instead of on the cowl lip. This difference is attributed to shock/boundary layer interactions and to three-dimensional effects.

Figure 18 shows the CFD predicted density contours on crossflow planes at various axial stations. These stations correspond to the following locations: a) on the second ramp, b) at the inlet, c) at the middle of the cowl, d) at the engine exit and e) at the vehicle end. The two ramp shocks are visible in the pressure contours of Fig. 18a and clearly exhibit a 3-dimensional behavior. The bow shock is attached to the leading edge of the waverider and produces a very clean flow field on the forebody absent of the ramp geometry.

Figure 18 shows that the flow into the inlet is fairly clean except for a weak shock that emanates from the ramp sidewall and interacts with the forebody boundary layer. Also evident is a thickening of the ramp boundary layer thickness

nearer the ramp sidewall. This is caused by the tendency of the flow to spill off the first ramp resulting in a sideways velocity component. This effect washes the boundary layer away from the symmetry plane of the vehicle. It is then stopped before the inlet station by the sidewalls on the second ramp. Another feature that should be noted in Fig. 18b is the shock emanating from the outer surface of the ramp sidewall. This feature is absent in the cycle analysis since the sidewalls were assumed to have zero thickness. The resulting high pressure region adds considerably to the net drag of the vehicle since the outer sidewall has an area component in the streamwise direction. This effect resulted in a negative net-thrust predicted by the nose-to-tail analysis, and therefore, creates a need to reduce the thickness of the sidewalls. At the cowl mid-point (Fig. 18c), the ramp shocks have clearly merged with the bow shock an expansion fan emanating from the lower surface of the cowl is evident.

Figure 18(d-e) depict the CFD predicted flow field on the aft portion of the vehicle. This flow field region is very complex due to the presence of the engine, although a significant portion of the waverider flow field remains unaffected. The bow shock remains attached to the leading edge for the entire length of the vehicle. This feature is desirable since any spillage of the high pressure gasses onto the upper surface would reduce the performance of the vehicle. Two flow field features that are clearly visible in the nozzle portion of the flow are the initial nozzle expansion and the shock caused by the second nozzle plane. These features appear to be nearly two-dimensional near the centerline, leading to the good agreement with the cycle analysis (Fig. 16).

Figure 19 shows the pressure contours on the lower surface of the vehicle. The impact on the surface pressure by the presence of the integrated scramjet is visible in this figure. The lower surface is composed of a large region of undisturbed flow with a fairly constant pressure. The remaining surface is exposed to the numerous shocks and expansion fans that originate from the integrated propulsion system. These include the ramp shocks, the sidewall shocks, the exterior cowl expansions, the engine shroud expansion, and the numerous nozzle waves.

Of particular interest in the current design are the forebody ramp system and the resulting flow field. Due to the curvature of the waverider forebody, an oblique intersection results between it and the first ramp. This intersection is visible in the pressure contours of Fig. 19. The strong pressure gradients that are present in this vicinity cause the flow to be diverted away from the vehicle symmetry plane beginning at the origin of the first ramp. This effect tends to reduce the amount of mass provided to the inlet. An intersection that is less oblique would reduce the spillage since the pressure gradient would be aligned more with the flow direction. This can be accomplished by reducing the curvature of the waverider forebody at the symmetry plane. In the current design, this spillage was effectively halted at the second ramp by using sidewalls. This is shown in the surface streamlines of Fig. 20.

CONCLUSIONS

Two methods were demonstrated for the conceptual design and analysis of a hypersonic waverider research vehicle: an engineering analysis code with a simplified nose-to-tail flow field analysis capability and a complete 3-D CFD code with a hydrocarbon/air capability. The methods have been shown to produce good agreement for waverider forebodies except in regions of strong viscous/inviscid interaction. The coupling of the cycle code with CFD to compute a single flow field was also demonstrated. Even though the cycle code has significantly less ability to predict detail, this coupling proved to be useful because it reduced computer requirements.

The nose-to-tail analysis of the waverider HRV clearly shown the benefits of the current design and revealed areas for improvement. The waverider forebody combines with the current ramp system to provide a uniform flow to the inlet of the scramjet. Further, the forebody shock remains attached to the leading edge for the entire length of the vehicle. This avoidsspillage of the high pressure air onto the upper surface that can significantly reduce lift. The analysis has also shown that the ramp sidewalls need to be thinner since they protrude far into the forebody flow field and cause unnecessary drag to the vehicle.

The analysis of the liquid oxygen-augmented preburning hydrocarbon scramjet indicates that the concept does indeed produce combustion of the main fuel within the scramjet engine. The preburning process provides a sufficiently elevated temperature flow into the main fuel injector region to support immediate combustion of the gaseous ethylene fuel. However, because of the significant amount of unburned

fuel at the combustor exit, there is a need for better mixing efficiency within the combustor. For the current fuel injector configuration, improved engine cycle performance could also be achieved at a lower overall engine equivalence ratio, limited by engine cooling requirements. Finally, there is currently a void of high-quality, CFD validation-type data for high-speed hydrocarbon combustion, leaving an uncertainty in any predicted results.

ACKNOWLEDGMENTS

This work was partially supported by NASA Ames Research Center under grants NCC2-498 and NCC2-746. The authors would like to acknowledge Mr. Thomas Whitaker of Sterling Software for graphics and technical support.

REFERENCES

[1] Blankson, I., "Propulsion/Airframe Integration Issues for Waverider Aircraft," AIAA Paper 93-0506, Jan. 1993.

[2] Kay, I. W., Peschke, W.T. and Guile, R. N., "Hydrocarbon-Fueled Scramjet Combustor Investigation," AIAA Paper 90-2337, July 1990.

[3] Arena, A. V. and Grant, M., "The Technical Design and Integration Issues of Hydrocarbon-Fueled Scramjet Missiles," JANNAF Report, Feb. 1991.

[4] Molvik, G. A., Bowles, J.V. and Huynh, L. C., "Analysis of a Hydrocarbon Scramjet with Augmented Preburning," AIAA Paper 92-3425, July, 1992.

[5] Molvik, G. A., Bowles, J.V. and Huynh, L. C., "Analysis of a Hypersonic Research Vehicle with a Hydrocarbon Scramjet Engine," AIAA Paper 93-0509, Jan. 1993.

[6] Bowles, J. V. Conceptual Studies Activities. Proceedings of the Second National Aerospace Plane Symposium. Applied Physics Laboratory, Laurel, MD, Nov. 1986.

[7] Vanderplaats, G. N. and Hansen, S. R.,"DOC Users Manual", Version 1.00, VMA Engineering, Goleta, CA, 1989.

[8] Schlichting, H., "Boundary-Layer Theory", Seventh Edition, McGraw-Hill Book Co., New York, 1979.

[9] Anderson, J. D., "Hypersonic and High Temperature Gas Dynamics," First Edition, McGraw-Hill Book Co., New York, 1989.

[10] Molvik, G. A. and Merkle, C. L., "A Set of Strongly- Coupled Upwind Algorithms for Computing Flows in Chemical Nonequilibrium," AIAA Paper 89-0199. Jan. 1989.

[11] Westbrook, C. K. and Dryer, F. L., "Simplified Reaction Mechanisms for the Oxidation of Hydrocarbon Fuels in Flames,", *Combustion Science and Technology*, Vol. 27, 1981, pp. 31-43.

[12] Gordon, S. and McBride, B. J., "Computer Program for Calculation of Complex Chemical Equilibrium Compositions, Rocket Performance, Incident and Reflected Shocks, and Chapman-Jouguet Detonations," NASA SP-273, 1976.

[13] Jones, W. P. and Launder, B. E., "The Prediction of Laminarization with a Two-Equation Model of Turbulence," *International Journal of Heat and Mass Transfer*, Vol. 15, 1972, pp. 303-314.

[14] Zeman, O., "Compressible Turbulence Subjected to Shear and Rapid Compression," Eighth Symposium on Turbulent Shear Flows, Munich, Germany, Sept, 1991.

[15] Luh, R. C., Pierce, L. E., Yip, D., "Interactive Surface Grid Generation," AIAA Paper 91-0796, Jan. 1991.

[16] Chan, W. M. and Steger, J. L., "Enhancements of a Three-Dimensional Hyperbolic Grid Generation Scheme," *Applied Mathematics and Computation*, Vol 51, pp. 181-205, 1992.

[17] Barnett, H. C. and Hibbard, R. R., "Basic Considerations in the Combustion of Hydrocarbon Fuels with Air," NACA Report 1300, 1959.

[18] McClinton, C. R., "Effect of Injection Angle on the Interaction Between Sonic Secondary Jets and Supersonic Free Stream," NASA TN D-6669, Feb. 1972.

[19] Klopfer, G. H. and Molvik G. A., "Conservative Multizonal Interface

Algorithm for the 3-D Navier-Stokes Equations," AIAA Paper 91-1601, June 1991.

Fig. 1 Hypersonic vehicle concept with an integrated hydrocarbon scramjet engine.

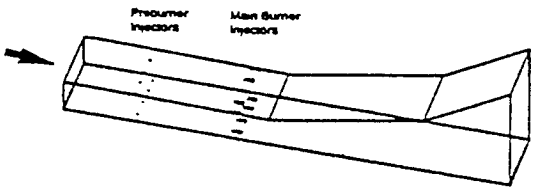

Fig. 2 Schematic diagram of the 3-D scramjet engine geometry

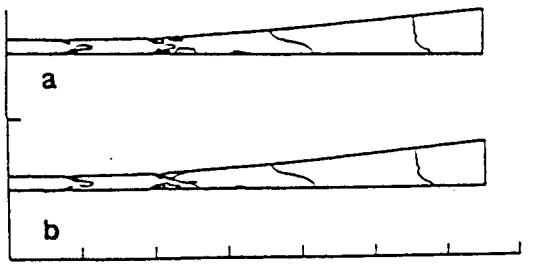

Fig. 3 Pressure contours at a) symmetry plane of top injectors, b) symmetry plane of bottom injectors.

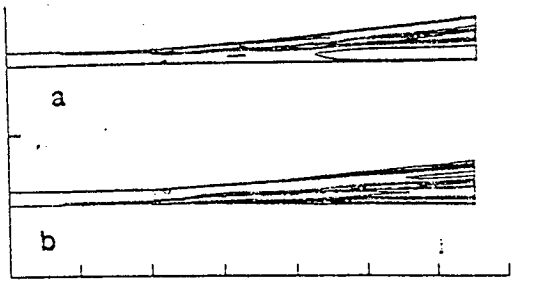

Fig. 4 Temperature contours at a) symmetry plane of top injectors, b) symmetry plane of bottom injectors.

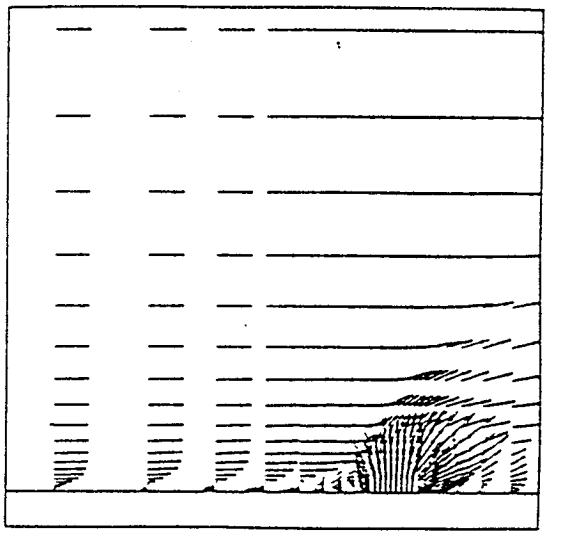

Fig. 5 Velocity vectors in vicinity of preburner injector

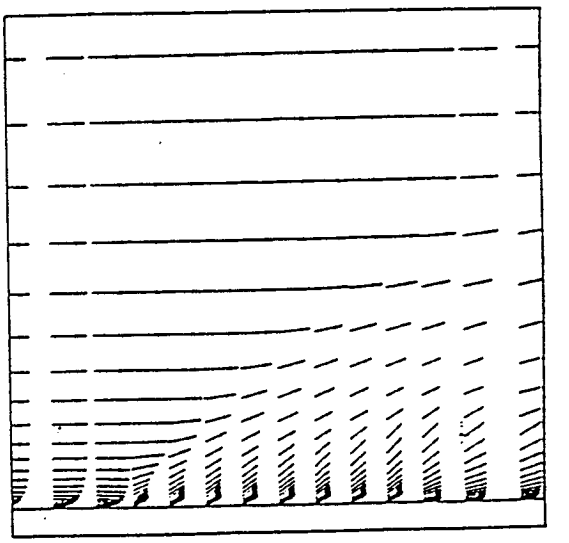

Fig. 6 Velocity vectors in vicinity of main burner injector

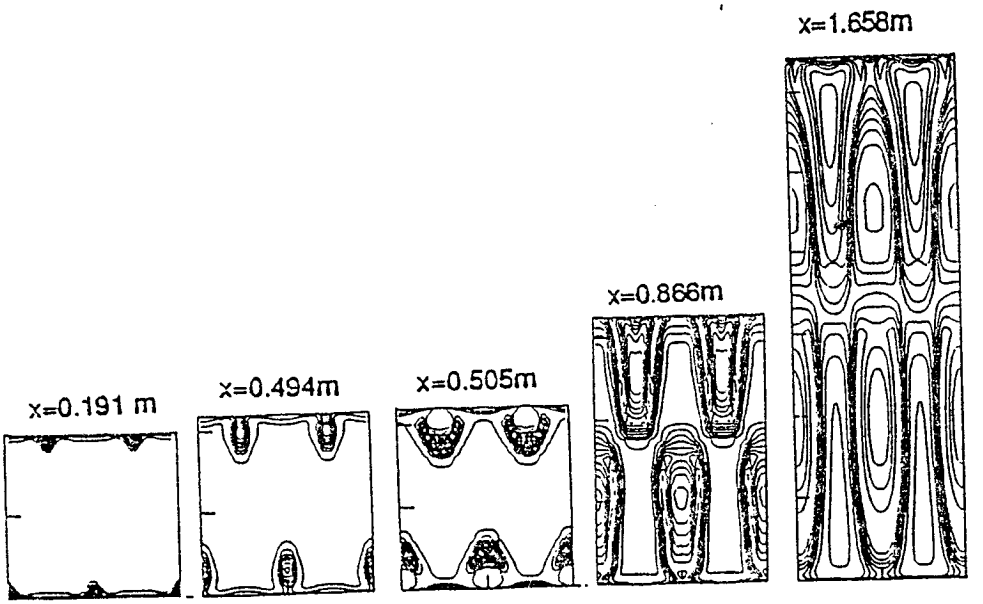

Figure 7 Temperature Contours at Indicated Axial Locations

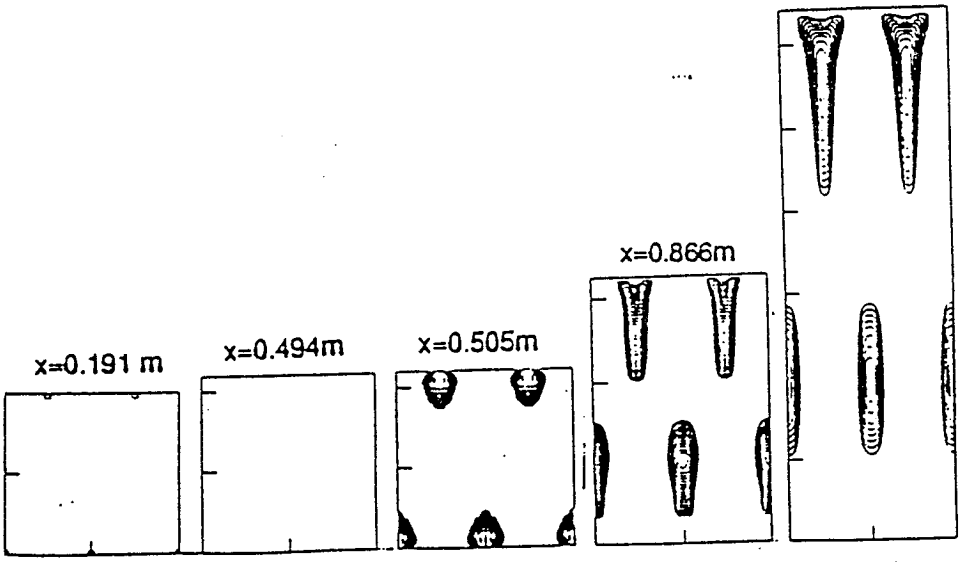

Figure 8 C_2H_4 Mass Fractions Contour at Indicated Axial Locations

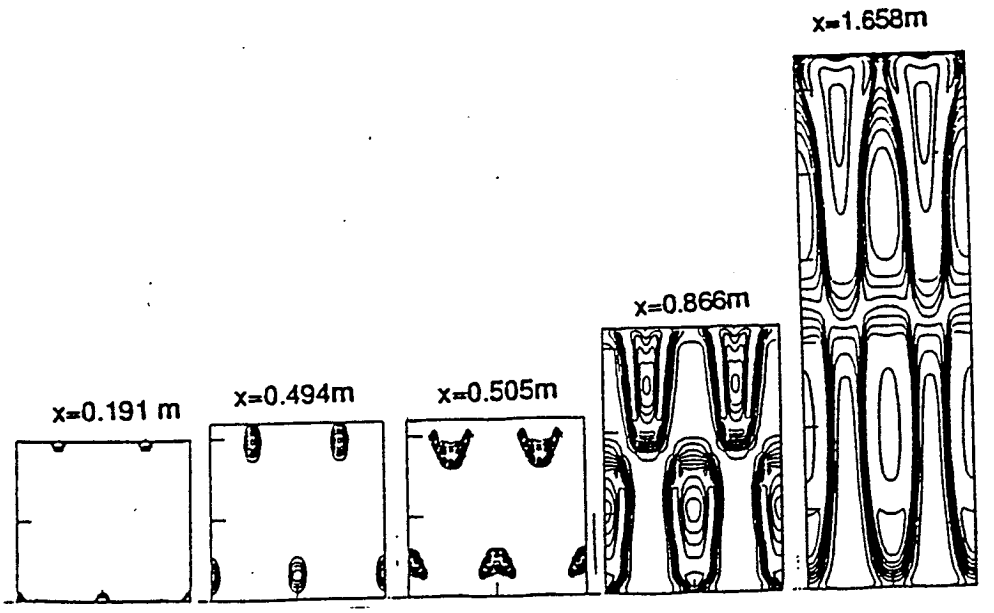

Figure 9 H_2O Mass Fraction Contours at Indicated Axial Locations

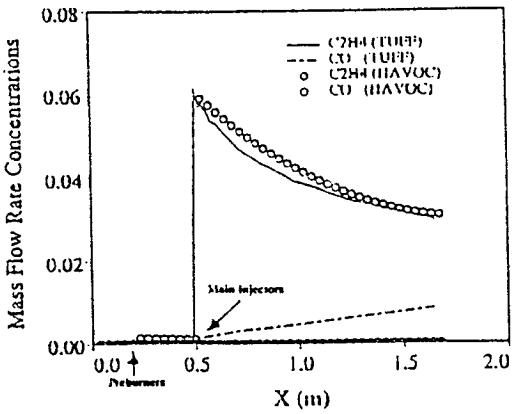

Fig. 10 C_2H_4 and CO mass concentrations as a function of axial location

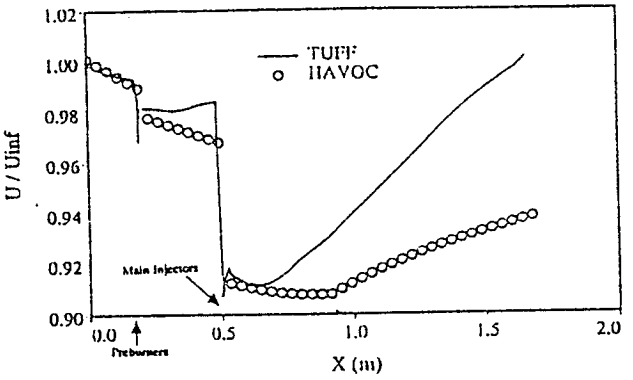

Fig. 13 Axial velocity as a function of axial location

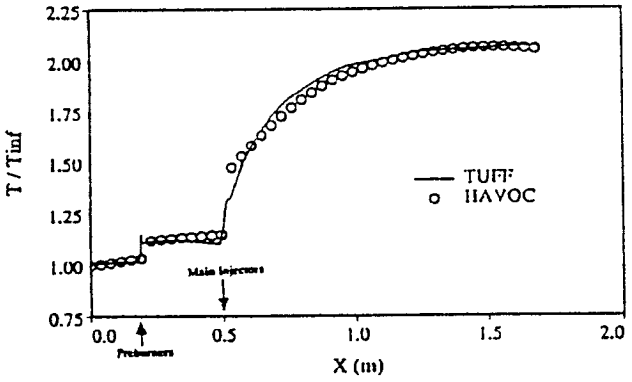

Fig. 11 Temperature as a function of axial location

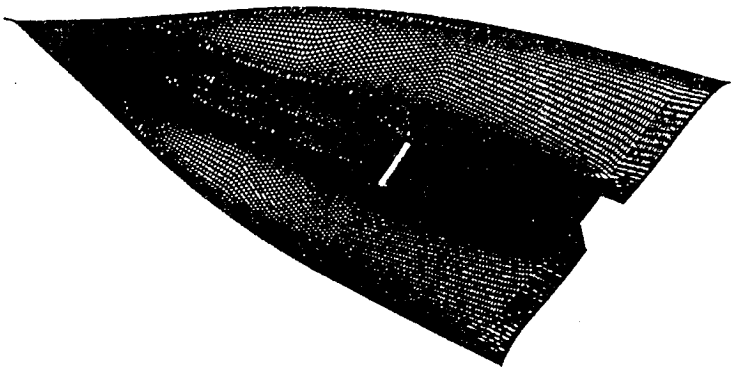

Fig. 14 Lower surface grid for the current waverider HRV design.

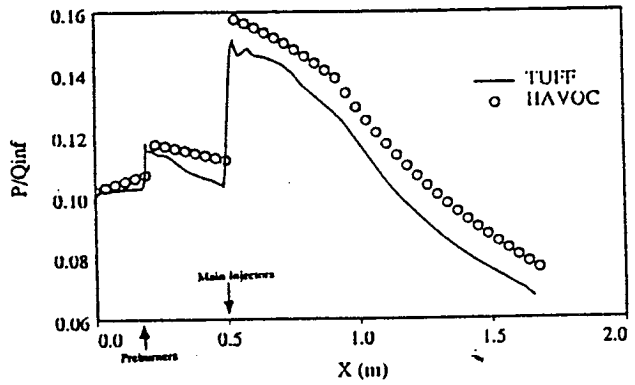

Fig. 12 Pressure as a function of axial location

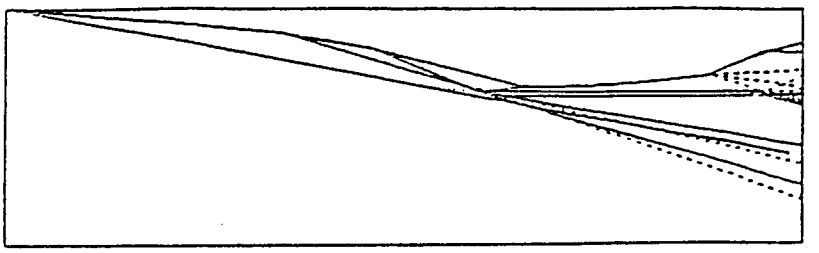

Fig. 15 HAVOC predicted flow field on the lower symmetry plane.

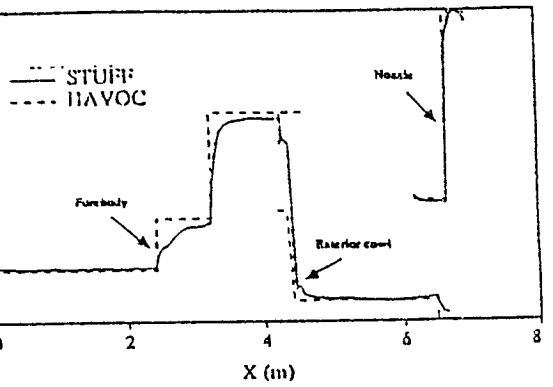

Fig. 16 Keel line pressure comparison.

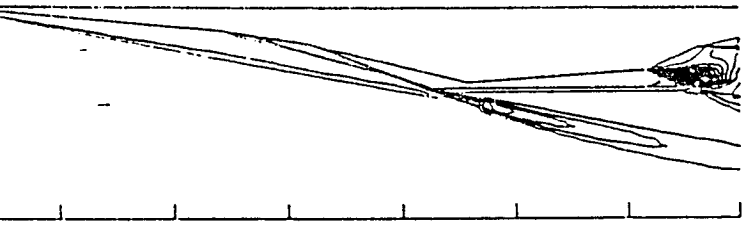

Fig. 17 CFD predicted pressure contours on vehicle symmetry plane.

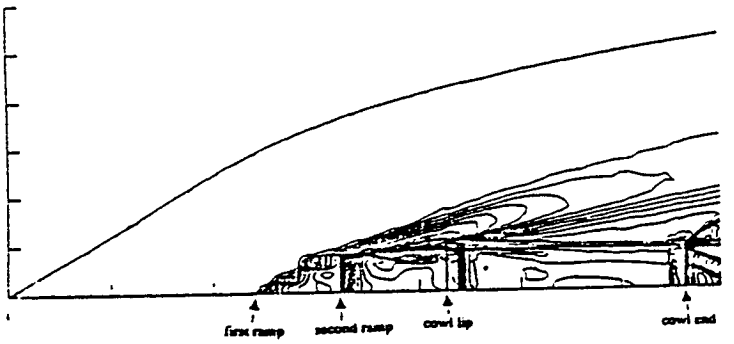

Fig. 19 CFD predicted surface pressure plot.

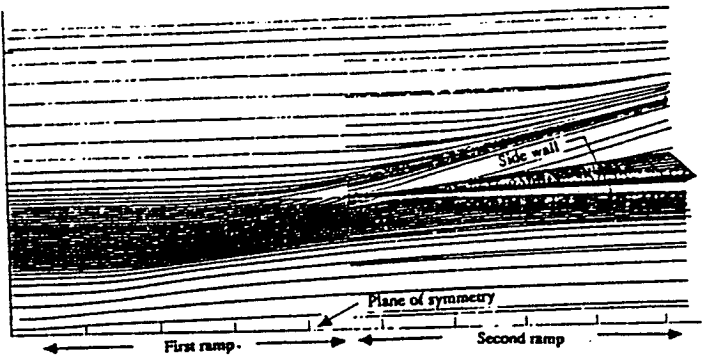

Fig. 20 CFD predicted surface streamlines on the forebody ramp system.

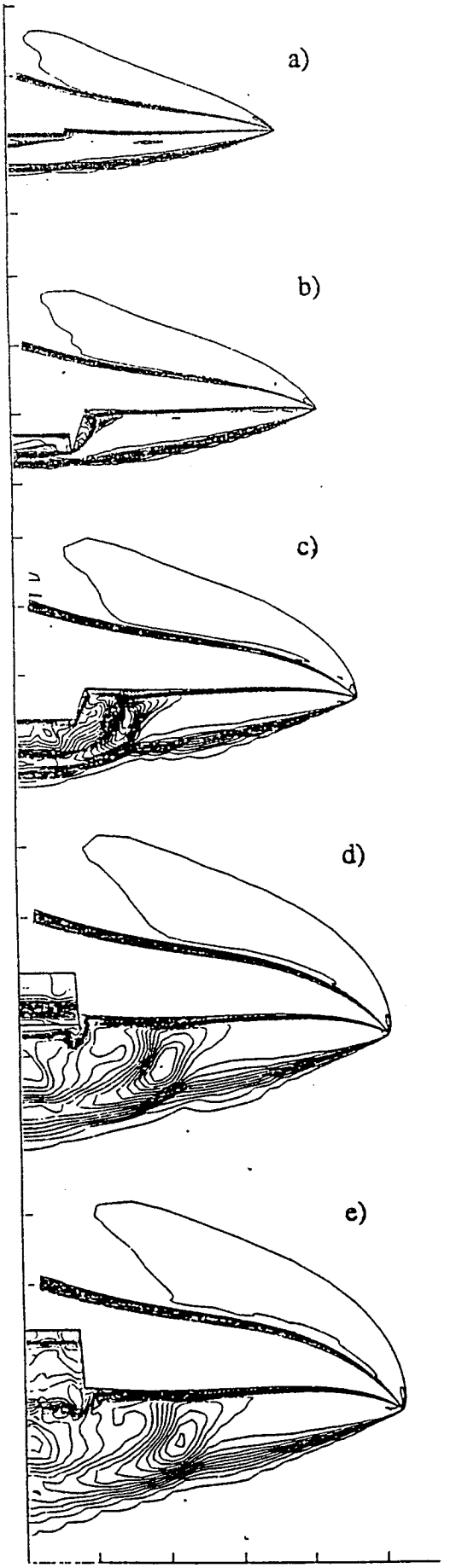

Fig. 18 CFD predicted density contours at various axial locations.

AIAA-94-2313

Computation of High Speed Turbulent Reacting Flows Relevant to Scramjet Combustors

J.R. Narayan and G.A. Molvik
MCAT Institute
Moffett Field, California

and

G. Wadawadigi
University of Texas at Arlington
Arlington, Texas

25th AIAA Fluid Dynamics Conference
June 20-23, 1994 / Colorado Springs, CO

COMPUTATION OF HIGH-SPEED TURBULENT REACTING FLOWS RELEVANT TO SCRAMJET COMBUSTORS

J.R. Narayan*
MCAT Institute, Moffett Field, CA.
G. Wadawadigi†
U. of Texas at Arlington, Arlington , Texas.
and
G. Molvik‡
MCAT Institute, Moffett Field, CA.

ABSTRACT

Computations are done on flow configurations that resemble the reaction zone in the scramjet combustor flows. Compressible, reacting, turbulent flow solutions are obtained. A two equation (k-ϵ) model with compressibility correction is used to calculate the flow field. A finite rate (8-species, 13-reaction steps) chemistry model for hydrogen-air combustion has been used. Computations are carried out using the Navier-Stokes solver TUFF. Predictions are compared with available experimental data and also those obtained by using the code UPS.

NOMENCLATURE

A, b	coefficients in Arrhenius rate equation
C_1,C_2,C_μ	turbulence model constants
E	total internal energy
f_n	mass fraction of species n
H	total enthalpy
h	static enthalpy
k	turbulent kinetic energy
k_f,k_b	forward and backward reaction rate constants
L	number of reaction steps
M_n	Molecular weight of species n
M_t	Turbulent Mach number
N	number of chemical species
Pr,Pr_t	laminar and turbulent Prandtl numbers
p	pressure
Sc,Sc_t	laminar and turbulent Schmidt numbers
T	temperature
T_a	Activation Temperature
t	time
$\vec{U}$	velocity vector
$\dot{w}_n$	production rate of species n
x	streamwise coordinate
x_j	j^{th} coordinate
y	transverse coordinate
δ_{ij}	Kronecker delta
ϵ	turbulence energy dissipation rate
ϵ_c	compressible dissipation rate
η	compressibility correction coefficient
γ	ratio of specific heats
ω	specific dissipation rate
μ	laminar viscosity
μ_t	turbulent viscosity
ν	kinematic viscosity
ρ	density
σ_k, σ_ϵ	turbulence model constants
τ_{ij}	stress tensor
Φ_j	flux vector in j^{th} direction
Subscripts	
t	turbulent quantity

*Senior Research Scientist, Senior Member AIAA.
†PostDoctorla Fellow, Member AIAA.
‡Senior Research Scientist, Member AIAA.

INTRODUCTION

Hypersonic travel requires propulsion systems which are different from the conventional ones used in most of the modern aircraft. The supersonic combustion ramjet (scramjet) is a system considered to be suitable for high speed applications. There has been a tremendous amount of activity in the area of scramjet research in recent years ([1] - [11]). Some of the related topics include inlet configuration, mixing layers, mixing enhancement, combustor configuration, finite rate chemistry models and chemical kinetics. The fuel used in the scramjet varies depending upon the application. For example, hypersonic waveriders using hydrocarbon fuels have been designed [12] for applications in the moderate hypersonic speed regimes. For Mach numbers of the order of 15 and above, hydrogen is generally considered to be the fuel of choice. In the present work, hydrogen is the fuel used in the computations.

The present work represents a computational ef-

fort in establishing a solution procedure for hypersonic propulsion applications. The entire task of establishing the solutions procedure must then be divided into smaller tasks dealing with subsets such as turbulence modelling, chemical kinetics, geometry etc. One such task is the topic for the present study. Here, the relevant flow features of the combustor, namely the mixing and chemical reaction between the fuel and oxidizer streams, is addressed. The flow field in a scramjet is complex. It is turbulent and compressible involving high heat release. The solution procedure should address all aspects of the flow field adequately. It should be capable of accurately modelling the turbulent field, taking into account the effects of compressibility, and addressing the changes associated with heat release. Also, the interactions between the distinct physical aspects of the flow such as the effect of heat release on turbulence, the interaction between turbulence and chemistry etc. must be properly addressed. Significant progress has been made in addressing these areas via accurate and realistic modelling in recent years [6].

Remarkable advances have been made in the area of turbulence modelling, accounting for a variety of factors that affect the flow field. Compressibility correction models to account for the effects of compressibility, near-wall turbulence models to deal with the transition from fully turbulent to zero turbulence, viscous dominated flow field near no-slip boundaries and modifications to models to account for flow curvature are some examples. A wide variety of turbulence models, including algebraic (zero-equation), one-equation, two-equation, Reynolds stress and large eddy simulation models, are available (for example references [13] - [15]) depending upon the sophistication and accuracy desired and the limits imposed by numerical solution procedures.

Thermodynamic and chemical kinetic models [16] applicable to the scramjet flows have been undergoing continuous improvements in recent years. Accurate modelling of thermodynamic variables as functions of temperature which are valid over a wide range of temperatures is an example. In flows such as the one associated with the scramjet, the time scales associated with fluid dynamics and chemical reaction (not to mention the turbulence scales) require that the combustion process be modelled via a finite rate chemistry mechanism. Such a mechanism should account not only for the major species (reactants and products) involved in the chemical reactions but also the intermediate transient ones which play a vital role in the reaction progress process. Accurate models for the chemical reactions in the scramjet combustor, thus, is a crucial aspect of the solution procedure.

The design of the combustor is strongly dependent upon factors such as the mixing between fuel and oxidizer streams, presence of shocks in the flow field, boundary layer effects, flow separation, extent of chemical reaction within the combustor and so on. The numerical solution procedure should have the capability of addressing all of these factors while maintaining the required accuracy and robustness. There is a glut of useful numerical solvers applicable for a wide variety of flows including all speed regimes. Computational algorithms which are fast and accurate are being improved everyday.

Even though there are a wide variety of sophisticated and physically accurate thermodynamic, chemical kinetic and turbulence models available it is not always possible to use the most accurate and elaborate versions in a numerical simulation due to the limitations imposed by computer memory requirements, computational economy, ease of use and adaptability to practical problems. Solutions often are required, especially in ihe engineering industry which is the end user for such solvers, in a short time using computers that may not be the fastest available. As a result, compromises must be struck between physical accuracy and computational feasibility and it is this aspect which differentiates between various solvers that exist today.

In the present study, an attempt is made to establish a solution procedure for scramjet combustor flow predictions from the perspective of the discussion above. The models chosen to represent the turbulent and chemistry fields reflect the compromise between physical accuracy and computational economy mentioned above. The code chosen for the computations is the TUFF [17] code and the solutions are compared with those obtained with the UPS [18, 20] code. The turbulence model chosen is the two-equation $k-\epsilon$ turbulence model with low Reynolds number modifications [13]. However, the Baldwin-Lomax algebraic model is also available as an option. The compressibility effects are included via the compressibility correction model proposed by Zeman [19]. The fuel used is hydrogen although the numerical solver can easily be modified for hydrocarbon fuels. A 9-species, 20-reaction steps chemical kinetics model for hydrogen-air combustion [16] is available. For the computations presented in this report, an abbreviated version (8-species, 13-steps) of this model has been used.

Mixing plays a major role in high speed combustor flows. The reaction zone is mainly confined to mixing layers that exist between fuel and oxidizer streams. Two flow configurations are chosen for the study. The first is the well known Burrows-Kurkov experiment [21] in which hydrogen and vitiated air streams (two-dimensional) mix and react. The second

case is that of an axisymmetric configuration [22, 23] where two coaxial jets (fuel and oxidizer) mix and react. Experimental data from compressible, reacting mixing layers is still scarce which hinders the validation of the calculation procedure. The available data from the above two experiments are used to compare with the predictions. The governing and secondary equations used in the computations have all been described in detail in the references cited above. Only an abreviated equation set will be given in the present paper. The computations were performed on the supercomputers of NAS and NASA Ames Research Center (C-90).

GOVERNING EQUATIONS

The equations used for computations are described in detail in references [6, 7, 10] and [24]. Only the forms of the modelled equations used in the present study are given here. Density-weighted averaging is used to derive the mean flow equations from the instantaneous coservation equations. The dependent variables, with the exception of density and pressure, are written as

$$\phi = \widetilde{\phi} + \phi'' \tag{1}$$

where the ϕ'' is the fluctuating component of the variable under consideration and its Favre-mean $\widetilde{\phi}$ is defined as

$$\widetilde{\phi} \equiv \frac{\overline{\rho\phi}}{\overline{\rho}} \tag{2}$$

In this equation, the overbar indicates conventional time-averaging. Density and pressure are split in the conventional sense as,

$$\rho = \overline{\rho} + \rho' \text{ and } p = \overline{p} + p' \tag{3}$$

The averaged continuity and momentum equations are

$$\frac{\partial \overline{\rho}}{\partial t} + \frac{\partial \overline{\rho}\widetilde{U_i}}{\partial x_i} = 0 \tag{4}$$

$$\frac{\partial \overline{\rho}\widetilde{U_i}}{\partial t} + \frac{\partial \overline{\rho}\widetilde{U_i}\widetilde{U_j}}{\partial x_j} = -\frac{\partial \overline{p}}{\partial x_i} - \frac{\partial \overline{\rho u_i'' u_j''}}{\partial x_j} + \frac{\partial \overline{\tau_{ij}}}{\partial x_j} \tag{5}$$

where

$$\tau_{ij} = \mu\left(\frac{\partial u_i}{\partial x_j} + \frac{\partial u_j}{\partial x_i}\right) - \frac{2}{3}\frac{\partial u_k}{\partial x_k}\delta_{ij} \tag{6}$$

with repeated indices indicating summation.

In the two-equation turbulence model, the two turbulence variables are the turbulent kinetic energy (k) and the dissipation rate (ϵ) [13] defined as

$$k \equiv \frac{\overline{\rho u_i'' u_i''}}{2\overline{\rho}} \tag{7}$$

and

$$\epsilon \equiv \frac{\overline{\rho\nu \frac{\partial u_i''}{\partial x_j}\frac{\partial u_i''}{\partial x_j}}}{\overline{\rho}} \tag{8}$$

Boussinesq approximation is used to obtain closure of the averaged equations. Here the Reynolds stress tensor is written as,

$$-\overline{\rho u_i'' u_j''} = \overline{\mu_t}\, S_{ij} - \frac{2}{3}\overline{\rho} k \delta_{ij}$$
$$S_{ij} = \frac{\partial \widetilde{U_i}}{\partial x_j} + \frac{\partial \widetilde{U_j}}{\partial x_i} - \frac{2}{3}\frac{\partial \widetilde{U_k}}{\partial x_k}\delta_{ij} \tag{9}$$

where μ_t is the turbulent/eddy viscosity defined as

$$\bar{\mu_t} = C_\mu \bar{\rho}\frac{k^2}{\epsilon} \tag{10}$$

with C_μ=0.09.

The modelled momentum equation, then, is,

$$\frac{\partial \overline{\rho}\widetilde{U_i}}{\partial t} + \frac{\partial \overline{\rho}\widetilde{U_i}\widetilde{U_j}}{\partial x_j} = -\frac{\partial \overline{p}}{\partial x_i} + \frac{2}{3}\frac{\partial \overline{\rho} k}{\partial x_j}\delta_{ij} - \frac{\partial}{\partial x_j}\left[(\bar{\mu} + \bar{\mu_t})\, S_{ij}\right] \tag{11}$$

The effects of compressibility are included via the model proposed by Zeman [19]. Here, the compressible dissipation terms are expressed as functions of the turbulent kinetic energy dissipation rate and the local turbulent Mach number. The compressibility effects are represented by a component of the dissipation rate (ϵ_c) given as

$$\epsilon_c = K_c \epsilon$$
$$K_c = \eta F(M_t)$$
$$M_t = \frac{2k}{a^2}, \tag{12}$$

where a is the local speed of sound and $F(M_t)$ is a function of the local turbulent Mach number (M_t). $F(M_t)$ is given by

$$F(M_t) = 1 - exp[-(\frac{M_t - M_{t_o}}{0.6})^2], \quad M_t \geq M_{t_o}$$
$$= 0, \quad M_t < M_{t_o}$$

with M_{t_o}=0.1 and η=0.75. The modelled turbulent kinetic energy equation is [6, 13]

$$\frac{\partial \bar{\rho} k}{\partial t} + \frac{\partial \bar{\rho} k \widetilde{U_j}}{\partial x_j} = P_k - \bar{\rho}\epsilon(1 + K_c) + \frac{\partial}{\partial x_j}[(\bar{\mu} + \frac{\bar{\mu_t}}{\sigma_k})\frac{\partial k}{\partial x_j}] \tag{13}$$

where

$$P_k = -\overline{\rho u_i'' u_j''}\,\frac{\partial \widetilde{U_i}}{\partial x_j} \qquad (14)$$

The modelled ϵ-equation used (no compressibility corrections) in the present analysis [13] is given below.

$$\frac{\partial \bar{\rho}\epsilon}{\partial t} + \frac{\partial \bar{\rho}\epsilon \widetilde{U_j}}{\partial x_j} = (C_1\, P_k - C_2 \bar{\rho}\epsilon)\,\frac{\epsilon}{k} + \frac{\partial}{\partial x_j}[(\bar{\mu} + \frac{\bar{\mu}_t}{\sigma_\epsilon})\frac{\partial \epsilon}{\partial x_j}] \qquad (15)$$

where P_k is the production term in the turbulent kinetic energy equation. The model constants used in the analysis are C_1=1.44, C_2=1.92, σ_k=1.0, σ_ϵ=1.3, Pr=0.72, Pr_t=1.0, Sc=0.22 and Sc_t=1.0.

The mass-averaged total energy can be written in terms of the total enthalpy as

$$\tilde{E} = \tilde{H} - \frac{\bar{p}}{\bar{\rho}} \qquad (16)$$

The correlations between the fluctuating velocity and the scalar fluctuations are modelled using a gradient-diffusion hypothesis. A typical model is of the form

$$-\overline{\rho u_i'' \phi''} = \frac{\bar{\mu}_t}{\sigma_\phi}\,(\frac{\partial \tilde{\phi}}{\partial x_i}) \qquad (17)$$

where σ_ϕ is a coefficient which, normally, is a constant. For $\phi = f_n$ (n represents the species) , $\sigma_\phi = Sc_t$, and for the static enthalpy, ($\phi = h$), $\sigma_\phi = Pr_t$. Using the above definition, and omitting the body force contribution, the time-averaged and modelled energy equation [6] is

$$\frac{\partial \bar{\rho}\tilde{E}}{\partial t} + \frac{\partial \bar{\rho}\tilde{E}\widetilde{U_j}}{\partial x_j} = \frac{\partial}{\partial x_j}\,(\overline{\tau_{ij}} - \bar{p}\,\delta_{ij} - \overline{\rho u_i'' u_j''})\widetilde{U_i} + \frac{\partial}{\partial x_j}[(\frac{\bar{\mu}}{Pr} + \frac{\bar{\mu}_t}{Pr_t})\frac{\partial \tilde{h}}{\partial x_j} + (\bar{\mu} + \frac{\bar{\mu}_t}{\sigma_k})\frac{\partial k}{\partial x_j}] \qquad (18)$$

where σ_k comes from the turbulent kinetic energy equation. The modeled species continuity equation is

$$\frac{\partial \bar{\rho}\tilde{f}_n}{\partial t} + \frac{\partial \bar{\rho}\tilde{f}_n \widetilde{U_j}}{\partial x_j} = \overline{\dot{w}_n} - \frac{\partial}{\partial x_j}\,[(\frac{\bar{\mu}}{Sc} + \frac{\bar{\mu}_t}{Sc_t})\frac{\partial \tilde{f}_n}{\partial x_j}] \qquad (19)$$

The modelled form of the mean species production rate due to chemical reaction ($\overline{\dot{w}_n}$) is given, for a finite-rate system involving L reaction steps and N species, in the following general form:

$$\dot{w}_n = M_n \sum_{l=1}^{L}(\nu_{nl}'' - \nu_{nl}') \times \{k_{fl}\rho^{m_l} \prod_{s=1}^{N}(\frac{f_s}{M_s})^{\nu_{sl}'} - k_{bl}\rho^{n_l} \prod_{s=1}^{N}(\frac{f_s}{M_s})^{\nu_{sl}''}\}, \qquad (20)$$

where

$$m_l = \sum_{s=1}^{N} \nu_{sl}', \quad n_l = \sum_{s=1}^{N} \nu_{sl}''$$

where, ν_{sl}' and ν_{sl}'' are the number of molecules of the scalar s involved in the l-th reaction step in the forward and backward directions, respectively. The forward and backward rate-constants of the reaction l are given by k_{fl} and k_{bl} respectively.

$$k_{fl} = A_l T^{b_l}\, exp[-\frac{T_{al}}{T}] \qquad (21)$$

where A_l, b_l and T_{a_l} are numerical constants specific to the given reaction step l. k_{bl} is determined from the equilibrium constant for the l-th reaction step and k_{fl}.

Solution of the modeled equations

The equations are discretized and integrated in space and time to obtain steady state solutions using the finite-volume based numerical solver TUFF [17]. The TUFF code contains many desirable features for the computation of three-dimensional, hypersonic flow fields. It has non-equilibrium, equilibrium and perfect gas capabilities along with an incompressible option. It employs a finite-volume philosophy to ensure that the schemes are fully conservative. The upwind inviscid fluxes are obtained by employing a new temporal Riemann solver that fully accounts for the gas model used. This property allows the flow field discontinuities such as shocks and contact surfaces to be captured by the numerical scheme without smearing. Total Variation Diminishing (TVD) techniques are included to allow extension of the schemes to higher orders of accuracy without introducing spurious oscillations. The schemes employ a strong coupling between the fluid dynamic and species conservation equations and are made fully implicit to eliminate the step-size restriction of explicit schemes. This is necessary since step-sizes in a viscous, chemically reacting calculation can be excessively small for an explicit scheme, and the resulting computer times prohibitively large. A fully conservative zonal scheme has been implemented to allow solutions of very complex problems. The schemes are made implicit by fully linearizing all of the fluxes and source terms and by employing a modified Newton iteration to eliminate any linearization and approximate factorization errors that might occur. Approximate factorization is then employed to avoid solving many enormous banded matrices. As mentioned before, the options for turbulence models include both zero and two equation models (both $k-\epsilon$ and $k-\omega$). For more details about the solution procedure the reader is directed to the reference cited above [17].

RESULTS AND DISCUSSION

Two reacting flow configurations have been chosen for the present study. As mentioned before, the Navier Stokes solver TUFF has been used for the computations. The first one is the case of coaxial jets [22, 23] where a hydrogen jet flows (inner jet) coaxially with an outer vitiated air (mass fractions: oxygen=0.246, water=0.209 and nitrogen=0.545) jet. A schematic of the flow problem is given in Figure 1. The two streams are, air (U=1380 m/sec, T=1180 K with p=107000 N/m2) and hydrogen (U=1774 m/sec, T=545 K with p=112000 N/m2)., The air stream is supersonic with a Mach number of 1.97 and the hydrogen stream Mach number is 1.00. The inlet mean velocity is assumed to have a step profile with the two jets having uniform speeds at the specified values (no experimental data available). The velocity in the lip region of the inner jet tube wall (finite wall thickness) is assumed to be zero. The inlet temperature profile is derived based on the experimental data given for a location just downstream of it (shown later). The inlet species mass fraction distributions are also chosen based on the experimental data provided at the same downstream location. A constant turbulence intensity level is used in the free stream for arriving at the initial distribution of turbulent kinetic energy and the dissipation rate. A 13-step, 8-species $H_2 - Air$ reaction model (Table 1) has been used for the finite-rate chemistry system considered here. A 81 X 91 grid (81 points in flow direction, 91 points in the radial direction) was used for the calculations. The inner jet/tube diameter (D=0.00236 m) is used as a reference length. The total length of the flow domain is equal to 43.1 D. The outer boundary (radial) of the flow domain is taken to be at y=17 D. A more detailed description of the flow parameters is given in Table 2. The region outside the limits of the air jet is assumed to be still air at a temperature of 273 K. The two-equation ($k-\epsilon$) turbulence model is used along with the finite rate H_2-Air chemistry model mentioned above. In all the figures shown in this report, y refers to the radial distance measured from the axis of the coaxial system of jets.

Figures 2 - 3 show the results of the computations. Figure 2 shows the computed and experimental distributions of species mole fractions. The figure is designed in a two-column format. The left side column represents the inlet (first x-location) data and the right side column is the data at the exit plane (x/D=43.1 D). As seen in these figures, the inlet data agreement between the computations and experiment is not perfect, especially around the jet edges, and this might affect the computed distributions at downstream locations. The comparison between predictions and experiment at the downstream location (x/D=43.1 D) is good given the above mismatch between the two data at the inlet. The development of the reaction zone after ignition is not predicted well. The experimental data indicates that the reaction zone (depicted by the water mole fraction distribution) spreads more quickly than the predictions indicate. The predictions show the reaction zone to be off-center whereas the experimental data shows the recation zone to be closer to the axis of symmetry. However, there is very good qualitative agreement berween the data with the peak values of the reaction products predicted very well. The flow domain was seen to have a wave-like structure as shown by the predicted profiles. The worst agreement seems to be for the case of oxygen. However, when the initial profiles of oxygen are compared one finds that there too is the worst agreement between computations and experiment which may be reason for the problem downstream. Figure 3 shows the comparison of static temperature data. The agreement between predictions and experiment is good qualitatively displaying similar trends. The uncertainty associated with the accuracy of the experimental data is unknown. There are considerable differences between the data presented by the two references [22, 23], especially in the temperature profiles. Overall, there is good qualitative agreement between the predictions and experiment.

The second test case considered is the Burrows-Kurkov experiment [21]. The flow configuration is two-dimensional. A schematic diagram of the configuration is given in figure 4. No-slip walls bound both the upper and lower regions (y=0 and y=y_{max}). The lower wall is inclined to form an expansion surface. Hydrogen is injected along this surface into a vitiated air stream. The two streams mix and react downstream of the injection location (inlet). The hydrogen stream is injected at a velocity of 1216 m/sec and a temperature of 254 K. The airstream comes in at a speed of 1764 m/sec and a temperature of 1270 K. Full details about the flow parameters and geometry are given in Table 3. In this case, the reference length used in the hydrogen jet width at inlet, h (h=0.004 m). The models for turbulence and chemistry are identical to the ones used for the coaxial jet case. The grid size is 81 X 121 (81 grid points in the axial (x) direction and 121 grid points in the transverse direction). The total length of the solution domain is 0.356 m (x/h=89). Available inlet data have been used for the first-plane profiles which improved the predictions remarkably over the solutions obtained with uniform profiles. The solutions are compared with the available experimental data at this location (exit) in figures 5-7. The solutions carried out with the space marching PNS code UPS [20] using the Baldwin-Lomax turbulence model are also given for comparison.

Figure 5 shows the compariosn between the predicted distributions of the species mole fractions and the corresponding experimental data. As seen in these figures, there is excellent agreement between the TUFF predictions and experiment. The predictions by the UPS code do not agree very well but still there is very good qualitative agreement with the experimental data. Figure 6 compares the predicted profiles of exit plane total temperature and Mach number with the experimental data. There is good qualitative agreement in the case of temperature and very good overall agreement in the case of the Mach number distribution. Figure 7 shows the comparison between the predictions and experiment of the lower wall (hydrogen jet side) pressure. Ignition causes the pressure rise in the profile. Ignition seems to be delayed in the case of the predictions accompanied by a more pronounced pressure rise.

High speed reacting flows such as the two cases studied here are complex inspite of their simple geometries. The interactions between the different aspects of the flow such as turbulence, chemical kinetics, heat release etc. are very difficult to understand and, to a large extent, impossible to model accurately. Modern day experimental facilities still cannot make complete measurements in such flows. Only mean values of temperature, velocity, pressure, species concentrations etc. are available, if any. Even then, the uncertainties associated with the data force one to accept them only with certain reservations. Given that, there is almost never a chance for perfect agreement between predictions and experiment in all the areas. While the advances made in measurement techniques improve every day, the fruits of these advancements (ie. accurate measurements) are not realized immediately. As a result, today's computations will have only old data for validation (in the present case, the best data is already four years old) purposes which is certainly the case here. Unless more accurate experimental data with minimum uncertainties are available, the best a computational effort can hope for, in terms of validation, is probably what is seen here.

CONCLUSIONS

Computation of the flow fields of two high-speed, turbulent, reacting flow configurations involving finite-rate chemical kinetics for hydrogen-air combustion have been carried out. A two-equation ($k-\epsilon$) turbulence model with compressibility corrections has been used. The predictions are compared with available experimental data. Good qualitative agreement is present between computations and experiment. More detailed experimental data is necessary.

ACKNOWLEDGMENTS

This work was supported by the Applied Computational Fluids Branch of the Fluid Dynamics Division at NASA Ames Research Center under the Cooperative agreement number NCC 2-715.

References

[1] Marvin, J. G., "A CFD Validation Roadmap For Hypersonic Flows", NASA Technical Memorandum 103935, 1992.

[2] Ebrahimi, H. B., "CFD Validation For Scramjet Combustor and Nozzle Flows, Part I", AIAA-93-1840, 1993.

[3] Vitt, P. H., Riggins, D. W. and McClinton, C. R., "The Validation and Application of Numerical Modelling to Supersonic Mixing and Reacting Flows", AIAA-92-0626, 1992.

[4] Riggins, D. W. and McClinton, C. R., "A Computational Investigation of Mixing and Reacting Flows in Supersonic Combustors", AIAA-92-0626, 1992.

[5] Eklund, D. R. and Northam, G. B., "A Numerical Study of the Effects of Geometry on the Performance of a Supersonic Combustor." AIAA-92-0624, 1992.

[6] Narayan, J. R. and Girimaji, S. S., "Turbulent Reacting Flow Computations Including Turbulence-Chemistry Interactions." AIAA-92-0342, 1992.

[7] Narayan, J. R., "A Two-Equation Turbulence Model for Compressible Reacting Flows." AIAA-91-0755, 1991.

[8] Eklund, D. R., "Calculation of Supersonic Turbulent Reacting Coaxial Jets." AIAA Journal, Vol.28, No.9, 1990, pp 1633-1641.

[9] Carpenter, M. H., "Three-Dimensional Computations of Cross-Flow Injection and Combustion in a Supersonic Flow", AIAA-89-1870, 1989.

[10] Drummond, J. P., Carpenter, M. H. and Riggins, D. W., "Mixing and Mixing Enhancement in Supersonic Reacting Flows", *High Speed Propulsion Systems: Contributions to Thermodynamic Analysis*, ed. E. T. Curran and S. N. B. Murthy, American Institute of Astronautics and Aeronautics, Washington, D. C., 1990.

[11] Drummond, J. P.,"A Two-Dimensional Numerical Simulation of a Supersonic, Chemically Reacting Mixing Layer", *NASA TM* 4055, 1988.

[12] Molvik, G. A. Bowles, J.V.and Huynh, L. C., "A Hypersonic Research Vehicle with Hydrocarbon Scramjet Propulsion: Design and Analysis", AIAA Paper 93-5097, 1993.

[13] Jones, W.P. and Launder, B.E., "The Prediction of Laminarization with a Two-Equation Model of Turbulence", *Int. J. Heat Mass Transfer*, Vol.15, 1972, pp 301-314.

[14] Launder, B.E., Reece, G.J. and Rodi, W., "Progress in the Development of a Reynolds Stress Turbulence Closure", *J. Fluid Mech.*, Vol.68, 1975, pp 537-566.

[15] Wilcox, D.C., "A Two-Equation Turbulence Model for Wall-Bounded and Free-Shear Flows", AIAA Paper 93-2905, 1993.

[16] Oldenborg, R. et al., "Hypersonic Combustion Kinetics - Status Report of the Rate Constant Committee, NASP High-Speed Propulsion Technology Team", *NASA TM* 1107, 1990.

[17] Molvik, G. A. and Merkle, C. L., "A Set of Strongly Coupled Upwind Algorithms for Computing Flows in Chemical Nonequilibrium", AIAA Paper 89-0199, 1989.

[18] Lawrence, S. L., Chaussee, D. S. and Tannehill, J. C., "Application of an Upwind Algorithm to the Three-Dimensional Parabolized Navier-Stokes Equations", AIAA 87-1112, 1987.

[19] Zeman, O., "Compressible Turbulence Subjected to Shear and Rapid Compression", Eighth Symposium on Turbulent Shear Flows, Munich, Germany, 1991.

[20] Wadawadigi, G. Tannehill, J. C., Buelow, P. E. and Lawrence, S. L., "A Three-Dimensional Upwind PNS Code for Chemically Reacting Scramjet Flowfields", AIAA 92-2898, 1992.

[21] Burrows, M. C. and Kurkov, A. P., "Analytical and Experimental Study of Supersonic Combustion of Hydrogen in a Vitiated Airstream." NASA TM X-2828, 1973.

[22] Cheng, T. S., Wehrmeyer, J. A., Pitz, R. W., Jarret, O. and Northam, G. B., "UV Raman Scattering Measurements in a Mach 2 H_2-Air Flame for Assessment of CFD Models." Proc. of the *Central States Meeting of the Combustion Institute*, Nashville, TN, 1991.

[23] Jarret, O. Jr., Cutler, A. D., Antcliff, R. R., Chitsomboon, T., Dancey, C. L. and Wang, J. A., "Measurements of Temperature, Density, and Velocity in Supersonic Reacting Flow for CFD Code Validation." Proc. of the *25th JANNAF Combustion Meeting*, Huntsville, Alabama, 1988.

[24] Williams, F. A., *Combustion Theory*. Addison-Wesley Publishing Company, Inc., Reading, MA, pp. 358-429, 1965.

Table 1. $H_2 - Air$ Reaction System

No.	Reaction
1	$H + O_2 \rightleftharpoons O + OH$
2	$OH + H_2 \rightleftharpoons H_2O + H$
3	$O + H_2 \rightleftharpoons OH + H$
4	$OH + OH \rightleftharpoons H_2O + O$
5	$H + OH + M \rightleftharpoons H_2O + M$
6	$H + H + M \rightleftharpoons H_2 + M$
7	$O + O + M \rightleftharpoons O_2 + M$
8	$H + O + M \rightleftharpoons OH + M$
9	$H + O_2 + M \rightleftharpoons HO_2 + M$
10	$OH + HO_2 \rightleftharpoons H_2O + O_2$
11	$H + HO_2 \rightleftharpoons H_2 + O_2$
12	$H + HO_2 \rightleftharpoons OH + OH$
13	$O + HO_2 \rightleftharpoons OH + O_2$
14	$HO_2 + HO_2 \rightleftharpoons H_2O_2 + O_2$
15	$H + H_2O_2 \rightleftharpoons H_2 + HO_2$
16	$OH + H_2O_2 \rightleftharpoons H_2O + HO_2$
17	$H + H_2O_2 \rightleftharpoons H_2O + OH$
18	$O + H_2O_2 \rightleftharpoons HO_2 + OH$
19	$OH + OH + M \rightleftharpoons H_2O_2 + M$
20	$OH + OH \rightleftharpoons H_2 + O_2$

Species : H_2, O_2, H_2O, OH, H, O, HO_2, H_2O_2 and N_2(inert)
M is a third body (all species included)

Table 2. Conditions for coaxial jet experiment

	H_2	Air
Mach No.	1.0	1.97
Temperature	545 K	1180 K
Pressure	0.112 MPa	0.107 MPa
Velocity	1774 m/s	1380 m/s
f_{H_2}	1.0	0.0
f_{O_2}	0.0	0.246
f_{N_2}	0.0	0.545
f_{H_2O}	0.0	0.209

Fuel injector diameter=0.00236 m
Lip thickness=0.000725 m
Nozzle diameter(air flow)=0.01778 m

Table 3. Conditions for Burrows-Kurkov Experiment

	H_2	Air
Mach No.	1.0	2.44
Temperature	254 K	1270 K
Pressure	0.1 MPa	0.1 MPa
Velocity	1216 m/s	1764 m/s
f_{H_2}	1.0	0.0
f_{O_2}	0.0	0.258
f_{N_2}	0.0	0.486
f_{H_2O}	0.0	0.256

Fuel injector height=0.004 m
Duct height at inlet=0.0938 m
Duct height at exit=0.1048 m

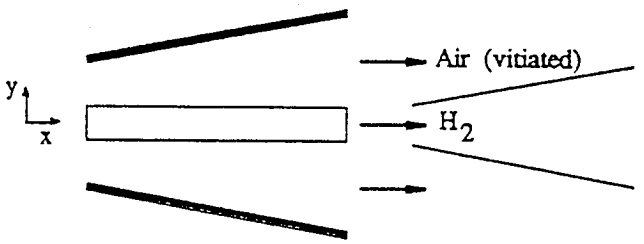

U_{air} = 1380 m/s T_{air} = 1180 K P_{air} = 107000 N/m^2

U_{H_2} = 1774 m/s T_{H_2} = 545 K P_{H_2} = 112000 N/m^2

Fig. 1 Coaxial jet case : schematic

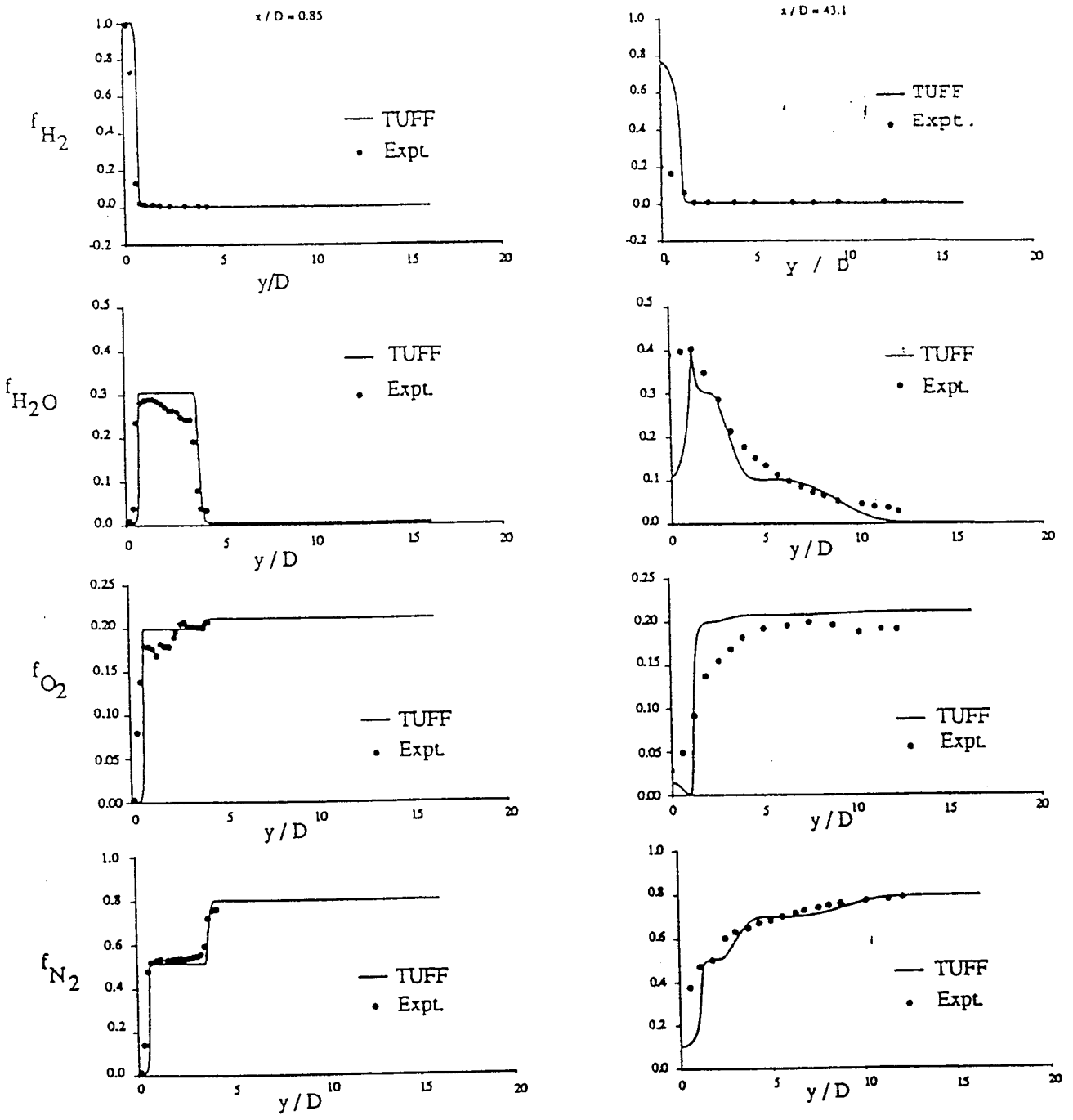

Fig. 2 Coaxial jet case: species mole fractions

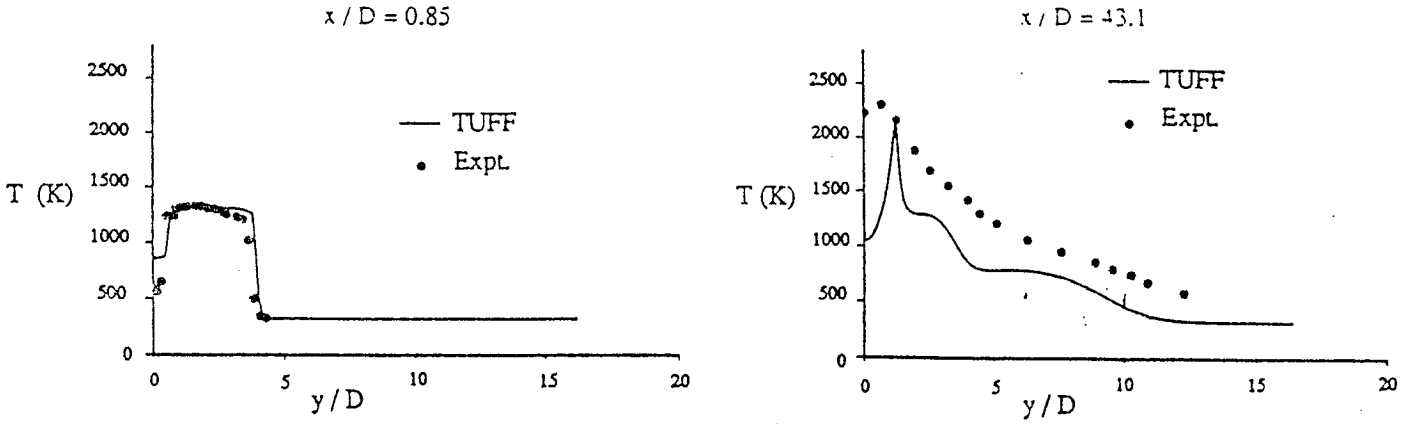

Fig. 3 Coaxial case : static temperature

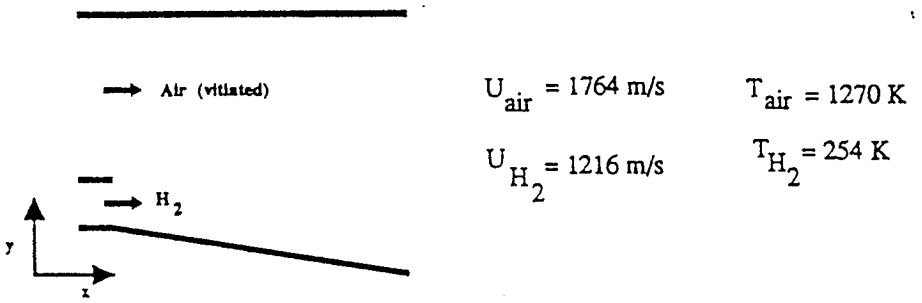

Fig. 4 Burrows-Kurkov expt. : schematic

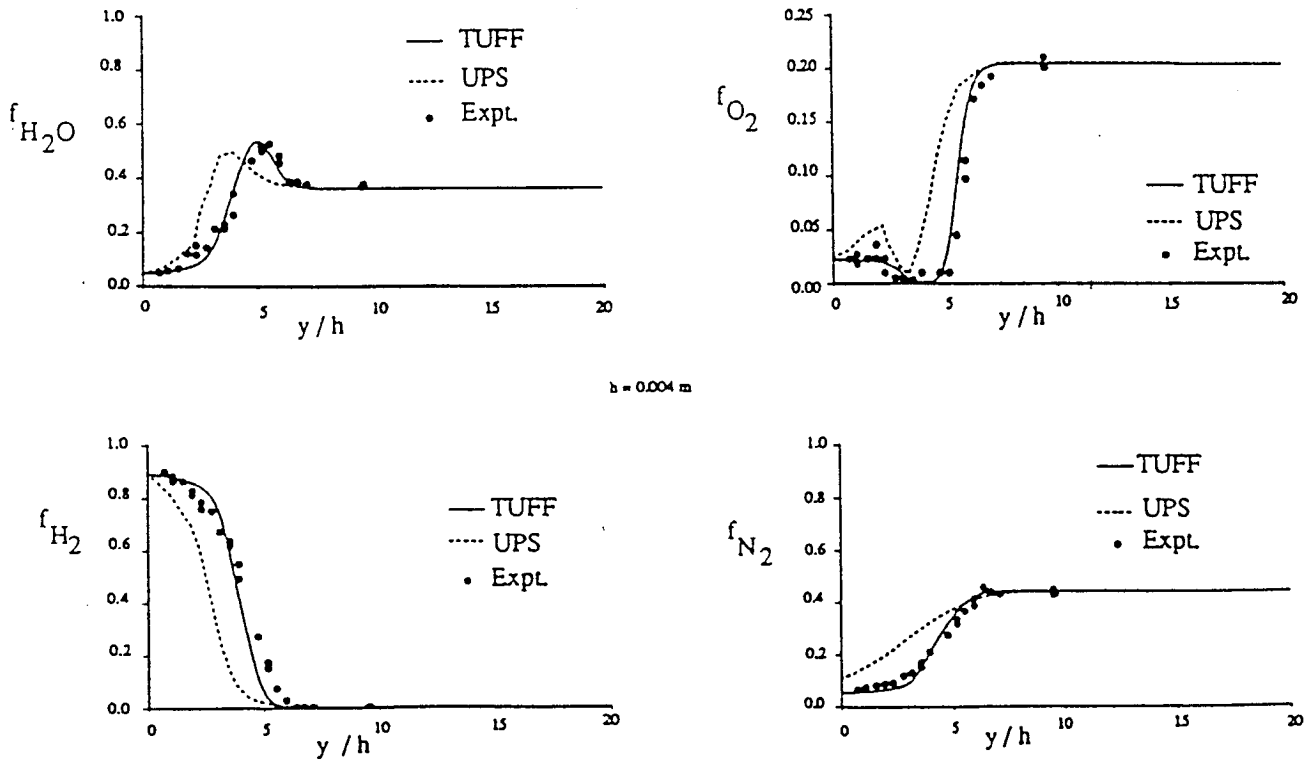

Fig. 5 Burrows-Kurkov expt. : species mole fractions at exit

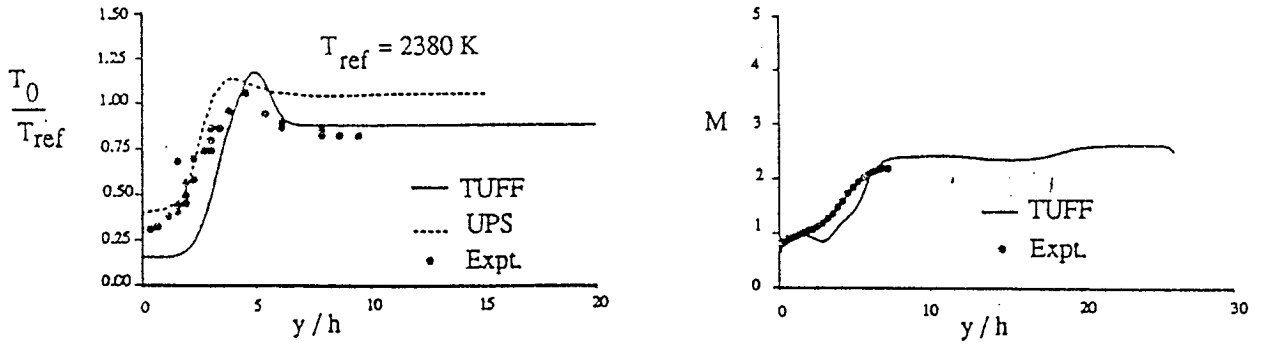

a) Total temperature

b) Mach number

Fig. 6 Burrows-Kurkov Expt. - Temperature and Mach number at exit

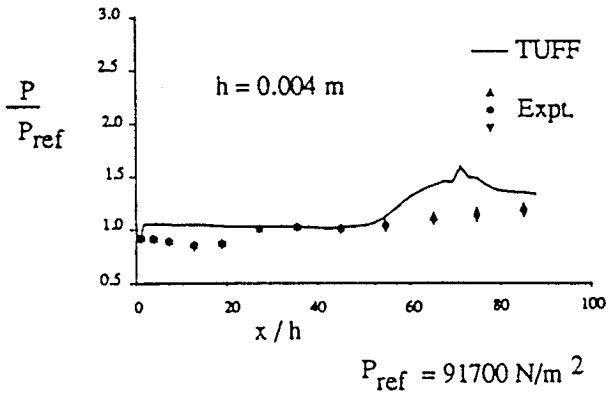

Fig. 7 Burrows-Kurkov expt. : wall pressure